Investigation of the Design, Manufacture and Testing of Additively Manufactured Coils for Electric Motor Applications

Cassidy Silbernagel, BSc

Thesis submitted to the University of Nottingham

for the degree of Doctor of Philosophy

June 2019

Contents

List of Figures

List of Tables

Abstract

Electric motor design has been relatively unchanged for nearly a century. However, there is a movement in our world to replace inefficient combustion technology with electricity. While current electric motor technology is being used in numerous areas, manufacturing has been limited to traditional techniques which result in inefficient and unreliable machines for achieving those electrification goals. As a result, there needs to be a shift in how these motors are manufactured and designed. Additive manufacturing (AM) can provide this shift, however, there has been both a lack of information on how to use AM to design for these applications and of electrical properties for AM materials processed by Laser Powder Bed Fusion (LPBF). This work helps to fill in some of this missing information.

The first part of this work used DfAM and first principles to design coils which help achieve the goals of efficient, powerful and robust electric motors. It was demonstrated that AM can greatly increase the fill factor of a motor which increases its power density and efficiency. It can minimise the amount of support material required which aids in creating coils with AM. AM can also modify the end-turns of a coil to aid in thermal dissipation which further improves efficiency and reliability.

Copper is a common material for electrical applications but has been very difficult to process with LPBF due to its high reflectivity and high thermal conductivity. Despite this, some have attempted to process copper but failed to provide any electrical properties such as resistivity. Despite a wide range of parameter optimisation, copper was not able to be processed in this work to a high density. Despite this, resistivity measurements with respect to initial build orientation and heat treatments were taken and found to be lower than fully dense AlSi10Mg. Artificial intelligence was also used to perform a secondary quality assessment of individual thin walls to aid in parameter optimisation. With the challenges of processing a high purity material to a high density, an aluminium alloy which can be processed to a high density was then studied.

AlSi10Mg is an alloy commonly used by LPBF, however, there has been an incomplete body of knowledge surrounding its electrical properties. Previous research has neglected initial build orientations, variations that heat treatment can cause, and used techniques that assumed isotropic properties. In this work, experiments were performed to characterise these effects to electrical resistivity and microstructure. In addition, a geometric accuracy study was performed in order to understand the differences between model and as-built dimensions.

The results from this work can be used as a guide to aid motor designers in using AM for electric motor manufacture. Through these improvements, electric motors can potentially become more powerful and reliable. They can then aid in global electrification and help reduce greenhouse gas emissions.

List of Publications, Conferences, and Awards

Published and Pending Journal Articles

"Electrical resistivity of additively manufactured AlSi10Mg for use in electric motors," *Additive Manufacturing*, vol. 21, pp. 395–403, May 2018. [1]

"Electrical resistivity of pure copper processed by medium-powered laser powder bed fusion additive manufacturing for use in electromagnetic applications," *Additive Manufacturing,* (Final reviewer decision pending), 2019

Conferences, masterclasses, talks

Canada Makes Additive Manufacturing Forum – Aerospace and Automotive Tooling, "How Additive Manufacturing has shaped the automotive sector and is driving it into the future," October 24, 2018, Waterloo, Ontario, Canada

Additive World Masterclass IV: Design for Additive Manufacturing, "How to (re)design your parts for Additive Manufacturing," October 26, 2017, Eindhoven, The Netherlands

Awards

Finalist: *Additive World Design for Additive Manufacturing Challenge 2018* - Student Category, Mar 2018, Additive Industries b.v., Eindhoven, The Netherlands

Runner Up (Panel): *East Midlands Doctoral Network (EmDoc) 3 Minute Thesis (3MT)*, Sep 2017, EmDoc 2017 conference, Nottingham, UK

1st Runner Up: *University of Nottingham 3 Minute Thesis (3MT) competition*, Jun 2017, LINK'17 Student- led interdisciplinary research conference, Nottingham, UK

Winner: *Additive World Design for Additive Manufacturing Challenge 2017 - Student Category*, Mar 2017, Additive Industries b.v., Eindhoven, The Netherlands

Winner: *Additive World Design for Additive Manufacturing Challenge 2016 - Student Category*, Mar 2016, Additive Industries b.v., Eindhoven, The Netherlands

Acknowledgements

Firstly, thank you to my supervisors Ian Ashcroft, Phill Dickens, and Michael Galea for all their feedback and insight which have helped me beyond measure. I also appreciate all the help received from the technicians of the Centre for Additive Manufacturing (CfAM, University of Nottingham, UK) Mark East, Mark Hardy and Joe White, as well as the support from Mirela Axinte and Romina Davoudi. Thank you to Richard Hague for leading and supporting this world class CfAM research group. I would also like to acknowledge the support from Martin Roe and the Nanoscale and Microscale Research Centre (NMRC, University of Nottingham, UK) for use of their SEM and EDX equipment, for Nesma Aboulkhair, Ian Maskery and Richard Selo for their support, feedback and also for their work in etching specimens, and also to Christopher Fox, who assisted with nanoindentation measurements. Finally, to Leonidas Gargalis for all his work in helping optimise and analyse the LPBF of copper.

Dedication

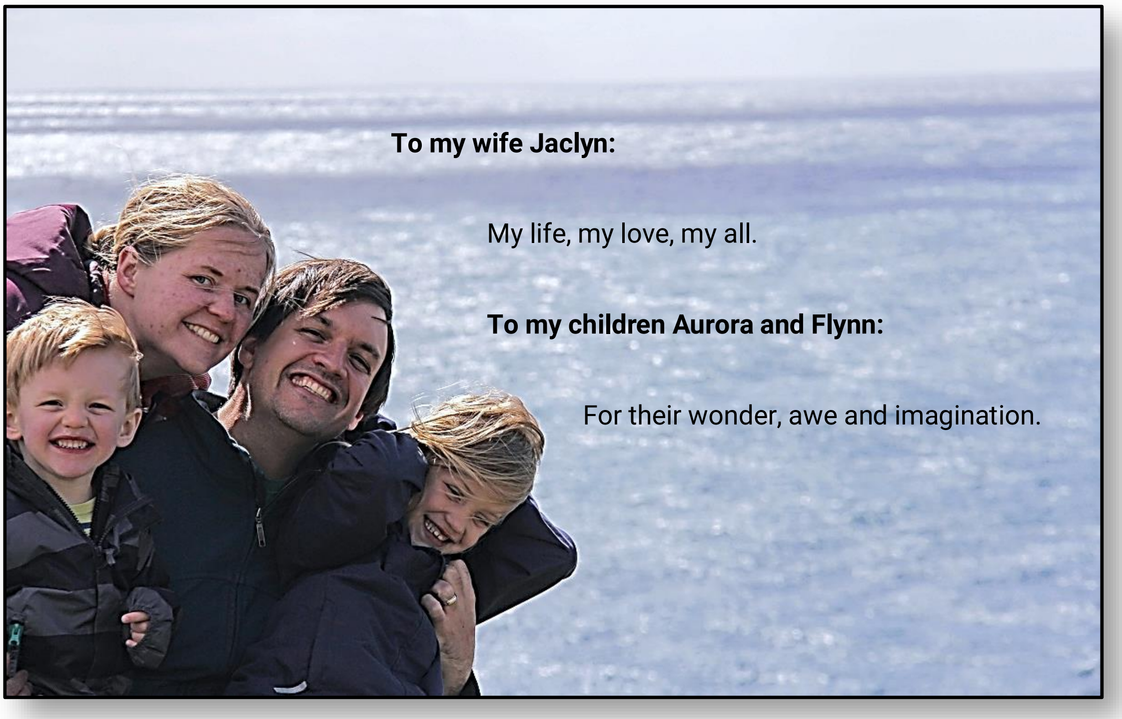

To my wife Jaclyn:

My life, my love, my all.

To my children Aurora and Flynn:

For their wonder, awe and imagination.

Abbreviations

2D	Two Dimensional
3D	Three Dimensional
3DP	3D Printing
AC	Alternating Current
AE	Autoencoder
AEA	All-Electric Aircraft
AI	Artificial Intelligence
ALM	Additive Layer Manufacturing
AM	Additive Manufacturing
ANN	Artificial Neural Network
API	Application Programming Interface
ASTM	American Society for Testing and Materials
CAD	Computer-Aided Design
CAE	Convolutional Autoencoder
CNC	Computer Numerical Control
CNN	Convolutional Neural Network
CPU	Central Processing Unit
CT	Computed Tomography
CW	Continuous Wavelength
DC	Direct Current
DCEC	Deep Convolutional Embedded Clustering
DDM	Direct Digital Manufacturing
DED	Directed Energy Deposition
DfAM	Design for Additive Manufacturing
DL	Deep Learning
DMLR	Direct Metal Laser Remelting

DMLS	Direct Metal Laser Sintering
DMP	Direct Metal Printing
EBM	Electron Beam Melting
EDX	Energy Dispersive X-Ray
EU	European Union
EV	Electric Vehicle
GE	General Electric
GHG	Greenhouse Gas
GPU	Graphics Processing Unit
HAZ	Heat Affected Zone
HIP	Hot Isostatic Pressing
IACS	International Annealed Copper Standard
IEC	International Electrotechnical Commission
IEEE	Institute of Electrical and Electronics Engineers
ILT	Fraunhofer Institute for Laser Technology
ISO	International Organization for Standardization
KNN	K-Nearest Neighbours
LBM	Laser Beam Melting
LCR	Inductance (L), Capacitance (C), and Resistance (R)
LDW	Lloyd Dynamowerke GmbH & Co. KG
LPBF	Laser Powder Bed Fusion
LPW	LPW Technology Inc.
MEA	More Electric Aircraft
MEPS	Minimum Energy Performance Standards
ML	Machine Learning
MLM	Micro Laser Melting
MLS	Micro Laser Sintering

MMF	Magneto-motive force
MNIST	Modified National Institute of Standards and Technology
MRI	Magnetic Resonance Imaging
PBF	Powder Bed Fusion
PCA	Principal Component Analysis
PD	Point Distance
PDMS	polydimethylsiloxane
PEO	Plasma Electrolytic Oxidation
PM	Permanent Magnet
ReLU	Rectified Linear Unit
RFN	Random Forest Network
RM	Rapid Manufacturing
RP	Rapid Prototyping
SCIM	Squirrel-Cage Induction Motor
SEM	Scanning Electron Microscope (Microscopy)
SFF	Solid Freeform Fabrication
SLA	Stereolithography (Apparatus)
SLM	Selective Laser Melting
SLS	Selective Laser Sintering
SS	Scan Speed
STL	Standard Tessellation Language file format
t-SNE	t-Distributed Stochastic Neighbour Embedding
UK	United Kingdom
USA	United States of America
VSD	Variable-Speed Drive
XCT	X-Ray Computed Tomography

Glossary

AlSi10Mg	Aluminium Silicon (10% weight) Magnesium (0.4% weight) alloy.
BH curve	A plot of a materials ability to retain magnetic flux given an external magnetic field.
Bulk properties	The material properties which are derived from a fully dense solid material with no voids.
Fill factor	The measure of the percentage of the slot area which is used as a conductor over the total area of the slot.
GRCop-84	NASA Glen Research Center Copper (Cr 8% weight, Nb 4% weight) alloy.
Hysteresis	For iron, it is a loss due to the amount of magnetic energy stored within it that is needed to be overcome to reverse the magnetic field.
Torque density	The ratio for a motor of output torque to its external volume.
Torque ripple	An engagement and disengagement of the rotor magnetic forces on the stator iron as it rotates.
Windage loss	In a rotating machine, it is the loss which occurs due to internal air friction of the rotating parts.

Symbols and Units

Elements

Al	Aluminium	Ni	Nickel
C	Carbon	Nd	Neodymium
Ce	Cerium	O	Oxygen
Cr	Chromium	P	Phosphorus
Cu	Copper	Pb	Lead
Fe	Iron	Si	Silicon
La	Lanthanum	Sn	Tin
Mg	Magnesium	Ti	Titanium
Mn	Manganese	Zn	Zinc
Nb	Niobium		

Formulas

ρ	Electrical Resistivity	F	Force
σ	Electrical Conductivity	I	Current
π	Pi	J	Current Density
ω	Angular Velocity	L	Length
$\bar{A}$	Specific Electrical Loading	N	Number of Turns of Poles
A	Area	P_{Cu}	Copper Loss
$\bar{B}$	Specific Magnetic Loading	P	Power
B	Flux Density	R	Resistance
D	Diameter	T	Torque
E	Static Electromagnetic Field	V	Voltage

Special Characters

®	Registered Trademark

Unit Prefixes (base ten magnitude)

n	nano (10^{-9})	c	centi (10^{-2})
μ	micro (10^{-6})	k	kilo (10^{3})
m	milli (10^{-3})	M	mega (10^{6})

Units of Measure
(*Unit Type*)

°	Degrees (*Angle*)
°C	Degrees Celsius (*Temperature*)
A	Amps (*Current*)
g/cm^{3}	Grams per cubic Centimetre (*Density*)
hr	Hours (*Time*)
Hz	Hertzs (*Frequency*)
K/s	Kelvins per Second (*Cooling Rate*)
g	Grams (*Mass*)
m	Metres (*Length*)
L	Litres (*Volume*)
mm/s	Millimetres per Second (*Velocity*)
mm^{2}	Square Millimetres (*Area*)
mm^{3}	Cubic Millimetres (*Volume*)
MW/cm^{2}	Megawatts per square Centimetre (*Laser Power Density*)
N	Newtons (*Force*)
px	Pixels (*Digital Length*)
rpm	Revolutions per Minute (*Rotational Speed*)
s	Seconds (*Time*)
S/kg	Siemens per Kilogram (*Specific Conductance*)
S/m	Siemens per Metre (*Electrical Conductivity*)
V	Volts (*Voltage*)
W	Watts (*Power*)
W/m*K	Watts per Meter-Kelvin (*Thermal Conductivity*)
μm/px	Micrometres per Pixel (*Digital Resolution Ratio*)
μΩ-cm	Micro-Ohm Centimetres (*Electrical Resistivity*)
Ω	Ohms (*Resistance*)

Chapter 1 Introduction and Motivation

1.1 Electric motors

All electric motors convert electrical power into mechanical power. There are many types of electric motors, but all are governed by the same underlying electromagnetic principles [2]. At a fundamental level, every motor has three parts. A rotating part called the rotor, a fixed non-moving part called the stator and a part that generates magnetic fields. The part that generates magnetic fields uses coils of wire, sometimes in conjunction with permanent magnets (PMs). From these core components, the basic active materials for an electric motor can be derived. These core components and materials have been developed and improved upon over the past one hundred years.

It is now estimated that in the EU, 69% of all electricity used in industrial applications is consumed by electric motors, as well as 38% in the services sector (non-residential buildings) [3]. This translates to 35-40% of all EU energy being consumed by electric motors. With this large amount of energy consumption, small gains in efficiency can greatly reduce both the amount of natural resources used as well as the amount of greenhouse contributing gases such as CO_2.

Historically, the golden age of electric motors was the mid to late 1800s where rapid advances in design and manufacturing occurred. Since then, all major advances in electric motor design have stemmed from new and improved materials [4], [5] or new manufacturing technologies which have led to new types of electric motors [2]. However, these ‘new’ manufacturing technologies still date back to the 1960s and 70s. These conventional manufacturing methods can have a negative effect on the repeatability and reliability of the electric motor, especially the motor coil windings [6]. In aerospace, this is a major bottleneck preventing electrical machines from finding a much more important role in the sector [7], [8]. However, there are modern manufacturing technologies such as Additive Manufacturing

(AM) which can overcome some of these historical limitations and will be the focus of this work. There are opportunities within the design and manufacture of electric motors that can leverage the advantages that AM can provide over traditional manufacturing such as a freedom of design and ease of manufacturing complex geometry. These advantages can result in higher power densities and higher efficiencies for existing designs which can in turn reduce the amount of greenhouse gases (GHGs).

Of the different areas where electric motors can be improved, there is an incomplete understanding on how AM can improve the design of electric motor coils, as well as how AM materials perform when used as electrical conductors. This is where this research will focus. Thus, before any widespread adoption of AM in the electric motor industry can occur, two things need to be understood.

Firstly, the mindset of electric motor designers needs to be shifted away from traditional manufacturing methods. The design of electric motors is tied directly to how they are manufactured, and these manufacturing methods have directly influenced how electric motors are designed. Before the widespread adoption of affordable 3D computer-aided design (CAD) tools, almost all motor designs were limited to 2D profiles extruded into 3D. These simple extruded designs were easily manufactured and analysed and thus were widely accepted and adopted. However, with modern 3D computing tools, motor designers have started thinking about how motors could move away from these traditional 2D designs [9]–[11]. However, as they are still limited to manual and semi-automated manufacturing methods, there are still limitations on design. AM does not have these same limitations, and although it is not entirely free from design limitations, it opens a wider range of freedom not currently experienced in electric motor design. Many improvements can potentially be achieved by AM, such as higher conductor utilisation and higher fill factors, better thermal management via controlled cooling and ventilation, and unique flux path geometry to reduce losses. Once a motor designer feels confident in the material properties of AM parts, they then need to embrace a Design for Additive Manufacturing (DfAM) mentality to move away from the traditional manufacturing mentality and help the electric motor industry incorporate AM. This is an area this research will address with respect to electric motor coils.

Secondly, the specific properties of AM materials related to their use within an electric motor need to be determined for motor designers to adopt AM. These properties extend beyond the traditional mechanical properties that are generally reported with each new material processed by AM. They include both the electrical and magnetic behaviour of materials and how they could differ from the traditionally manufactured properties. The potential material candidates for use in AM will be based on the materials currently found in electric motors. A thorough investigation of these materials with AM has only just begun and will potentially lead to a new golden age of electric motor design. Some researchers are already investigating AM and LPBF to manufacture soft magnetic materials for use in electric motor rotors and stators, reporting on their magnetic and electrical properties [12]–[17]. Some investigations also report that LPBF can process PMs [18]. However, there are relatively few published works relating to highly conductive materials such as copper and aluminium processed by AM with their corresponding electrical properties. Those which have published these electrical properties have either assumed isotropic material properties by using indirect eddy-current measurement techniques [19], or have neglected initial build orientation and heat treatment effects. This is also an area which this research aims to address. But an understanding of what AM is, how it works, and how it affects design first needs to be addressed.

1.2 Additive Manufacturing (AM)

AM has been called many different names over the past 30 years. Each term giving some insight into how the technology was being used at the time. Rapid Prototyping (RP) [20] was generally used for one-off proof of concept prototypes. Rapid Tooling [21] was used to create custom and flexible tooling, tooling inserts, jigs and fixtures. Rapid Manufacturing

(RM) [20] (now more commonly called AM) is used to create end-use parts or functional pieces. Several other generic or equivalent terms include 3D Printing (3DP) [22], Direct Digital Manufacturing [23], Additive Layer Manufacturing, and Solid Freeform Fabrication (SFF) [24].

One of the main attractions to AM is that it enables the manufacture of parts that could not otherwise be easily made using traditional subtractive (e.g. CNC machines) or formative (e.g. metal casting) techniques. AM provides a new tool for designers, who can then create optimised AM parts using some guiding principles. These principles are often referred to as DfAM and will be discussed later in this chapter.

AM can also be a faster and more economical way to make parts. This is especially true when the part is complex, is made from an expensive material, or is no longer available through previously accessible distribution channels. For example, German rail company Deutsche Bahn has demonstrated this by printing plastic and metal replacement parts for trains that are no longer in production.

In December 2015, a new standard was issued that defined terms and principles used in AM, ISO/ASTM 52900:2015 [25]. This standard was a collaboration between the F42 committee for the American Society for Testing and Materials (ASTM) and the ISO/TC 261 technical committee for International Organization for Standardization (ISO). It defines common terminology, references common file formats used in AM, provides some basic AM principles, and establishes seven categories of different AM processes.

These seven categories are (in alphabetical order):

i. Binder Jetting
ii. Directed Energy Deposition (DED)
iii. Material Extrusion
iv. Material Jetting
v. Powder Bed Fusion (PBF)
vi. Sheet Lamination
vii. Vat Photopolymerisation

Of these seven categories, the majority of metal AM parts are created within the category of powder bed fusion. Within that category, there are many different types of technology that can process metal. The most common metal process is Laser Powder Bed Fusion (LPBF), which as the subject of this thesis, and is discussed in more detail in the next section.

1.3 Laser Powder Bed Fusion (LPBF)

Powder Bed Fusion (PBF) has been defined as:

> *“An additive manufacturing process in which thermal energy selectively fuses regions of a powder bed.”* [25]

Of the many processes that are contained within PBF, Laser Powder Bed Fusion (LPBF) is a generic term for any laser-based process within this category, with several trade specific names describing the same process. LPBF is also known as (in alphabetical order):

- Direct Metal Laser Remelting or DMLR [26]
- Direct Metal Laser Sintering or DMLS® (EOS GmbH) [26]
- Direct Metal Printing or DMP (3D Systems Corporation)
- Laser Beam Melting or LBM [27]
- LaserCUSING® (Concept Laser GmbH) [26]
- Laser Metal Fusion (TRUMPF Laser Technology)
- Micro Laser Melting or MLM [28]
- Micro Laser Sintering or MLS (EOS GmbH) [28]
- Selective Laser Melting (SLM)

In this thesis, the term Laser Powder Bed Fusion (LPBF) will be used.

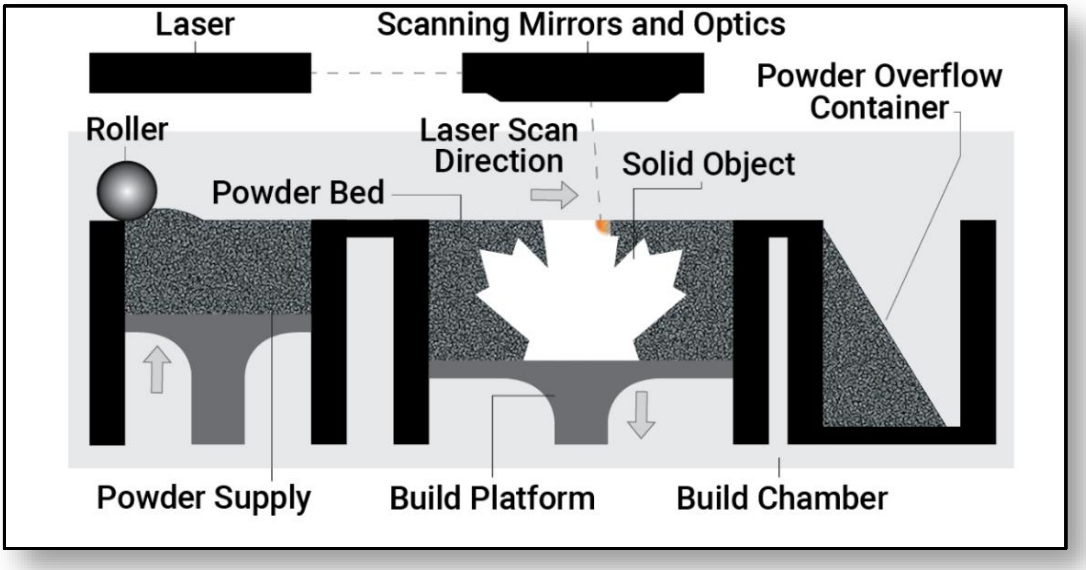

Figure 1-1: Laser Powder Bed Fusion example machine set up (Thesis original commissioned art [29]).

All LPBF methods start with a powder bed, an example is seen in Figure 1-1. A thin layer of metal powder, between 0.02mm and 0.1mm, is spread flat over a build platform. This layer of powder is then selectively irradiated by a laser beam which supplies a significant amount of thermal energy to the powder, dependent on the absorptivity of the laser radiation by the metal in the powder bed. The aim is that in the irradiated regions only, the powder is fully melted, to the point where it fuses to itself and to the previously solidified layers below. The build platform is then lowered, a new layer of powder is deposited, and the process is repeated, layer by layer, until the part is complete. Due to the reactive nature of some powdered metals, the process takes place in an inert, nearly oxygen-free environment, typically filled with either nitrogen or argon gas. The build chamber often has a heated bed in order to raise the temperature of the powder. This lowers the amount of energy required to melt the powder by the laser and helps reduce stress resulting from the rapid solidification of the molten metal. Although the terms DMLS and MLS contain sintering as part of their name, the process aim is to melt the material, not just sinter as their names suggest. LPBF processes fully melt the material and can potentially result in fully dense parts. LPBF can also result in significant residual stress, depending on material, geometry, and laser parameters, and thus there is a need to design support structures to prevent part distortion during the build. Residual stress occurs due to the large thermal gradient during LPBF process causing differential thermal expansion and contraction and results in deformation and potentially cracking and failure if not controlled [30].

LPBF has now matured from a research tool to industrial application and is being used in aerospace and healthcare to transform their respective industries. Companies, such as GE, are rapidly adopting and exploring the possibilities of using this technology, as with GE's successful implementations of the Leap fuel nozzle tip and custom engine brackets [31]. Individuals are also benefiting from the highly customised and highly detailed implants that can be made using bio-compatible metals in LPBF [32]. However, there are still many industries that have not fully explored the possibilities and potential of AM. One of these areas is the manufacturing and design of electric motors, as mentioned previously. But in order to enable the transformative power that AM can provide to any industry, a shift in manufacturing mentality needs to take place by understanding how to use the guiding principles of DfAM.

1.4 Design for Additive Manufacturing (DfAM)

AM has a design freedom that is not as constrained as traditional manufacturing. This design freedom enables several principles that can be taken advantage of because of AM. These principles include reducing assembly part counts by consolidating multiple parts into one, improving performance by creating complex internal geometry, reducing weight by removing excess material, and automating some of these processes by means of topology optimisation. When transitioning from traditional design to DfAM, a few different approaches can be taken. The following approaches are listed from quickest to implement to the most effort to implement.

Figure 1-2: DfAM level one – Direct replacement parts such as a 3D printed wrench [33].

The first and easiest scenario is to take an existing design, without modification, and create it using AM technology (see Figure 1-2). This is advantageous when the single part is excessively complex, making it difficult to produce using traditional methods. It is also desirable to use AM if it is made from materials that are expensive and minimal waste is desirable. In addition, if the parts are no longer available through previous supply chains, then AM can be an effective source for replacement parts.

Figure 1-3: DfAM level two- Modify existing parts such as using topology optimisation on a bracket [34].

The second is to follow DfAM [23] rules to redesign a single part to either improve performance or decrease weight (see Figure 1-3) by the use of design optimisation methods [35]–[37] and/or to make the part better suited for AM [38]–[40]. This allows for direct replacement parts to be made while making them either lighter, cheaper, or stronger. It involves minimal redesign of assemblies and can be trialled and tested while minimising the risk associated with adopting a new manufacturing technology.

Figure 1-4: DfAM level three – Combine multiple parts as with the GE Leap fuel nozzle before redesign [41] (right) and after redesign [42] (left).

The third scenario is to combine multiple parts to aid in part reduction, reduce assembly costs, and enhance performance (see Figure 1-4). This occurs once a company or individual are comfortable with DfAM and have proven its value with individual parts. By combining parts, significant improvements can be had in terms of assembly cost, parts cost, inventory reduction, weight reduction, and performance increases. This is the situation that allowed the GE Leap fuel nozzle to go into mass production. It still looks and behaves very similar to the original and can fit into existing assemblies, while still providing the previously mentioned benefits (although it is only the tip that is manufactured via AM, with the rest of the assembly being cast with minimal post-processing [43]).

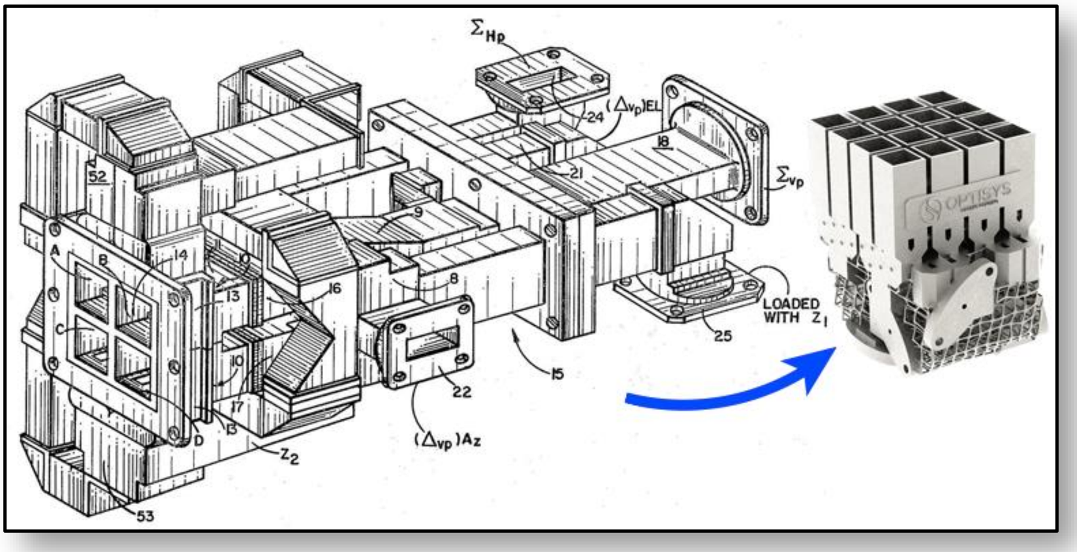

Figure 1-5: DfAM level four – Redesign from first principles such as the reimagined antenna design by Optisys [44].

The fourth is to completely rethink the overall assembly and redesign according to basic first principles and analysis of design requirements (see Figure 1-5). While this complete redesign can yield the greatest results, it takes the most time and effort to achieve. It requires a mastery of DfAM as well as the functions and purposes of the intended application. Despite the vast amount of effort this approach takes, this is where AM can be a transformative and disruptive technology for many different industries.

By combining DfAM, LPBF, and characterised AM materials, the electric motor industry could potentially be transformed. New families of electrical machines could be created that were impossible to manufacture using traditional methods. Some researchers have already started to investigate aspects of AM with electric motors [45]–[47], but they have not fully combined all of these elements. This research helps fill some of the existing gaps and encourages this adoption to take place.

1.5 Significance and novelty of this research

For electric motors to be able to benefit from the advantages that AM can provide, there are two areas that need to be addressed. First, there needs to be an understanding of how DfAM can be used for electric motors as current motor designers have demonstrated a lack of understanding of the potential that AM has in redesign. This research addresses the design and manufacture of electric motor coil windings, as well as the advantages and considerations that are required to create them using AM. The research also proposes design guidelines based on DfAM that can aid in either the retrofitting of motor coil windings into existing motors or for creating new winding geometries for new motor topologies.

Second, there needs to be a characterisation of the electrical properties of metal parts created through AM as there is an incomplete body of published data relating to these properties. This research aims to address this gap of understanding how metals processed by AM behave electrically as will be shown in the Literature Review with respect to initial build orientation, heat treatments, and using a direct resistance measurement technique. Pure copper is a widely used and popular choice for electrical machines due to its low resistivity, but electrical data has not been published for it as processed on a 200 W AM machine with a small spot size, despite numerous attempts to process it. The aluminium alloy AlSi10Mg has been widely researched, however, there has not been a comprehensive investigation into the electrical properties as processed by AM. This work fills in this lack of electrical knowledge for this alloy. Both materials are thus characterised in this research in the as-built condition according to build parameters that maximise relative density. The as-built electrical properties are modified through post-processing, and based on this work, AlSi10Mg has now been investigated and reported in the journal Additive Manufacturing [1]. Any differences found in resistivity then needed to be understood according to processing parameters, microstructure, geometry, and post-processing.

1.6 Thesis overview

<table>
<tr><td colspan="3">Aim: To show how using DfAM can improve upon electric motor coil design and to address the lack of directly measured electrical properties of highly conductive metals processed by LPBF.</td></tr>
<tr><td>Design for Additive Manufacturing</td><td colspan="2">Material Characterisation</td></tr>
<tr><td><i>Design of electric motor coils</i></td><td><i>Processing of pure copper</i></td><td><i>Processing of AlSi10Mg</i></td></tr>
<tr><td colspan="3">Objectives</td></tr>
<tr><td>Design and manufacture electric motor coils for an existing electric motor and characterise the coil properties.</td><td>Determine the LPBF processing parameters for pure copper to maximise relative density and directly measure the electrical resistivity and to evaluate machine learning as a parameter optimisation aid.</td><td>Directly measure the electrical resistivity of LPBF AlSi10Mg alloy with respect to initial build orientation and determine how to minimise resistivity via post-processing.</td></tr>
<tr><td colspan="3">Methodology</td></tr>
<tr><td>Develop different 3D CAD models of coils based on first principles that can be compared using DfAM which are then constructed out of LPBF AlSi10Mg and evaluated.</td><td>Fabricate thin walls and test cubes using a range of laser scan parameters and strategies to then construct rectangular bar specimens. Use machine learning to aid in quality assessment compared to a traditional parameter optimisation.</td><td>Construct rectangular bar specimens using previously optimised LPBF parameters and subject them to various post-processing treatments. Evaluate methods to improve surface finish.</td></tr>
<tr><td>Chapter 4</td><td>Chapter 5</td><td>Chapter 6</td></tr>
</table>

Figure 1-6: Overview of thesis aims, objectives.

1.6.1 Aim

This research aims to show how AM can improve upon electric motor designs by using the principles of DfAM to fit an existing electric motor with AM coil windings. This research also aims to address the lack of directly measured electrical properties of highly conductive metals processed by LPBF and compare them their traditionally manufactured properties. The materials explored will be pure copper which is difficult to process in LPBF machines but is highly desirable in electrical applications due to its low resistivity, and the aluminium alloy AlSi10Mg which is easily processed but has not been studied exclusively for electrical properties.

1.6.2 Objectives

This research will:

- Design and manufacture replacement electric motor coils motor using DfAM
- Determine the electrical resistivity of LPBF pure copper based on the maximum density achieved through parameter optimisation in a 200W LPBF machine
- Use machine learning to help aid in the evaluation of process parameterisation
- Determine the electrical resistivity of LPBF AlSi10Mg alloy and how to minimise resistivity through heat treatment post-processing

1.6.3 Methodology

The methodology for investigating the electrical properties of a material processed by LBPF is shown in Figure 1-7.

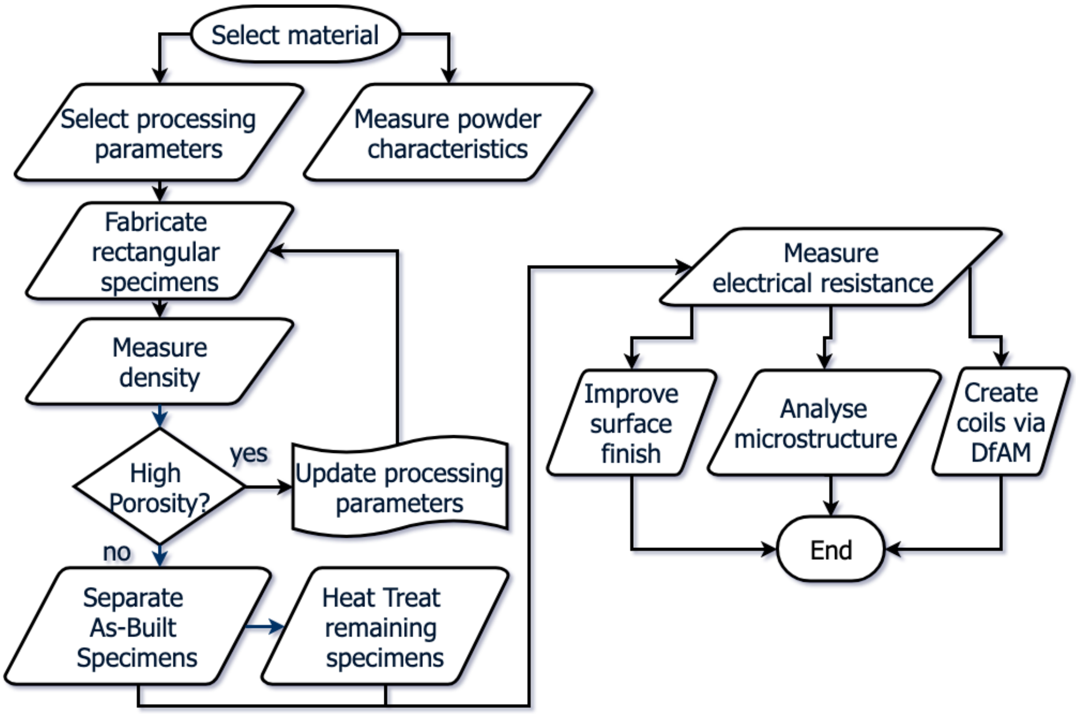

Figure 1-7: Methodology of research for investigating electrical properties of AM materials.

1.6.4 Structure

Chapter 1: An overview of areas this research covers: electric motors, AM, LPBF, and DfAM.

Chapter 2: A literature review of the most recent and relevant research surrounding:

- Electric motors and current AM efforts to create electric motors
- Summary of AM processes resulting in conductive parts
- Pure copper processed by LPBF
- Aluminium alloys processed by LPBF
- Machine learning in AM

Chapter 3: A review of the materials and methods used in this research.

Chapter 4: The results of using first principles and DfAM to create and analyse an AM design for electric coils for an electric motor.

Chapter 5: The results and discussion of processing pure copper with a 200 W LPBF machine including machine learning quality assessment and determining the resulting resistivity.

Chapter 6: The results and discussion of determining the resistivity of AM processed AlSi10Mg along with improving and understanding the surface finish and tolerance.

Chapter 7: A discussion of the previous chapter’s results, demonstrating how this research achieved its aims and objectives including what has been added to literature and how it fits.

Chapter 8: A brief conclusion and recommendations for future work.

Chapter 2 Literature Review

2.1 Introduction

This thesis covers topics including the design of electrical coils using DfAM, material characterisation of both copper and AlSi10Mg, and machine learning. But before covering these topics, a review of past and current knowledge surrounding these areas needs to be addressed. First, a background on electric motors and motor coil windings along with the latest research investigating the use of AM with electric motors. Then a summary of AM processes that can produce high density and conductive parts. Next, the latest information on processing copper with LPBF, followed by processing aluminium alloys with LPBF. Following this, an overview of research that has combined machine learning and artificial intelligence with AM to improve AM processes. At the end of each of these sections, the key findings from the literature review will be presented and summarised with the gaps in the current knowledge identified and will be used as motivations for this work.

Before discussing electrical motors, as well as copper and aluminium processed by LPBF, it is important to understand the basics of why these materials are of interest for electric motors. A critical component of an electrical machine is its motor coil windings which help create an electric field. These windings are usually comprised of a series of coils. The coils are wires made of a conductive material surrounded by an insulative material. The conductive core must have a low electrical resistance in order to minimise Joule losses. Joule losses are calculated by the I^2R loss of a wire where I is the current being passed through a wire and R is the resistance of that wire. This loss manifests as excess unwanted heat. The resistance of a wire is determined by the electrical properties of the base material.

One of the key electrical properties of a material is its electrical conductivity (measured in siemens per metre with units of S/m) or electrical resistivity (measured in ohm-metres or for ease of reading, micro-ohm centimetres with units of µΩ-cm). Electrical conductivity and resistivity describe the same property and are the inverse of each other, where one siemens equals one Ω^{-1}. Another common measure is the International Annealed Copper Standard (IACS) percentage. This percentage of conductivity compares the conductivity of a material to a commercially standard material, where 1.7241 µΩ-cm equals 100% IACS. Both electrical resistivity measured in µΩ-cm as well as IACS will be reported. The lower the resistance, the less loss occurs in the material when current passes through it.

Typical materials used in conductive wires are alloys made from copper, silver, gold, or aluminium. Table 2-1 contains common metals and alloys which are either already used in creating electrical wires or are of interest to process with LPBF. This table also has an additional property called specific conductance. While this is not a typical derived unit, it is useful in determining the amount of conductance per mass of a material for the same length and volume, given in siemens per kilogram. Higher values will be able to carry more current per kilogram of material. Traditionally, wires made from these common conductors are manufactured by producing conductive cores by pressing and/or rolling and then soaking them in a melted insulation bath that becomes the insulation cover once it’s cooled.

Description	***Electrical resistivity (µΩ-cm)***	***Density (g/cm^3)***	***Specific Conductance (S/kg)***
Pure Silver	1.586 [48]	10.492 [48]	6010
Pure Copper	1.6729 [49]	8.94 [50]	6686
Commercially pure Copper	1.7241 [51]	8.94 [50]	6488
Pure Gold	2.192 [48]	19.37 [52]	2355
GRCop-84 Cu alloy	2.45 [53]	8.87 [53]	4602
Pure Aluminium	2.6548 [54]	2.688 [52]	14013
1350 electrical Al alloy	2.82 [55]	2.705 [55]	13109
AlSi10Mg cast alloy	4.91, 4.26-5.56 [56], [57]	2.659 [56]	7659
Beryllium Copper 25 alloy	7 [58]	8.23 [58]	1736
Yellow Brass (70% Cu, 30% Zn)	8.85 [50]	8.44 [50]	1339
50-50 Solder (50% Pb, 50% Zn)	15 [58]	8.89 [58]	750

Table 2-1: Electrical resistivity, density and specific conductance of common metals and alloys used in electrical applications at room temperature.

After comparing the materials listed in Table 2-1, the ones which hold the most interest are copper based materials, as well as aluminium based materials. While both silver and gold have low resistivities, their high densities and high costs make them prohibitive to use in electric motor applications. Copper alloys generally have much higher resistivities compared to pure copper which is undesirable. While GRCop-84 is attractive, there is no supply of this alloy outside of NASA distribution channels, however this may change in the future as it is an alloy of high interest. Thus, pure copper is a logical material to process using LPBF due to its low resistivity, but as will be seen in Section 2.9, it is extremely difficult to process. Despite this difficulty, there has not been any electrical characterisation of copper processed by LPBF which has taken direct measurements, or which have accounted for initial build orientation or post heat treatments. Therefore, pure copper will be investigated in this work. Alternatively, pure aluminium and the 1350 alloy (which is 99.5% pure Al) are attractive to process due to their low resistivities and high specific conductance, but as will be seen in Section 2.10, high purity aluminium has the same difficulties in processing with LBPF as with pure copper. Thus, the AlSi10Mg alloy is desirable to characterise electrically due to its ability to process to a high density, despite it inevitably having a lower conductivity. AlSi10Mg, despite being widely researched, has lacked a thorough investigation into the electrical properties with respect to initial build orientation and post heat treatments. Therefore, AlSi10Mg was the second material to be investigated for use in electric motor coil applications. But before these materials are used to manufacture coils, it is important to learn how DfAM can be used to design the coils by first investigating how they function.

Key findings from this section

- Both copper and aluminium are attractive to use for electrical applications
- A pure metal which will likely to be difficult to process by LPBF should be researched
- Pure copper processed by LPBF has not had direct electrical measurements taken
- An alloy which is easier to process by LPBF should also be studied for conductivity
- AlSi10Mg has lacked resistivity measurements measured for various conditions

2.2 First principles of electric motor coils

In order to make the most use of DfAM, it is advantageous to go back to first principles. For an electric motor coil, this is understanding the governing principles to produce a magnetic field and how it affects the properties of an electric motor. All non-linear motors have a rotating component called the rotor, and a stationary part called the stator. There are a countless number of different electric motor designs, but all follow the laws of electromagnetism and material science. The basic principle that underpins all electrical machines consists of nothing more than the force that is experienced by a current carrying wire within a magnetic field, as seen in Figure 2-1.

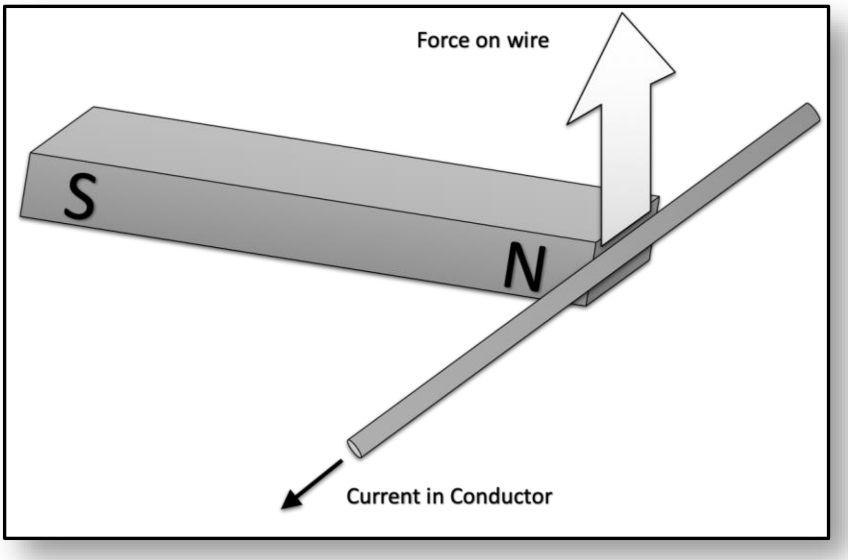

Figure 2-1: Force on a wire within a magnetic field.

A force (F in newtons) is created when a length of wire (L in metres) with a current (I in amperes) running through it is put into a magnetic field that is uniform in flux density (B in teslas), as stated in Equation 2-1.

$$F = BIL \tag{2-1}$$

A single wire with current creates a magnetic flux, which is the path in which a magnetic field flows as it connects a north and south magnetic source. Flux lines are often used as a visual representation of this magnetic field. Flux can be generated by using a single wire with a current or can be enhanced using coils of wire as seen in Figure 2-2. The effect of this concentrated flux is called the magnetomotive force (mmf).

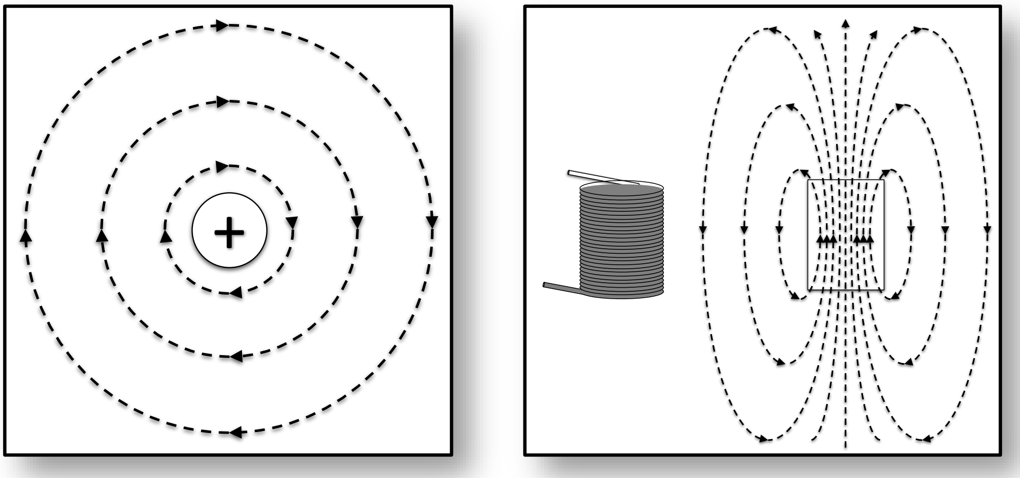

Figure 2-2: Visualisation of magnetic flux lines in a single wire (left) and in an air coil winding (right).

The mmf can be calculated by the number of turns (N) that a coil has, and by the current (I in amperes) flowing through the coil as seen in Equation 2-2 with units of ampere-turns.

$$mmf = NI \tag{2-2}$$

For a given motor design, the same mmf can be achieved through either a single turn of wire with very high current, or many turns with a much lower current. The mmf does not depend on the coil geometry or if the turns are loosely or tightly wound. However, the length of coil will affect other properties such as the resistance of the coil as seen with Equation 2-3. The resistance of a specimen can be directly measured by an ohm-meter but can also be calculated by the following Equation 2-3.

$$R = \frac{\rho L}{A} \tag{2-3}$$

Electrical resistance (R) is the product of the electrical resistivity (ρ) measured in μΩ-cm and the length of the specimen (L) in cm, divided by the cross-sectional area (A) of the specimen measured in cm^2.

As electric motors convert electrical energy into mechanical energy, some of the energy is converted into heat. This is considered a loss and lowers the efficiency. One of the largest sources of loss that apply to all motors is copper loss. Copper loss is due to the resistance (Equation 2-3) experienced by an electrical current when flowing through a conductor, due to the conductor's inherent resistivity. It accounts for about half to two-thirds of the total loss of the motor [59]. Regardless of the specific conductor material involved (copper, aluminium, brass), this is still called copper loss. Copper losses result both from the DC component of the currents in the coil as well as the AC components. However, the latter only become important for high speed and high frequency applications. Therefore, traditionally the DC copper loss is the dominant component and usually the AC losses in the copper are neglected. Thus, for traditional designs, the copper loss is calculated using DC resistance. Copper loss (P_{Cu} in watts) is a function of the total resistance of the material (R in ohms) and the total current (I in amperes) passing through the material, as in Equation 2-4.

$$P_{Cu} = I^2 R \tag{2-4}$$

To reduce the copper loss in a motor, a few different steps can be taken. First, the conductor material can be replaced with one that has a lower electrical resistivity, thus reducing the resistance of the material. Next, the total amount of conducting material can be increased while keeping the current the same which will also reduce the resistance of the coils. This is often referred to as increasing the fill factor of the motor. The fill factor is a measure of the percentage of the slot area which is used as a conductor over the total area. This percentage is lowered when there is unused space, excessive insulation, or poor utilisation of the space through randomly distributed conductors. Lastly, it is best to keep the conductor's temperature as low as possible, as resistance increases as a function of temperature.

It is important to also recognise that if the copper loss cannot be reduced, the copper loss as a percentage of the overall motor efficiency can be reduced. The concept is due to electrical power being defined as voltage times current, and that the copper loss depends on the amount of current passing through the coil. Therefore, by increasing the voltage, one can decrease the current (and thus the copper loss) and still maintain the same expected power rating. Another perspective is that if the current is not decreased, then an increase in voltage results in more electrical power. This allows the same DC loss, but the system has more power overall, therefore the motor is more efficient.

Another important relationship within an electric motor is the production of output torque and power. Torque is simply defined as a force acting at a distance and is the main factor which defines the size of a motor. This force is derived from the electromagnetic force (BIL) in Equation 2-1. However, when this concept is applied to an electric motor, the magnetic flux, current, and length need to be averaged over the entire surface of the rotor. This averaging over the surface of the rotor for magnetic flux (B) results in a specific magnetic loading ($\bar{B}$), for current (I) it results in a specific electrical loading ($\bar{A}$), and length (L in metres) becomes the surface area of a cylinder. The distance at which this force acts is half the diameter (D in metres) of the rotor. This relationship is demonstrated in Equation 2-5.

$$T = (\bar{B}\bar{A}) \times (\pi DL) \times \frac{D}{2} = \frac{\pi}{2}(\bar{B}\bar{A})D^2L \qquad (2\text{-}5)$$

Power is typically defined as a work performed over a period of time, but in a rotary situation, it becomes a torque acting through an angular velocity. This power relationship can be simply written as seen in Equation 2-6 where power (P in watts) is a product of torque (T in newton-meters) and angular velocity (ω in radians per second), where torque is defined in Equation 2-5.

$$P = T\omega = \frac{\pi}{2}(\bar{B}\bar{A})D^2L\omega \qquad (2\text{-}6)$$

Power is a function of volume (D^2L) and angular velocity (ω in radians per second). One implication for this equation is the cost of an electric motor. For a given power and specific loadings, the motor can either be large and slow, or small and fast. However, a larger but slow motor will consume more raw materials and be more expensive to manufacture than a smaller faster motor. But conversely, a small fast motor typically needs a reduction device such as gears or belts to bring the speed down to operating parameters. These add additional cost and may decrease reliability and increase maintenance.

As these equations govern almost all electric motors, there are some insights that can be learned, including how AM can potentially use these principles to redesign electric motors. The first is that electrical machines are generally constrained by two main limits, namely the electromagnetic limit and the thermal limit [60]. The electromagnetic limit is defined by the electromagnetic circuit of the machine and is governed by the geometry and the properties of the soft magnetic materials used in the design of the machine. Conversely, the thermal limit is defined by the losses being produced in the machine as excess heat. As described previously, for the most common low-speed machines, a major component of these losses is the copper loss that, in practice, is driven by the electrical loading of the machine. Therefore, by addressing these two constraints, several improvements for electrical machine design can be achieved. For example, if one was to consider machines for transport applications, where weight and volume of a machine are important, then by improving these limits, significant improvements can be made.

As will be seen in Chapter 2.6, AM has been used to print some inactive components of an electric motor such as the housing, shafts and other accessories. While this can reduce the weight of a motor, it does not address the two limits described previously. To address the electromagnetic and thermal limits, active components need to be manufactured using AM which have known and understood properties and are comparable to traditionally used materials. If these properties are known, then AM can address these two limits.

While the electromagnetic limit is partly governed by geometry, the largest factor for it is defined by the material properties for the soft magnetic components. Since AM has a freedom of design not seen by traditional manufacturing, there is some potential that this limit could be adjusted. However, geometry has not been the limiting factor for increasing this limit, but rather it is the material properties. As the AM soft magnetic materials are based on traditional materials, it is not seen by the author that the properties will be increased greatly until two things can occur which can lower iron losses. First, when AM can fully control the three-dimensional grain orientation in a working machine component as has been partially demonstrated [12], [61]. Second, when AM can create an amorphous structure using soft magnetics, which is actively being researched [62], [63]. Both potential breakthroughs will greatly lower the eddy current and hysteresis losses respectively in iron.

By increasing the thermal limit, a motors torque density can also be increased. An increase in torque density can greatly improve a motors performance. As this limit is defined by the amount of heat being generated through losses, being able to decrease these losses raises this limit. For most machines, copper loss is the dominant form of loss. By increasing the amount of copper in the slot (fill-factor), the resistance for a coil can decrease, or conversely, the current can increase while keeping the loss constant. This improvement can greatly benefit the performance of electrical machines. In addition, by being able to remove excess heat from the coils, the resistance of the coil decreases as it is a function of temperature. By addressing these two areas, fill-factor and heat dissipation, AM can greatly improve the overall machine performance. Thus, the remainder of this research will primarily focus on how AM can improve coil design.

With these principles in mind, the next step is to look at the functional requirements for a motor coil beyond the basic equations. These requirements need to consider additional limitations such as available space, AM size restrictions, insulation and printability. A few design options can then be conceptualised and evaluated based on these criteria.

Key findings from this section

- The dominant source of loss in a motor is from the motor windings copper loss
- Increasing the electromagnetic and thermal limits of a motor increases performance
- Electromagnetic limit increases are limited by existing material properties
- The thermal limit can be increased through better design, enabled by AM

2.3 Evaluation of motor coil windings

In addition to the first principle equations discussed previously, there are additional design considerations that need to be addressed. These requirements can aid in the design of coils which will not only improve winding performance, but also allow for manufacturing limitations such as supports and overhangs, and aid in an efficient insulation application and thermal dissipation.

2.3.1 Types of windings

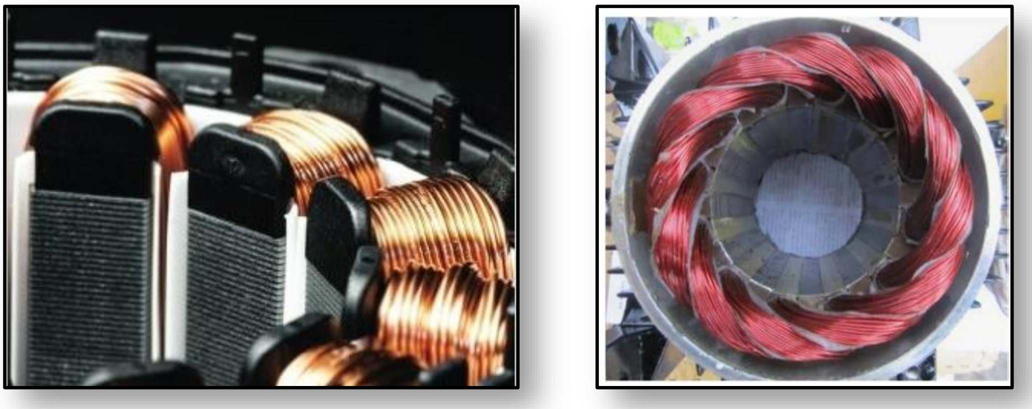

Figure 2-3: Concentrated stator windings [2] (left), and distributed stator windings [65] (right).

Motor coil windings are typically classified into two broad categories, either concentrated windings or distributed windings. Concentrated windings wrap an entire coil around a single tooth of a stator, forming a large single grouping of wires as in Figure 2-3 (left). Distributed windings share wraps between multiple poles or teeth, forming a large interwoven network of wires around many teeth, see Figure 2-3 (right). With distributed windings, there are several more sub-types, as the slot can share the space with different phases of windings creating multiple layers of windings within the slot. This allows a slot to share phases which can smooth out the air-gap flux density to be more sinusoidal in a rotating magnetic field. It can also improve the performance of the motor through lower harmonics and better power quality by incorporating various patterns of winding. These pattern choices are configurable depending on the performance characteristics desired in the final motor. However, there are a few negative design considerations for distributed windings. Firstly, the end turns are long and overlapping compared to concentrated. In addition, distributed windings typically have lower fill factors (35-45%) than concentrated (50-65%) [64]. Also due to the limitations of most AM build volumes, creating large AM distributed windings would be difficult to manufacture. Assembly of large AM distributed windings into a motor would also be a challenge due to the rigidity of AM parts. Thus, due to the manufacturing and assembly constraints, it is recommended to initially focus on concentrated windings for AM built coils which are smaller, compact, and can be assembled individually into the motor.

2.3.2 Concentrated windings

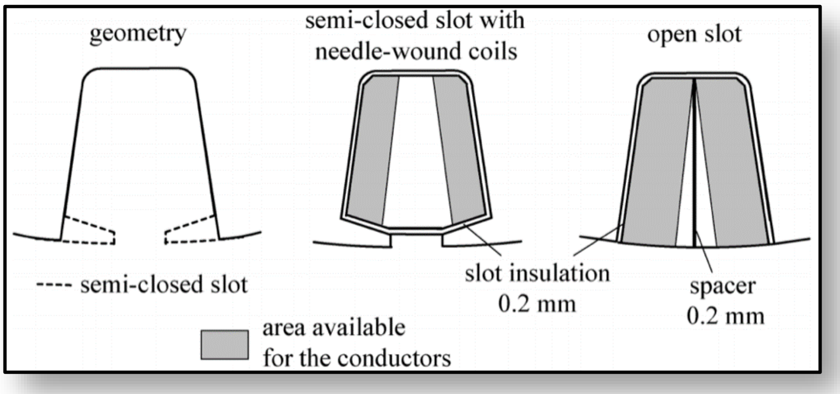

Figure 2-4: Examples of different slot geometries including open and semi-closed [66].

The main advantages of concentrated windings are that they can have higher slot fill factors and that they can be pre-formed. However, available space within the slot for a concentrated winding can vary depending on the motor configuration. The slot can either be open, or semi-closed as seen in Figure 2-4. While an open slot configuration allows easier installation of a pre-wound coil into it, it also reduces the amount of iron which interacts with the rotor which can significantly reduce the torque that the motor can generate [66]. Therefore, it is advantageous to be able to fill a semi-closed slot as much as possible.

There have been many innovations to incorporate a semi-closed slot with a pre-wound coil, which also can allow AM coils to be easily installed. These innovations all require the stator to be segmented in some way. Either the entire rotor is segmented, or some part of the tooth is removable, as seen in Figure 2-5.

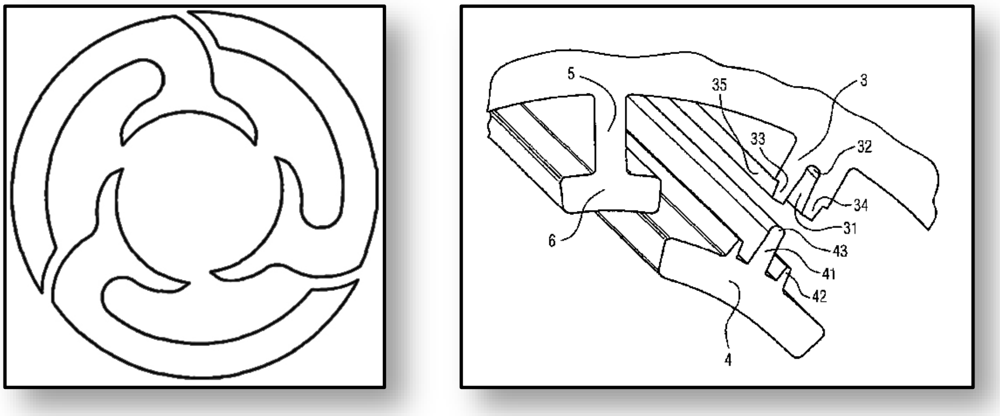

Figure 2-5: Examples of rotors with segmented [67] (left), and removable tooth geometry [68] (right).

As AM has the capability to manufacture a wide range of different geometries, the design decision was made that there would be no limitations in using the entire slot volume. Despite having this freedom, there are still several challenges that AM needs to address.

2.3.3 Challenges with windings

Aside from bearing failures (which account for 40-50% of all electric motor failures), 30-40% of failures in induction motors occur due to winding faults (either in the stator or in a wound rotor) [69]. These two areas account for the majority of failures, with the next highest area being rotor bar and end-ring faults which account for 5-10% of failures [70]. These winding faults are typically associated with failures in insulation which cause short circuits to either adjacent windings, or to the soft magnetic core. These failures are due to the vast number of stresses experienced by the windings including thermal, electrical, mechanical, and environmental [71]. As there are entire books dedicated to the study of monitoring the conditions to avoid these types of failures, only a brief overview will be given [71]. Some of the root causes of failure that can be addressed by AM are overtemperature events, defective design, and defective manufacture.

AM can be used to design and customise the shape and size of the windings in order to better fill the slot and improve design. These custom shapes can minimise the use of small bundles of wires which are used to form a single conductor. While these bundles do reshape to better fill the slot, fill factors are still limited to around 50%, with advanced winding techniques reaching up to 60-75% [64]. Alternatively, AM can consistently achieve high fill factors without the need of bundles as they have some additional disadvantages. One is the random placement of conductors within the slot. This random placement can cause voids and localised pinch points which can damage the insulation through overtemperature and thermally induced mechanical stresses that could lead to failure [6]. AM can overcome this through deliberate placement of the conductors in the slot, in addition to the specific placement of insulation as it is integral to the design of AM windings. By reducing the number of wires, the total number of potential failure points from insulation faults can potentially be reduced.

These bundles are also used for both ease of assembly as well as to minimise the skin effect in high frequency applications. The skin effect is only seen in AC applications [72], [73] and is a phenomenon wherein the electrons preferentially migrate closer to the outside surfaces of the conductor rather than in the centre of the core. This effect is magnified at higher frequencies, typically above 1 kHz. This effectively reduces the cross-sectional area in which the current flows. As demonstrated by Equation 2-3, as the effective area of the cross-section is reduced, the resistance will increase. However, high frequencies are not typically used in electric motor applications but should be kept in mind as thick conductors larger than 10 mm may experience skin effects at lower frequencies.

In addition to addressing those areas of failure, there are additional sources of inefficiency and loss such as the end windings. End windings are the portion of the wires which exit the slot and then turn out and back around into a different slot. These are seen as an area of inefficiency due to the 2D nature of traditional electric motor design which only use the conductor in the slot to generate torque. As these end windings (also called end-turns) do not contribute, they only add to the overall length of the winding which increases its resistance as seen in Equation 2-3. These end windings are also subject to the same fault conditions as with the stator windings [71]. AM can specifically design these end windings to be more robust by specifying their geometry including changing their geometry so that they act as better thermal heat sink. This is an area which will be explored by this work and is contained in Chapter 4 and can potentially reduce overtemperature events.

One final area that is a challenge with manufacturing windings is the manufacturing scale and ability to automate the creation of traditional windings. Typically, windings are creating either using a needle through which a wire is fed and then used to wrap around the teeth of a stator, by pre-forming the windings and then fitting them onto a stator, or through manual methods by wrapping a wire by hand around the stator teeth [66]. However, until a motor is going to go into mass production, the manual by-hand method is used for creating windings, which is slow, expensive, and error-prone, even in large electric motors which are typically always manually assembled and constructed [74]. AM can potentially provide a cost comparative manufacturing solution to these small manufacturing runs while also providing the additional benefits that AM can provide over traditional winding methods. Therefore, the next decision was to decide upon a motor topology to select for AM windings.

Key findings from this section

- Concentrated windings can be fit into an existing motor with high fill factors
- Windings are prone to several failure modes, some of which AM can help avoid
- Small production runs of motors have manually assembled windings

2.4 Selection of electric motor for retrofit with AM

With the first principles in place for what comprises a winding, the next step is to find a specific motor to apply them towards. Specifically, one which utilises a concentrated winding scheme would be preferable. In addition to this, the motor should not be overly large, due to the manufacturing volume constraints to which most LPBF machines are limited. This requires a motor which is typically under a few kilowatts for power output. One final requirement would be the ability to print all elements of the electric motor in the future, including the rotor and stator. While this requirement is not necessary, it opens the possibility to create a fully 3D printed electric motor. The next step is to identify a potential motor category that could meet these requirements. However, selection of a motor topology is highly application specific and thus needs to be readdressed for each new application.

2.4.1 Comparison of electric motor categories

There are four broad categories of types of electric motors. The first and oldest type is the DC motor, which is driven by a DC current. Then there are AC induction motors (also nicknamed squirrel-cage induction motors), and AC synchronous motors (also called brushless AC motors or PM motors). The final type are reluctance motors (which includes stepper motors) and are known for their simplicity and robust operation. From these different types of motors, there are some different advantages and disadvantages to weigh in order to determine the type that is best suited for AM.

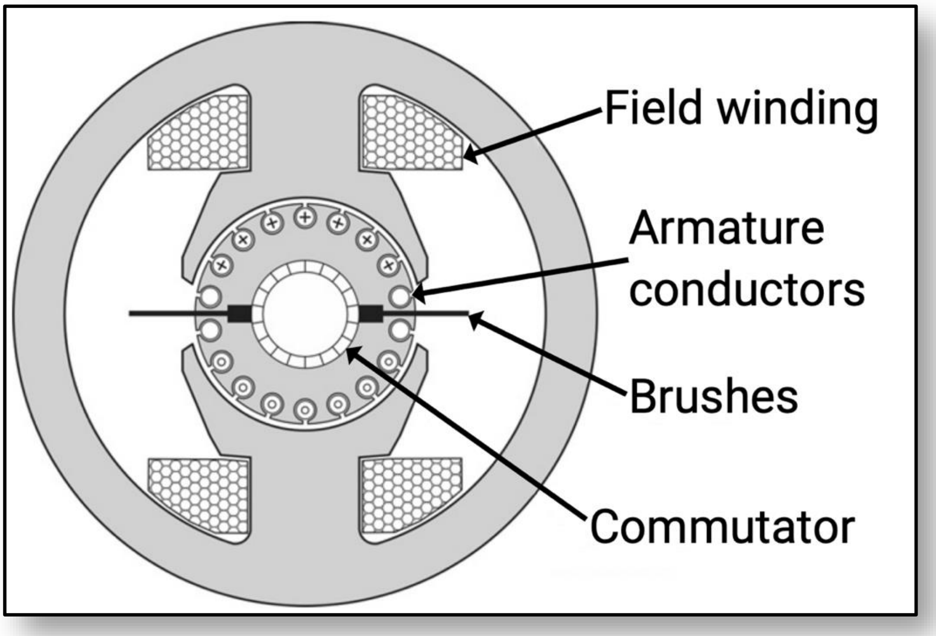

Figure 2-6: Conventional layout of a brushed DC motor [2].

For DC motors, the speed and torque are able to be controlled through simple changes in the current delivered to the rotor [2]. They have a very high starting torque (up to five times rated torque) and are very quick to start and stop, including quick reversing and accelerating. They are also free from AC harmonic waveforms, which reduces some electrical losses and noise [75]. However, the rotor construction is complex and expensive due to the number of electrical connections that are required. They also have brushes (seen in Figure 2-6) that result in a number of different negative effects. Brushes cause electromagnetic noise that can interfere with other electronics, they can create sparks which could lead to an explosion risk, and they require regular maintenance and servicing, at least every few thousand hours.

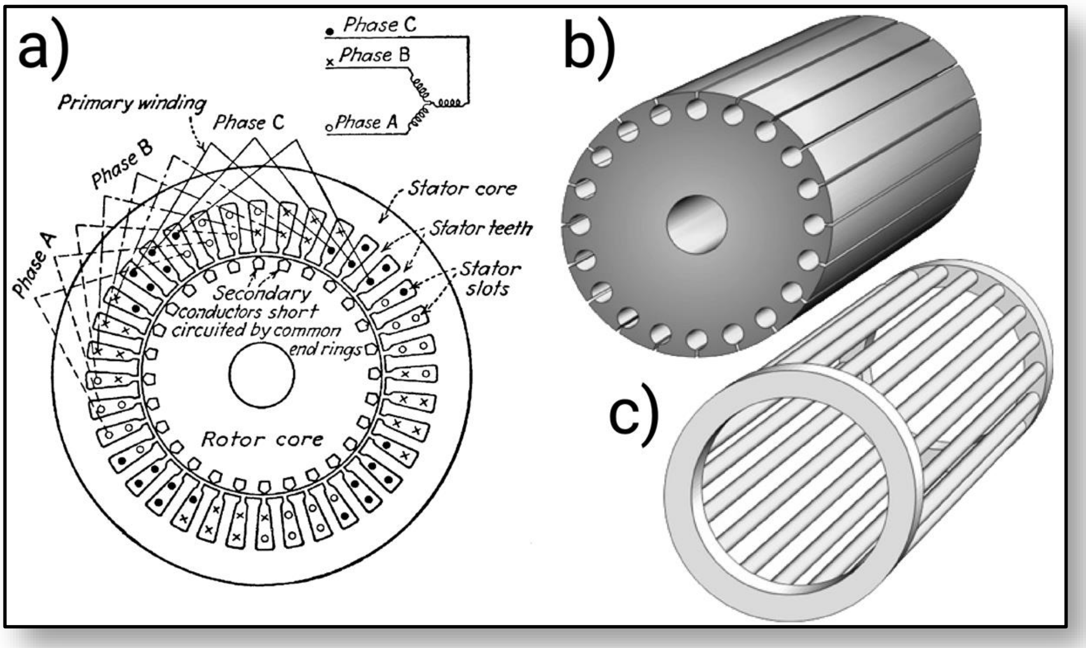

Figure 2-7: Diagram of windings in a 3-phase 4-pole AC induction "squirrel-cage" motor [76] (a), along with a squirrel cage assembly: iron core with axial holes (b), and conductor bars with end-rings (c) which fit together to form the rotor [2].

For AC induction motors (also called squirrel-cage induction motors or SCIMs), the rotor is simplified (seen in Figure 2-7 b and c) and more economical to produce than a DC rotor. It has no sliding parts such as brushes; thus, it avoids the negative effects mentioned previously. AC induction motors are robust and able to run at high speeds and can operate in a wide range of ambient conditions including explosive environments or underwater. However, they are much more difficult to control speed wise compared to DC motors as it requires a controller [2]. Even with a controller, speed is still a function of the load applied, where higher loads lead to a slower rotation. Coil windings are distributed (seen in Figure 2-7

a) and are more complicated than concentrated windings leading to increased copper and weight [76]. They also require a specialised power source and/or inverter to function. There is also a risk of unwanted induced currents within the motor and bearings which if not properly managed, can lead to damage in the bearings and unintended electrical shock [75].

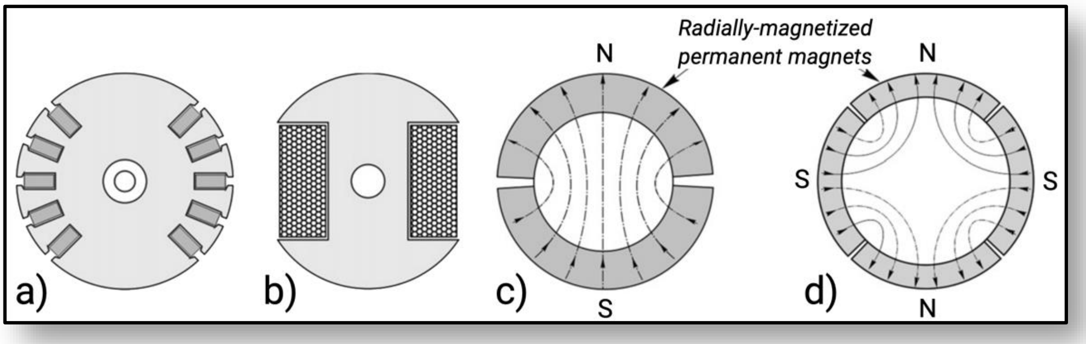

Figure 2-8: Synchronous motor rotors, 2-pole cylindrical winding (a), 2-pole salient concentrated winding(b), 2-pole permanent magnet rotor (c), 4-pole permanent magnet rotor (d) [2].

For AC synchronous motors, the speed is constant and independent of the load applied unlike induction motors. This is partly due to the use of PMs in the rotor (seen in Figure 2-8 c and d), or a DC field (seen in Figure 2-8 a and b) rather than an induced current (such as in SCIMs). Magnets consume no additional power and are more compact than rotor field windings, resulting in higher motor power density and higher motor efficiency due to the lack of rotor losses and brush resistance [75]. However, they do require additional controllers and sensors for variable speed operation. They are not self-starting and need some additional method to produce run-up torque. PMs are expensive and are sensitive to temperatures above 100 °C, and lead to the motor having cogging, which is an engagement and disengagement of the rotor magnetic forces on the stator iron as it rotates, resulting in torque ripple. If magnets are not used, then the wound rotors have additional DC power requirements that consume power and have additional rotating components (such as slip rings) that can require maintenance [2]. Coil windings are typically distributed and are nearly identical to AC induction motors and have the same disadvantages as such, however they can be manufactured with concentrated windings.

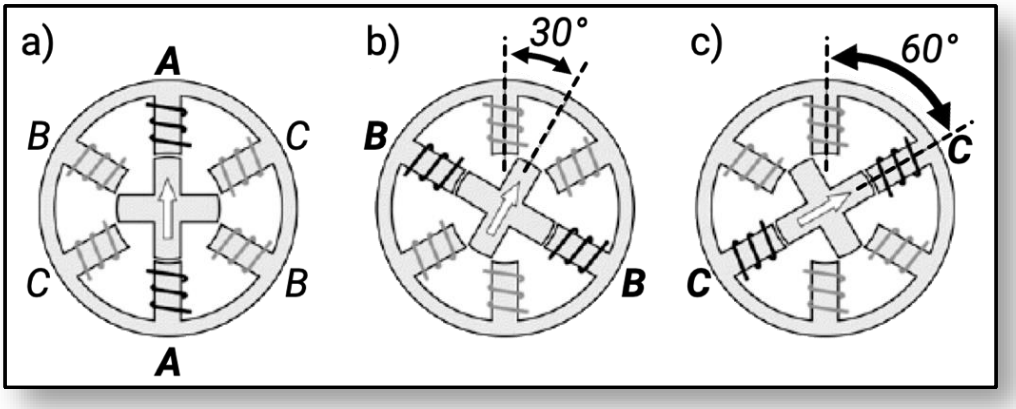

Figure 2-9: Operation of 30° per step stepper motor with phase A engaged (a), followed by phase B (b), and then phase C (c) which is then repeated [2].

For reluctance torque motors such as stepper or a switch reluctance motor (SRM), the rotor is extremely robust and the most economical to manufacture due to it being a laminated iron core with no magnets and no windings as seen in Figure 2-9. The stator is comprised of concentrated windings which are easier to install and have higher fill factors [75]. The operation of the motor simply requires the engagement of each phase in turn in order to rotate the rotor as seen in Figure 2-9. It's starting torque is very high, with full torque production capable at a standstill [2]. Also, the motor loss is mainly in the stator, which is easier to cool than the rotor. However, the motor can develop mechanical resonances which cause large vibrations. Due to it developing torque through reluctance, high levels of magnetic reluctance can be very loud. Also, output torque is not smooth and can have significant torque ripple [77].

Motor Type	***Pro for AM***	***Con for AM***
DC Motor	• Concentrated windings	• Very complicated rotor
AC Induction	• Simplified rotor	• Distributed windings
AC Synchronous	• May use concentrated windings	• Typically distributed windings • Magnets on rotor
Reluctance	• Concentrated windings • Single material rotor	• Potential for uneven torque output and vibration

Table 2-2: Summary of pros and cons for different motor types for manufacturing for AM.

After comparing the different types of motors as seen in Table 2-2, the motor category which best suits the original goals of AM electric motor manufacturing is the reluctance motor, specifically the SRM. They lack PMs, have concentrated windings, typically within an open slot, and are available in the size required for manufacturing AM windings. For these reasons an SRM was obtained to test the suitability of creating AM windings, with some of the key pieces of knowledge for SRMs presented in the next section.

2.4.2 Reluctance torque motors

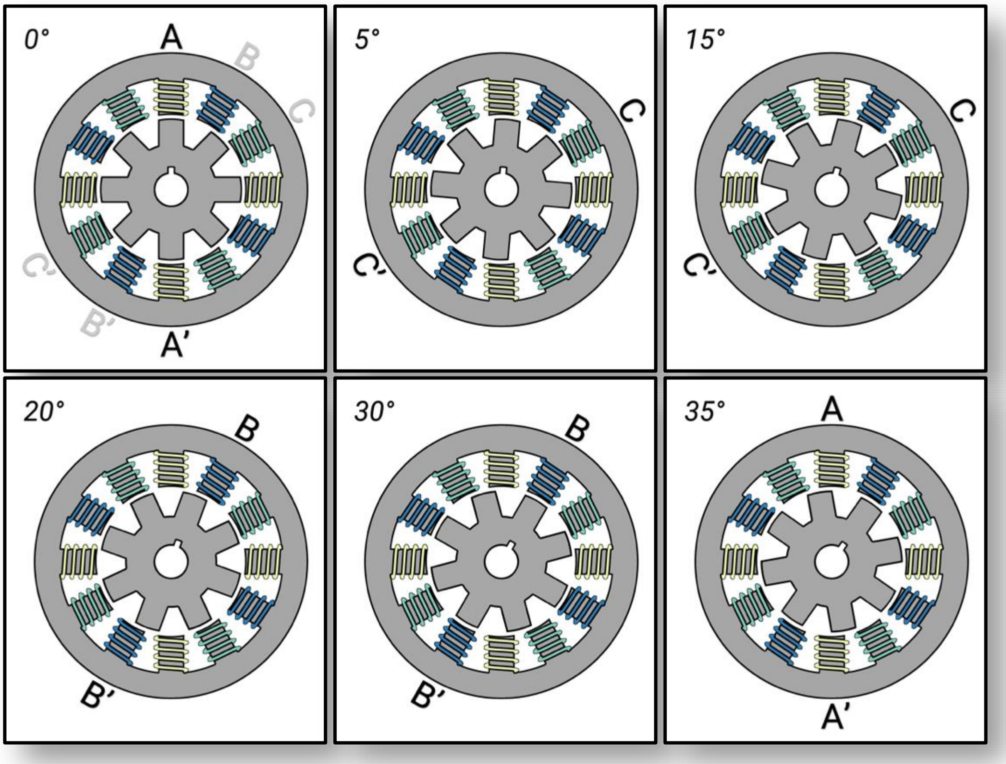

Figure 2-10: Typical 12-pole/8-tooth switched reluctance motor showing the progression of rotor angles between 0° and 35° as phases A, B, and C are activated (in bold letters).

Reluctance torque motors are also called doubly salient reluctance machines since teeth are on both the rotor and stator. Popular types of these motors are stepper motors (which have an equal number of rotor and stator teeth) and SRMs (which typically have a fewer rotor teeth than stator teeth). Some uses for SRMs are found in the Dyson X020 motor for high speed compact applications, augmented with PMs in the Tesla Model 3 motor, in some washing machine designs, and other industrial applications which require robust operation in high temperature environments. The SRM as seen in Figure 2-10 has twelve stator teeth, but only eight rotor teeth, and is shown with a progression of rotor angles as the three different phases (A, B & C) are activated. This differing number of teeth between the rotor and stator allows a set of rotor teeth to be between a set of stator teeth when one phase is engaged so that it can rotate to the next position as seen in the zero degree position of Figure 2-10 when phase A is aligned and where the rotor could rotate to either phase B or C. Stepper motors became popular due to their ability to be discretely controlled with open loop control through microcontrollers and computers. SR motors have been an area of interest for researchers and industry since the 1980s due to the lack of magnets and electrical windings in the rotor.

Rather than the ‘BIL’ method of torque creation, these motors rotate due to reluctance torque. Reluctance is manifest by irons seeming unwillingness to be in any position that does not allow it to be aligned perfectly within an existing magnetic field. It can be seen when an iron bar, which is free to rotate, is placed within a magnetic field. The bar will initially rotate so that it aligns itself with the magnetic field. But if disturbed from that alignment, it will experience a torque to return to that alignment. In the case of a reluctance motor, rather than a single bar as a rotor, these motors have a specific multi-bar rotor that is constantly creating torque as it tries to align with the activated coils. The coils never allow the rotor to fully align itself with the magnetic field as that scenario results in zero torque. The equations that govern this torque production are not as simple as those derived previously, as they depend on the partial derivatives for flux, current, and position of the rotor in non-linear relationships [78]–[80], where simulation software is typically used to determine torque and power in the pre-construction phase of development.

The construction of the stator has many teeth that are individually wound to produce a magnetic flux in them. The rotor is a laminated iron core with no magnets and no windings. The air gap between the rotor and stator is small to maximise flux to flow from the engaged windings into the rotor as air acts as a resistance for flux. The spacing and number of teeth between the rotor and stator is an important factor for torque production. If the space between a winding nearest the rotor tooth is too large or are overlapping too much, the resulting torque is minimised. Rotation is achieved when the phases are engaged sequentially, with each in the sequence being the next closest to a rotor tooth in order to maximise reluctance.

Key findings from this section

- There are many types and variations of electric motors for different applications
- SRMs typically have concentrated windings, open slot geometry, and simple rotors
- Of the many types of electric motors, SRMs hold the highest potential for AM

2.5 Current electric motor trends

Despite electric motors having been around for over a hundred years, there are still several areas that are seeing continued research and development. This research is driven by new materials, new applications for electric motors, improved control systems and power electronics, new requirements for energy savings, and new challenges in the industry with existing solutions [81]. Within these areas, there are a few where additive manufacturing could aid in the development of new solutions. These include the areas of high efficiency motors, electric vehicles applications, and the pursuit of the more-electric aircraft.

2.5.1 Increasingly efficient electric motors

As stated in the introduction, nearly 35-40% of all electricity consumed within the EU is by electric motors [3], typically within the industrial industry. Thus, small increases to energy efficiency can save a considerable amount of money and resources. These industrial uses have a wide range of specific applications such as pumps, fans and compressors, most of which can benefit from energy saving machines such as variable-speed drives (VSDs) [82]. In

2005, VSDs were installed in 25% of new motor installations, and by 2014 had grown to 30-40% [83]. As the desire for more efficient motors grew, standards for different classes of motors emerged based on the motors efficiency, namely IEC 60034-30-1:2014 [84]. This international standard published by the International Electrotechnical Commission (IEC) establishes a set of efficiency values for electric motors given the parameters for an electric motor. These start with IE0 at the lowest and potentially can go up to IE5, see Table 2-3.

IEC Code	***IEC Classification***
IE0	Below Standard Efficiency
IE1	Standard Efficiency
IE2	High Efficiency
IE3	Premium Efficiency
IE4	Super Premium Efficiency
IE5	Ultra-Premium Efficiency

Table 2-3: IEC codes and classifications for electric motor efficiencies.

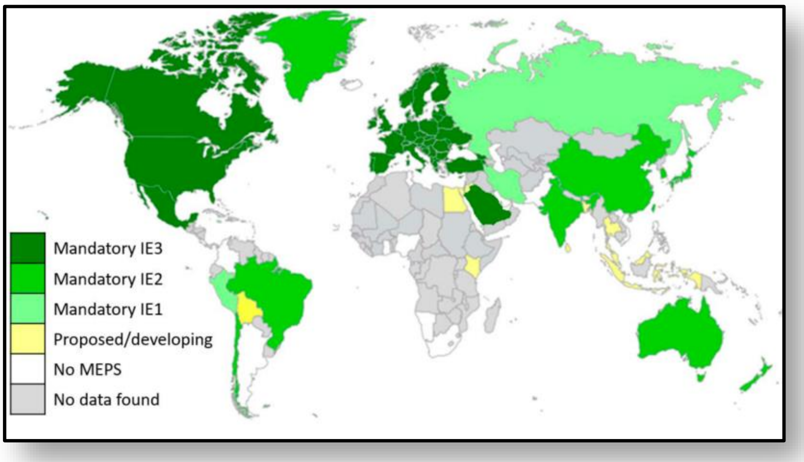

Figure 2-11: Minimum energy performance standards (MEPS) being adopted all over the world [85].

IE3 rated motors have been required in the United States since 2011, and in EU countries since 2015 as seen in Figure 2-11. While IE4 was only recently defined as a standard in 2014, IE5 is being envisioned and may be in the next updated version. However, IE5 has some questioning if this level of efficiency is even possible with current technologies as no machines were available for purchase at this classification [83]. One of the most widely used motors for industrial applications is the SCIM, which up until very recently, was not available in an IE4 rating, let alone how it could achieve an IE5 rating using current technologies. However, other types of motors such as a VSD-fed PM synchronous motor have been long established as IE4 capable. However, the high and rising cost of rare-earth PM materials make them undesirable for applications which are either high temperature or cost sensitive. Thus, research is currently going into SCIMs using new technologies to improve materials that minimise losses, modifying the geometry for increased torque development, improving manufacturing processes to minimise the air gap, and improved reliability for rotor core construction to reduce eddy currents due to burrs and imperfections [83].

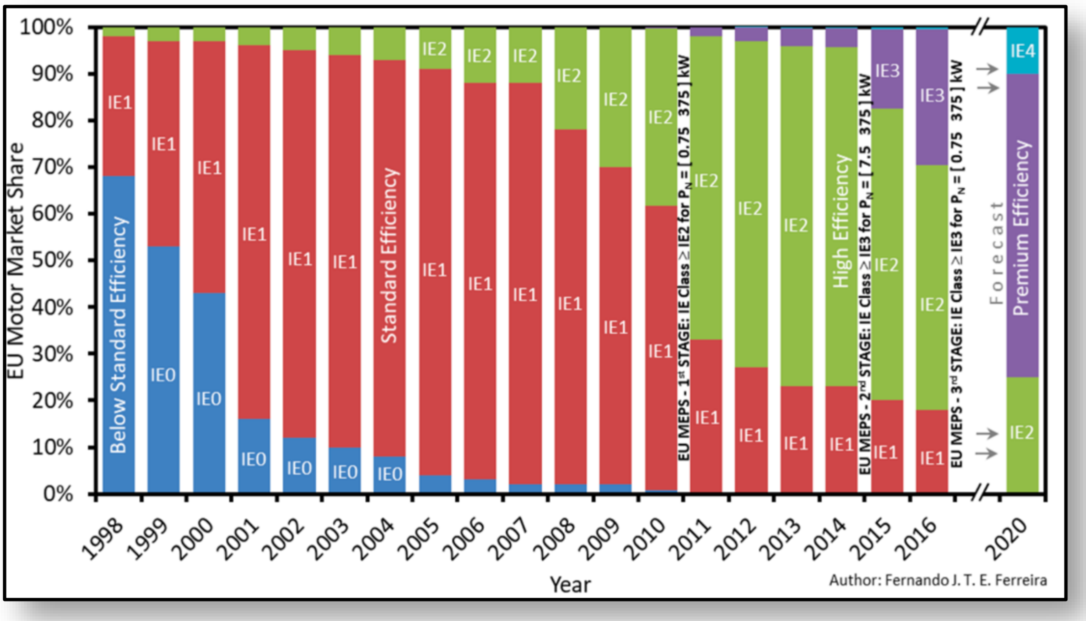

Figure 2-12: EU electric motor market share for the 0.75-375 kW power range broken down by year and IEC category including a forcast for 2020 [85].

One last aspect that can improve motor efficiency is rewinding the motor during repair. Over the lifetime of a motor (12-20 years), it is expected that it will be repaired or rewound with new coils 2-4 times [85]. In [85], the opportunity is explored to retrofit these motors so that the efficiency and reliability of a motor can be improved upon once it is repaired. Despite the IE3 requirement for all new motor installations in the EU, most motors in use are still IE1 or IE2 due to their long lifespan (see Figure 2-12). An actual review of over 4000 electric motors in Switzerland in 2013 showed that most motors have been in service 2-4 times longer than the expected life of the motor. Thus, there is potential to retrofit older inefficient motors to make them more efficient. However, retrofitting also has the challenge to ensure that IE3 and IE4 motors maintain their high efficiencies. While these standards mostly impact industrial motor requirements, another sector which has a desire for high efficiency motors are electric vehicle applications.

2.5.2 Electric vehicles

The electric vehicle (EV) industry is a fast-growing market with high demands for an efficient and robust vehicle power train. This growth is partially driven by the desire to limit the amount of GHGs entering the atmosphere like CO_2. In 2009, it was estimated that 25% of all GHG emissions were from the transportation industry [86]. This large contributor to GHGs can be offset by EVs if they employ efficient drive trains, converters, and are supplied with electricity which was generated using low emission sources such as wind or solar power.

One important piece for EVs is the power train, typically consisting of at least one electric motor. Despite making up about 28% of the total number of cars on the road in 1900, the lack of efficient motors and rechargeable batteries, along with the development of the inexpensive Model T, prevented EVs from thriving [86]. Nearly 100 years later, EVs started to become popular again with new electric cars being manufactured such as the General Motors EV1 (which was later cancelled and destroyed by GM) and the Toyota Prius. It is now estimated that there are between 2 and 3 million EVs on the road in the world [87] with estimates of between 9 and 20 million by 2020. Despite this large number of cars on the road, there is no single EV motor topology in use. According to [88], all Tesla vehicles (except for the Model 3), the Chevy Spark, the Toyota RAV4, and a few others use a SCIM motor. The Hyundai Sonata uses a surface mount PM motor, and almost all other production automotive motors use an interior PM geometry, with some other applications using alternate topologies such as switched reluctance motors. Even within these topologies, there are distributed windings (Figure 2-13 left) and concentrated windings (Figure 2-13 right). However, most motors are manufactured with a distributed winding pattern. As a result, there is still considerable research going into developing new EV motors in order to improve reliability and performance, and reduce manufacturing and material costs [89].

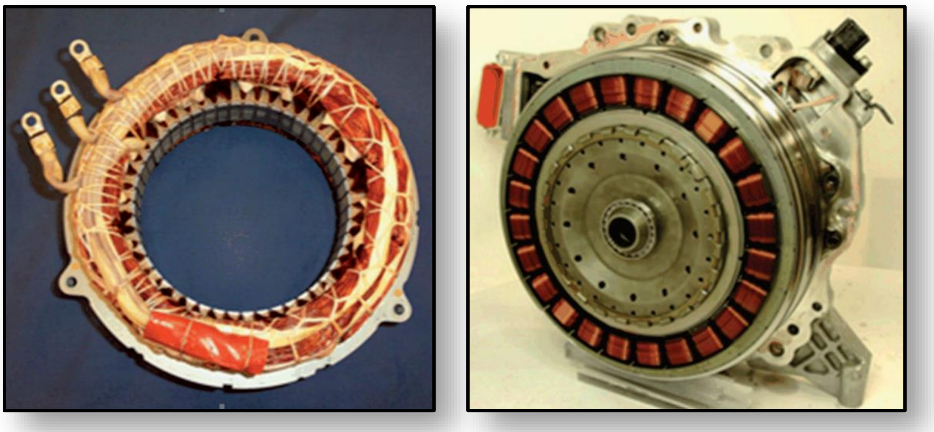

Figure 2-13: A distributed winding pattern found in a 2004 Toyota Prius (left) and a concentrated winding pattern found in the 2011 Hyundai Sonata (right) [88].

One area of interest which is being researched in order to meet some of those goals of improving reliability and reducing material costs is to develop topologies which do not use rare-earth elements, a major component in most PMs. This is due to the scarcity of some of these elements, large price fluctuations, and lack of competition for rare-earth element production with China dominating 96% of worldwide production [90]. Thus, in order to avoid a constrained supply chain for these elements, motor designers are creating topologies without them [91]. These motors include the SCIM used by several auto manufacturers, as well as non-rare earth containing PM machines, and SRMs. A recent review of research into rare-earth-free motors [91], has shown that these motors can achieve similar performance to the standard PM machines in terms of torque density and efficiency, in addition to being more robust and cost effective. In addition to the EV market for electric motors, another opportunity is in the aerospace industry with the more and all electric aircraft movements.

2.5.3 More and all electric aircraft

Aircraft have a few different energy systems onboard which aid in the operation of the aircraft. These systems include mechanical and electrical, as well as pneumatic and hydraulic. In order to minimise the number of systems on board, there is a movement to replace the pneumatic and hydraulic systems with electrified versions. This will increase overall reliability and quicken repairs while also decreasing weight, costs, fuel consumption, and maintenance as electrical systems are easier to replace or repair [92]. These auxiliary systems consume approximately 5% of the total fuel of the aircraft [93]. When it's considered that 2% of global GHG emissions are produced by air transport with a rise to 3% by 2050 [94], it is important to try and offset this through electrification and higher efficiencies. This is why both the Boeing 787 and the Airbus A380 have increased the use of electrical energy onboard [95], and thus have created a demand for technology development which can support the more electric aircraft (MEA) and ultimately the all-electric aircraft (AEA) in the future. It is estimated than an AEA could reduce the weight of an aircraft by 10%, while also reducing fuel consumption by 9% [96]. However, the aerospace industry has been slow to adopt some of these advancements due to need for having these new systems meet the high reliability requirements and prove airworthiness [8].

While part of the pursuit of the MEA surrounds designing and manufacturing efficient and compact power electronics and control systems, additional tasks are being researched such as moving an aircraft while on the ground, often called either electric taxi (e-taxi) or Green Taxi [97]. This aim is to control the manoeuvring of the aircraft on the ground without the use of additional trucks or vehicles, and without using the main engine's turbo fans. The electric motors which are needed for this require high torque density in order to make them as compact as possible, as well as high reliability in order to survive the harsh environments an aircraft operates within. Many researchers have explored the design space for such a motor [98] and have been able to generate prototypes which demonstrate these requirements [99].

Figure 2-14: The Airbus E-Fan personal all-electric aircraft AEA at the Paris Air show in 2015 [100].

With an annual air travel passenger increase of 6.2% from 2012 to 2017 (with similar growth projected for the next 20 years), and the currently record low price of jet fuel, which is expected to inevitably rise, there is a need to reduce operating costs for air travel. This has led some to envision the AEA such as the Airbus E-Fan [101] personal aircraft (seen in Figure 2-14) to remove the dependence on air-breathing engines, or at least develop hybrid gas/electric propulsion systems [102]. While the main challenge of moving towards an all-electric propulsion system for an aircraft is battery technology and getting the required energy density to enable ranged flight, a second challenge comes from achieving the required power densities from existing motors. For example, some have proposed power density goals for the electric motor industry to reach, with 10 kW/kg being a short term goal in the next 10 years, 20 kW/kg in 15 years, and 50 kW/kg in 25 years [95]. To put this in perspective, current electric motors in electric cars have a power density of between 0.5 to 2.5 kW/kg [88] with most being below 2 kW/kg. This requires a 5-fold increase in electric motor power densities in order to meet the proposed short-term goals, and over an order of magnitude increase for long term goals.

The goals of creating highly efficient motors to meet increasing IEC standards, robust and cost-effective motors for electrical vehicles, and compact and reliable motors for aircraft are very lofty. While current research is incrementally improving these motors, there still needs to be a stepped improvement in order to achieve these goals. Some have proposed that additive manufacturing can be this improvement, so the next section will thus explore the current research into electric motors and additive manufacturing.

Key findings from this section

- Electric motors have increasing demands for efficiency and reliability
- Incremental changes cannot achieve some of the goals set out for future motors
- There is potential to retrofit existing motors to increase their efficiency/performance

2.6 Electric motors and AM

To date, research into the use of AM with electric motors has taken three different routes. The first is to explore the concepts of using AM to manufacture electric motors, however, the required materials and machinery to manufacture the proposed geometries are not available, so the research is limited to conceptual designs and simulations [45]–[47]. The second is to develop materials for AM which are currently being used to manufacture traditional electric motors, such as hard and soft magnetic materials [12]–[17], and use AM to manufacture proof-of-concepts using those materials. The third path, in which this review will focus, is to demonstrate partial or fully working prototypes using some AM parts, but lack suitable materials or equipment to demonstrate a fully functional motor. As a result, despite claims of the world’s first 3D printed motor, there has been no evidence for a 100% purely AM motor, but it is getting closer to be a reality.

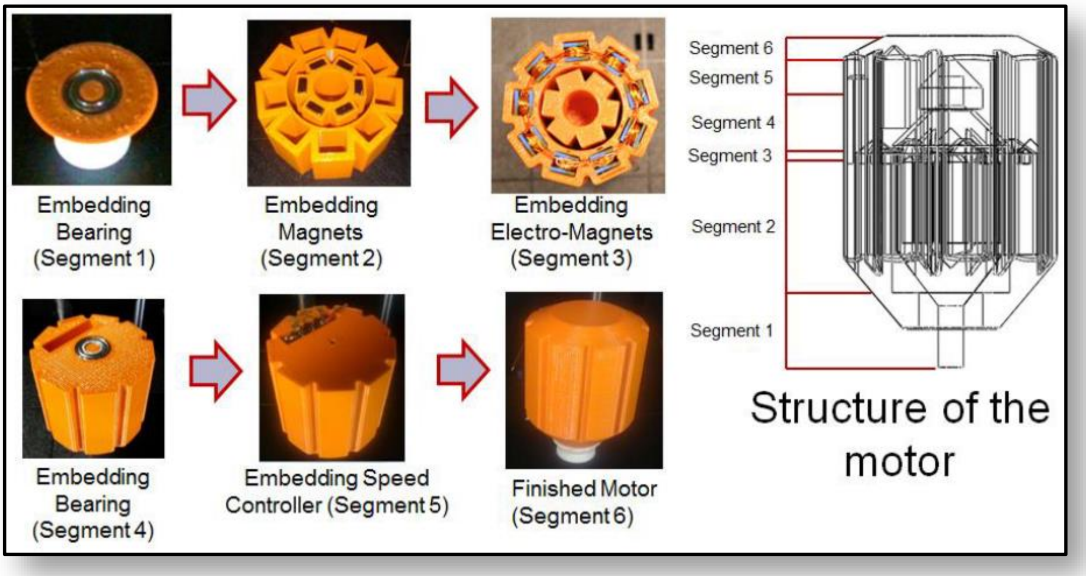

Figure 2-15: An example of mixing traditional methods and materials with 3D printed design [103].

Some of the earliest examples of building electric motors with AM technology involve using FDM and plastic. One of them is a motor which had DfAM in mind so that some parts are 3D printed, however, the printed parts are plastic with traditional magnets, windings, and bearings placed into it [103]. While incorporating a number of pauses into the build which were used to then place the traditional parts into the build, it does not greatly improve what an electric motor could be, as it is inherently weaker by relying on plastic parts to hold the entire motor together, seen in Figure 2-15. In [104], this concept was improved upon slightly by incorporating some iron powder into the filament used for the stator, but the majority of the motor is still plastic, with traditional magnets and copper wire making up the active materials of the motor. Despite this use of iron-filled filament, the motors presented in [104] are conceptual motors only, and are bolted onto a workbench for demonstration purposes.

Another group of researchers have focused on developing rotors for electric motors, using a number of different materials. In [105], a lightweight rotor was designed and manufactured for a PM machine using H13 steel powder from an unknown source. The rotor successfully demonstrated the ability of AM to decrease weight and improve acceleration times, however, the H13 material did not have a high enough magnetic permeability to achieve the goal of sensorless control of the motor. In [106], a 30 mm diameter, 45 mm long rotor for a SRM was made out of a custom iron-cobalt powder which was mixed by the VTT Technical Research Centre of Finland. The resulting material was able to be printed to a relative density above 99.9%, with a magnetic BH-curve provided for the material. While the resistivity of the material was lower than what would be desired for this application, and the design was a simple extrusion of a 2D design, it did demonstrate the potential of using this material as a rotor. Similarly, in [107], a switched reluctance rotor for a food processor motor was created using MS1 powder from EOS. The MS1 powder was a maraging steel with approximately 18% nickel, 9% cobalt, and 5% molybdenum content. As seen in Figure 2-16, the design of the rotor incorporates some complexity such as a 5% skew and rib feature which helps reduce torque ripple and windage loss but was not designed using DfAM.

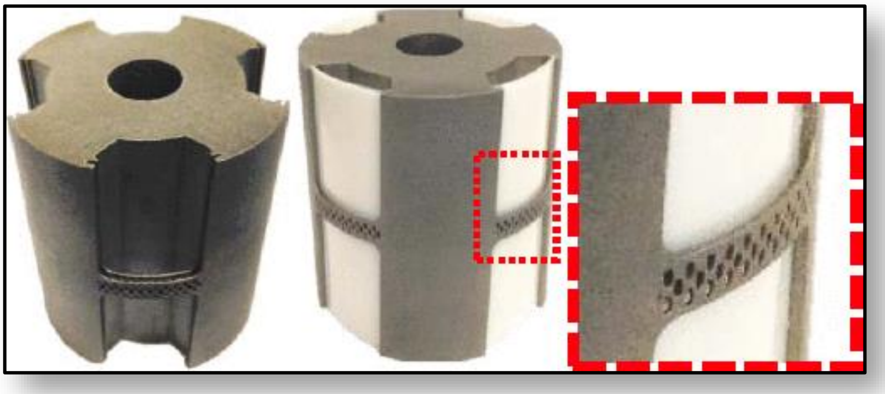

Figure 2-16: An additively manufactured switched reluctance rotor made from maraging steel [107].

Besides developing rotors for electric motors, another area of research is in creating highly conductive coils which can be used in a motor. Some of these highly conductive materials and methods may or may not be suitable for electric motors. For example, in [108], small silver interconnects were created on a flexible substrate using a custom built jetting process. These interconnects were on the order of less than 1mm in height, and despite good range of geometries demonstrated, would be unsuitable for coils due to size limitations and a reported resistivity of approximately 30 µΩ-cm or 5.7% IACS.

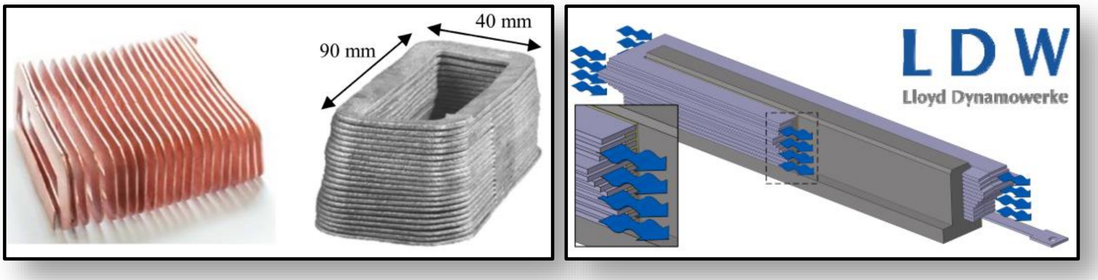

Figure 2-17: Examples of coil designs that have been cast using copper, aluminium [109], and incorporating novel geometry such as air cooling passages [110].

Rather than using AM to create larger coils, some work has been performed with using casting as seen in Figure 2-17. In [109], [110], Fraunhofer IFAM collaborated with Lloyd Dynamowerke GmbH & Co. KG (LDW) in Bremen Germany to create some coils for a PM motor used in a crane application. They noted all the same advantages that creating custom AM coils can provide, such as increased fill factor, variable cross-sectional shape, and freedom of geometry. However, the results were still limited in terms of what is achievable with the lost-foam casting process such as geometry constraints, minimum wall thicknesses and achievable tolerances. The resistivity was close to that of the bulk materials, with the cast copper (>99.9% purity) coils being 1.79 µΩ-cm or 96.3% IACS, and the aluminium alloy (Rotoren-Al 99.7) measuring between 2.90-2.99 µΩ-cm or 57.8-59.5% IACS.

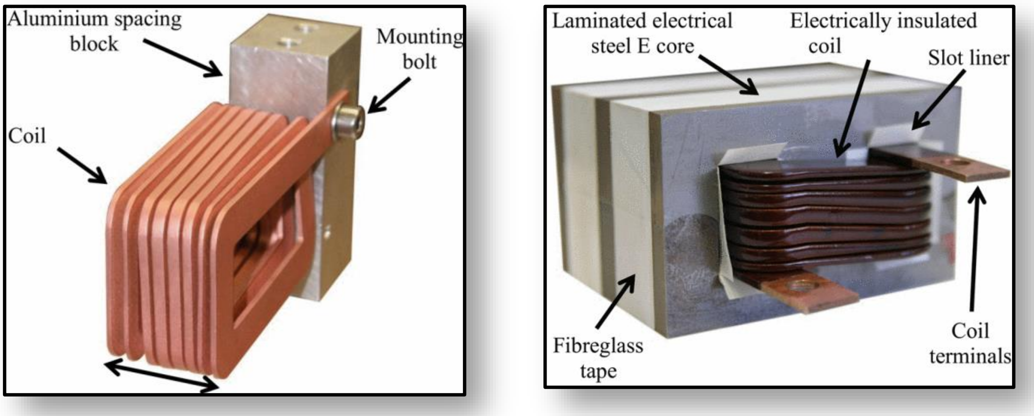

Figure 2-18: AM copper coil mounted in prep for insulation(left) and in a steel core for testing(right) [111].

While casting has shown to create highly conductive large coils, AM has an additional freedom and potential that cannot be achieved by casting such as dimensional accuracy and surface finish. In [111], these properties were investigated in order to develop a copper winding which was optimised to minimise power loss in an 400 Hz AC application. Both the machine and powder used to create the coil were not reported. After manufacture, it was drip coated on a rotating fixture with an air-drying polyester varnish and then mounted into an electrical steel core for testing as seen in Figure 2-18. Electrical resistivity was measured and found to be 51% IACS, much less than the anticipated 100% IACS. However, the research demonstrated the advantages of using AM for custom shaped coils to minimise losses.

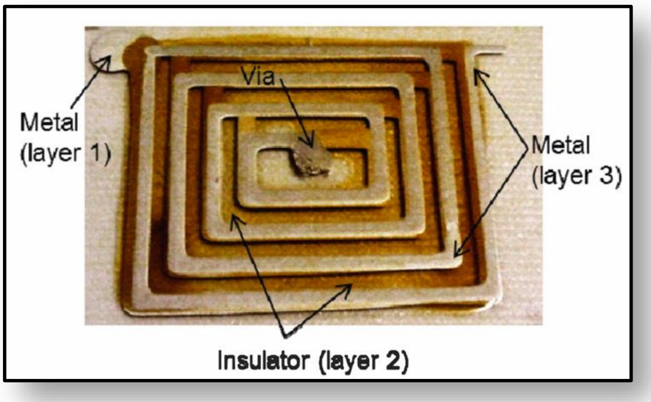

Figure 2-19: Prototype coil for an MRI machine made using a multi-material extrusion AM process [112].

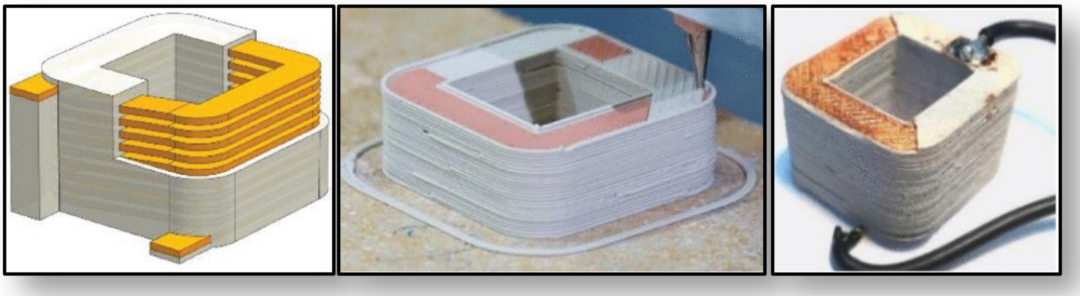

Figure 2-20: Prototype switched reluctance motor coil made using a multi-material extrusion AM process, with the CAD design (left), printed coil (centre), and post sintered (right) [113].

Another advantage that AM has over casting is the ability to use multi-materials. A few researchers have investigated this aspect of creating coils with AM. In [112], researchers created windings for use in an magnetic resonance imaging (MRI) machine using an extrusion-based method which utilised both a conductive and insulative material, as seen in Figure 2-19. While the specific materials used for the metal and insulation were not specified, the typical resistivity for the metal layers were reported to be < 10 μΩ-cm (> 17%

IACS). In [113], a different multi-material extrusion system was used to create a copper ceramic coil for a proposed switched reluctance motor, as seen in Figure 2-20. The coil was fabricated using copper and ceramic pastes, and then sintered using an undisclosed method. This research focused on the performance of the coil in terms of maximum current draw, current density, copper loss and temperature rise. In the end, they were able to create a coil that was 87% dense with a conductivity of 71% IACS.

While there are some patent applications being filed [114], [115], and a number of other electro-mechanical devices being researched [116] there is still a lot of room to explore this area of AM and electric motors. The concepts of how AM can influence an electric motor from the design of the coils to the design of an entire machine is still being explored. Electric motors have a potential to be improved and changed by AM, but AM must first provide the materials and properties that electric motor designers need for this change to occur.

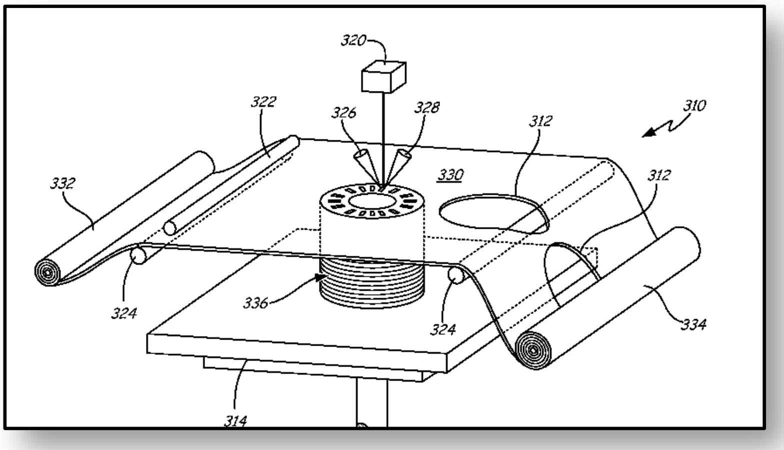

Figure 2-21: Patent drawing of 3D printed electric motor process using a sheet lamination method [114].

Key findings from this section

- Electric motors have high interest for AM, but function and performance not reported
- Motor windings have great potential, but properties and/or DfAM have been ignored

2.7 AM process review for conductive materials

Of the seven categories of AM mentioned in Chapter 1.2, conductive metals can be processed to some degree with each of them. However, not all the resulting metal parts would be suitable for complex geometries in electrical applications. As the selection of an AM process is highly dependent on application specific requirements, the pros and cons for each of the seven categories will then be presented for electrical windings in Table 2-4. Then only the processes that can achieve the following will be reported upon in Table 2-5.

1. Metal parts with high porosity tend to have much higher resistances than solid direct metal fabrication methods [117]. Thus, only the highest as-built density or highest post-processed densities are reported.
2. The process must have the ability to create highly detailed structures such as a continuous electric coil. This structure may have supports if the support structures are removable, and the resulting coil will not have adjacent windings connecting as to create a short circuit.
3. The process must be able to build windings for a generic small traditionally manufactured electric motor in the 1 kW range. This type of motor would typically require coils in the range of 20 mm wide, 50 mm long, and 20 mm tall. This requirement is limited for this research purposes only.
4. The AM process must have demonstrated that there is a potential to produce highly conductive materials (i.e. copper, silver, gold, aluminium) with a high relative density.
5. Only processes which have published either conductivity or density measurements are included, which is why processes which show promise for high density and highly conductive materials such as direct metal jetting [118], [119], have not been included.
6. If a process has demonstrated limited conductivity with low density but no other work has demonstrated higher conductivities, the best conductivity will be reported.

Binder Jetting	Pros	• Self-supporting [120] • Medium detail quality • Easy to process materials to green state [121] • High enable volume production capability • Can use difficult to weld materials
	Cons	• Low green state density [122] • Excessive heat in sintering could deform delicate geometry • Excessive shrinkage to achieve high density [123] • Sensitive to surface oxides and contamination which inhibits sintering • Requires significant post-processing to reach high density
Directed Energy Deposition (DED)	Pros	• High-density with many metals available [124] • Potential for multi-materials and grading between materials [125] • High material deposition rates [126] • Can be applied to existing parts on non-planar surfaces
	Cons	• Low detail resolution • Poor surface finish • Support structures difficult to achieve [127]
Material Extrusion	Pros	• Simple process with many materials available • Multi-material capable [113]
	Cons	• Low density before sintering [128] • Typically non-conductive if filament based
Material Jetting	Pros	• Multi-material capable including metals [129] • High detail resolution [130] • Scalable technology
	Cons	• Low density with post-processing required • Slow build times [131] • Slow new material development
Powder Bed Fusion (PBF)	Pros	• High density with many materials [132] • High detail resolution
	Cons	• Supports required • Potential for residual stresses [30] • Material is generally required to be weldable • Highly reflective materials difficult to process with lasers [133]
Sheet Lamination (SL)	Pros	• Solid metal parts [134]
	Cons	• Limited geometry possible
Vat Photo-polymerisation	Pros	• High resolution
	Cons	• Low density • Photopolymers only • Difficult to load photopolymers with solid material [135]

Table 2-4: Comparison of AM processes for creating electric motor coils.

AM Process	Material	Density	IACS	Ref.
Binder Jet	Copper	85.5% with sinter	n/a	[120]
Binder Jet	Copper	97-99% with HIP	n/a	[121], [122]
DED	Copper	Near 100%	n/a	[125], [126]
Extrusion (Filament based)	Ni-Sn in PA6	30% Ni-Sn by vol.	0.05%	[128]
Extrusion (Paste based)	Copper	87% post sinter	71%	[113]
Jetting (Ink jet based)	Copper	n/a	10%	[130]
Jetting (Ink jet based)	Silver	n/a	12.7%	[129]
Jetting (Laser film transfer)	Copper	n/a	8.3%	[131]
PBF (Electron Beam based)	Copper	99.3%	97%	[136]
PBF (Electron Beam based)	Copper	99.5%	101.9%	[132]
PBF (LPBF)	Copper	96.47%	n/a	[137]
PBF (LPBF)	Copper	97.8%	n/a	[138]
PBF (LPBF)	Copper	66-68%	n/a	[139]
SL (Ultrasonic based)	Copper	n/a	n/a	[134]
Vat Photopolymerisation	Copper	60% by weight	5-8%	[135]

Table 2-5: Comparison conductive material properties from a literature review of the seven AM process categories.

After comparing these processes in Table 2-4 and in Table 2-5 for their ability to use materials that are highly conductive and dense, the process which best meets the ability of creating coils for electric motors is PBF, specifically LPBF. However, there is a general lack of reported electrical properties, especially those which take into consideration initial build orientation or post-heat treatments. While all of the processes in Table 2-4 and Table 2-5 meet some of these needs, none except LPBF meet all of them. Binder jetting is generally not able to create highly conductive parts without significant sintering and distortion to the original part. DED cannot achieve the detailed resolution required for creating coils without post machining. Material extrusion can create multi-materials but has the same issue as binder jetting. Material jetting has not demonstrated the ability to create large conductive parts while sheet lamination cannot produce the complex geometries required for electrical coils. Vat photopolymerisation simply does not have the ability to load resins with enough conductive material to make them usable for this application. While Electron Beam Melting has proven the ability to create highly conductive parts, it lacks the fine resolution and smoother surface finish which can be achieved by LPBF. While LPBF is not a perfect process as it still requires support structures and the need to relieve residual stress, it is able to create large, dense, highly detailed and conductive parts in several different materials.

Despite much research into AM of copper and other conductors, little work has been done to characterise AM materials conductivity and electrical properties. Most research specifies density (or porosity), hardness, and/or other mechanical properties such as tensile strength. AM research which has published electrical properties mostly comes from thin films, which are not recommended for electric motor applications, or use indirect measurement techniques that measure eddy currents and assume isotropic material properties. However, it has been shown that generally, as-built AM mechanical properties are not isotropic [23], [27], [140], and thus the assumption that electrical properties are isotropic in order to use eddy current electrical measurements which require isotropic properties for accurate results needs to be questioned when applied to AM parts. Next is a deeper look into PBF.

Key findings from this section

- Many AM process can produce conductive metal parts, including using copper
- Despite much research, little/no work has been done to provide electrical properties
- Those which have been given, rely on isotropic properties for accuracy of resistivity
- LPBF has the greatest potential to create ready to use, high conductivity windings

2.8 Powder Bed Fusion (PBF)

PBF creates parts from a powder bed by using an external heat or energy source to fuse the powder together through either sintering or melting. It includes a few different processes.

These processes include LPBF and Electron Beam Melting (EBM), among several others. Within each of these generic processes, there are several additional trade names all describing the same process, see Chapter 1.3.

PBF has the advantage that a wide range of materials can be processed, provided that generally the material is weldable as LPBF is a micro laser welding process, and that a spherical powder can be produced to allow the powder to spread easily [23]. Further, parts that are melted can have significant strength advantages over other non-melted AM processes, as the material properties can be close to that of wrought material. Depending on the process and material, support structures may not be needed, as the powder bed becomes the support, however LBPF typically always uses supports. Build speeds can also be fast depending on materials and process, with processes that preheat the powder bed to just below melting being the quickest because it allows for a fast scan speed. Electron beam scan speeds are the fastest of any PBF process due to the lack of mechanical parts needed to direct the beam. Processes that use lasers result in a high level of detail and fine features. EBM can process materials that are highly reactive in oxygen as the process occurs in a near vacuum, and thus can be made quicker and cheaper than subtractive methods.

PBF also has some disadvantages. Surface finish is generally rough (similar to sand casting) and needs post-processing in order to achieve tight tolerances. Methods that require support structures require additional (typically manual) work to remove them from the final part, including EBM. Excess powder removal is common to all PBF processes and requires additional design foresight to ensure that there are no trapped powder regions within the part. Long channels and holes can be especially difficult to remove all unprocessed powder from all PBF processes. EBM specifically requires either powder blasting, ultrasonic vibration, or mechanical methods to remove the powder, as the remaining powder no longer acts as a light metal powder, but clings together like wet sand due to the quick pre-scan which pre-heats and partially fuses the powder and prevents a phenomenon known as smoking [141]. Thus, certain geometries, such as deep narrow cavities are especially difficult to produce with EBM.

Of all PBF processes, LPBF has the greatest ability to create fine detailed, and highly conductive metal parts. LPBF machines are usually capable of creating parts that fit within a 250 mm cube, which is large enough for the scale of motor coils in this research. As there is a wide range of available materials with LPBF, many have processed conductive materials. Sections 2.9 and 2.10 will discuss copper and aluminium respectively processed by LPBF.

A few PBF processes other than LPBF have been used to processed copper and copper alloys. For example, EBM of copper has been reported [132], [136], [142], [143] by a number of researchers. In [136], multiple copper powders were tested including two which were over 99.99% pure, and another which was air atomised resulting in 99.8% purity. The results showed parts which were 99.3% the density of wrought copper and had an electrical conductivity of 97% of that of commercially pure copper. In [142], 99.91% pure copper was processed and a final density of 99.95% and electrical conductivity of 96.24% IACS. In [143], 99.94% pure copper was processed to a maximum density of 99.95% and showed elongated grain growth, beyond layer thicknesses, in the build direction. In [132], 99.95% pure copper was processed and was optimised for electrical conductivity, achieving 101.9% IACS which exceeds commercially pure copper but is not quite the conductivity of 99.999% pure copper (103.06% IACS) [49]. However, in all cases where electrical measurements were given, the method reported did not directly measure resistivity. Rather it indirectly calculates near surface conductivity using induced eddy currents and assumes isotropic material properties [19] while also being sensitive to surface roughness and surface contamination.

Copper alloys and mixtures have also been sintered by laser to various success [144]–[147], but as the use of a CO_2 laser was used, and due to the age of this research, few relevant findings can be drawn from this early research.

There have been other highly electrically conductive materials processed with LPBF such as gold and silver. In [133], pure gold was processed with a maximum relative density of 89.6%. However, the cost of gold is prohibitive for use in an electric motor. Electrical measurements were also not taken. In [148], silver was processed and evaluated through simulations, but density measurements were not taken, nor electrical properties measured. In both cases, surface finish was rough due to a lack of fusion caused by limited laser power and the high reflectivity and high thermal conductivity which limited the depth of the melt pool.

Overall, there is a lack of electrical properties reported for materials processed by PBF. When those properties are reported, they do not use direct measurement techniques such as the four-wire resistance, but rather indirect induction eddy-current techniques which assume isotropic properties when they calculate resistance [19]. But due to the unique microstructure of PBF parts compared to cast or wrought, and how mechanical properties in the as-built condition display anisotropic properties, it cannot be assumed that electrical properties are isotropic. Thus initial build orientation also needs to be considered, including any effects that powder spreading could have on those properties. Copper processed by LPBF will next be covered in more detail including challenges and the resulting resistivity.

Key findings from this section

- EBM has created highly conductive parts, but all assumed isotropic conditions
- Gold and silver have been processed by LPBF, but low density was a challenge
- General lack of direct electrical measurements which report initial build orientation

2.9 Processing copper with LPBF

Pure copper is widely used in electrical components due to its balance of low electrical resistivity and moderate commodity price compared to gold and silver. But pure copper has proven difficult to process by LPBF. As a result, there are few published papers. Challenges arise in reaching a high density [149] due to an inability to fully re-melt previously deposited copper. Its high thermal conductivity [150] causes rapid heat transfer away from the melt pool through the previously solidified material. An unstable melt pool [151] due to in part from the rapid formation of oxide layers [152] on the skin of the melt pool adds to the difficulties in processing LPBF of copper. Despite this, copper is an attractive material for many applications, and several companies including Aerojet Rocketdyne [153] and Fraunhofer [154] have promoted their ability to research the material, despite not actually producing any published results with the announcements. To overcome these challenges, researchers have explored a few different options.

The first is to overcome its high thermal conductivity. This conductivity is 390 W/m*K and is the second highest of any element, next to only silver [49]. This means that once it is provided with heat, it can quickly dissipate this heat away from the source of the heat. When trying to melt copper powder with a moving heat source, achieving full melting and fusing of the powder is difficult. For example, some of the first tests of copper with LPBF technology used only a 90 W laser which resulted in very poor processing, where density measurements were not reported [152]. Even with a 200 W laser, if the spot size is too large, the resulting laser power density is not high enough to fully melt pure copper. This was seen in [139] where the resulting parts that were only 66-68% dense. As a result, high power lasers (400 W and 1 kW) have been used in [137] to create high density parts (96.47% relative density), however no electrical measurements were taken. Similarly, in [138], a 1 kW laser was used to create parts with densities up to 97.8% but again, no electrical measurements were taken. Other than high laser powers, another way to overcome its high thermal conductivity is by having a high pre-heat temperature which reduces the thermal gradient between the unmelted and melted powders. Recently, the company TRUMPF GmbH + Co. KG (Germany) released a new LPBF machine, the TruPrint 5000, which can preheat up to 500 °C [155] which is the highest of any commercial LPBF machine. In the press release, they also state that with the addition of a green laser, copper can be processed. Unfortunately, green lasers were not a viable commercial option at the commencement of this work and were unavailable to work with for this research. However, using a green laser can be used to overcome another challenge of printing copper, its high reflectivity.

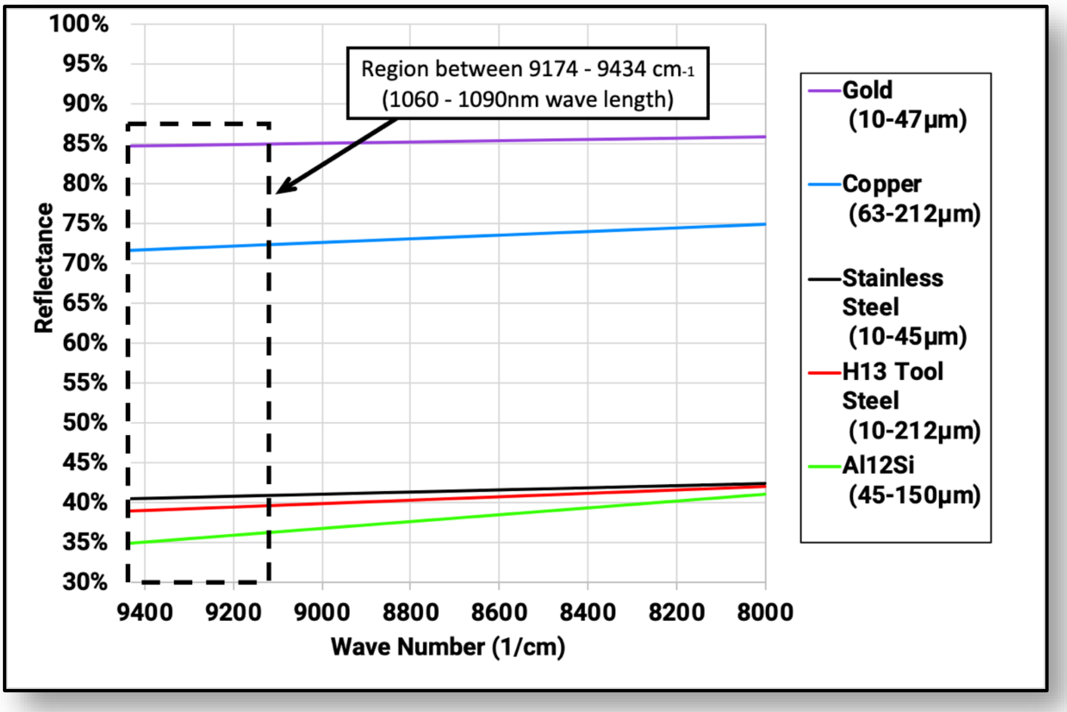

Figure 2-22: Percentage of reflectance of different metal powders including copper (second from the top in blue) (Recreated from original source [156]).

Copper is very reflective at the typical laser wavelengths used in LPBF. Typically, LPBF uses a laser wavelength of 1094 nm. At this wavelength, solid copper reflects 90-98% of the thermal energy [157]. However, powders are more absorbent, with copper powder reflecting only 71-72% of the energy, as seen in Figure 2-22, which also depended on particle size [156] where larger particles reflected more than smaller particles. Using different wavelengths of lasers is also being explored with copper [158] as it has a higher absorption to wavelengths less than 550 nm [157]. For example, the Fraunhofer Institute for Laser Technology (ILT), have stated that they are investigating processing copper via LPBF using a green laser [154] at a wavelength of 515 nm which is absorbed much greater than the near IR lasers. Traditionally used in science and medicine, it has been announced that the laser will be custom built with power up to 400 W specifically to process copper. TRUMPF has also demonstrated the printing of copper with a green laser [159] which has been used in welding and has a maximum power of 1 kW with a wavelength of 515 nm and a focus diameter of 150 µm [160]. Blue lasers are also now being investigated to weld copper with wavelengths of 450 nm [161] and powers up to 700 W [162]. However, there has not been any AM research using these types of lasers to process copper to date.

Lastly, to make copper more suitable for LPBF, researchers have investigated a few different Cu alloys and modifications to the powder itself. One such Cu alloy is GRCOP-84 [163], [164] (and potentially GRCOP-42 [165] which was only announced in early 2019), however, this alloy is very limited and primarily only available to those involved in NASA research. GRCOP-84 has 8% Cr and 4% Nb and was developed by the NASA Glenn Research Center to work best with rapid solidification technology like LPBF. This is in order to minimise the growth of Cr_2Nb precipitates which gives it excellent high-temperature strength and good creep resistance whilst also retaining relatively high thermal and electrical conductivity at 68% IACS. Copper alloys with 3.3-5% tin have also been processed by LPBF by Ventura et al. [166]–[168], with high-density structures being created with a resulting conductivity of up to 24.1% IACS and through thermal ageing were able to improve this to 43.2% IACS [166]. They used a four-wire Kelvin measurement with specimens measuring 1 x 1 x 60 mm however they were processing an alloy and neglected initial build orientation with their measurements. In [169], the goal of printing high conductivity material was researched using a 300 W LPBF machine as well as a DED powder blown machine with a 1250 W laser. Copper powder for the experiments was first reduced by hydrogen gas to remove oxides, and then coated with a few nanometres of polydimethylsiloxane (PDMS) to inhibit oxidation. The PDMS would then be vaporised in the AM process. Experiments were performed using LPBF on both steel and copper substrates. The maximum density achieved was 91%, and electrical measurements were made. However, the conductivity was far below expected (maximum 16% IACS) for this density and copper purity (99.4%). It was found that the copper used in the experiment had 0.6% phosphorus in the starting powder, which has a severe negative effect on conductivity as seen in Figure 2-23.

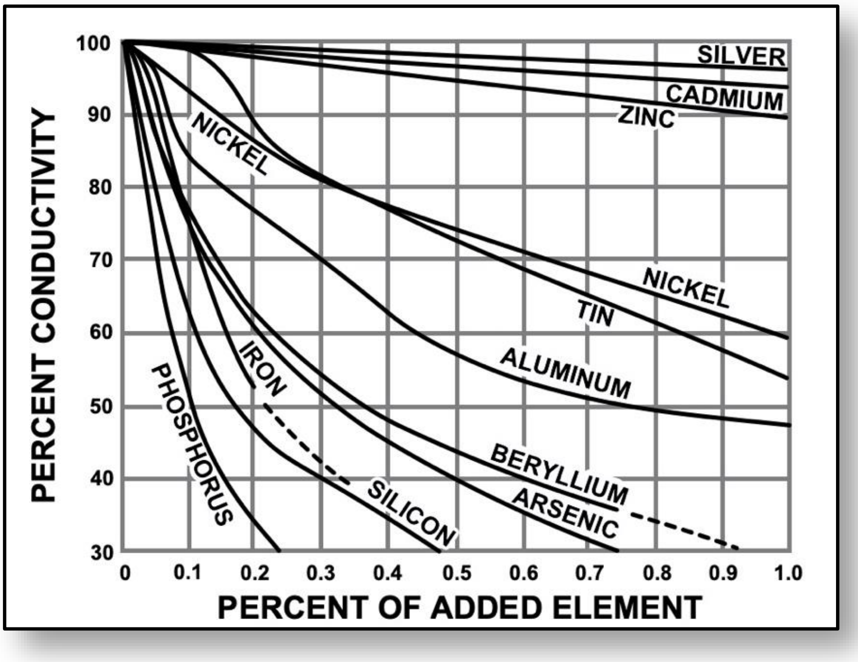

Figure 2-23: Influence of dissolved impurity elements on the electrical conductivity of copper at ambient temperature (1980 Olin Corporation) (Recreated from original source [169]).

Elemental modification to pure copper may improve processability, but it always negatively influences the resistivity of the copper. This is the effect which was seen in [169] with the phosphorus content. Typically, when copper powder is created through an air atomisation process, small amounts of phosphorus in the range of 0.1-0.3 weight per cent, is added to the molten copper before atomisation. When atomised, the phosphorus forms a protective oxide shield to the copper and reduces oxygen in the copper by forming a phosphorus pentoxide (P_2O_3) compound. But this also adds residual phosphorus particles into the resulting copper powder [170]. In electrical applications, even this small amount of phosphorus has a very large negative effect on conductivity, where just 0.1% phosphorus reduces coppers conductivity by 50% (see Figure 2-23).

As electrical conductivity is an area of interest for processing copper with LPBF, there have been a few researchers who have tried to overcome the challenges mentioned above and have either demonstrated conductivity or reported the resistivity. One way to accomplish this is using a small laser spot diameter with a 200 W laser in order to achieve high laser power densities which can overcome some of the challenges of processing copper with LPBF. For example, 99.7% pure copper was processed in [151] using a 200 W laser with a small laser spot diameter, achieving a density of 73%. Despite not reporting the resistivity, they demonstrated a functioning printed circuit board with an LED light. In both [149], [171] Lykov et al. were also able to produce copper parts using a 200 W laser and small laser spot diameter. Densities ranged from 88.10% to 99.12%. However, it is believed that the 99% density was not the actual density, but rather a result of poor polishing technique and/or poor thresholding measurement technique. This is due to the 88% measurement being obtained through an Archimedes measurement (a volumetric measurement) rather than optical porosity measurement (a single slice measurement dependent on the applied polishing technique). Optical measurements are a valid method for obtaining a relative density for a material, but the polishing technique needs to be perfect. This is especially true for very soft materials like pure copper where improper polishing (too much pressure) tends to smear material over top pores creating artificially high densities. The polished images for the 88% result appear to be a higher density than the image for the reported 99% dense result, thus furthering the belief of poor polishing techniques.

To summarise, processing copper by LPBF has proven to be difficult. In order to use copper in LPBF applications for electrical applications, these difficulties either need to be overcome or they need to be accepted and quantified. This research will process high purity copper which is free of detrimental elements with a 200 W LPBF machine that has a very small laser spot diameter in order to investigate the resulting electrical properties. Knowing the challenges that have been faced by others, the processing parameters will be optimised to achieve a density which is as high as possible but will likely be below 90% based on this literature review. Once this high-density parameter set is found, despite the potential for high porosity, it will examine the electrical resistivity of the pure copper and will use the direct measurement four-wire Kelvin test method. This research will then compare the effect on the resistivity of initial build orientation and post heat treatments. As copper is difficult to process with LPBF in a pure form, an alternative strategy will be employed for a second material. An aluminium alloy, AlSi10Mg, will be explored in the next section, and while it will not have as high of a potential conductivity as a pure metal, it should be within an order of magnitude to the baseline properties but with better LPBF processability.

Key findings from this section

- Copper is hard to process with LPBF due to high reflectivity and thermal conductivity
- High densities have been achieved primarily only by high-powered lasers
- LPBF machines rated at 200 W or lower have not reached 90% dense with copper
- Alloying elements, especially phosphorus, have negative effects on conductivity
- Few have reported any resistivity measurements, those that have did not process pure copper, and ignored initial build orientation and post heat treatments

2.10 Aluminium alloys with LPBF

LPBF has been used to process copper [152], silver [148], gold [133], and aluminium [172]. But few have reported on the electrical properties of the produced material, and none have reported if these properties were isotropic or not. While silver, copper, and gold have a lower resistivity than aluminium, the cost of silver and gold prevent them from being used for anything other than thin film conductors. Pure aluminium has been difficult to process with AM as it suffers from many of the same problems of pure copper. In [172], it was shown that challenges arise in reaching a high density (89.5%), as there are issues of oxidation, an inability to process without a high power laser due to its high thermal conductivity, high reflectivity and an unstable melt pool [172]. As a result, aluminium alloys have mainly been processed. However, recently, relatively pure aluminium has been printed with a 400 W laser [173], achieving a density of 99.5% as part of a study of LPBF of aluminium-silicon alloys. An advantage that aluminium has over copper is that while it has approximately 60% higher resistivity than copper, it weighs about 70% less. This allows it to have the highest specific conductance out of all materials, as seen in Table 2-1. Aluminium also costs significantly less than copper which has had high fluctuations in price in the past. Thus aluminium can carry more current per kilogram or per dollar than copper. This gives it an advantage in applications where weight or cost is an important design requirement such as in aerospace [174], automotive [175], or in high-frequency applications [176].

While pure aluminium has a better conductivity than any of its alloys it is too soft to be processed in the manufacture of traditional electric wires. Thus the 1350 alloy was developed for electrical purposes. It is 99.5% pure aluminium and is rated at 61.2% IACS [55]. When pure aluminium is melted and cooled quickly, it shrinks quickly resulting in hot tears and cracking [177]. The casting industry has developed a range of alloys which contain some silicon and magnesium to help counteract this phenomenon while also increasing strength. AlSi10Mg is a casting alloy that was developed as an alternative to pure aluminium which was too soft to use in many engineering applications. It was adopted early by AM as an easy to process metal powder for LPBF [172]. As with pure aluminium, AlSi10Mg has a high specific conductance, and is better per kilogram even when compared to pure copper and silver, despite not having as low a resistivity as pure aluminium.

Some investigations have processed AlSi10Mg and reported some electrical conductivity measurements, but each has lacked vital information crucial to adopting it for actual electrical applications. One paper reported on a mix of 1% by weight carbon nanotubes in AlSi10Mg processed with LPBF. But the claimed resistivity was in the order of one-tenth of that of pure silver and failed to characterise the base alloy [178]. Another claimed conductivity with respect to various heat treatments [179] but ignored initial build orientation. They also used an indirect measurement method which cannot directly determine bulk properties. Another paper compared a single as-built AlSi10Mg specimen to one which was annealed [180], but it also failed to include initial build orientation and used the same indirect measurement method which resulted in values which were 10% lower than that expected for cast versions of this alloy (Table 2-1).

While AlSi10Mg has been studied extensively in LPBF as seen in these two recent review papers [181], [182], there has not been any focus on any electrical characterisation, perhaps due to it being more of a structural alloy. The focus has been on reporting the microstructure and physical-mechanical properties. Emphasis has been on how to optimise processing parameters [183], [184] or heat treatments [185], [186]. Those who have reported electrical properties have not correlated them to the initial build orientation or heat treatment. Also, only non-contact indirect surface measurement methods have been used which assume isotropic conductivity [19]. While this can be assumed with cast versions of the alloy, which are isotropic, the grain structure and texture produced by AM is distinct from that of cast.

Additional aluminium alloys have been studied for their mechanical properties, but none have reported electrical properties. In [187], aluminium alloys 2022 and 2024 were fabricated, which are copper-magnesium aluminium alloys. Through parameter optimisation, a final density of 99.5% was achieved. In [188], aluminium alloy 6061 was processed with LPBF, however, results were very poor with many cracks and high porosity visible. This was due to the fact that this alloy tends to hot tear during casting and welding. In [189], aluminium alloy 7075 was used as a starting point to develop a custom alloy better suited for LPBF processing. The non-modified alloy showed similar signs to 6061 developing microcracking, even when silicon was added up to 2%, the maximum density was around 95%. However, by increasing the silicon content to 4%, the microcracking was eliminated and a density of 98.9% was achieved.

In order to design AM parts for electrical applications, the actual AM properties are needed and cannot be assumed to be the same as cast. This research will examine the electrical resistivity of an AlSi10Mg alloy using a direct four-wire (Kelvin) test method. This method can directly determine bulk (non-surface) electrical properties. This research will also compare how initial build orientation and heat treatment affect resistivity.

Key findings from this section

- Pure aluminium suffers from the same challenges to process by LPBF as copper
- Mainly Al alloys have been processed by LPBF, with AlSi10Mg being one of the first
- Despite a large body of research on processing conditions and mechanical properties of Al alloys, no electrical properties have been directly measured
- All published resistivity values have been indirectly measured (assumed isotropic) and have neglected initial build orientation and post heat treatments

2.11 Machine Learning (ML) and AM

While AM is touted as a purely digital manufacturing method, the reality is that there is still a lot of manual human intervention at all stages of the process. However, because the core of AM is digital, it allows the introduction of other digital technologies which can help remove some of this human interaction. One of these areas is finding and deciding upon the optimal processing parameters while developing a new material for LPBF. As copper is difficult to process, there can be difficulty in qualifying the differences between different parameters. An emerging field of research which helps with organising and finding patterns in large amounts of data is Machine Learning (ML). With ML, qualifying the optical micrographs can greatly aid in processing materials such as copper. ML is a subsection of a larger area of computer science which is often called Artificial Intelligence, or AI. In AI, a program can accomplish a task which is typically thought to only be accomplished by something that has some intelligence. ML furthers this concept by learning a task for which it wasn’t explicitly programmed. With exposure to more data, algorithms continue to improve. Within ML, there is a further subsection called Deep Learning. In Deep Learning, algorithms are organised into multiple layers of processing. These algorithms can find patterns and solve problems that are unable to be seen directly. At the core of each of these areas, lies computer programming, linear algebra, and statistics.

Through these types of algorithms, AI has been able to perform tasks which were thought impossible a decade ago. In 2016, AI was able to make the adjustments in a 2001 Nobel prize winning experiment in under an hour [190] (which was the motivation to think to use ML in this work). These same adjustments took the practised and experienced researchers ten times longer to figure out. In 2017, AI mastered the game of chess in four hours starting from scratch [191] and mastered the game of Go without any human training in 40 days [192]. It is now able to diagnose retinal disease from 3D models at a level which matches or exceeds that of human experts [193]. In this research, ML will be used with images gathered from the parameter optimisation of pure copper in order to cluster and organise the parameter sets into different levels of quality, and aid in the decision-making process to find the parameters which result in the highest quality. But first, a review of what ML is and how it is used, followed by current state of the art uses of AI with AM applications, and finally how images are clustered them into discrete groupings, which is how this research will use ML.

2.11.1 Machine learning architecture and background

The basis of ML comes from the concept of neural science. The neuron accepts information from several sources, determines if it should fire, and when it fires, it sends that information to other neurons. This pattern continues until an output value is reached and provides some new information based on the input. In ML, this concept of neurons is applied as a feed forward neural network with cells, as seen in Figure 2-24. Input cells pass information to a hidden (also called fully connected) layer, which then feeds into output cells. The weight values (black lines between cells) are what is learned through the ML process. By increasing the number of hidden layers (and thus the number of connections), a deep network or Artificial Neural Network (ANN) is created (Figure 2-24). These networks can be trained using known outputs so that it can learn the connections that match the output given the inputs which lead to it. These outputs can be classification labels (e.g. cat/dog), numerical values (e.g. images), or a mirror of the inputs (e.g. verification). This ML can then be applied to new inputs which have not been encountered before and can provide new outputs based on its previous training.

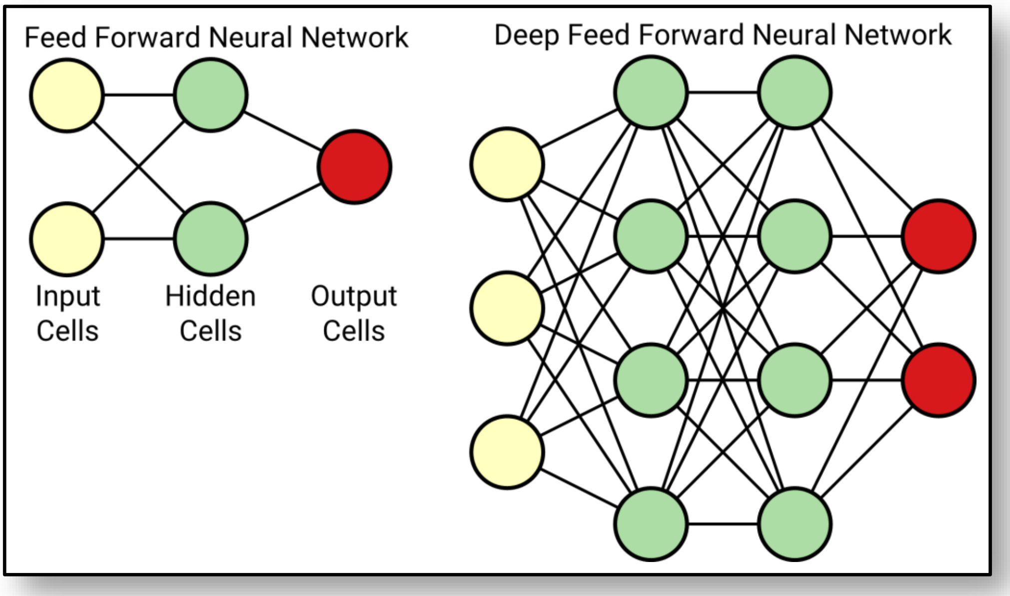

Figure 2-24: Examples of basic feedforward and deep feedforward neural networks.

Cells use real numbers as both input and output. When a cell receives an input, it multiplies this number by a weight. A weight is another real number and can be represented as the black lines between the circular cells seen in Figure 2-24. When the input is multiplied by the weight, the result is passed into an activation function. This activation function can be a wide range of available mathematical functions as seen in Figure 2-25, to determine what the value should be that is passed onto the next cells which are connected to it.

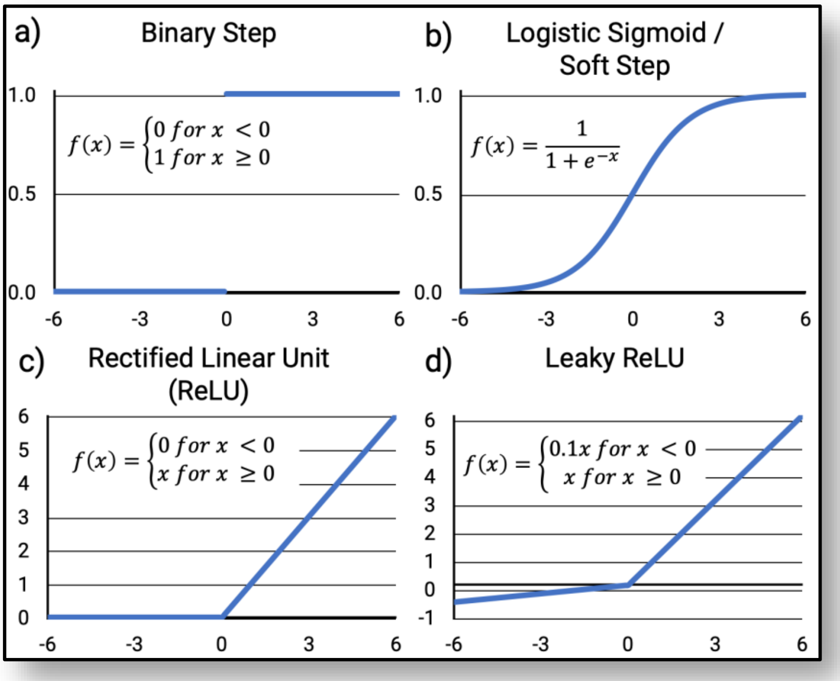

Figure 2-25: Examples of four step functions with outputs given the corresponding input; the binary step (a), the logistic sigmoid or soft step (b), the rectified linear unit or ReLU (c), and the leaky ReLU (d).

A step-based activation function (Figure 2-25 a) either returns a 0 (does not fire) or a 1 (does fire), but there are situations and reasons why a step function should not be used (such as in a deep network). As such, there is a range of other functions which can pass values between 0 and 1 such as the logistic sigmoid function (Figure 2-25 b), others which pass values above 1 like the Rectified Linear Unit (Figure 2-25 c), and others which can pass negative values such as the Leaky ReLU (Figure 2-25 d). The choice of activation depends on the architecture and purpose of the network being used.

This pattern of cells receiving and sending values continues through the entire network. However, images can also be fed as an input into a neural network. An image is simply a grid of pixels where each pixel is a single value between 0 (black) and 255 (white) for greyscale images. Colour images contain three values for each pixel, where each value represents either red, green, or blue. However, when this pixel data is fed into an ANN, they lose all positional meaning.

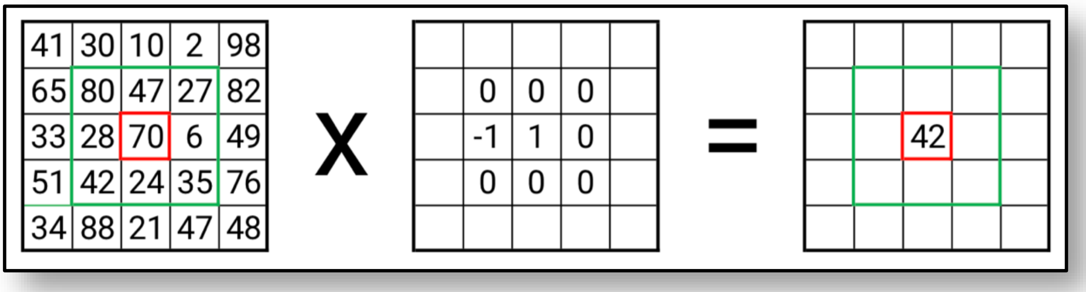

Figure 2-26: A simple example of how a convolution creates a new function.

To overcome this limitation, a new type of neural network was created based on the mathematical idea of convolutions, named the Convolutional Neural Network (CNN). Convolutions create a new function based on the input of two different inputs. An example of a convolution can be seen in Figure 2-26. The original image is seen on the left as a 5x5 matrix of numbers. The convolution matrix (also called a filter) is represented as a 3x3 matrix and is being applied to the original image matrix at the location highlighted in red, with the region of interaction highlighted in green. The resulting matrix (or feature map) on the right is a 5x5 matrix, but only a single value is shown, as this filter needs to pass over the entire original image to fully populate the new matrix. This feature map contains the sum of the products of each corresponding location. In this example, all zeros multiply to equal a zero sum but 42 is a result from -1*28 + 1*70. This specific filter in Figure 2-26 can enhance the vertical right edges of an image, with an example seen in Figure 2-27.

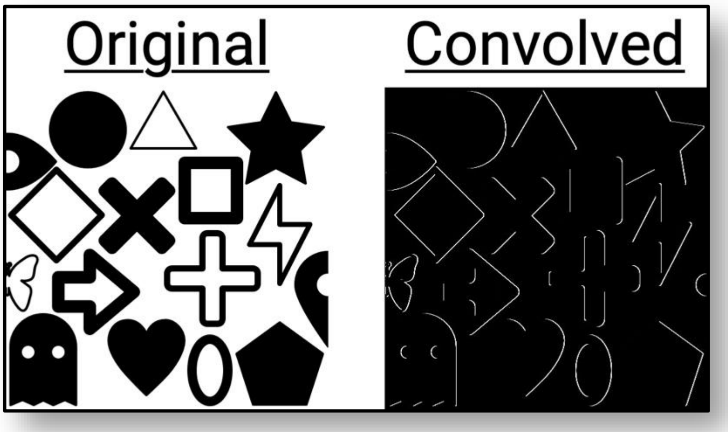

Figure 2-27: An example of applying a convolution matrix to enhance vertical right edges.

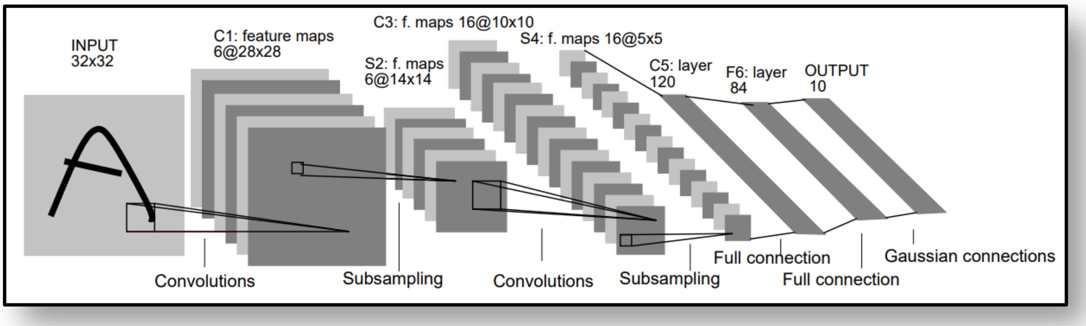

Figure 2-28: Typical Convolutional Neural Network architecture [194].

The CNN is used in ML to turn an image into a compressed data structure which retains information about the patterns and positional information of the original image. The original architecture for a CNN can be seen in Figure 2-28 which has seven layers. This CNN uses two convolutional layers, which use filters (as one function) applied to the input image (a second function) to create a new output called a feature map. These filters correspond to learned features which the CNN identifies as significant such as a vertical lines, edges, or other patterns. The activation function within a CNN is typically always the ReLU as it yields better results than any other. The example in Figure 2-28 also has two subsampling layers which are applied to the convolutional output feature maps.

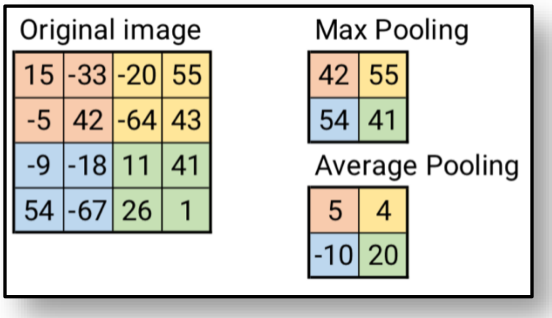

Original image

15	-33	-20	55
-5	42	-64	43
-9	-18	11	41
54	-67	26	1

Max Pooling

42	55
54	41

Average Pooling

5	4
-10	20

Figure 2-29: Example of subsampling using max pooling and average pooling.

Subsampling (such as max or average pooling) is a technique which reduces the size of a matrix while retaining the majority of information from the original image, as seen in Figure 2-29. These smaller feature maps can then be fed into an ANN to perform desired tasks. This architecture has been used since 1998, however, with the recent advances in both central processing unit (CPU) and graphics processing unit (GPU) technology, CNNs have become faster and more powerful and have been used to quickly classify millions of different images with thousands of different image categories [195].

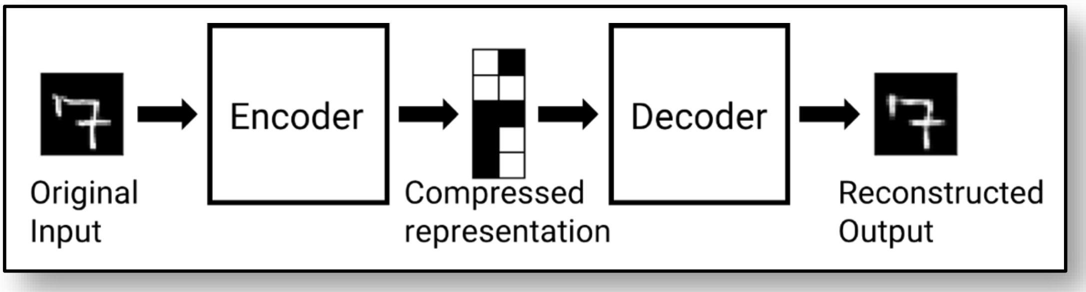

Figure 2-30: Typical concept for an autoencoder.

An Autoencoder (AE) is another specialised type of neural network which has been around since about 2006. AEs are able to reduce high-dimensional data such as images to a low-dimensional compressed representation [196]. AEs typically are comprised of two halves, namely an encoder portion and a decoder portion, with a compressed representation of the original input between the two, as seen in Figure 2-30. For images, the encoder of the AE is the same as the convolutional and pooling layers found in the CNN. The decoder portion is the opposite of the encoder, with deconvolutional and unpooling layers. The compressed representation in the middle is also called the latent space of the AE. The AE network is trained over many iterations to match the output as closely as possible to the input while reducing the error between the two, typically using the mean square error or other similar error measurement technique. There are two parts which make the AE useful, the error calculation comparing the input to output, and the compressed latent space representation. Initially the AE was seen as an alternative way to encode data using the latent space to be more efficient in data processing, however, other applications have emerged for using the error calculation such as fraud detection. For example, if the model is trained with only valid transactions, when a fraudulent transaction is passed through, the error becomes much higher than normal, indicating that it has a high probability of being fraudulent.

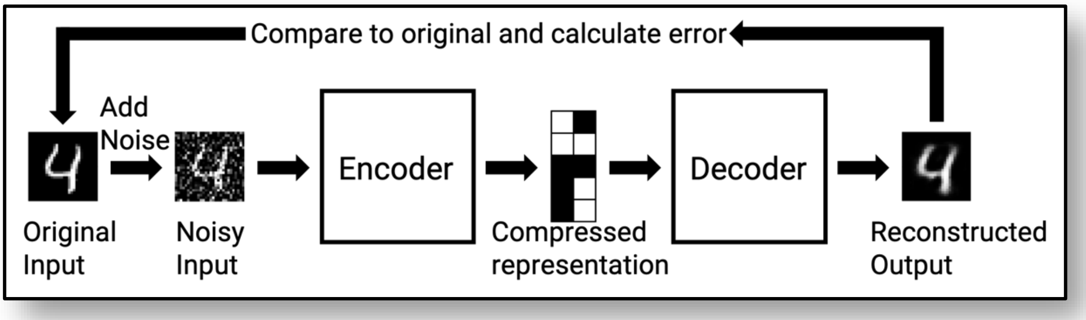

Figure 2-31: Concept for a denoising autoencoder.

Another application is to eliminate specific noise from images. Rather than using a perfect input image, it is a noisy version of an image. When the error is calculated for the output, it's compared to the original rather than the noisy version. This results in the network being optimised to eliminate the noise and produce a perfect output, seen in Figure 2-31. After it has been trained, it can then be used on new images it has not encountered before to reduce the noise and clean up the input image, and if the noise is similar to that it was trained with. This application has been shown on not just simple images, but on complete high-resolution images, producing remarkable recreations, as seen in Figure 2-32.

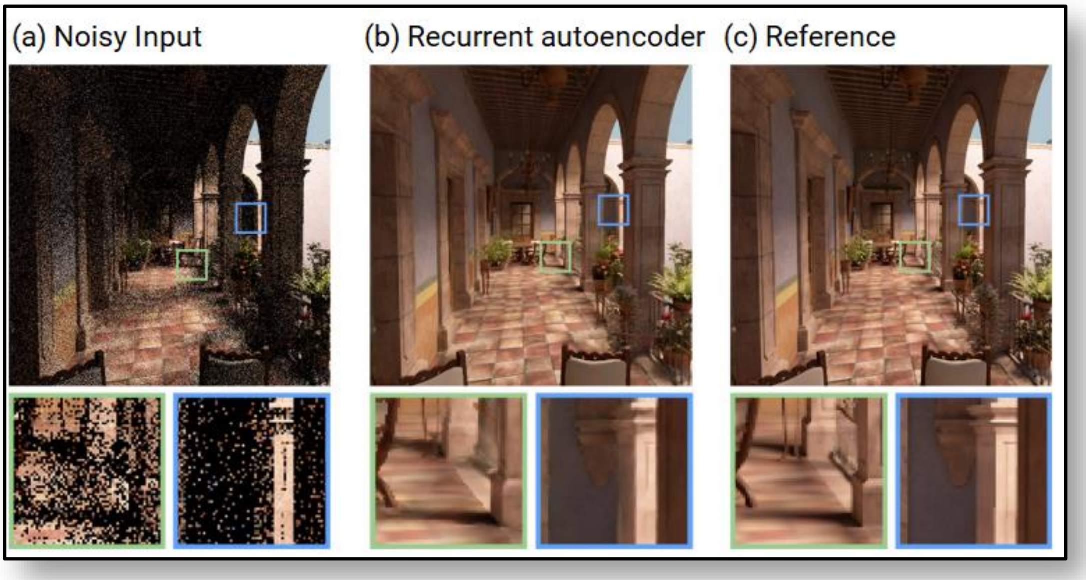

Figure 2-32: Example of a denoising autoencoder: a) noisy input, b) autoencoder output, c) original reference image [197].

Both ANNs and AEs are considered supervised learning applications, which means that the network is trained using data that has known ground truth labels or output values. When these ground truth labels or values are available, the ML problem is considered supervised, as it requires supervision to create the labels. However, when the output values are not known, or for which there are no labels, unsupervised learning is required. Clustering is an unsupervised method within ML which has become very efficient at finding patterns and organising data when no label is given. An example of the t-SNE clustering graphing algorithm [198] with handwritten digits is shown in Figure 2-33. Given a population of data points, there are a number of different algorithms which can group clusters together based on their similarity. This is a non-trivial problem when using high-dimensional data, such as images. There are several existing solutions which are purely statistical in nature that can be applied to this type of problem, such as K-Means, and K-Nearest Neighbours (KNN).

Figure 2-33: Example of raw input before clustering, showing handwritten digits from the MNIST dataset, graphed in 2D using the dimensional reducing t-SNE graphing method.

But where ML comes into play rather than statistics, is when an autoencoder is paired with these algorithms to produce better clustering results. Due to the nature of the latent space representation of the AE, clusters of data can be better seen when compared to traditional dimensionality reduction techniques such as Principal Component Analysis (PCA). PCA is a statistical method that transforms the original data to a desired number of dimensions. These new dimensions are used to explain the amount of variation that existed in the original data. The higher the number of dimensions for PCA, the better it represents the original data. While PCA does a good job at reducing the dimensions and explaining variance within the original data, it does not correlate any potential spatial relations that existed in the original data. However, the latent space of the AE does both jobs. This latent space can then be used in clustering algorithms which help further improve the accuracy of image clustering applications.

While applications for AI have also prompted advances in natural language processing (Siri / Hey Google), computer vision for self-driving cars (Tesla / Waymo), and facial recognition, it also has been making its way into AM. Most instances for AM and AI involve using it for in-process monitoring for defect detection, however there is potential for AI to apply to many more applications in AM.

2.11.2 Uses of machine learning in AM

While there has been a number of announcements of companies adopting AI and Big Data to help in process monitoring and control, only published applications will be covered here. There are many potential applications where AI can be used with AM. One application which is actively being researched is using images of each layer of a PBF process to detect defects or problems in the build.

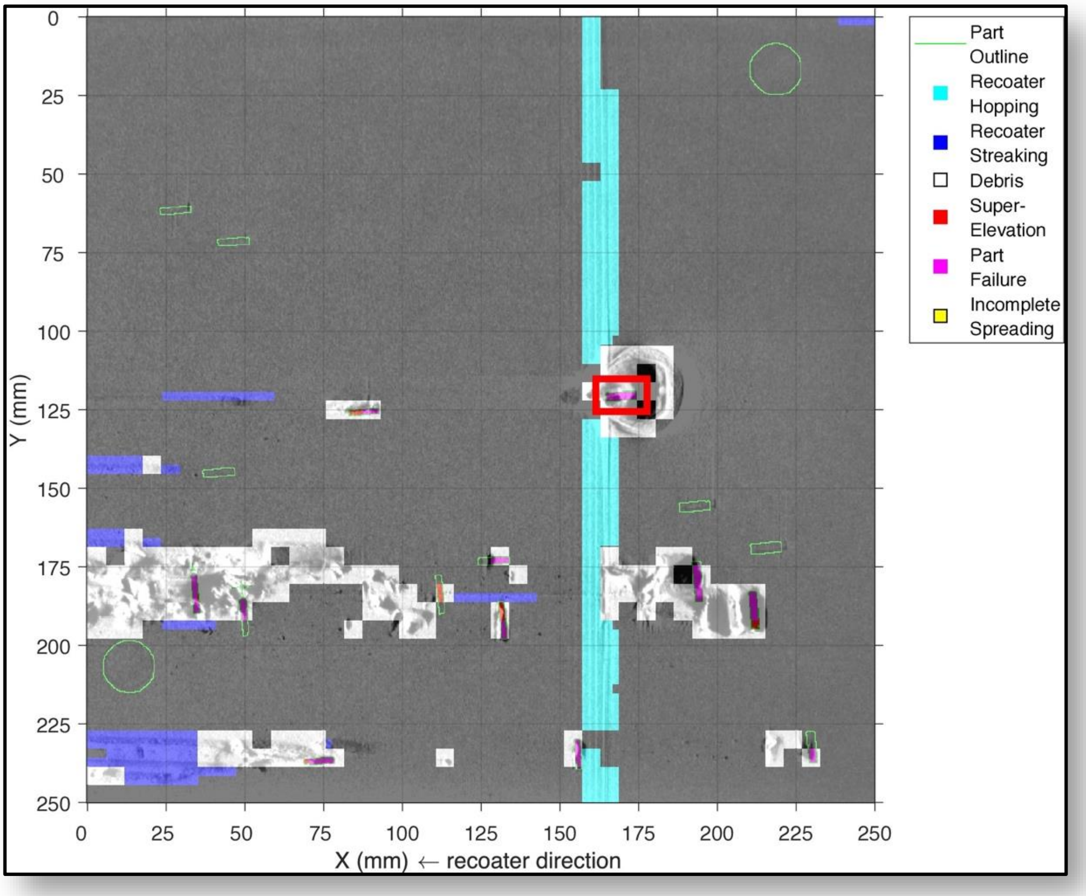

Figure 2-34: Identification of various defects in a layer of PBF [199].

For example, in [199], a shallow ML classifier was used which identified different types of visible problems which occur in a PBF build. This supervised classifier was trained on labelled images to recognise different defects such as recoater hopping (wavy bumps in the powder perpendicular to recoater travel), recoater streaking (indented lines along the direction of recoater travel), debris, superelevation (areas raised above the powder bed), part failure, and incomplete spreading (areas on the powder bed that are not fully covered by powder creating a shallow hole). Each of these can be seen in Figure 2-34. These defects were then superimposed upon the images of each layer and highlight areas of concern. It is currently used as a diagnosis tool post-build but is in the development stages of being a direct feedback control loop for real-time control.

In order to get the most out of supervised learning, additional data sources can be incorporated, such as computed tomography (CT) data. This occurred in [200] where a supervised ML algorithm was developed to detect anomalies during a PBF build. Many images were taken during the build and fed into the ML algorithm which then either classified portions of the image as having a defect or not having a defect. This was trained in conjunction with processed CT data which was analysed by a human and labelled with defect locations. It was then trained further and was found to have over 80% accuracy with further cross-validation experiments.

Similarly, X-ray CT data can be used as in [201], where Inconel 718 was analysed using a supervised learning algorithm known as a Random Forest Network (RFN). The RFN was used to both classify defects and determine optimal processing parameters. Cylinders which were 4mm tall with a 2mm diameter were imaged using X-Ray CT and analysed using statistics. The result was that the researchers were able to narrow down the causes for different types of failure and defects in the build.

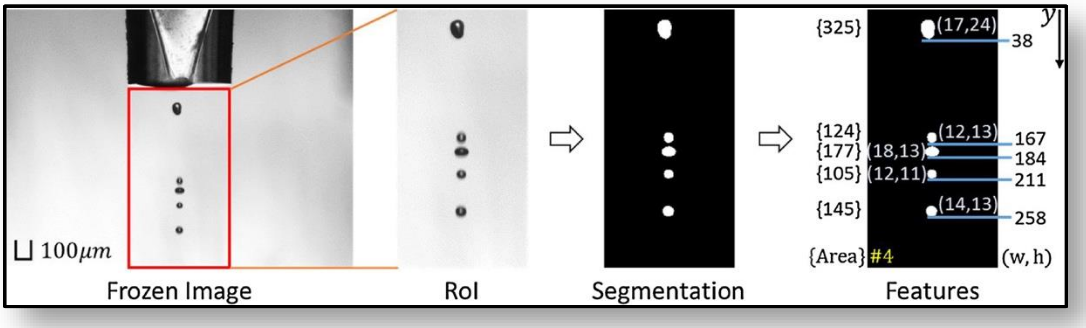

Figure 2-35: Analysis of a jetted droplets to determine various properties through machine learning [202].

Beyond PBF, ML can be used with processes such as material jetting. For example, in [202], ML was used for droplet inspection as a closed-loop control system for the Vader Systems liquid metal jet printing machine. First, an image was taken at a set time after a voltage was applied to create a droplet. A region of interest was identified below the nozzle of the original image and was extracted and analysed for droplet features, as seen in Figure 2-35. This image was segmented to identify and label different features including the number of droplets, as well as the area, height, width, and vertical location of each droplet. The segmented image was used as the input to a ML network, along with the voltage parameters which were used to create a droplet. The network was then trained to correlate the image with the applied voltage parameters. It was then tested with new images in order to predict the voltage parameters used to create the image. Using this training method, the algorithm can then be used as a closed-loop real-time feedback mechanism to ensure quality jetting. The waveform was a constant trapezoidal shape and was not varied.

In addition to process monitoring and optimisation, a ML model can be used to predict geometrical deviations in 3D printed parts as in [203]. This learned deviation of the printed geometry to the CAD model input can inform the part designer of the expected tolerances of the printed part. This algorithm can aid low-quality built printers to achieve the same level of accuracy as higher-quality printers. It can also be used as a tool for those using DfAM to manufacture parts to greater tolerances and accuracy.

In the course of process parameter optimisation for new materials for AM, a lot of experimental data is generated. Some of this data is in the form of images of scan tracks or printed test specimens. From imaging the top surface of a test print, a sense of the quality of the parameters can be determined. However, this quality is a subjective judgement and becomes especially difficult when there is varying quality within a single test specimen. This is a type of problem that AI and ML can potentially aid in. Image classification and clustering are two areas of ML which are of potential benefit in determining print quality.

2.11.3 Image clustering autoencoders

Within the last few years, the concepts of clustering images and autoencoders have combined into the Convolutional Autoencoder (CAE) resulting in ever-improving results. In [204], the concept of pairing a convolutional autoencoder together with a clustering model was introduced. Previously, the clustering was performed with traditional ANNs. Images were reduced to pixel values and fed into the input cells of the ANN. The hidden dense layers would then compute values which would then predict if the image was one of the pre-determined classes. In the example of the MNIST database (a database of 70,000 handwritten digits), the output would be a prediction of if the input image was a number 0 to 9. However, feeding images into this type of network causes features that are spread over multiple pixels to be lost. As a result, they are not able to preserve the local structure of images. But a CNN can preserve this data and can make more representational compressions to the data when paired with an autoencoder. The centremost layer of the CAE can be used for clustering. But what made the work in [204] unique is their combination of deep learning, the clustering AE, and use of convolutional layers. They also proposed a Deep Convolutional Embedded Clustering (DCEC) technique which combined these concepts along with a secondary clustering output attached to the latent space of the AE. Once the CAE is trained, the DCEC is then iterated upon to minimise the error in the clustering layer, while still retaining the CAE in order to preserve the original features. This work was shared and made opensource on GitHub [205]. They were able to achieve an accuracy of 88.97% on the full MNIST dataset.

While 89% accuracy is good, it does not represent the best that can be achieved on this dataset. An easy to implement ANN that is often used as a benchmarking tool [206] is able to achieve an accuracy of over 99%. This high accuracy has to do with the training method and simplicity of the dataset. When training an ANN, the input is given, and the output makes its prediction. This prediction is then compared to the actual ground truth, and the weights are then adjusted to reduce the error between predicted and actual. With the MNIST dataset, it has been shown that the prediction can be made usually by just a single pixel [207]. This underlying pattern is discovered in training by the ANN, and which achieves its high accuracy. However, as previously mentioned, this method does not preserve the features that we would recognise as a handwritten digit. This is where CNNs excel, but when used for clustering, there is still room for improvement.

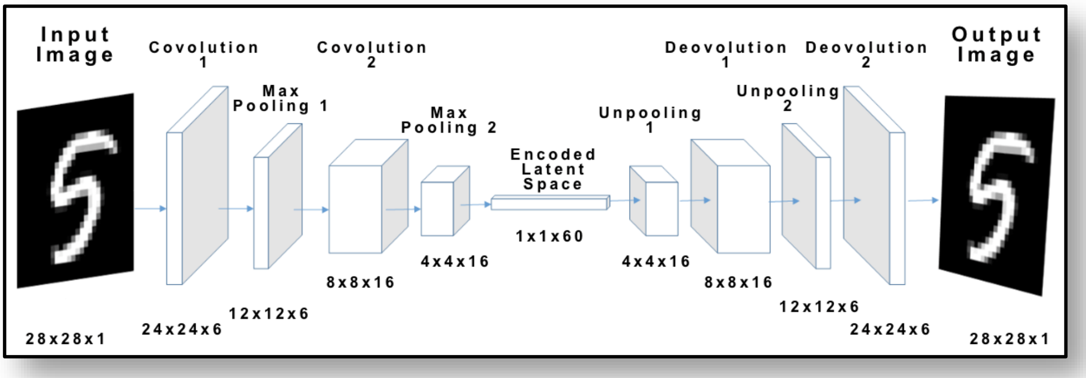

Figure 2-36: Autoencoder architecture employed by [208] in order to promote clustering.

In [208], this disparity between the ANN and CAE accuracy is addressed. They found that the pre-training portion mentioned in the DCEC method contributes the most to the final accuracy, with the second part of clustering contributing less than 15-20% of the final accuracy. Here they propose an improved clustering technique in the pre-training phase of the CAE. Rather than the traditional method of calculating the loss of the CAE (comparing the output to the input and making them as similar as possible) which aims to reproduce the original image exactly, they propose a new loss function. This loss function does a comparison within each batch of the learning and compares the latent space distance between all points. The points that are closest to each other are treated as being the same, and one mathematical formula is applied to them in order to promote their sameness, while all other points have a separate formula applied to them. This pairwise loss function is also combined with the traditional comparative loss function between the input and output in order to maintain reconstruction similarity. They also adopted an AE structure that is much shallower than most, with only three convolutional layers and no flattening of the encoded latent space. This elimination of the flattening helps in feature perseveration. With this new architecture and pairwise loss function, they have been able to achieve an accuracy of 97.4% on the MNIST database, with an accuracy of 87% in the pre-training phase alone.

In this research, these previous two works are adopted and modified in order to cluster image data taken of single-wall copper tracks produced by LPBF. This resulting output can then be used as a method to determine the quality of the test tracks. Once the quality of the tracks can be determined, the process parameters can be automatically optimised. One of the applications for copper LPBF parts is in exploiting its high electrical conductivity. Having custom designed copper parts can potentially be used in electric motor applications, but before designing such parts, a review of what research areas are being investigated for electric motors is first needed.

Key findings from this section

- ML is a digital technology which can aid in various AM aspects
- Convolutional autoencoders can aid in clustering similar groups of images
- To date, there have been no ML applications aiding in parameter optimisation

2.12 Summary

Materials such as copper and aluminium are used for electrical applications as they are cost effective and have a low resistivity. Pure copper and pure aluminium are very reflective at the wavelengths of lasers used in LPBF and have very high thermal conductivities that conduct heat away from the heat source. For these reasons, pure copper and pure aluminium will be very difficult to process with LPBF but they have the lowest potential resistivity. Alloys of these elements can aid in processing with LPBF, but at the expense of low resistivity as alloying elements are detrimental to conductivity. In order to prove out these two concepts (processability of a pure element verses an alloy), pure copper and an aluminium alloy, AlSi10Mg, have been chosen to process with a 200 W LPBF machine.

But in order to use any AM material for manufacturing of electric motor coils, a review of the first principles of coils needed to take place, including how coils are manufactured traditionally, challenges with those coils, and how AM can redesign them. As copper losses are the dominant source of loss in an electric motor, AM needs to be able to address this loss through its freedom of design. While AM cannot increase the electromagnetic limit of a motor due to inherent material property limitations, AM can potentially increase the thermal limit of a winding which will increase motor performance and efficiency. AM can also help avoid some of the failure modes which exist in traditional windings due to a lack of control of the conductors in the slot, while also increasing the fill factor of the motor, and dissipating heat from the end windings.

As most non-mass-produced motors rely on manual hand-manufacture for windings, AM has the potential to provide an alternative without the same issues that plague manual windings. But in order to achieve this, the motor and type of windings needed to be identified for an initial investigation into this. Concentrated windings which can fit an open slot, which is often found in an SRM was identified as the desired candidate for using AM windings. Using AM, some of the future trends of electric motors can potentially be achieved such as higher efficiency motors, robust and economical electric vehicle motors, and reliable and compact motors for enabling the more and all-electric aircraft. Because of this, AM has become a topic of interest for electric motor designers, and some have started to investigate this area. But of those who have, either function or performance has not been demonstrated or have not used DfAM in the design process. Only proof-of-concept parts have been created, along with motors with non-AM active components. Therefore, this was identified as a gap in the literature knowledge on how best to use AM to create windings. Thus, this work will help address how to use AM to create windings, from design to manufacture. This will be the first area that this work will address.

While AM can produce conductive parts, electrical properties have not been typically reported. Those who have measured electrical properties have not used direct electrical measurements, but rather surface eddy-current based measurements which rely on isotropic properties for accurate results. AM has shown that mechanical and other properties are not generally isotropic, thus this indirect method is flawed for resistivity measurements on AM parts. For those few who have used direct methods for measuring resistivity, initial build orientation and heat treatments have been ignored.

The review of LPBF for pure copper and AlSi10Mg has shown that there was an opportunity to measure and provide direct resistivity values with respect to initial build orientation and post-heat treatments. The literature has shown that pure copper will be very difficult to process with a 200 W LPBF machine, even with a small laser spot size. Regardless of relative density, pure copper has not been properly measured for resistivity. And despite a large body of knowledge for AlSi10Mg, it too has not had its resistivity properly characterised. These are the second and third areas that this work will focus in order to help fill in this gap in the literature.

As pure copper did not have a published parameter set for use in LPBF (unlike AlSi10Mg), part of that work dealt with finding a parameter set that maximised relative density. But due to the challenges that copper has with LPBF, it was theorised that ML could be used as a quality assessment tool to aid in parameter optimisation. Thus, ML was reviewed and found that there have not been any applications in AM for parameter optimisation. This work will investigate this topic and is included as part of the work of copper. In the next chapter, the methods, materials and apparatus that was used will be detailed and explained.

Chapter 3 Materials and Methods

3.1 Introduction

In this chapter the materials and experimental methods use in the thesis will be described. The chapter is structured as follows;

- Materials
- AM equipment
- Laser scanning parameters
- Manufacture and preparation of specimens
- Electrical test methodology and equipment
- Software and computational methods
- Machine Learning parameters

3.2 Metal powders

As explained in Chapter 2.1, copper is a very attractive material to use for electrical applications due to its low resistivity. The highest purity of copper is of most interest in order to maximise electrical conductivity, as it has been shown in the previous chapter that even small amounts of other elements can drastically affect conductivity. While it will be difficult to process it to a high relative density, there has been no work showing how it will perform electrically when processed with LPBF. In addition to copper and explained in Chapter 2.1, AlSi10Mg is an attractive aluminium alloy for use in electrical applications due to its high specific conductance, its low density for lightweight applications, and ability to be processed to a high relative density. It has been shown that AlSi10Mg can be processed to a high density with LPBF equipment, thus enabling it to be a potential material to be widely adopted for electrical applications despite having additional alloyed elements which will affect resistivity. Thus, a potentially high conductivity pure metal which is hard to process by LPBF (pure copper) will be compared to an alloy which is easy to process by LPBF (AlSi10Mg) but has a lower conductivity.

The powders were characterised in terms of shape, size, and elemental composition. For particle sizing, a Mastersizer 3000 from Malvern Instruments Ltd. (UK) was used. It was equipped with an Aero S dry powder disperser to transport the powder via vibratory action and 1 bar of air pressure into the detector. The detector was set to detect between 0.5% and 15% laser obscuration with between 3 and 10 measurements taken per sample, with averages of the measurements being reported.

Powders were also imaged and analysed using a desktop Hitachi High-Technologies Corp. (Japan) TM3030 scanning electron microscope (SEM) with backscattered electron detection. Images were taken using an acceleration voltage of 15kV along with an energy dispersive X-ray (EDX) spectrometer for elemental composition analysis.

Powders were stored in air-tight containers between use in order to minimise oxygen contamination, however the sieving and loading of powders into the AM machines did introduce a source of oxygen exposure.

3.2.1 Copper powder

Samples of gas atomised copper powder were obtained from ECKA Granules GmbH (Germany), who were rebranded in 2017 as part of Kymera International (USA). Several other companies were contacted to supply copper powder, however, only ECKA met all the requirements for high copper purity (99.5%+), quick availability and reasonable price. Originally, ECKA ‘Copper AK’ was purchased which was an air atomised copper powder. However, during the purchasing process, it was discovered that phosphorus is detrimental to conductivity [169], and the ‘AK’ product had 0.46wt.% of phosphorus, as seen in Figure 3-1. An alternative ‘Copper AN’ product, which was gas atomised in a nitrogen atmosphere was subsequently purchased, which has phosphorus specification of < 0.05%.

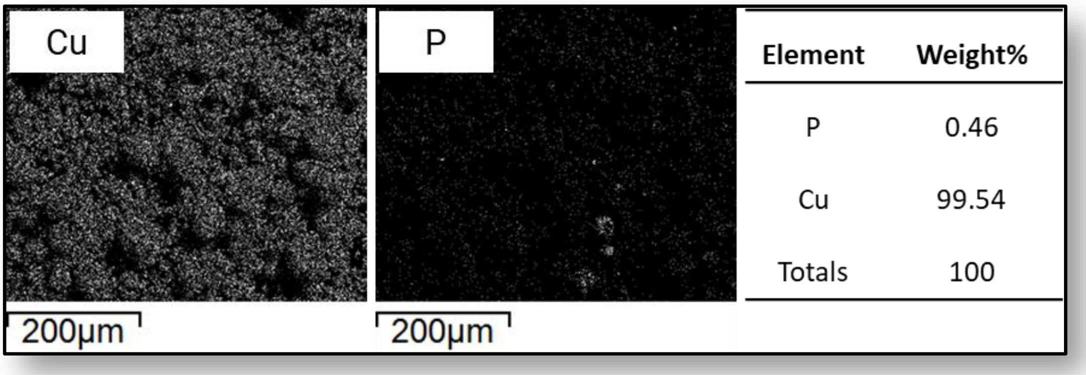

Element	Weight%
P	0.46
Cu	99.54
Totals	100

Figure 3-1: Elemental analysis using EDX on the Copper AK powder with traces of phosphorus shown.

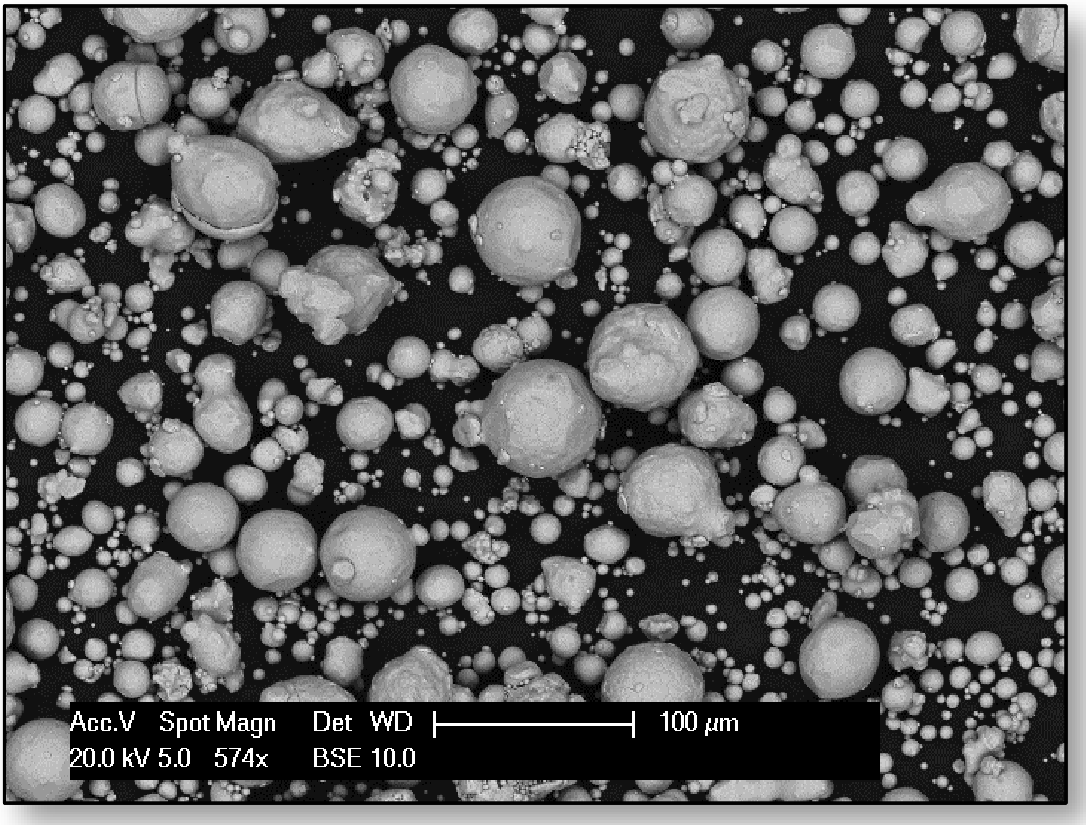

Figure 3-2: SEM image at a 574X magnification of copper AN powder.

The nitrogen atomised Copper AN was a spherical powder (See Figure 3-2) with a minimum 99.9 weight per cent copper purity. It had an apparent density of 4.80 g/cm^3 (ISO3923/1) with 90% of the particles below 65.3μm. It has a size distribution as seen in Figure 3-3 with an average D50 of 38.0μm. D50 is the measurement for particle size at which 50% of the cumulative measured particles are below this value.

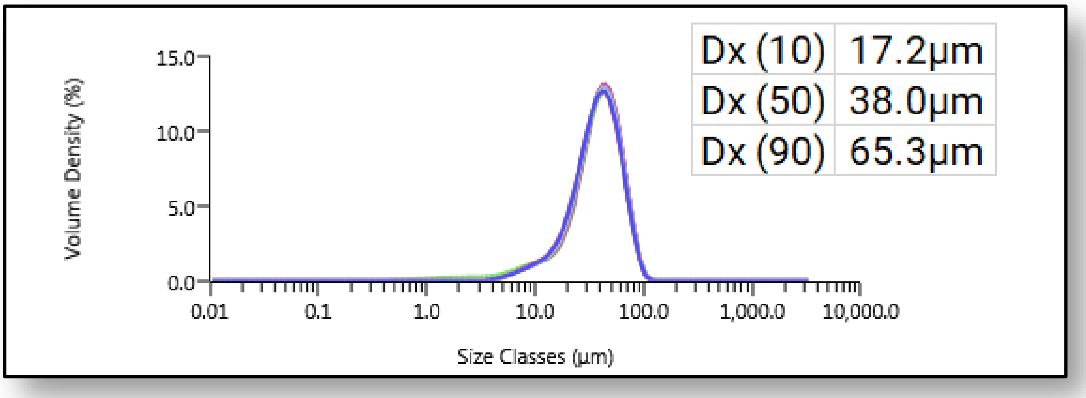

Figure 3-3: Dry particle size analysis on the copper sample from ECKA.

It was confirmed through EDX analysis that the phosphorus content of Copper AN was below 0.002 wt.% with no other interstitial elements detected. The particle shape and size distribution met the requirements needed for good flowability in the LPBF process, while the purity enabled the potential for high electrical conductivity.

3.2.2 AlSi10Mg powder

An argon gas atomised AlSi10Mg metal powder alloy was obtained from LPW Technology Ltd. (UK). The wrought version of this alloy has a density of 2.68 g/cm^3 and a melting range of 570-590 °C.

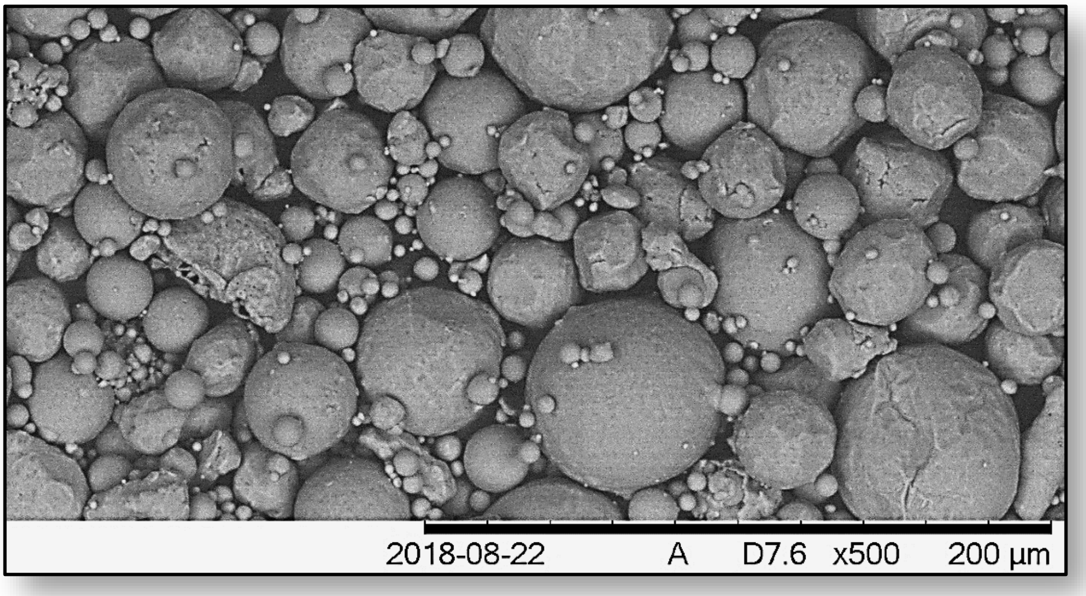

Figure 3-4: SEM image at a 500X magnification of sieved AlSi10Mg powder.

The powder was spherically shaped (See Figure 3-4) with few satellites or irregular shapes. The original powder had a size specification of 99.5% below 63 μm and 7.89% below 20 μm. The measured powder had a powder size distribution as seen in Figure 3-5. The measured powder had an average D50 of 29.7 μm. The measured powder was still within the original size specification despite it having been processed and sieved many times since the original specification. LPW provided the chemical composition as seen in Table 3-1 and is compared with the acceptable range (at the time of purchase) for the alloy and was found to be within specification. The solid material was analysed for elemental composition in Chapter 6.2.

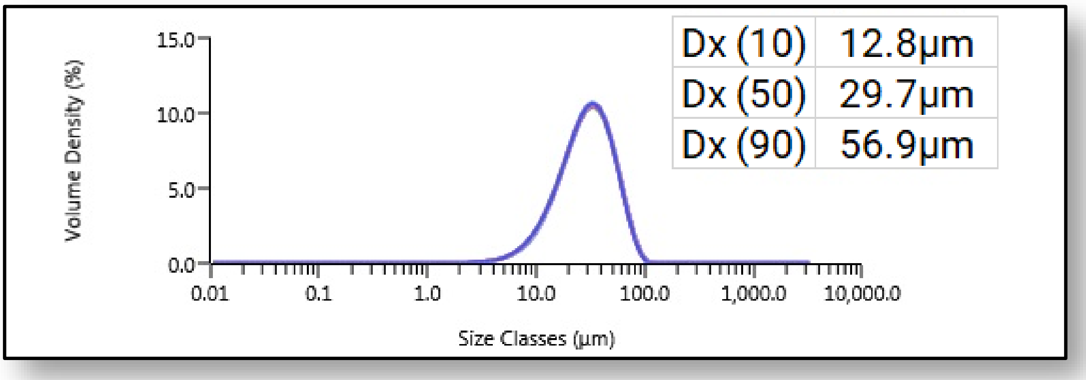

Dx (10)	12.8μm
Dx (50)	29.7μm
Dx (90)	56.9μm

Figure 3-5: Particle size distribution of sieved AlSi10Mg powder.

Source	***Al***	***Si***	***Mg***	***Fe***	***Mn***	***Cu***	***Pb***	***Zn***	***Ti***	***Ni***
LPW	89.13	9.71	0.408	0.501	0.061	0.051	0.043	0.040	0.021	0.015
Typical Range	87.15-90.8	9.0-11.0	0.20-0.45	< 0.55	< 0.45	< 0.05	< 0.05	< 0.1	< 0.15	< 0.05

Table 3-1: Chemical composition in weight percentage of the AlSi10Mg alloy powder provided by LPW.

The particle shape and size distribution also met the requirements needed for good flowability in the LPBF process. The powder composition provided by LPW was within the acceptable range for the AlSi10Mg alloy and thus should exhibit the mechanical properties and processability as found in literature.

3.3 AM equipment

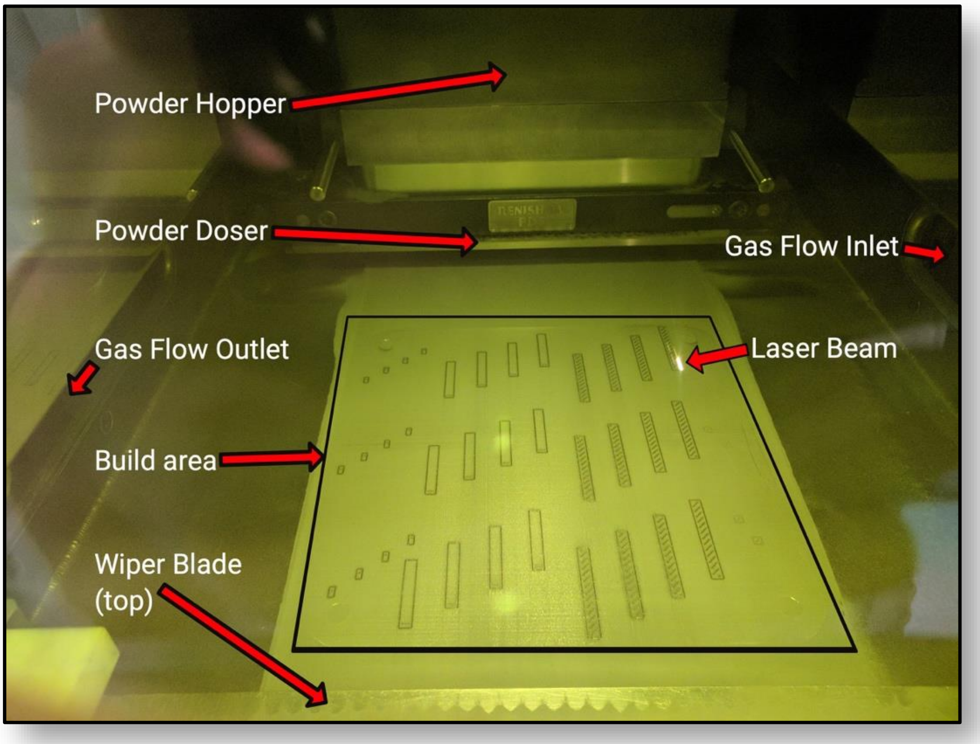

Figure 3-6: Creation of AlSi10Mg electrical test specimens within a Renishaw AM250 LPBF machine.

Copper and AlSi10Mg were processed on different Renishaw plc (UK) LPBF machines which have similar layouts internally, with the AM250 LPBF machine shown in Figure 3-6. An overhead hopper contains metal powder which is dispensed via gravity and a dosing mechanism. This mechanism opens and closes via the wiper and has precise openings in the bottom of the hopper to allow for controlled volume dispensing. This dosed powder falls behind the build area and is wiped forward onto the build area by a soft-edged silicone blade. Excess powder is further pushed into an opening past the build area which is connected to bottles. These valved bottles are removable so that the overflowed powder can be sieved for reuse. An inert gas flowed across the build area perpendicular to the powder deposition direction. The Renishaw machines are ideal for exploring the processing of new materials with LPBF due to their open architecture and ability to control nearly all the variables in the LPBF process. These parameters will be described more in Section 3.4. Another aspect of the Renishaw machines which is ideal for materials such as aluminium and copper is the ability to minimise oxidation via use of a vacuum and argon purge.

When comparing the lasers of different LPBF machines, an important aspect to keep in mind is the laser power in comparison to the laser spot size, called the laser power density, seen in Equation 3-7.

$$Laser\ power\ density = \frac{laser\ power}{laser\ spot\ size} \tag{3-7}$$

Copper was processed using an AM125 LPBF machine which was equipped with a 200 W D-Series redPOWER ytterbium fibre CW laser from SPI Laser (UK) with a wavelength of 1070 nm (±10 nm) and a spot size of 35 μm (±5 μm). This resulted in an average laser power density of 22.1 MW/cm^2 (±6.19 MW/cm^2). It had a build volume of 125 mm^3 with a base plate heater, set to 170 °C, which was maintained at this temperature throughout the build process. A vacuum and argon purge were used in the build chamber in order to keep oxygen content below a maximum of 500 parts per million, however actual processing conditions were lower. Mild steel substrates were used as this has been found to be a suitable material to build copper parts upon as there was good bonding between these two materials [152]. The AM125 was the ideal choice for copper due to its high laser power density resulting from a small spot size. Without this small spot size, a machine with a 70 μm laser spot diameter (as with the AM250) would need to operate an 800 W laser to achieve the same laser power density.

AlSi10Mg was processed using an AM250 LPBF machine which was equipped with a 200 W redPOWER ytterbium fibre continuous wavelength (CW) laser made by SPI Laser (UK) with a wavelength of 1070 nm (±10 nm) and a spot size of 70 μm (±5 μm). This resulted in an average laser power density of 5.28 MW/cm^2 (±0.75 MW/cm^2). It had a build volume of 250 mm x 250 mm x 360 mm (X, Y, Z) with a base plate heater, set to 80 °C, which was maintained at this temperature throughout the build process. A vacuum and argon purge were used in the build chamber in order to keep oxygen content below a maximum of 900 parts per million, however actual processing conditions were lower. Parts were built upon baseplates made from aluminium alloy 5083 which is known for its ability to retain its strength after welding, making is suitable for use in LPBF which is a powder based micro-welding process. Alloy 5083 has between 4.0-4.9% Mg, 0.4-1.0% Mn, and typically less than 0.4% Fe and up to 0.4% Si. As the balance is Al, it is a compatible alloy for building AlSi10Mg parts upon. The AM250 was the ideal choice for processing this alloy due to its large build volume and ability to create large parts.

3.4 Laser scanning parameters

As there are two different materials being studied with two different LPBF machines, two completely different processing parameters were needed for this research. As AlSi10Mg had been widely researched as noted in Chapter 2.10, an optimised processing parameter set for the AM250 had already been published and was chosen to be used. However, pure copper had not received the same amount of attention, thus the processing parameters needed to be investigated for the AM125, using the findings from Chapter 2.9 as a reference for the parameters.

3.4.1 Copper parameters

Unlike AlSi10Mg, there was not an optimised set of processing parameters for pure copper with the AM125 LPBF machine. Thus, an investigation into the printing parameters which would achieve the highest possible density and highest electrical conductivity was necessary. The variables investigated in order to determine optimal processing conditions, based on prior work in this area, are listed in Table 3-2.

Variable	***Value or Range***
Laser power (W)	200 (maximum available)
Laser spot diameter (μm)	35 (minimum)
Powder bed temperature (°C)	170 (maximum allowable)
Laser scan speed (mm/s)	50 to 1250 (in increments of approx. 25)
Laser point distance (μm)	30 to 200 (in increments of approx. 25)
Layer thickness (μm)	30, 45, 60
Laser beam focus position (mm)	-10 to 10
Hatch spacing (μm)	50 to 175 (in increments of approx. 10)
Scan strategies	Stripes, Islands*, Rotation*, Nested Contours, Pre-sinter, Re-melt, Multiple Scan, Offset Hatch
**Scan strategy rotation (°)*	0, 67, 90

Table 3-2: Table of LPBF variables and the corresponding value or range to be tested with pure copper.

Laser power defines the laser power density which will interact with the top surface of the powder and is used to melt the powder below. The maximum laser power was used as it has been found in literature that high laser powers are needed to fully re-melt the previously deposited copper layers. Laser spot diameter also influences the laser power density and was a variable which was fixed within the LPBF equipment, as it was not adjustable in the Renishaw line of LPBF machines. Powder bed temperature was set to the maximum allowable value in order to pre-heat the powder and lower the energy requirement needed to melt the powder. Laser scan speed and laser point distance influence the length of time in which the laser interacts with the top surface of the powder. In the Renishaw LPBF machines, the laser scan speed was calculated by the point distance divided by the laser exposure time (in μs). When a specific laser scan speed was tested, several point distances were also tested, and the laser exposure time was calculated and used in the Renishaw software to define the speed. For example, for a laser speed of 200 mm/s and point distances of 50 and 100 μm, the exposure times would be 250 and 500 μs respectively.

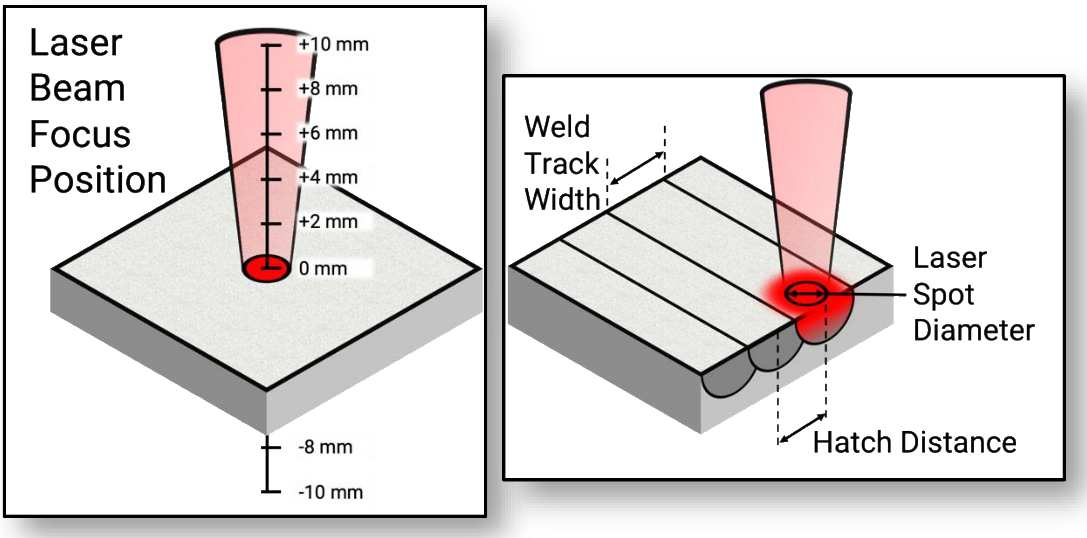

Figure 3-7: Example of the focus position of the laser beam (left), and example of hatch distance, laser spot diameter, and weld track width (right).

Layer thickness defines the amount of material that the laser needs to fully melt, as well as how well the powder spreads on the powder bed. Thick layers spread well but make it difficult for a laser to fully melt, whereas thin layers are easier to fully melt, but may have issues spreading the powder due to issues of spreading particles which are larger than the desired layer thickness. Laser beam focus position (Figure 3-7 left) adjusts the location of the focus and changes the spot diameter as well as the energy profile of the laser spot (edges of the laser become less defined). If the actual laser focus position was not located at the zero position, this method can correct for it. Hatch spacing (Figure 3-7 right) influences the amount of overlap a laser weld track has with previous tracks in the same layer. An overlap occurs when the hatch distance is less than the weld track width and is desirable to ensure the fusion of adjacent tracks. Note that the laser beam spot diameter, weld track width, and hatch distance can and usually are all different dimensions.

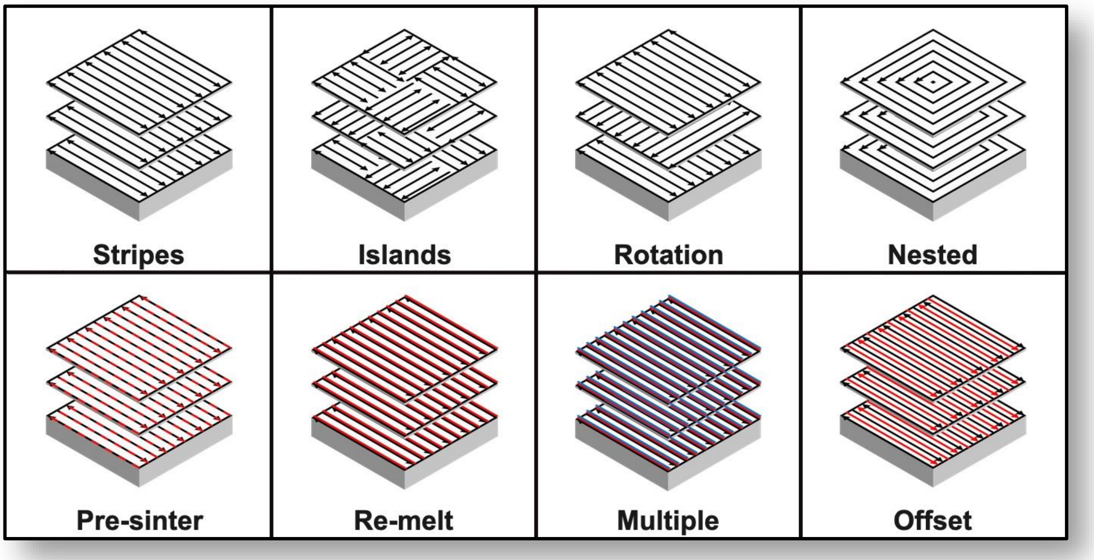

Figure 3-8: Examples of the scan strategies which were used in the manufacturing of cubes, with single scan strategies along the top and multiple scan strategies along the bottom.

The scan strategies shown in Figure 3-8 can be divided into single scans per layer (stripes, islands, rotation, and nested), and multiple scans per layer (pre-sinter with lower laser powers first, re-melt by repeating the scan, multiple scans, and an offset scan between tracks). Rotation of the scan pattern by either 0°, 67° or 90° were tested with both island and rotation scan strategies. Stripes are long unbroken scans from one side of the part to the other, reversing direction for each hatch while maintaining the same axis for each scan on each layer. An advantage of long tracks is that if a melt pool is unstable over short distances, but becomes stable over longer ones, then there will be less discontinuities in the track. Islands break up these long scans into multiple smaller areas (called islands) where the axis of the scans are perpendicular for each layer, but the overall location of the islands is not changed. The island scan pattern creates shorter clustered tracks where the heat is more concentrated within the islands, and thus reduces thermal gradients over the island. Rotation can be used for both stripes and islands, where the entire pattern of scans is rotated by a certain amount (typically either 90° to repeat every few layers, or 67° to minimise repeats). Rotated scan patterns help even out defects from layer to layer, with 90° patterns repeating the same scan locations every fourth layer but have exactly opposite patterns every other layer. 67° patterns repeat exactly every 360th layer but are within 1° of an exact repeat every 43rd layer, within 8° every 16 layers, and are within 4°of an exact opposite pattern every 8 layers. Nested contours scan the entire area as a series of decreasingly sized contours in an attempt to maintain long tracks while also scanning close to previous scans to help reduce thermal gradients.

Multiple scans per layer attempt to increase density by melting more material than a single scan can achieve. Pre-sinter is a striped scan strategy where the first scan is by a lower laser power, followed by a higher laser power in an attempt to sinter the material and aid in increasing density, as this has been shown to work with alloys such as AlSi10Mg [183]. Re-melt is similar except that the first scan is a higher laser power, followed by either equal or lower laser power in an attempt to melt any unmelted powders which may exist in areas of discontinuities and irregularities by using the same laser power and pattern. Multiple scan is also a striped scan strategy where three (or more) scans occur on the same layer in the same locations, where each scan is either equal to or lower than the first scan in order to attempt to fully melt any discontinuities or gaps in the initial scan. Finally, offset hatch is also a striped scan strategy where the second scan is offset by half of the hatch distance to fuse the areas between the original scan tracks and melt any unfused powder in this region.

The method for parameter optimisation was as follows. First, single scan tracks were created to define the processing window for scan speed as seen in Figure 3-9(a). Next, thin walls were fabricated, as shown in Figure 3-9(b), to evaluate the intralayer bonding with a layer thickness being varied in the range 30-60 μm at intervals of 15μm. Thin walls were also used to evaluate the effect of focus position on quality. Cubes were then fabricated to evaluate hatch distance, rotation and scan strategies with respect to density and interlayer bonding according to Section 3.5 and are seen in Figure 3-9(c). The scanning strategies presented in Table 3-2 were used in an attempt to minimise defects and increase the density of the as-built parts. A further discussion of the optimisation of these processing parameters will be contained within Chapter 5 - Processing of Pure Copper with LPBF.

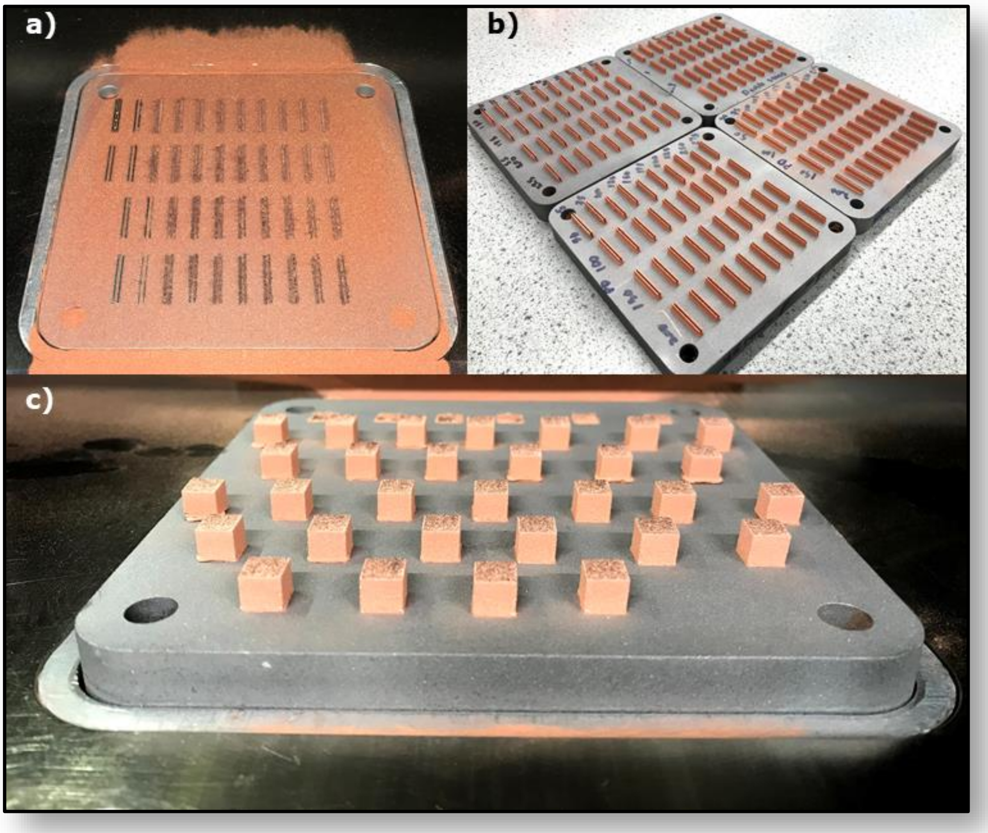

Figure 3-9: As-built scan tracks (a), thin walls (b), and cube specimens (c), of pure copper for parameter optimisation.

3.4.2 AlSi10Mg parameters

Specimens were processed using a previously optimised parameter set from [209] which was optimised for density by a design of experiments using a Renishaw AM250 LPBF machine. The design of experiments first optimised the laser power, laser scan speed, layer thickness and hatch spacing, then further optimised the hatch spacing with different scan strategies. This optimised parameter set can be found in Table 3-3 and was used in order to maximise as-built density.

Variable	***Value***
Laser power (W)	200 (maximum available)
Laser spot diameter (μm)	70 μm (±5 μm) (minimum)
Powder bed temperature (°C)	80 (maximum allowable)
Laser scan speed (mm/s)	571
Laser point distance (μm)	80
Laser exposure time (μs)	140
Layer thickness (μm)	25
Laser beam focus position (mm)	0
Hatch spacing (μm)	130
Scan strategies	Islands as per [27] with 67° rotation per layer and a field overlap of 10 μm

Table 3-3: Table of LPBF parameters used with AlSi10Mg.

Parts were spaced out on the build plate as shown in Figure 3-6, with the wiper blade moving from front to back (seen in the bottom of the image), and gas flow from right to left in the image. This spacing maximises the potential for all parts to successfully complete because if there was a defect or part failure which damaged the soft wiper blade, the defect in the blade and resulting raised powder line on each layer would not interfere with any other part, since nearly all parts were not overlapped in the X direction (left to right).

3.5 Manufacture and preparation of specimens

In order to characterise the density and microstructure of a material manufactured by LPBF, small specimens are needed. These specimens need to be large enough to demonstrate the material properties and characteristics of the material, while also being small enough in order to minimise manufacturing time, material usage, and preparation time. A 5 mm cube fulfils all these requirements and allows many of them to be built on a single build platform in order to test a large number of parameters at one time. These 5 mm test cubes are used to study both density and microstructure by cutting the cube in half and studying the interior surface. These cubes can be cut in order to study the top XY plane, or the side XZ and YZ planes.

In addition to density and microstructure, electrical test specimens are needed for testing resistance. The resistance of a specimen can be directly measured by an ohm-meter but can also be calculated as seen previously in Equation 2-3. As both AlSi10Mg and copper are highly conductive materials with low resistivity, in order to achieve a resistance which was high enough to measure (greater than 100 µΩ), the ratio of length over cross-sectional area needs to be balanced. This requires the length of the specimen to be significantly longer than the dimensions for the cross-section, at least one order of magnitude larger. The cross-sectional dimensions of the specimens need to be large enough to be robust for the testing method, but the length also needs to be within the acceptable limits for manufacturing. This size was different for both AlSi10Mg and copper due to the different ways they were electrically tested. These specimens were built in three orientations, vertical, horizontal and at a 45° angle. This is similar to what has been done for mechanical testing [185].

In order to calculate the resistivity of the material to a high degree of accuracy, the resistance, length, and cross-sectional area need to also be known to a high degree of accuracy. This requires the length and dimensions of the cross-section to be known with high confidence. However, because LPBF can sometimes have a rough surface finish, this can cause deviations in these measurements. Therefore, it’s critical to remove this roughness in order to measure these dimensions accurately. This method was different for both materials. All the differences and details of manufacture and preparation for these two materials will be detailed in the next sections.

3.5.1 Copper specimens

As copper first required parameter optimisation to occur before electrical testing, cubes were used to evaluate density for each test parameter set as mentioned in Section 3.4.1 -

Copper parameters. Cubes were designed to be 5 mm in size as seen in Figure 3-10. To measure density and reveal macro structures such as inter-layer bonding, cubes once printed and removed from the baseplate, were encapsulated in a non-pressurised cold mount resin. It was decided to cold mount as opposed to a pressurised hot mounting process since the heat and pressure could skew density measurements and deform as-built features due to the ductility and anticipated porosity of the processed copper.

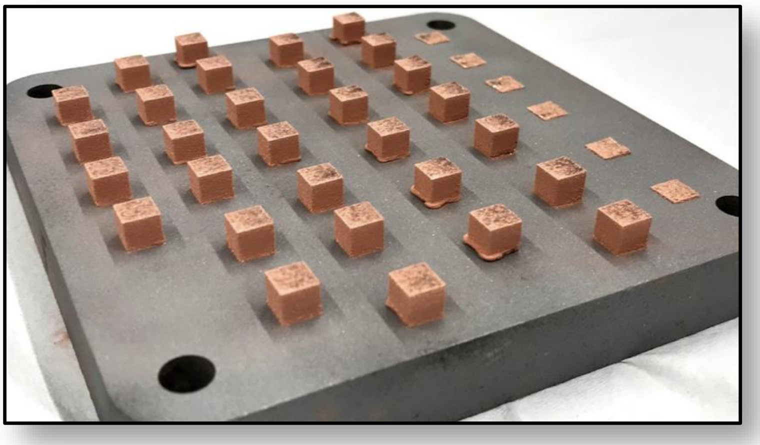

Figure 3-10: Build plate containing copper test cubes with the first row supressed during the build due to unstable build parameters.

Test cubes were first ground using course grinding paper to reach the area of interest, and then fine grit paper to remove scratches from the previous step. Specimens were then polished according to the Struers ApS (Denmark) guide for pure copper. The overall procedure can be seen in Table 3-4. After initial optical imaging, grain boundaries were identified using a macro etch solution of 50 mL Nitric Acid (1.40 pH) and 50 mL water with a submersion into the solution for 2 seconds followed by a water rinse.

Surface	*Fluid/ Suspension*	*Speed (rpm)*	*Pressure (Newtons)*	*Duration (Minutes)*
240 Grit paper	Water	300	Hard	As desired
1200 Grit paper	Water	300	Light	Until plane
MD-Largo	DiaPro Allegro 9 µm diamond	150	40	4
MD-Mol	DiaPro Mol R3 3 µm diamond	150	25	2
MD-Chem	OP-S Colloidal Silica	150	10	2

Table 3-4: Grinding and polishing procedure for pure copper.

Test cubes were also imaged and analysed using an FEI XL-30 field emission scanning electron microscope (SEM) with backscattered electron detection. Images were taken using an acceleration voltage of 20kV along with an EDX spectrometer for elemental composition analysis which was performed using an Oxford Instruments ISIS system.

Density measurements using the Archimedes principle were attempted using a Helium Pycnometer made by Micromeritics (USA), model AccuPyc 1330. It was calibrated using a sphere with a known volume of 318.5510 mm^3. The maximum specimen size that was able to be tested in this machine was a cylinder 17 mm in diameter and 35 mm long. This method however relies on closed porosity to derive a density measurement. Open porosity becomes a challenge due to complete infusion of the helium into the structure. If open porosity exists, the volume calculated by the pycnometer can be compared to the externally measured volume for a relative density measurement.

Electrical test specimens were designed and printed at 2 mm x 2 mm x 25 mm. These dimensions were chosen for three reasons. First, so that the expected resistance for each bar would be at least 100 µΩ at 100% IACS. Second, so that they would be mechanically robust enough for the handling and soldering used in electrical testing described in Section 3.6. Third, so that many specimens could be printed on the AM125 despite having a smaller build volume compared to the AM250. Laser-scan parameters for these specimens were selected from the set that resulted in the highest density for the previous test cubes.

Test Case	*Parameters*
Number of specimens per test case	3
Initial Build Orientations	Horizontal, 45°, Vertical
Post Heat Treatment Temperatures	As-built, 800 °C, 1000 °C
Post Heat Treatment Dwell Duration	0.5, 1, 4 hours

Table 3-5: Test cases for copper electrical specimens.

Specimens were created for each of test cases as shown in Table 3-5. The orientation of the specimen was classified according to the normal of the cross-section of the bar which also correlates with the direction of the longest edge of the bar. These test cases resulted in the creation of sixty-three specimens (as only nine specimens were needed for as-built), seen in Figure 3-11 along with two test coils. Temperatures for heat treatment represent the range at which copper will sinter [210] before it melts at 1083 °C [49].

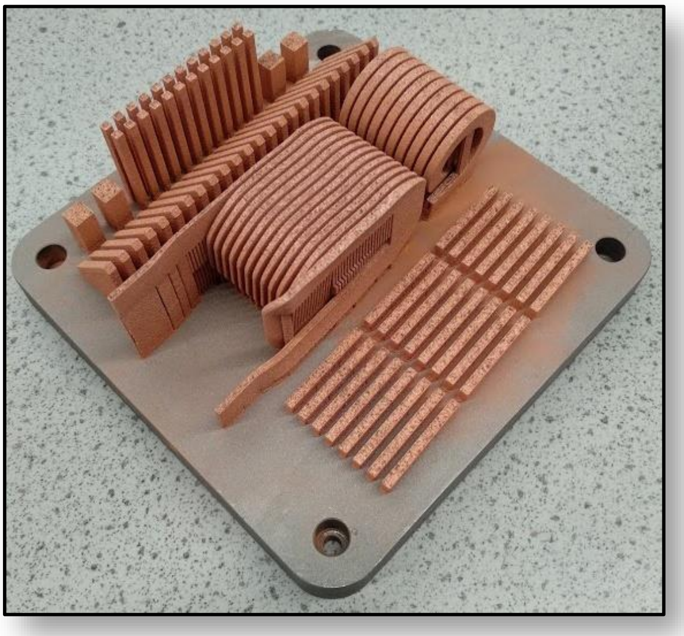

Figure 3-11: Build plate with electrical test specimens manufactured in vertical, horizontal and 45° orientation along with prototype coils and test cubes.

Heat treatments were conducted in a tube furnace with an argon inert atmosphere. Test specimens were placed in crucibles to avoid any contamination. The ramp up temperature was set at 10 °C per minute for all heat treatments, followed by furnace cooling to room temperature.

Test specimens were lightly surface ground using 800 grit paper by hand to remove the rough as-built finish. After heat treatment and light hand grinding, specimens were individually measured along all dimensions, in a minimum of four places using

Mitutoyo digital calipers which had an accuracy of ±0.02 mm. This was done to accurately determine the cross-sectional area and length of each specimen.

3.5.2 AlSi10Mg specimens

As no parameter optimisation needed to take place for AlSi10Mg, many 5mm test cubes were not needed. Instead, only a few cubes were printed for each post-heat treatment in order to study microstructure and verify density. Electrical test specimens were designed and printed at 6.5 mm x 3.5 mm x 50 mm. These dimensions were chosen for two reasons. First, so that an expected resistance for each bar would be at least 100 μΩ by using the highest cast values found in literature. Second, so that they would be mechanically robust enough for the clamping method used in electrical testing described in Section 3.6.

Test Case	*Parameters*
Number of specimens per test case	4
Initial Build Orientations	Horizontal, 45°, Vertical
Post Heat Treatments	As-built, Annealed, T6-like [186]

Table 3-6: Test cases for AlSi10Mg electrical specimens.

Specimens were created for each of test cases as shown in Table 3-6 resulting in 9 test cases and 36 total test specimens. The T6-like heat treatment was developed in [186] to be similar to the quench and aging process seen with a typical T6 in order to achieve high strength with higher ductility. However, due to the unique starting grain structure in LPBF compared to cast, the casting T6 process does not achieve the desired results when followed exactly. Thus, a T6-like process was developed for LPBF and was used in this work. Similar to copper testing, the direction of the longest edge of the bar defined the name of the orientation. These three orientations were chosen as they replicate orientations used in mechanical testing as seen in previous literature [211]–[213]. Horizontal parts were not built in the X direction as seen in Figure 3-12 as the laser scan parameters rotated the pattern every layer, in an effort to minimize any effects that X verses Y orientations may have. It is also important to note that there could be other factors such as wiper blade and gas flow directions which could still cause differences between X verses Y directions; however, it was decided that these effects would be ignored.

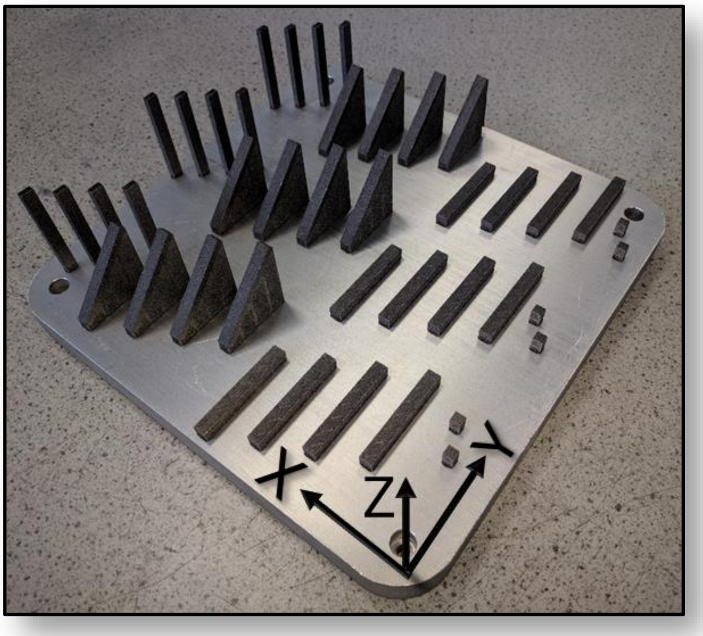

Figure 3-12: Build plate (250 mm x 250 mm) with electrical test specimens printed in vertical, 45°, and horizontal orientations along with 5 mm specimen cubes.

Twelve test specimens (four of each orientation) and two 5 mm cubes (Figure 3-12) were removed from the build plate to be tested in an as-built condition. A Carbolite furnace rated to 800 °C with Eurotherm 2408 temperature control was used for heat treatment. A typical annealing heat treatment [214] was performed on a similar set of specimens by placing the test specimens and cubes in a preheated furnace set to 300 °C for two hours and then removing to be air cooled. A T6-like heat treatment [186] was performed on the remaining twelve test specimens and 5 mm cubes by placing them in a preheated furnace set to 520 °C for one hour and then quenched in 20 °C water. The quenched test specimens were then dried and put into a different preheated furnace for artificial aging, set to 160 °C for six hours and then removed to be air cooled.

Figure 3-13: 3D printed jigs used for polishing specimens as to keep them as square as possible.

After heat treatment, electrical test specimens were surface ground and polished using a manual grinding and polishing machine. First, the specimens were ground with 400 grit grinding paper and water at 300 rpm until all traces of the original as-built surface were removed. Then 800 grit grinding paper was used to remove any deep scratches and defects. Specimens were held using the jigs in Figure 3-13 to keep specimens as square as possible. Surfaces which had supports attached to them were ground first. Afterward, the ends which had the smallest surface area were ground using the circular jig seen in Figure 3-13. The other jig was used for the sides with the largest surface area, followed by the remaining smaller side. After removal of surface defects, specimens were individually measured three times along all dimensions, in a minimum of five places using a Mitutoyo Corporation (Japan) digital caliper which had an accuracy of ±0.02 mm. This was done to accurately determine the cross-sectional area and length of each specimen.

The 5 mm test cubes were sectioned using a CNC circular cutting saw to expose the XY plane (top view) and YZ plane (side view). They were then ground flat and polished according to the Struers ApS (Denmark) application notes for the metallographic preparation of aluminium and aluminium alloys, specifically silicon cast aluminium as that was the closest match to LPBF AlSi10Mg. The procedure for the polishing can be seen in Table 3-7. The polished sectioned cubes were imaged and then etched using Keller's reagent for 10 seconds to help reveal the microstructure with further imaging.

Surface	*Fluid/ Suspension*	*Speed (rpm)*	*Pressure (Newtons)*	*Duration (Minutes)*
240 Grit paper	Water	300	Medium	Until plane
MD-Largo	DiaPro Allegro 9 µm diamond	150	30	4
MD-Mol	DiaPro Mol R3 3 µm diamond	150	25	3
MD-Chem	OP-U NonDry Colloidal Silica	150	15	1

Table 3-7: Polishing and grinding procedure for silicon content aluminium alloys.

In order to determine and correlate microhardness with the test cubes, nanoindentation was performed using a Micro Materials Ltd. (UK) NanoTest NTX based machine with a calibrated Berkovich indenter. Fifteen indents were made per specimen, spaced 30 µm apart with a force of 100 mN.

Test cubes were imaged using a Nikon Corporation (Japan) Eclipse LV100ND microscope with a 2560 x 1920 pixel colour sensor. These images were used for microstructure analysis as well as optical density measurements.

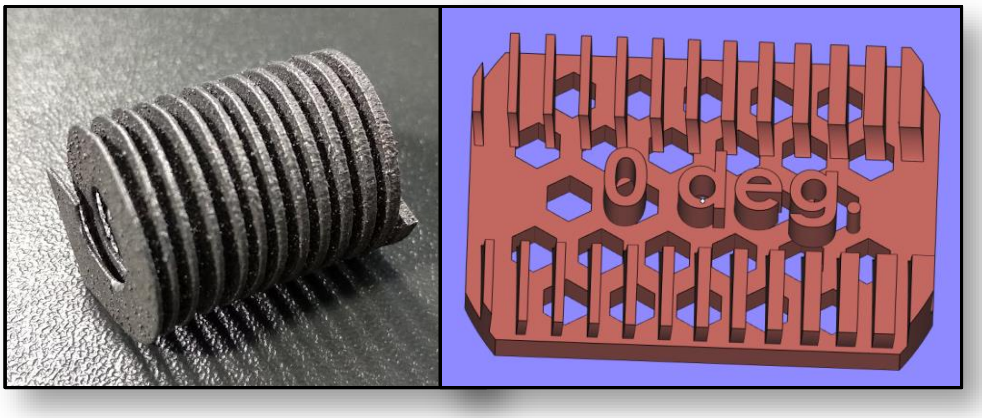

Figure 3-14: Test specimen for geometric analysis, a variable thickness coil (left) and corresponding section indicating location of section (right).

To determine the dimensional accuracy of the LPBF process with AlSi10Mg, a geometric test specimen was created as seen in Figure 3-14 (left). This coil geometry was representative of an electrical coil, with the exception that this coil has a continuously variable thickness in order to test different printed thicknesses. The coil was 18 mm in diameter and 26 mm long.

The coil was sectioned in CAD at a specific radial angle and attached to a back plate seen in Figure 3-14 (right). This back plate was made with through holes in order to aid in the hot resin mounting process and was designed to fit within a 30 mm circle which was the diameter for the hot mounting process. After hot mounting, the specimen was ground and polished using the aluminium polishing procedure mentioned previously.

Once polished, the specimen was imaged and measured using Nikon software using image tools to determine the maximum and minimum wall thicknesses. These tools rely on an accurate pixel to distance ratio, given in Table 3-8. This ratio was used with the images and analysed using the Nikon software.

Microscope Magnification	***Quick Save (1280 x 960 px) Resolution Ratio [µm/px]***	***High Quality (2560 x 1920 px) Resolution Ratio [µm/px]***
5X	2.494	1.247
10X	1.239	0.620

Table 3-8: Distance to pixel ratios for images obtained from Nikon Eclipse microscope.

3.6 Electrical test methodology and equipment

In order to determine the resistivity for a material, the cross-sectional area and length of each specimen was needed in addition to the resistance. This resistance was measured directly using an ohm metre. Traditional two-wire ohm metres measure the resistance of the wires as well as the subject, as seen in the left of Figure 3-15. This method is acceptable when $R_{\text{sample}} >> R_{\text{wire}}$. However, when measuring short samples of low resistivity materials, this method cannot provide accurate measurements for the sample. It is also important to note that there is an additional contact resistance between the wire and the sample which is not shown.

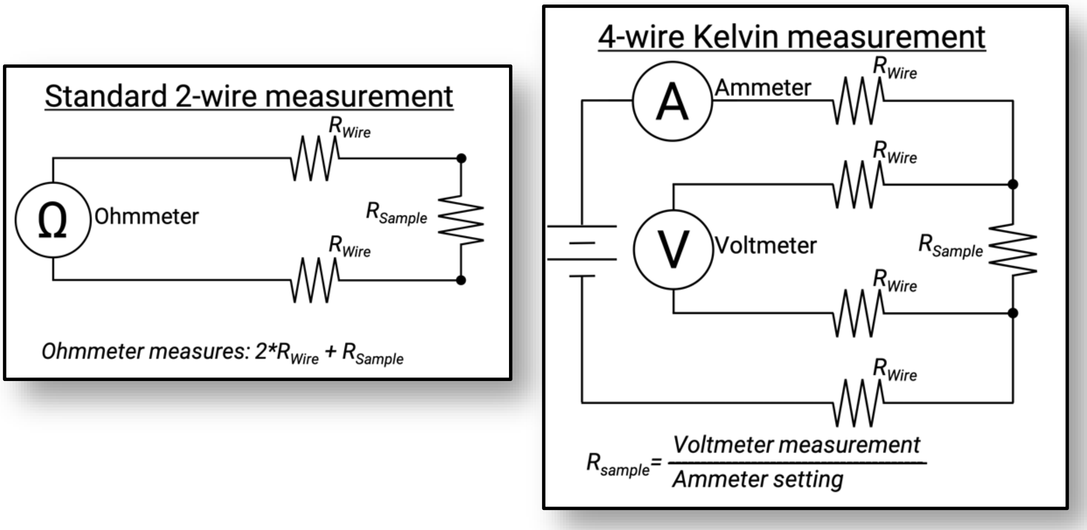

Figure 3-15: A common two-wire resistance measurement method (left), and a four-wire Kelvin resistance measurement method (right).

Four-wire Kelvin resistance measurements eliminate the condition of needing $R_{\text{sample}} >> R_{\text{wire}}$ by providing a constant current through the sample, as seen in the right of Figure 3-15. The amount of current that flows through the voltmeter is negligible compared with the amount that flows through the sample. By using Ohms law ($V=IR$), the exact resistance of the sample can be obtained.

Electrical DC resistance testing was performed using a Valhalla Scientific Inc. (USA) 4300B digital micro-ohmmeter, seen in Figure 3-16. This DC four-wire Kelvin resistance measurement meter was calibrated to within 5% accuracy by an external vendor and verified internally through tests using precision low-resistivity resistors and current shunts. It could generate a current between 0.1 mA to 10 A and was able to measure the voltage from 20 mV to 2 V, with a minimum sensitivity of 1 μV.

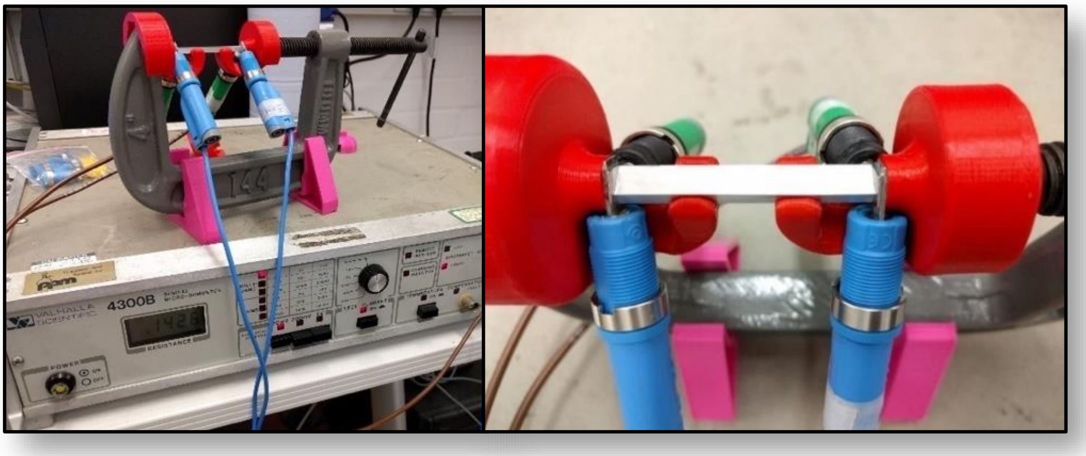

Figure 3-16: Electrical test jig (left) and set-up showing polished aluminium test specimen clamped between four-wire Kelvin probes (right).

Additional AC electrical testing was performed using a Rohde and Schwarz UK Limited (UK) Hameg HM8018 LCR-Meter. This AC four-wire resistance measurement meter was calibrated using the internal calibration technique before the measurements were taken. It was equipped with the four-wire HZ17 Kelvin test leads with probe tips. It was able to measure AC resistance at frequencies of 100 Hz, 120 Hz, 1 kHz, 10 kHz, and 25 kHz. It has a maximum resolution of 1 mΩ and a basic accuracy of 0.2%.

Each specimen was tested a total of five times, once on its own for a base reading, and then two more times where each instance was a combination of two measurements in succession, being flipped around in the test stand for AlSi10Mg (Figure 3-16) to reverse the specimen, and reversing the connections for pure copper. This was in accordance to ASTM B193-02 “Standard Test Method for Resistivity of Electrical Conductor Materials” [51].

Figure 3-17: Copper test specimen soldered directly to electrical tabs in order to minimise contact resistance as measured by a 4-point probe.

Copper specimens had electrical tabs soldered on to them in order to minimise contact resistance between the specimen and the voltage probes as seen in Figure 3-17. However, for AlSi10Mg specimens, soldering was unable to be performed on this alloy due to an inability for any type of solder to wet the surface. Welding was undesirable due to the excess heat that flows into the specimen, which could disrupt the microstructure created in each of the heat treatment cases. Each electrical measurement for AlSi10Mg was thus clamped using a force of approximately 4000 N in order to minimise contact resistance between the probes and specimen. Forces greater than 4000 N would buckle the specimens. This contact resistance could not be eliminated through the use of four-wire measurements as this resistance was between the specimen and the voltmeter connections but can be minimised through ensuring that contacts are clean of residue and oxides, that the contacting faces are flush with each other, and that the clamping force is sufficiently high. These steps were taken with each AlSi10Mg specimen which was tested. The resistance of the contacts was also measured when no sample was loaded between the probes in order to obtain a baseline measurement, and this measurement was subtracted from the results. Results were then averaged with the corresponding standard deviations determined. An alternative method to determine the contact resistance, which was not used but would be used in future work, would be to fabricate a second specimen which was twice the length of the first. From measuring the resistances (R_1 and R_2) from these two specimens, both the contact resistance (R_C) and the material resistance (R_M) could be determined as $R_1 = R_C + R_M$ and $R_2 = R_C + 2R_M$.

$$\rho = \frac{RA}{L} \tag{3-8}$$

Electrical resistivity (ρ) measured in μΩ-cm was calculated by Equation 3-8 where R is the measured resistance in μΩ, A is the cross-sectional area of the specimen measured in cm^2, and L is the length of the specimen in cm. Resistivity is also a function of temperature, but for this investigation, only room temperature values will be reported, as the full temperature dependency of resistivity has been previously reported for both copper [48] and cast alloys A319 and A356 which are very similar to that of AlSi7Mg [215].

3.7 Software and computational methods

As AM is a digitally based technology, several different software applications were needed. These applications were used to design the shapes which were to be printed, to prepare the resulting models for printing, and to translate the models into machine specific formats with the corresponding processing parameter sets. Once a print was finished, software tools were used to determine characteristics such as density and dimensional accuracy, with other tools being used for statistical analysis and organisation of data. Additional analysis could be done with more computationally intensive software tools such as those used in ML.

3.7.1 Design and model preparation

Parts and designs beyond basic primitive shapes such as cubes and specimens were created using Solidworks 2017-2018 by Dassault Systèmes (France). Solidworks was an easy to use 3D computer-aided design software package which has partnered with the University of Nottingham to provide this software. Parts were then exported to the STL file format, using a deviation tolerance below 0.005 mm and an angle tolerance below 5°.

FLatt Pack software from Added Scientific Ltd. (UK) was used for lattice generation. Flatt Pack stands for The **F**unctional **Latt**ice **Pack**age for Additive Manufacturing. It was able to generate several unique lattice types, either in a customisable pre-defined envelope or within a custom imported volume. It was also able to functionally grade lattice densities within a given volume.

Materialise Magics from Materialise NV (Belgium) version 21.1 was used to load and fix and make slight modifications to STL files. STL files were checked in order to ensure only desired volumes were printed (no noise shells), which were fully closed, with no inverted normals or holes. STL files with a high number of triangles (>500,000) were fixed so that only a low number (less than 100) of overlapping or intersecting triangles remained after fixing. Files with lower numbers of total triangles were fixed as to have no overlapping or intersecting triangles.

MTT AutoFab software was provided by Renishaw plc (UK) and was used to prepare STL files for building on either the Renishaw AM250 or AM125 LPBF machines. It can generate primitive shapes such as cubes as well as support structures for attaching a part to the build plate and supporting any overhanging areas. Individual material files can be produced for different scan strategies and layer thicknesses for a defined material. This program also slices STL files and generates the machine code (.mtt file) to build the final parts.

QuantAM build preparation software was also provided by Renishaw plc (UK) and was the replacement to MTT AutoFab for their newer LPBF machines. It was used to verify the .mtt file, which was generated my MTT AutoFab, as well as visualise scan strategies and scan paths prior to building. It was also able to give a visualisation of energy density for different scan strategies.

3.7.2 Analysis

After images were taken of specimens on the microscope, density measurements were made through threshold selection of contrasting areas in the open-source software Fiji [216]. Fiji was a version of ImageJ software which comes pre-bundled with common plug-ins and libraries. Within the software, pixel ratios from the microscope (Table 3-8) were used with the images to take accurate measurements of features within pictures. Custom macros were also written to automate different tasks. One was written to determine the profile and average thickness of the thick or thin walls for geometrical analysis. Another was written to split up a larger image into smaller images while centring the main features within the smaller image for use as input images for machine learning.

3.8 Machine Learning (ML)

ML was developed within the Python programming language [217] using version 3.5. It was an open source software package that was available for free on Mac OS, Windows, and Linux. It was installed using the open source Anaconda Python distribution in order to manage the coding environment and allow it to be installed to different machines without interfering with any existing python environments. Within Anaconda, open source Spyder software was used in order to write, debug, and run python scripts. Scikit-learn [218] was also used in Python for clustering and other analytical tasks.

For implementing ML, Tensorflow [219] was selected as the platform within Python. Tensorflow was originally developed within Google and was made open source in 2015. It has become one of the most popular ML libraries due to it’s easy to use programming implementation along with its ability to run on not only a computers CPU, but also on any available GPU which greatly speeds up computations due to the greater number of computing cores within a GPU.

Keras [220] was used to act as the application programming interface (API) for Tensorflow. It is an easy to program interface between common ML workflows and methods. It focuses on being user-friendly yet powerful.

A Convolutional Neural Network (CNN) [194] was used in conjunction with an Autoencoder (AE) [196] to reduce the high-dimensional image data into a simplified reconstructed output, as seen previously in Figure 2-30. The resulting Convolutional Autoencoder (CAE) was based on the Deep Convolutional Embedded Clustering (DCEC) technique of [204], as it could be used with both labelled and non-labelled data. However, as this data was unlabelled, only the pre-training portion of the DCEC was used. In order to promote clustering, the specific architecture of [208] was used as it was found in that research that the training which occurs after the pre-training contributed less than 15-20% to the final accuracy. Thus, the architecture that was used for the AE is much shallower than most, with only three convolutional layers and no flattening of the encoded latent space. The elimination of the flattening helps in feature preservation.

The autoencoder, patterned after [208], was comprised of two sets of convolutions and maximum pooling with batch normalisation, with a convolutional layer which acted as the middle latent space of the autoencoder. The remainder of the autoencoder was comprised of two sets of convolutional 2D transpose and 2D up-sampling layers along with batch normalisation. The number of convolutional filters used was 64 for the first layer, 128 for the second, and 200 for the middle latent space. The DCEC from [204], which was made opensource [205], had a number of variables which can be changed to fine-tune the process. These variables (called hyperparameters) are not learned but are pre-set before the process of learning. The hyperparameters are described in more detail in the work of [204] and [208], and include lambda set at 0.001, a batch size of 512, an alpha set to 0.9, the number of final clusters to be determined through additional analysis of the dataset, the number of nearest neighbours as 9, and the number of top anchor points investigated for each training as 7.

In order to determine the number of clusters which was appropriate for clustering, a method known as the gap statistic [221] was utilised. This method was designed to aid in estimation of the number of clusters within a set of data by giving a gap value for the different number of clusters, with the highest gap value indicating the optimal number of clusters. Here it was applied to the output images from the autoencoder. Initially, the latent space of the autoencoder was going to be used in clustering, however, it was found that clustering the output was more useful and informative. Before applying the gap statistic to the output images, a principle component analysis (PCA) was required on the data in order to reduce the number of dimensions, as there were 4096 dimensions for an image that was 128 x 32 pixels. PCA is a statistical method that transforms the original data to a desired number of dimensions. These new dimensions are used to explain the amount of variation that existed in the original data. The higher the number of dimensions for PCA, the better it represents the original data. However, with continuous data such as the images used in this research, lower PCA dimensions are required to find the optimal number of clusters. Too many PCA dimensions cause the gap statistic to form a logarithmic trend line which then recommends the maximum number of clusters being tested. For this data, between 2 and 10 dimensions for PCA were explored to find the optimal number of clusters, K.

In the process of parameter optimisation, there were times when two tests appeared to have a similar quality, despite having different parameters applied. After many tests, it was possible to determine which parameter set to use, but only by additional test methods such as density measurements. In order to obtain these density measurements, 5 mm cubes are manufactured using the parameters being investigated, then removed from the base plate, sectioned by a saw, mounted into resin, ground flat, polished to a mirror quality, then imaged using a microscope and manually analysed using thresholding limits in image processing software. These additional steps require a significant amount of additional time and resources. To quicken this process and develop an alternative method for quality assessment, it was theorised that the top surface of a thin wall could be used. By imaging this top surface, and using a method to rank the corresponding quality, the time to reach the final parameters could potentially be shortened. In order to remove a human-based subjective assessment of quality, it was proposed that ML could potentially be used to learn patterns and grade the resulting thin walls.

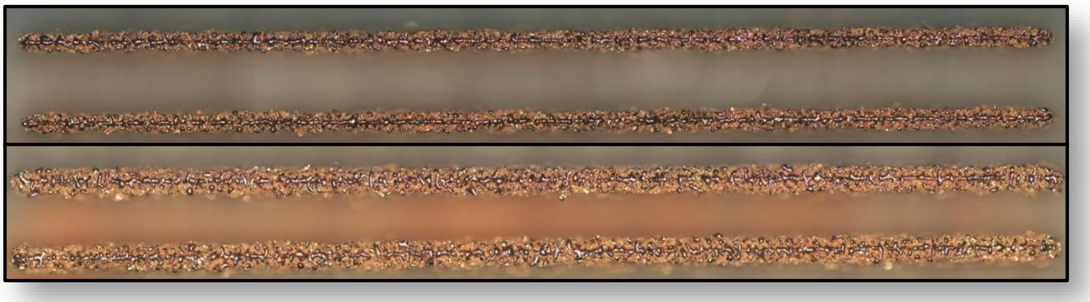

Figure 3-18: Full scan track images taken by microscope, with a point distance of 50 µm and scan speed of 250 mm/s (top), and point distance 200 µm and scan speed of 75 mm/s (bottom).

The first step was to gather the raw image data (Figure 3-18) which would be fed into a ML architecture, specifically a convolutional autoencoder (CAE) which was described in Chapter 2.11.3. These images were taken by microscope while keeping all optical settings such as physical light brightness, white balance, contrast, and focus as constant as possible. In order to ensure that there were high quality tracks to compare with in the data set, in addition to thin wall images, the single scan tracks were also included in the raw data. As the autoencoder cannot take the original high-resolution 38 megapixel raw images as input as seen in Figure 3-18, the images were sectioned and scaled and modified into a format which could be fed into the autoencoder. The original colour images contained two thin walls which were produced with the same processing parameters. These large stitched images were approximately 15,000 pixels long by 2,540 pixels tall. The images also had a variable colour background due to the out of focus features at the base of the thin wall. Through a series of custom-macros written for ImageJ, the images were cropped to remove the track ends, scaled down and de-colourised, separated into two tracks, then segmented so that the track was centred with the background removed, with a random selection seen in Figure 3-19.

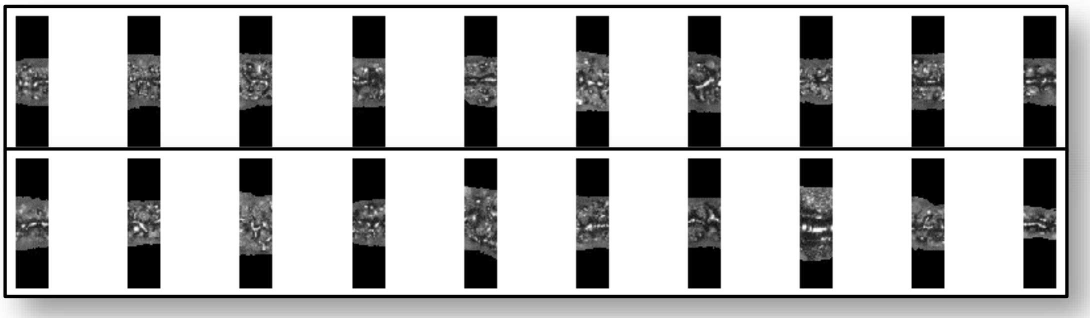

Figure 3-19: Selection of random images processed and ready to feed into an autoencoder architecture.

The final 47,448 images are grey scale (where each pixel has a value between 0 and 255), approximately 0.004 Megapixels with an exact dimension of 32 pixels long by 128 pixels tall. These dimensions were chosen as they are direct powers of 2 (2^5 = 32 and 2^7 = 128) and are more accommodating to the autoencoder architecture. After these images were run through the autoencoder, the reconstructed output removed many of the finer details that were unique to each image. This enabled the images to be better clustered to find patterns in the data. The resulting output from the autoencoder can be seen in Figure 3-20.

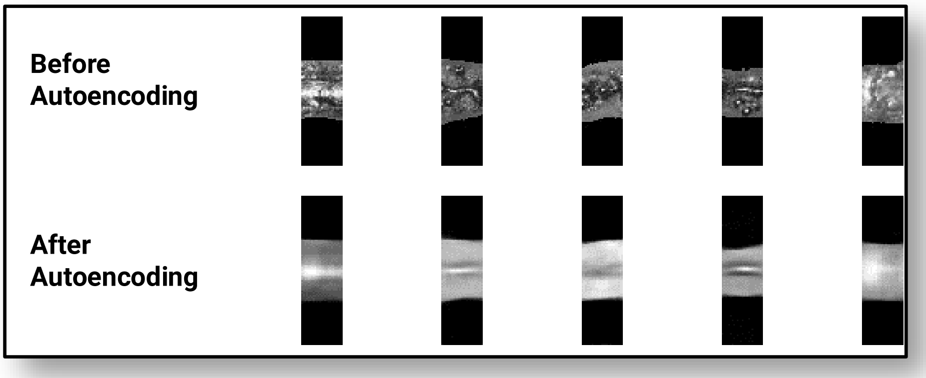

Figure 3-20: An example of the input images fed into the autoencoder and the resulting output image.

In order to determine the correct number of clusters to use for this data, the gap statistic was used along with principle component analysis (PCA) in order to simplify the data. For this data, between 2 and 10 dimensions for PCA were explored to find the optimal number of clusters, K, as seen Figure 3-21 with the highest gap value highlighted in red. Using a PCA of 2 resulted in only 2 clusters which was not large enough to correctly capture the continuous nature of the data. PCA values higher than 4 started to represent the logarithmic trend line, which was undesirable. However, a PCA value of 3 was ideal for the gap statistic to fairly determine the number of clusters to be visualised with a cluster count of 28, which was also identified with a PCA value of 4, further strengthening the idea that 28 was the ideal number of clusters for this data set.

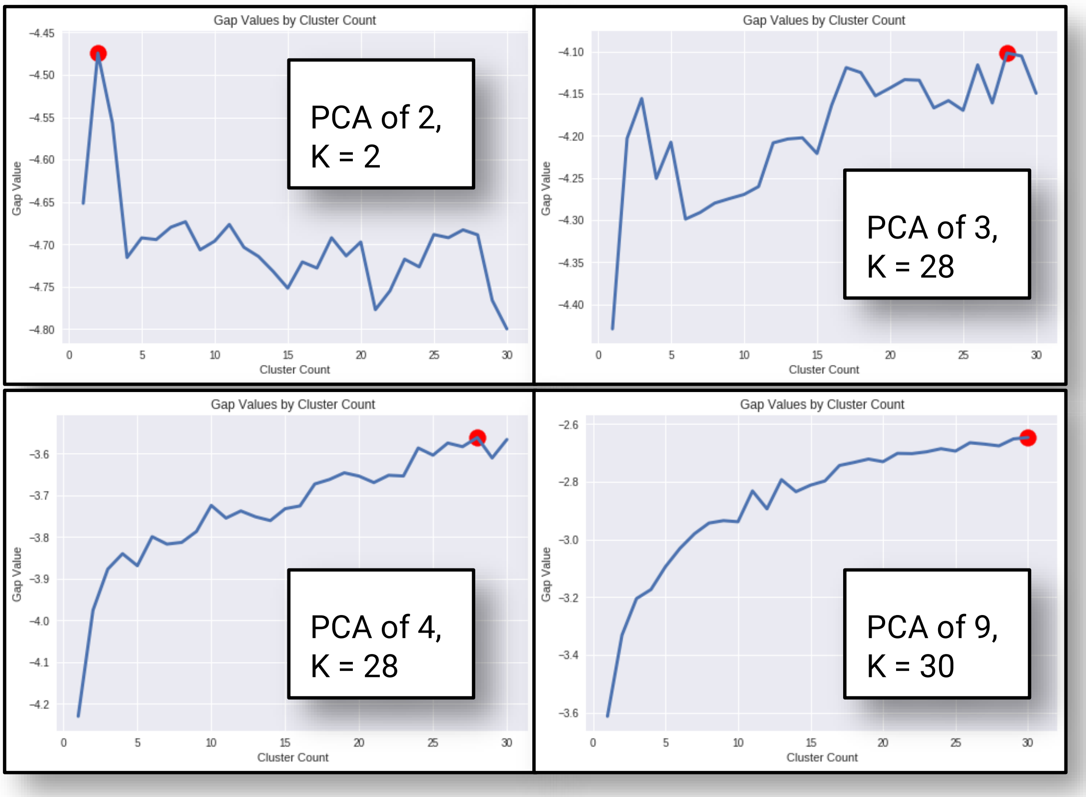

Figure 3-21: Gap statistic graphs indicating the ideal number of clusters in the decoded image data, with PCA value tested and resulting number of clusters.

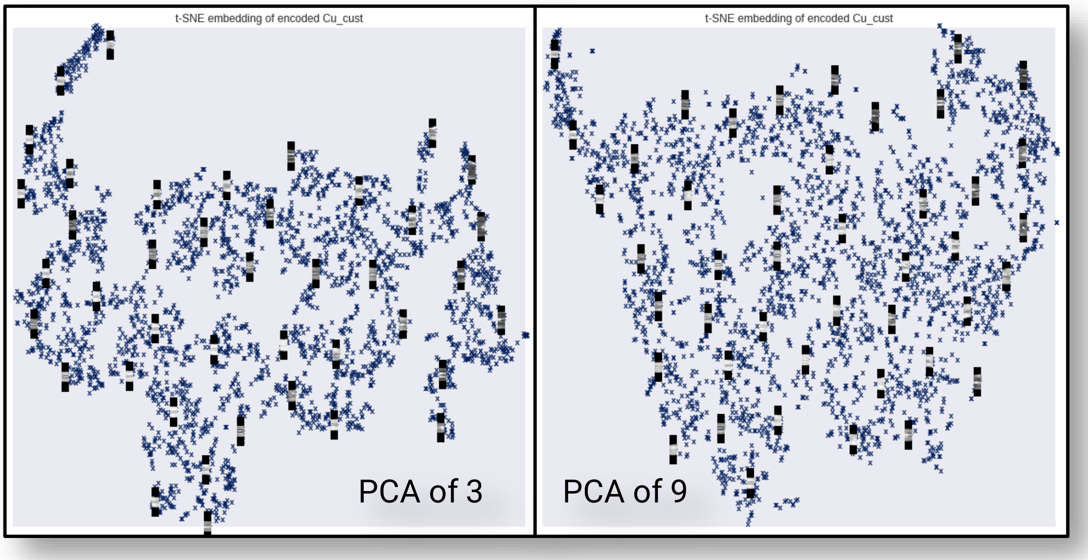

Figure 3-22: Visualisation of clusters using the t-SNE graphing algorithm.

To visualise the clusters, the dimensional reducing t-SNE graphing method [198] was used as seen in Figure 3-22. This method is not an exact representation of what the clusters look like, but rather it interprets the number of dimensions (3 for a PCA of 3 and 9 for a PCA of 9) into a two-dimensional image. Due to the continuous nature of the data, using a higher number of dimensions reduces the definition of the clusters as with a PCA of 9, which also was seen by the logarithmic trendline in the gap value.

Once the optimal number of clusters was identified, a clustering algorithm was applied to the non-PCA reduced data to group images together. As there were a large number of clustering algorithms within the Scikit-learn [218] ML toolkit, the KMeans Mini Batch [222] algorithm was selected due to its speed and ability to report the location of cluster centres. These locations were used to obtain several images which were closest to them. Those images were found to be similar in appearance and fairly represented the type of image within the cluster. The clusters were then manually analysed. This was necessary because the ML was unsupervised and hence lacking the labels to separate good from bad quality weld tracks that a supervised approach would require.

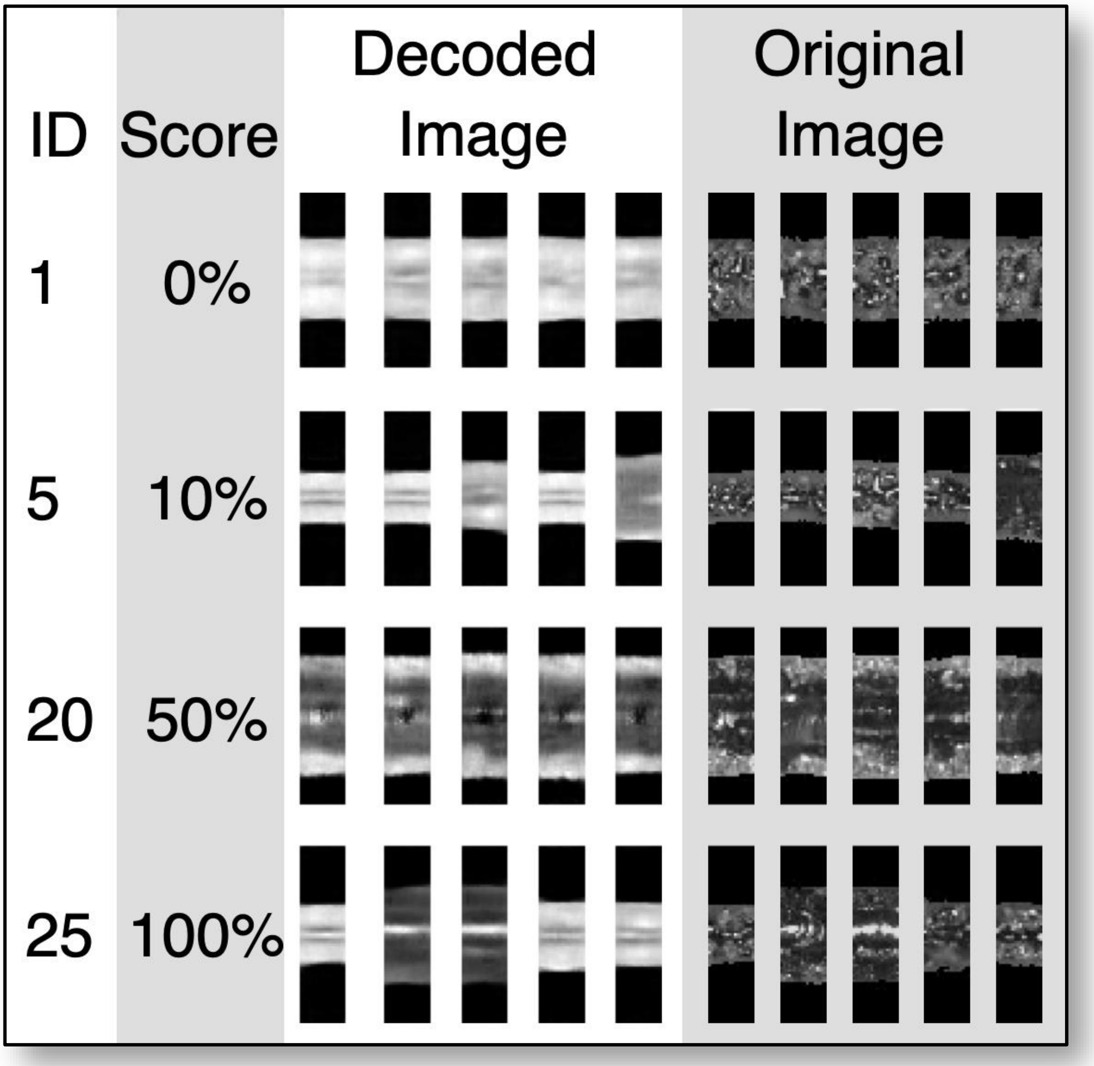

Figure 3-23: Sample of clustered images with a manually assigned quality score and original image.

The top 20 images from each of the 28 clusters were evaluated and scored, a small selection of these are seen in Figure 3-23. For each cluster, a score of between 0 and 100 was applied, based on the assessed quality of the cluster. Scores of 0 were applied to clusters which showed signs of balling or an unstable melt pool. Scores of 100 were applied to clusters where the images demonstrated high quality continuous weld tracks. For example, if all the images in a cluster showed no indication of continuous tracks, the score for the cluster was low. If some of the images in the cluster showed some well-defined continuous tracks, the cluster was scored higher. If the majority of images showed well defined and continuous tracks, it was given a maximum score. While this score did involve a human-based assessment, it was applied to a cluster of features, and not an entire track. This assessment was then applied to all tracks equally without further human-bias.

3.9 Summary

This research sets to establish the viability of using AM as a method to produce electrical coils within an electric motor. In order to explore this potential, the electrical properties of materials that are manufactured by LPBF need to be identified. Two materials are the focus of this research, pure copper and an aluminium alloy AlSi10Mg. Pure copper is attractive due to its lower resistivity. AlSi10Mg is attractive due to its high specific conductivity and ability to be processed to a high relative density using LPBF. AlSi10Mg processing parameters were derived from previously published results, whereas the processing parameters for pure copper had to be derived from scratch. These materials were processed on Renishaw AM equipment, pure copper on an AM125 due to its higher laser power density and AlSi10Mg on an AM250 due to its larger build volume.

Different types of specimens were created with both materials. To analyse density and the quality of processing parameters, small 5 mm cubes were created which minimises material usage and maximises the number of parts per build. For electrical resistivity determination, small rectangular specimens were created in order to provide enough resistance to measure, a minimum of 100 μΩ for both materials. For geometrical analysis, custom coils were designed and modified to represent an electric motor coil as well as to test the accuracy of different sized walls printed by LPBF. With each of these specimens, different equipment was used to measure and analyse different properties including density, hardness and microstructure. To ensure that the processing parameters were compared equally, standard grinding and polishing techniques were followed. Heat treatments were performed to compare how it affects other characteristics such as electrical conductivity and microstructure.

To determine the resistivity of the material processed by LPBF with respect to initial build orientation and heat treatment, electrical tests were performed using a well-defined test standard, ASTM B193-02, “Standard Test Method for Resistivity of Electrical Conductor Materials”. This standard defines the needed equipment to use such as a four-point probe micro-ohm metre and knifed-edged callipers, as well as the standardised method to follow such as taking two measurements back to back while reversing the polarity of the probes. By following this standard and using multiple specimens for each test case, an accurate description of the relationship between resistivity and the test cases can be determined.

As part of this research, numerous software tools were used to accomplish these tasks. These include CAD software to create custom designs, to tools which prepare the resulting designs to be manufactured by AM. Other tools were used for post-analysis and organisation, as well as ML algorithms to aid in the classification of the results of parameter optimisation. Having a high freedom of design with high conductivity materials could be especially useful in designing coils for electric motors or other electromagnetic devices. In the next chapter, this freedom of design will be explored for electric motors, specifically how it can potentially change how we manufacture coils for electric motors.

Chapter 4 Using AM in Electric Motor Coil Design

4.1 Introduction

Additive manufacturing is often touted as an enabling technology which has a freedom of design that is unmatched by any other manufacturing method. However, there are a few things which need to be better understood before engineers can confidently design for AM. The first is an understanding of the expected material properties from a part that is manufactured through AM, including how post-processing may affect them. This requires a valid processing parameter set for the desired material, and a complete dataset of properties in as-built and post-processed conditions. The next is the knowledge of the limitations of the specific process being used for manufacture. This requires a knowledge of the machine, processing conditions such as layer thickness, surface finish and tolerances. Lastly, a complete understanding of the item being replaced or redesigned is paramount, as this unlocks the transformative power that AM allows through redesign.

Through this research, some of these requirements are addressed for redesigning electric motor coils. The electrical properties for both pure copper and the aluminium alloy AlSi10Mg are reported in Chapter 5 and Chapter 6 respectively. These properties are explored for the as-built condition as well as for various post heat treatments. In addition to these properties, the surface finish was investigated in relation to how it affects the tolerances of the printed components, with new techniques for improving the surface finish of AlSi10Mg being presented on a regular basis [223]–[226]. The knowledge of LPBF and how it affects designs has been researched and is generally well known and published [38], [40], [227]. However, the final element required to enable the adoption of AM to manufacture motor coils is to redesign the coils for AM. This will be addressed in this chapter.

A review and breakdown of what makes an effective electric motor coil design will first be discussed. Following that, various design options will be explored in the context of the new design freedom afforded by AM. Finally, a specific example of fitting a motor with AM coils will be explored. These results will then be discussed and summarised at the end of the chapter.

4.2 Motor winding design

Figure 4-1: Example of a traditional tightly wound copper coil made from rectangular cross-sectional wire with paper and Kapton tape insulation (Provided by the Power Electronics, Machines and Control Research Group at the University of Nottingham).

Traditional conductors are limited in a few ways. First, there are only a fixed number of available cross-sections for use in winding motors. Only certain circular diameters or set-sized rectangular wires are available, as seen in Figure 4-1. Circular packing factors, or the maximum amount of circular material that can fit into a given area, limit the fill factor when using round wire. Conversely, rectangular wire cannot perfectly fill an angled slot. There will always be unwanted gaps due to geometric constraints when using circular or rectangular profiles. In addition, there will also be gaps due to the manual assembly of the wire coils around the teeth in the slot. Here, AM can vary the conductor cross-section to fill all available space so that there are no unwanted gaps, all the while maintaining a constant cross-sectional area.

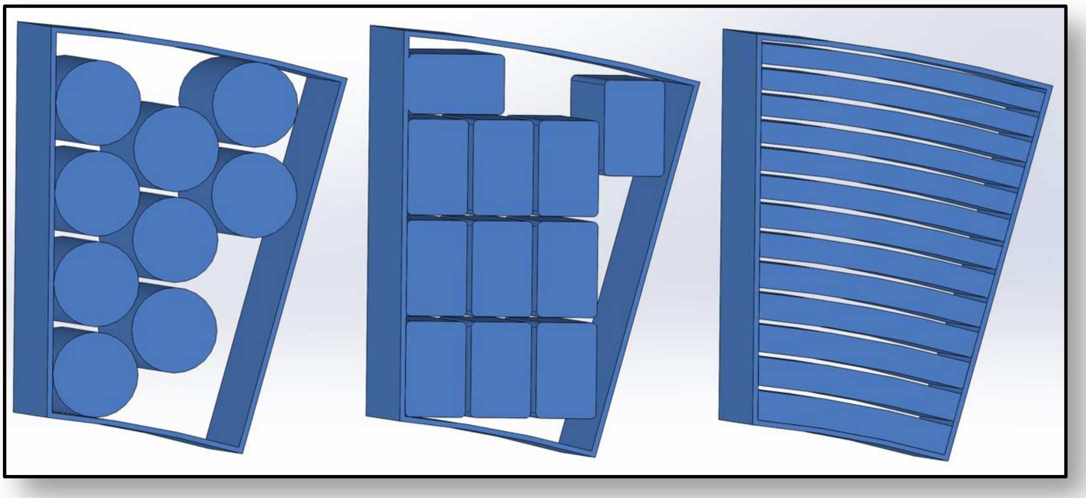

Figure 4-2: Comparing the maximum number of windings given a specific shape (circular, rectangular, or variable) of equal cross-sectional area that can fit within a traditional half-slot volume.

This advantage for AM was tested as seen in Figure 4-2, with a wire diameter of 4.11mm which corresponded to an American Wire Gauge of 6, however any size from any standard such as the Standard Wire Gauge or IEC 60228 (the International standard for wire sizes) could be used. This area was used in a set volume which was patterned after a traditional half-slot geometry. Using a circular profile, it was found that only nine windings would fit. By changing the winding shape to a rectangular profile, but keeping the cross-sectional area the same, eleven windings fit into the same space, which increased the fill factor by 12%. By moving to an AM generated shape, thirteen windings were able to fit, which increased the fill factor by 23% over the circular cross-section. In all these cases, a minimum clearance between the sides of the slot volume and windings, as well as between windings was maintained.

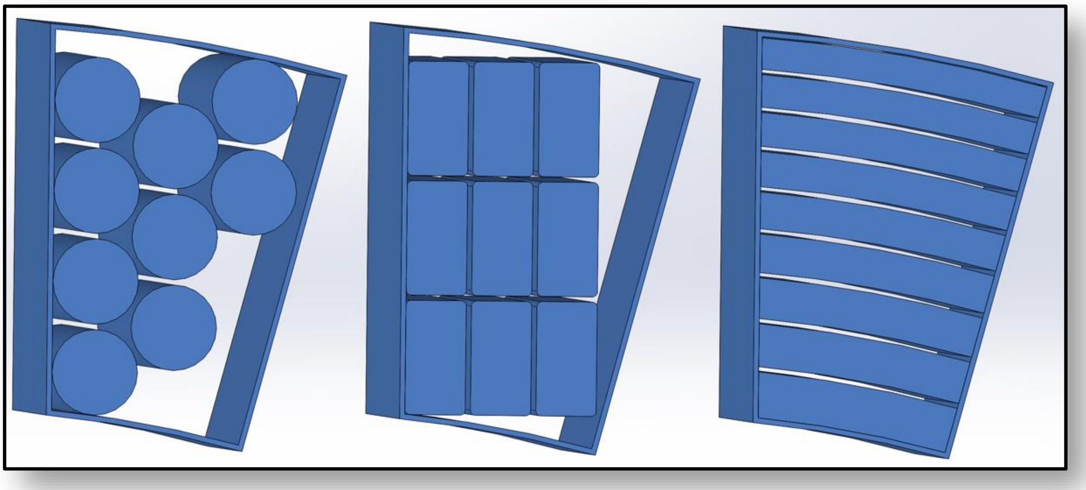

Figure 4-3: Comparing the maximum cross-sectional area of different shaped windings (circular, rectangular, or variable) that can fit within a traditional half-slot volume.

If rather than keeping the cross-sectional area the same, the number of windings was kept the same (with the cross-sectional area increased) as seen in Figure 4-3, the following insights were observed. The rectangular profile only increased the fill factor by 10% over the circular, but the cross-sectional area increased by 19% over the previous cross-section. The AM cross-section had the largest advantage, increasing fill factor by over 29% and increasing the cross-sectional area by over 55%. The theoretical fill factor for this AM coil is 82% versus the 53% for the circular cross-sections. These simple comparisons clearly showed that a custom AM shape enables the largest potential gains in a motor's efficiency. The next step was to design an entire generic winding which utilised these basic findings to evaluate how AM can improve fill-factors and use DfAM principles such as minimising supports and overhanging areas through design and choosing an initial build orientation.

4.2.1 2D design of windings

The perceived advantage of AM is that it can make use of the entire slot and improve fill factor. Thus, the next question is how to best arrange the AM windings in order to optimise for AM manufacturability and electrical considerations. AM manufacturability includes minimising the amount of overhanging areas in order to reduce the need for support material. Supports increase build time, increase part cost, and increase the amount of post-processing required for each part. Electrical considerations include minimising the end turn length to lower the resistance of the coil, as well as increasing the ratio of torque-producing copper in the slot to total copper. In addition, the design freedom that AM allows enables an electrical motor designer to precisely control the geometry such as to place conductive material exactly where the designer requires it to be within the slot. This can be used to various advantages such as better thermal management and reducing the amount of insulation between turns that is required.

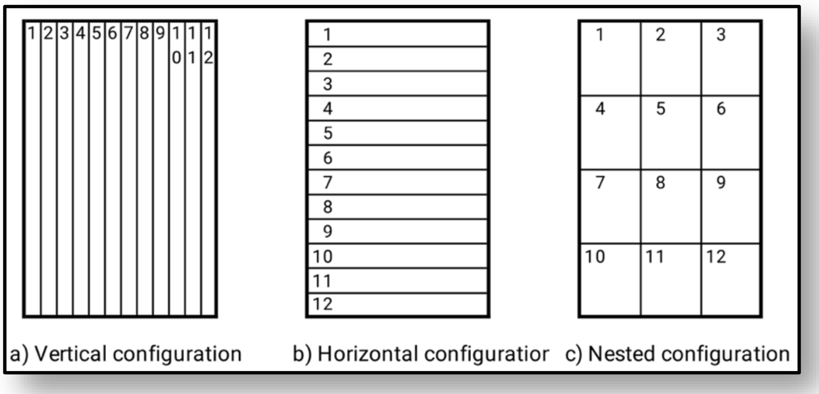

a) Vertical configuration b) Horizontal configuratior c) Nested configuration

Figure 4-4: Division of equal areas in either a vertical (a), horizontal (b), or nested (c) configuration.

In order to evaluate these additional considerations, the geometry was represented in an easy to visualise manner as seen in Figure 4-4. Here, a simplified slot is shown as a rectangular area, divided into twelve equal parts which represent different locations for a conductor. Three primary design patterns were considered. One was to have all the conductors aligned side by side so that the longest edge was orientated vertically (a). Another was to stack the conductors on top of each other so that the longest edge was aligned horizontally (b). Lastly, was to nest the conductors (c) in a grid so that the length and width of the conductors were of similar length. Depending on the layout of the divisions, the maximum amount of needed insulation varies compared to the enclosed area.

The advantage of vertically aligned conductors was to potentially eliminate any support material that would normally be required, while also maintaining the height of the slot resulting in the shortest winding. The aspect ratio of each conductor leads to it having the greatest surface area when compared to the other two. This aspect ratio would be advantageous in applications of high frequency due to the skin effect (which was discussed in Chapter 2.3.3). This stacking arrangement of the conductors also had the negative effect of leading to a much wider coil due to the need for a minimum clearance for manufacturing and insulating.

The advantage of stacked horizontal conductors was that it not only maintains the slots original width, it also could compress vertically due to it acting more like a spring rather than a rigid geometry. This could be of benefit if the manufacturing clearance is much larger than the insulating thickness, as it would allow the winding to compress into a smaller volume than in which it was manufactured. While this geometry could potentially have the largest need for support material, if the winding was manufactured on its side, the amount of support material would be greatly reduced.

The advantage of the nested conductors was that they minimised the overall surface area that would be needed for insulating. This minimisation could potentially lead to a smaller overall winding, which would help minimise the resistance of the coil and thus lower copper losses. However, this geometry would also be more rigid and would not maintain the height or width of the original slot. The next step was to model these concepts in CAD to determine if these benefits would materialise in 3D.

4.2.2 3D design of windings

In order to explore the full implications of the ideas presented previously, five different generic 3D CAD coils were designed and analysed, as seen in Figure 4-5. These designs incorporated the 2D features which were shown in Figure 4-4. The 3D windings seen in Figure 4-5 have two vertical configurations (a & b), two nested configurations (c & d), and one horizontal (e). Winding (a) is entirely vertical and resembles a spiral when seen from above. However, in order for the inner terminating part of coil (a) to be connected electrically, it needed to have a jog in the wire which crosses above the rest of the coil which increased height of the coil. In order to avoid this jog, coil (b) was designed to also be primarily vertical, but with two spirals on top of each other. Coil (c) was a nested design which had six spirals stacked on top of each other, with three loops per spiral. Coil (d) was also nested, but rather than stacked spirals, it resembles three nested springs, where each spring has six vertical loops. Coil (d) best represents a traditionally wound coil configuration. Coil (e) was an entirely horizontal configuration which resembled a wide flat spring. Additional design factors can be summarised for these coils in Table 4-1.

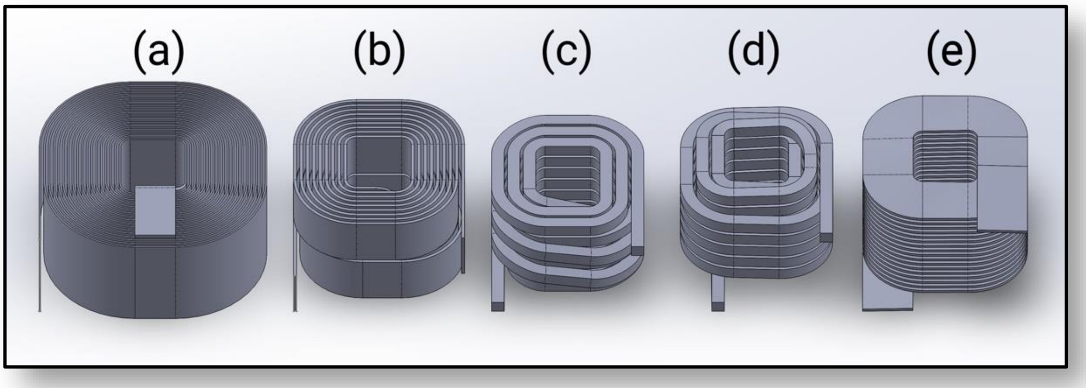

Figure 4-5: Five different 3D modelled coils representing how AM could be used for design.

Coil	***Configuration***	***Design Factor to Investigate***	***Cross-section dimensions***
a	Vertical	Minimise support material	16 mm x 0.25 mm
b	Vertical	Better terminal geometry	8 mm x 0.5 mm
c	Nested	Minimise length	2 mm x 2 mm
d	Nested	Compare traditional design	2 mm x 2 mm
e	Horizontal	Minimise overlapping	0.5 mm x 8 mm

Table 4-1: Comparing the main design factor to investigate for the corresponding 3D modelled coils.

The windings seen in Figure 4-5 were not designed to any specific application but were designed with generic parameters so that they could be easily modified and compared. These parameters were kept constant and can be found in Table 4-2

Parameter for design	*Value*
Cross-sectional area	4 mm^2
Number of conductors in the slot	18
Centre winding core dimension	10 mm by 10 mm
Clearance between all surfaces	0.5 mm
Terminal extension from centre of core	17 mm

Table 4-2: Properties for comparing different designs of windings.

By maintaining these dimensions, the different designs could be compared in terms of volume, surface area, effective wire length, envelope dimensions, required supported area, and fill factor, with these key comparators being listed in Table 4-3. An example of vertical support area and on-side support area for coils (a) and (e) can be seen in Figure 4-6. The key factors to look at are minimising wire length (in order to minimise resistance), minimising the required supported area (in order to aid in AM), and maximising fill factor (in order to increase power density).

Coil	***Volume (mm^3)***	***Surface Area (mm^2)***	***Wire Length (mm)***	***Coil Height (mm)***	***Coil Width (mm)***	***Coil Depth (mm)***	***Vertical Support Area (mm^2)***	***On-side Support Area (mm^2)***	***As-Built Fill Factor***	***Vertically Compressed Fill Factor***
a	5,907	47,409	1,477	17.1	36.2	37.1	74	17,541	*31%*	31%
b	4,806	20,432	1,201	16.5	26.2	28.0	297	7,062	*51%*	53%
c	4,551	9,109	1,138	14.5	24.2	27.5	1,894	1,365	*66%*	80%
d	4,379	8,768	1,095	19.3	24.2	25.0	1,868	1,228	*50%*	57%
e	4,680	19,902	1,170	18.3	26.2	27.0	8,762	120	*46%*	87%

Table 4-3: Comparative properties of the five different 3D modelled coils which could be made using AM.

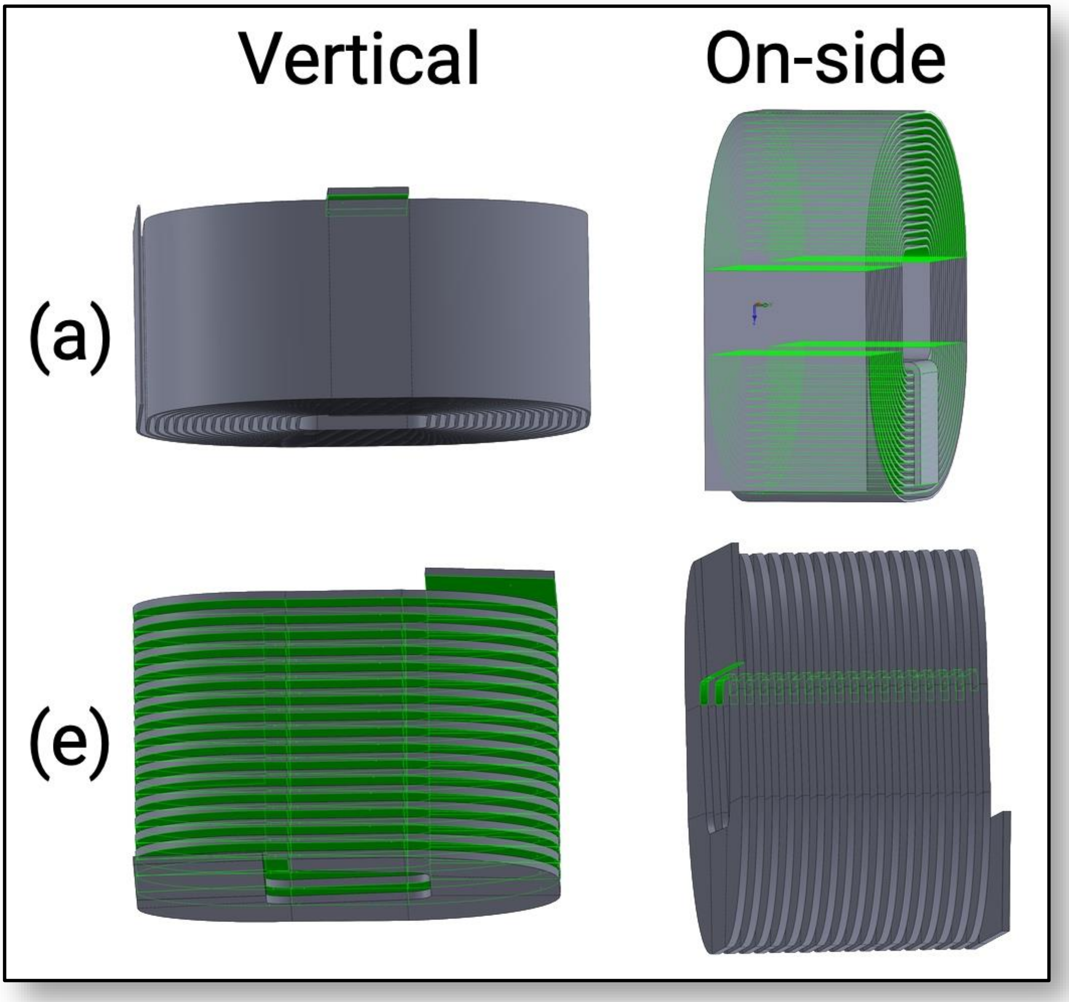

Figure 4-6: Comparison of the supported surfaces (highlighted in green) for coils (a) and (e) using either the default vertical position, or by rotating the coil to be on-side.

The volume of the coils was proportional to the effective wire length, as all coils had the same cross-sectional area. Surface area was proportional to the cross-section aspect ratio, where both coils (c) and (d) had the lowest around 9,000 mm^2, (b) and (e) both with around 20,000 mm^2, and (a) had the highest with over 47,000 mm^2, confirming the 2D analysis. As wire length determines resistance (when all cross-sectional areas are equal), the lowest resistance would be seen with coil (d), which is modelled after a traditional coil winding method. However, except for coil (a), the other coils were all within 10% of each other. Therefore, resistance/wire length alone was not a good enough indicator of which coil design was superior and additional properties need to be examined.

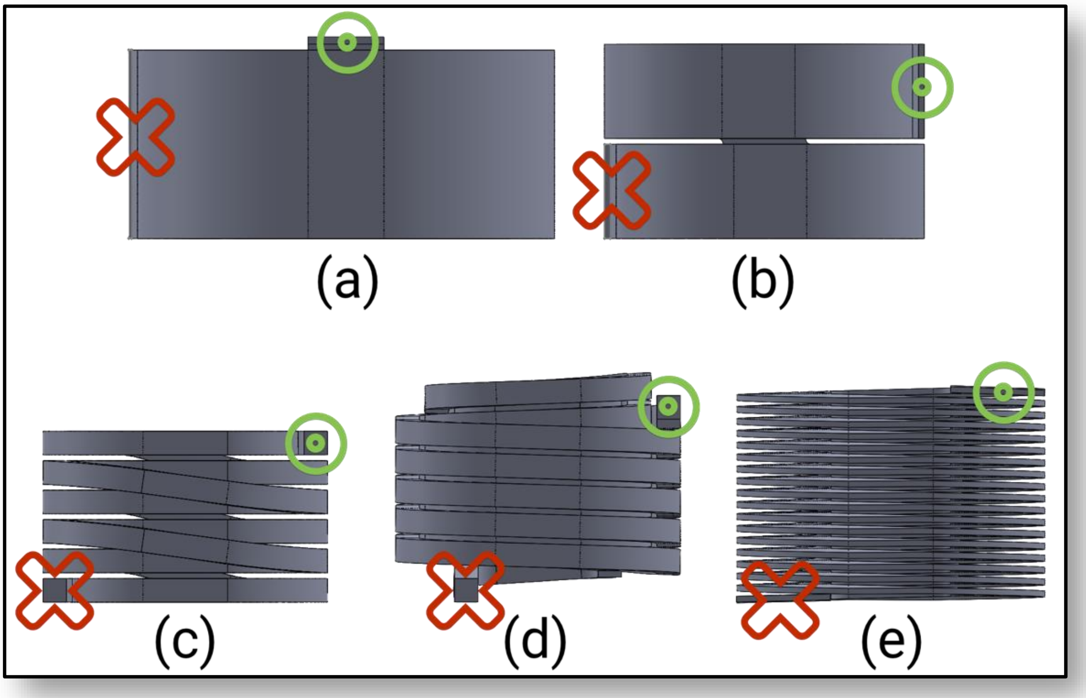

Figure 4-7: The front view of the coils, showing their comparative heights, as well as inlet electrical terminal highlighted by a red cross, and outlet terminal highlighted by green circles.

The coil with the largest coil height was surprisingly (d) due to the fact that in order for the end of the winding to terminate outside of the coil, it had to drop down considerably in order to clear the other turns of wire as seen by the red cross in Figure 4-7 (d). As (d) was designed in a traditional winding manner, this type of wire jog is also commonly seen in traditionally wound coils as seen previously in the top wire of Figure 4-1. An alternative winding method was employed in the design of (c) to eliminate this jog, as all three layers of the coil are in the same plane and comprise six in-plane spirals, rather than having three nested springs as seen in (d). This is also why (c) was the shortest, as these in-plane spirals simplified the design so that height was a function of the cross-sectional height and the number of vertical clearances between spirals. The wire termination jog was also seen in the design as indicated by the green circle in Figure 4-7 (a) which had just a single in-plane spiral, which is why (b) was designed to eliminate the jog by having both vertically aligned cross-sections and two in-plane spirals. The widest and deepest coil was (a), which confirmed the 2D analysis as it had the greatest number of vertical clearances.

One important property for any coil that will be created by AM, is how to support and post-process the coil. This requires minimising the number of supports and making the supports easily removeable. Therefore, the five designs were evaluated according to this principle. As all parts need to be supported on the bottom surface, only the additional supports which are not at the bottom were analysed, as seen in Figure 4-6. In that figure, the vertical orientation of the coil, as well as the on-side orientation have the faces highlighted which would need supports. The exact values for the surface area was given in Table 4-3. While the design intent of (a) was to eliminate supports, due to the end wire jog, this was not possible, however it did have the lowest total support area of any coil in any orientation. The next lowest was the on-side orientation for coil (e) which only required supports on the portion of the coil which was on the inner surface of the coil. However, the opposite orientation for both (a) and (e) resulted in the highest amount of supported area. The other coils were in the middle of these two extremes. However, the location of the supports is important to note. While (a) does have the least amount of supports, the location of these supports is in a tight area right above the coils. Whereas (e) has a considerable amount of vertical clearance for the supports. When comparing (a) and (e), the most favourable orientation and design for AM is (e) as the supports would be easier to remove.

Fill factor is an important property for any coil, with higher percentages leading to more efficient and more powerful electric motors. The as-built fill factors calculated in Table 4-3 were calculated with the slot area being the same as the height and width of the as-built coil. The compressed fill factor used the same width, but removed the vertical gap clearances, effectively compressing the spring to fit into a smaller slot height. Because coils (a) and (b) were built in a vertical configuration, the compressed fill-factors did not vary considerably. As coil (c) was much more compact than coil (d), it benefited greater in the compression fill factor despite both (c) and (d) having the same number of vertical gap clearances. Coil (e) had an average as-built fill factor, but since it is essentially a single spring, it benefited the most from compression and resulted in it having the highest fill factor at 87%.

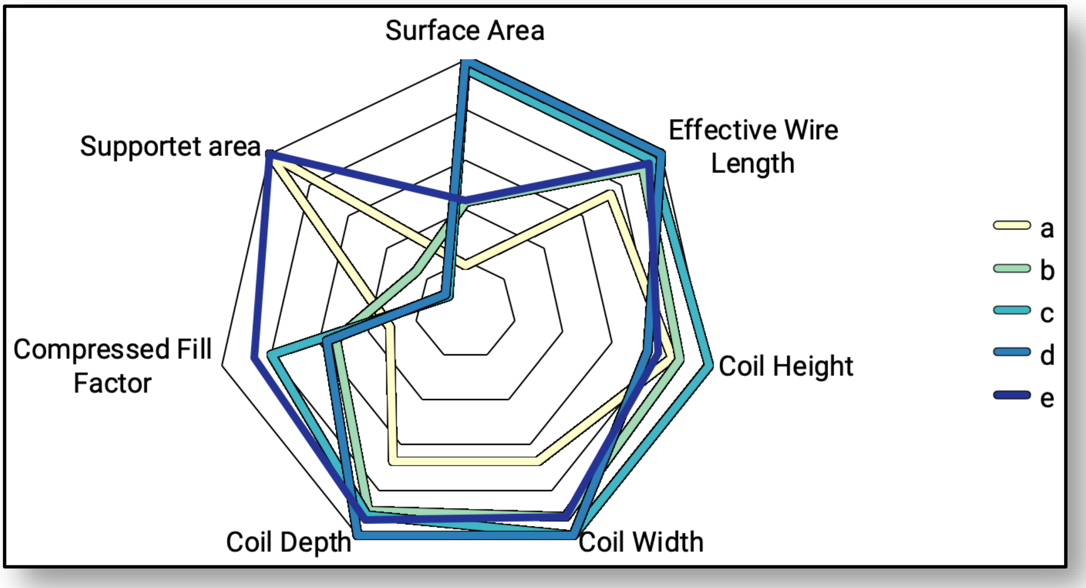

Figure 4-8: Evaluation of performance criteria based on the comparative properties for each coil.

In order to evaluate all performance criteria, the values for each category found in Table 4-3 were plotted and can be seen in Figure 4-8. By comparing all the properties which contributed to the radar plot, coil (e) on-side showed the greatest potential when comparing all the properties and was chosen to be utilised for the remainder of this research. However, there are specific applications which would warrant use of one of the other designs. As stated previously, high frequency applications may favour a much higher cross-sectional aspect ratio as seen in (a). However, despite the difficulties of removing support material from designs (c) and (d), there are potential reasons for using a nested design.

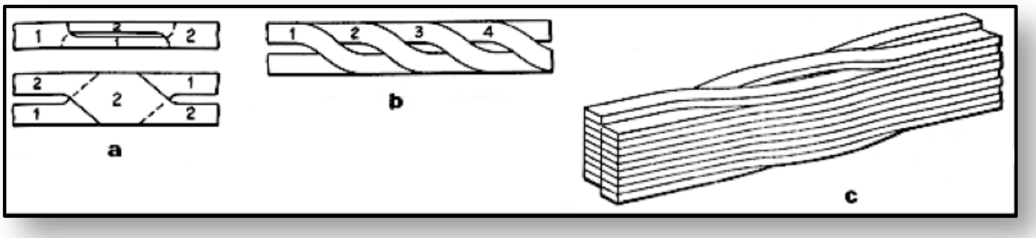

Figure 4-9: A few ways to twist conductors in order to minimise eddy currents [228].

For applications which would see high eddy current formation in the slot like high RPM electric motors with high frequency, there have been some innovative ways to minimise eddy current losses within the slot conductor [228]. This involved weaving conductors around each other as seen in Figure 4-9. However, the methods in that work were theoretical in nature as the traditional manufacture of such designs proved near impossible. However, with AM, these designs could prove themselves to be a viable solution to those types of applications.

4.3 Retrofit of Switched Reluctance Motor

An SRM was obtained within the Power Electronics, Machines and Control Research Group at the University of Nottingham, which met the criteria set forth previously. The motor was being used with custom control algorithms on a test bench. The as-purchased traditionally-built motor is shown in Figure 4-10 (right) along with an empty stator and casing, as seen in Figure 4-10 (left). A full list of parameters can be found in Table 4-4. The empty stator was used to test the viability of retrofitting an existing motor with AM windings.

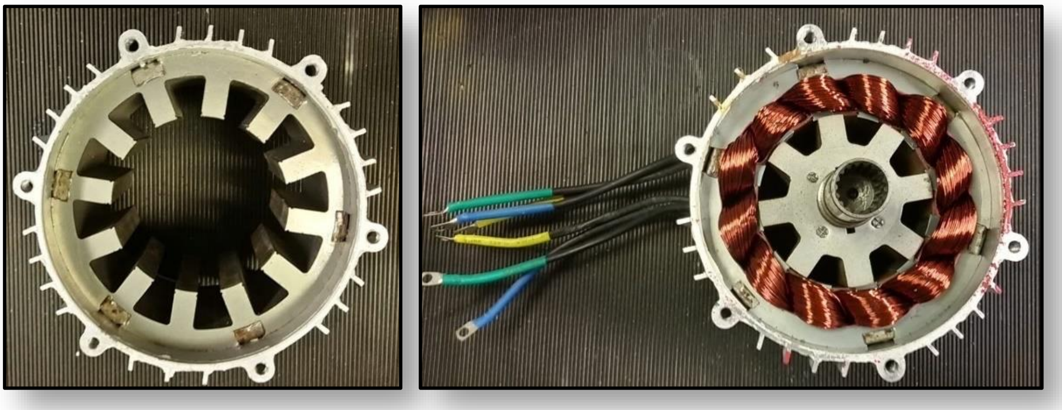

Figure 4-10: A 12-8 SRM with only the stator and outer casing (left) and a fully assembled motor (right).

Parameter	***Value***
Rated Power	1.5 kW
Maximum Speed	6000 rpm
Rated Peak Voltage	36 V
Rated RMS Current	26 A_{rms}
Stator Poles	12
Rotor Poles	8
Stator Outer Diameter	138 mm
Axial Stack Length	80 mm
Number of Turns and Poles per Phase	13 x 4

Table 4-4: List of parameters for the 12-8 SRM used in design.

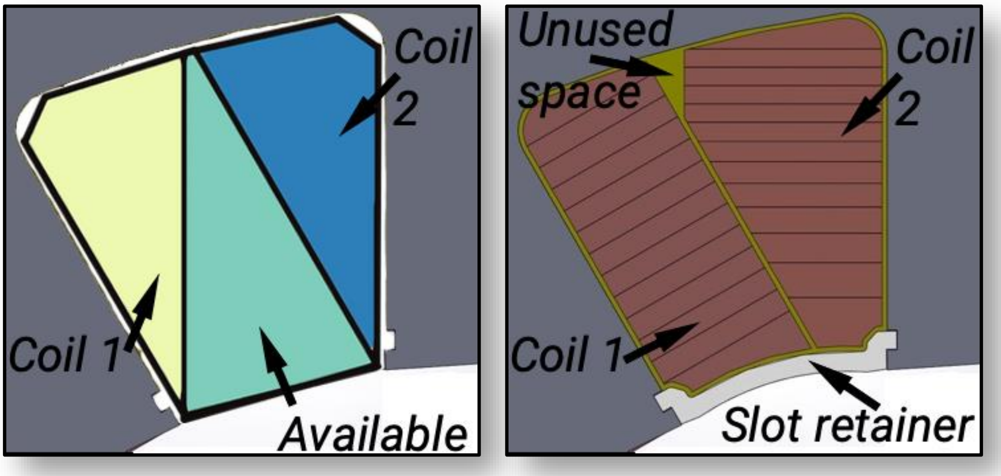

Figure 4-11: Division of the slot by theoretical shapes with equal sized downward triangles with available space in-between them (left) and the actual design using the maximum amount of space (right).

The first step was to model the entire motor (excluding windings) by CAD. As the coils were pre-formed, there was a requirement to maximise the fill factor without compromising the assembly process. This either required both coils to have the same exact profile for the coils to be the same and fit side by side in the slot, or to have different shape profiles but share the same cross-sectional area. However, the problem with having both coils the same profile was that it does not maximise the fill factor. This can be seen by the yellow and blue downward facing triangles in the left of Figure 4-11 which represent the identical coils, with the middle green upward facing triangle representing an empty space that is unused. The yellow and blue coils could be installed independently of one another with no interferences between the two. However, if the yellow and green areas are used for one coil, and the blue for a second coil, then the fill factor is maximised, but the coils are no longer the same cross-sectional area. This would also require the blue coils to be installed first, which would allow the yellow-green coil to be installed afterward. Instead of using the entire yellow-green area for one coil, part of the green area could be used for the blue coil, which would slightly reduce the fill-factor, but could be used to maximise the usable area for both coils, while making both cross-sectional areas the same. This path was taken for design, as seen in the right of Figure 4-11. Coil 1 which had a more rectangular cross-sectional shape was named the 'block', while coil 2 which had a more triangular shape was named the 'wedge'. Despite having different shapes, as long as both coils have the same cross-sectional area, and the same number of turns, both coils will perform the same with similar resistances (although minor differences may occur due to the length of the end turns).

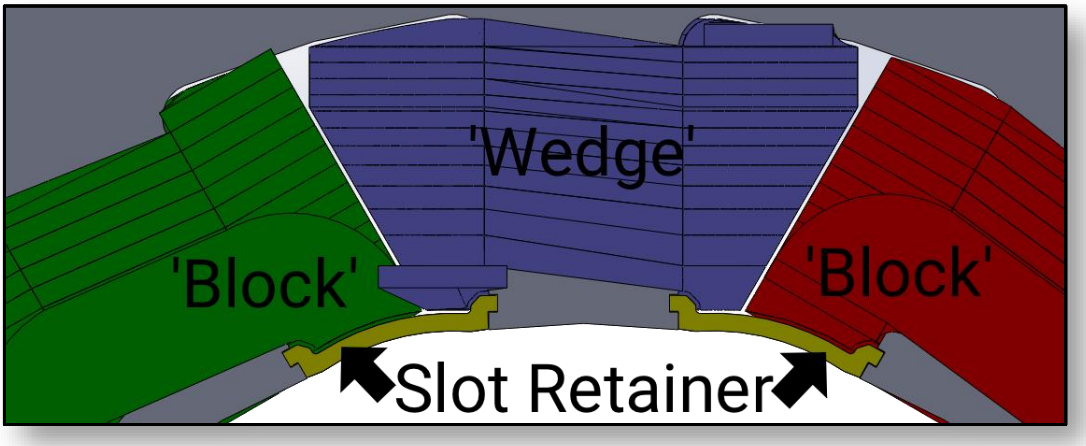

Figure 4-12: Front view of the two coil designs along with the redesigned slot retainer shown in yellow.

As this design had an open slot, a simple curved piece of plastic was needed to retain the windings, which fit into grooves at the end of the stator teeth. As these grooves were a few millimetres from the end of the tooth, there was an option to redesign the slot retainer in order to gain more area in the slot. The redesigned slot retainer can be seen in white in Figure 4-11 (right), as well as in yellow in Figure 4-12. This redesigned slot retainer gained an additional 2.4% slot area for the coil redesign compared to the original retainer. Due to the need to have the retainer assembled by sliding it into place after the coil was assembled, the bottoms of the coils needed to be designed so that there was an axial clearance for it as seen in Figure 4-12. This caused some changes to the coils themselves in order to allow for the bottom loop to be able to wrap around this clearance as seen in Figure 4-13. This caused the ‘wedge’ design in the left of Figure 4-13 to have the corner of the bottom loop to extend further out in order to maintain the same cross-sectional area while allowing for the retainer clearance. For the ‘block’ design in the right of Figure 4-13, the bottom loop needed to turn upward and around the clearance area required for the retainer.

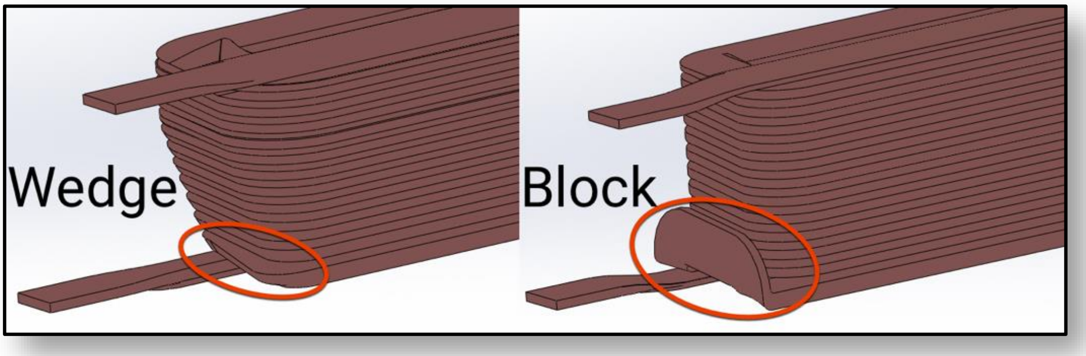

Figure 4-13: Modifications to the coils circled in red to allow the axial installation of the slot retainer.

Fill factor is defined as the total copper area divided by the total available slot area. Without using the redesigned slot retainer and maintaining a minimum clearance between the edges of the coil and the slot, the maximum fill factor which could be achieved would have been 94.0%. Despite having a triangular section at the base of the slot which could not be used for winding due to assembly constraints, by using the redesigned slot retainer and maintaining the same slot clearance, the maximum fill factor which could be expected was 93.5% compared to the original area. The actual fill factor for the larger slot area by virtue of the redesigned slot retainer was 91.3%. However, due to manufacturing, assembly, and insulation requirements, the expected manufactured fill factor would typically be lower.

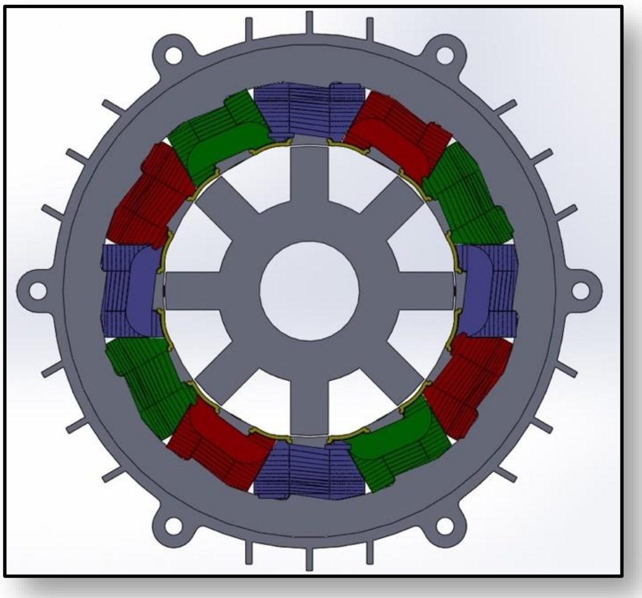

Figure 4-14: A fully populated motor with redesigned coils that are coloured according their phase.

In order to better understand if this fill factor was achievable, a ‘wedge’ and ‘block’ were printed using a material extrusion method with plastic which was less expensive and time consuming than printing in metal. In the final design, six of each coil design would be needed, with a pair of each design needed for each phase of the motor as seen in Figure 4-14. However, for this test, one of each were printed, along with the redesigned retainer.

The printed windings were printed as a merged piece so that individual loops were not present. This allowed the parts to be printed more easily and accurately. While the accuracy of these types of printers is not as high as LPBF, it proved accurate enough for the 0.25 mm clearances which were tested. It was found that the redesigned slot retainer was a perfect fit and required no further changes. The clearance tolerance on the length of the windings was found to be too tight, and additional clearance was added. The parts were reprinted and found to fit onto the motor perfectly, with enough clearance between coils and between the retainer, as seen in Figure 4-15. The next step was to print them using AlSi10Mg.

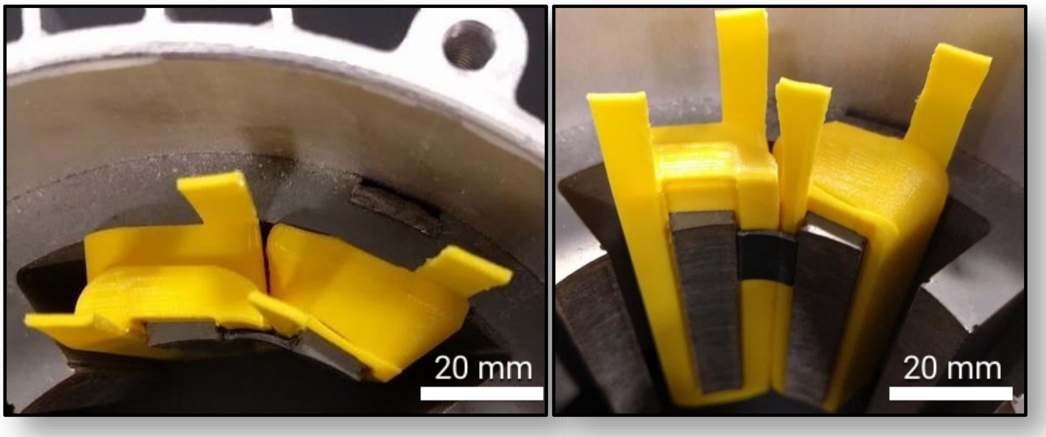

Figure 4-15: Plastic printed windings to prove fit and assembly into an SRM.

AlSi10Mg was chosen to print the windings due to its ability to be printed to a high density, and to further refine the resistivity values with a larger specimen. Printing these coils in copper was not an option as the Renishaw AM125 build volume was not large enough to accommodate this design. These metal-printed parts can be seen in Figure 4-16, with the ‘wedge’ design on the left, and the ‘block’ design on the right.

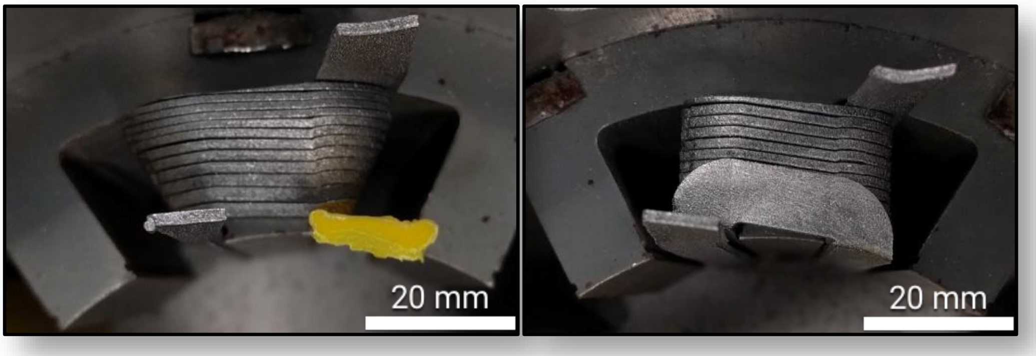

Figure 4-16: 3D printed aluminium windings assembled into an SRM with a 'wedge' design (left) and a 'block' design (right).

The windings were printed with the maximum fill factor discussed earlier, despite the potential issues with assembly clearance. As a result, the windings needed to be hand filed on all outside edges in order to achieve a proper fit into the motor. This filing was required due to the large attached particles that form in the LPBF process, as will be discussed in Chapter 6.5. Once these particles were removed, the resulting printed tolerances allowed the windings to be assembled into the motor. However, only the 'wedge' was able to have the retainer properly installed, as the tolerance stack-up of the 'block' was large enough so that the retainer could not fit properly. With some additional hand filing, the 'block' was also able to be installed next to the previously printed plastic windings, as seen in Figure 4-17.

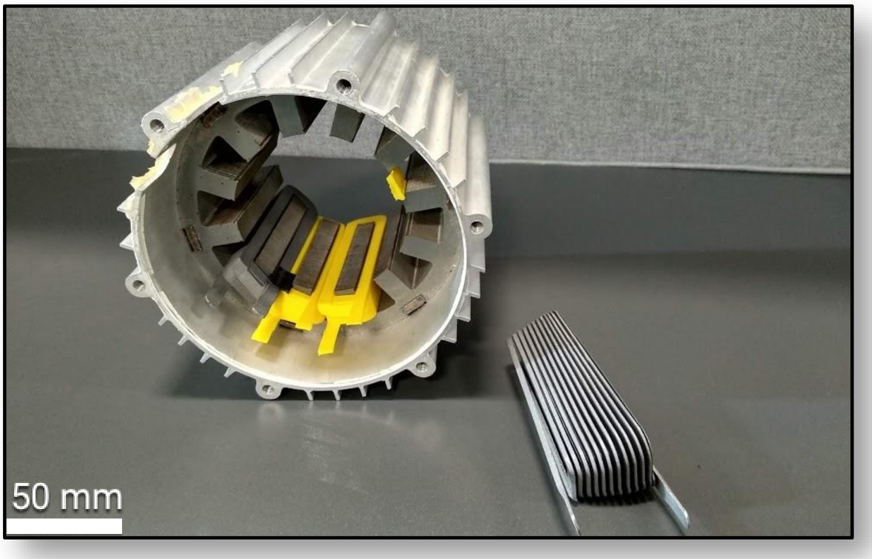

Figure 4-17: Assembly of 3D printed windings in the electric motor.

These AlSi10Mg windings were then tested electrically as seen in Figure 4-18 to refine the resistivity of this 3D printed alloy. These larger parts allowed the resistivity of this alloy to be refined to a greater accuracy than what was found in previous studies. The full results and procedure of these tests is reported in Chapter 6.4. The average resistivity for the ‘block’ coil was 4.87 µΩ-cm, and the ‘wedge’ coil was 5.18 µΩ-cm. The average of these two coils was 5.03 µΩ-cm.

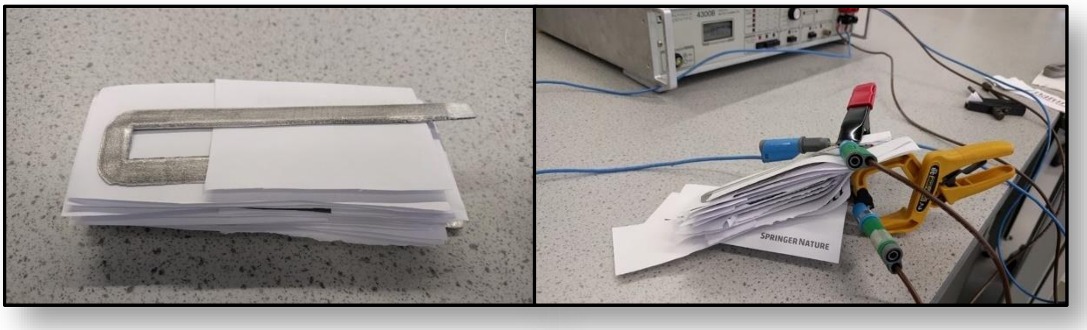

Figure 4-18: Electrical testing of 3D printed aluminium windings with paper insulation.

4.4 Discussion

4.4.1 Improved reliability

Additive manufacturing provides a level of freedom in design that has not been encountered before in traditional manufacturing techniques. This is especially true for methods which are based on hand assembly, such as electric motor coils. While there have been some attempts to use casting as a method to create coils [109], [110], it is still generally done by hand for small production runs, or by automation in mass production that emulates the process of handmade coils. AM opens a new variable to electric motor designers to further optimise specific applications. No longer are designers limited to set sizes of pre-made wires which they must try and fit into a specific slot geometry. Through AM, the number of wires in the slot can be reduced which can in turn improve reliability. For example, the original motor used here was wound with thirteen loops of wire, but each loop was comprised of 20 smaller gauge wires, which results in 260 wires in the slot verses the 13 that were used in the redesign. By reducing the number of wires, the number of potential faults from insulation failures can potentially be reduced as it reduces the magnitude of the thermally induced mechanical stresses that could lead to failure [6]. Because stator insulation failure accounts for 30-40% of all reported induction motor failures [70], improving this area for an electric motor through freedom of design could prevent a lot of downtime.

4.4.2 Increased Fill-Factors

Another area of improvement that this freedom of design opens is increased fill factors. While it may not be possible to have a 100% fill-factor, by increasing this above what is currently available through traditional methods, several areas are improved. These include higher torques and rated power for the same current loading, higher efficiencies, and cooler operating temperatures for a given load. These improvements have been shown with a fill factor of 78% [229] using a compressed forming method, however it has been suggested that fill factors above 74% using this method for compressing windings risk compromising the wire insulation [230]. But all the advantages of high fill factors can be assumed to be the same for AM windings without the added risk of compromised insulation. However, due to these increase fill factors, the amount of heat which can build up in the windings becomes more difficult to remove and can require more advanced cooling systems which can counteract some of the advantages of fill factors above 80% [231].

4.4.3 Improved Thermal Dissipation

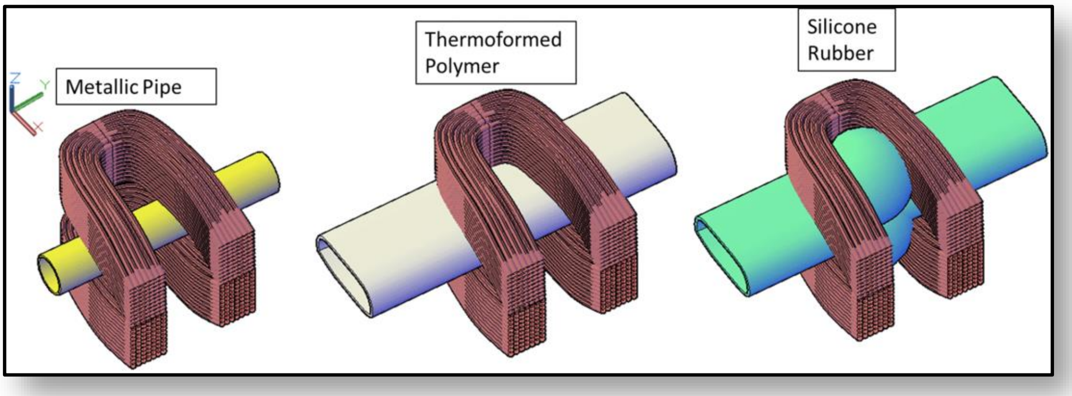

Figure 4-19: Examples of current research into removing heat from end-turns in an electric motor [232].

However, some of these concerns with thermal management in high fill factor stator windings can be addressed through innovative design. Specifically, design of the end-turns can be particularly helpful with managing heat. For example, recent work, seen in Figure 4-19 has shown that embedding a pipe into the end-turns and running coolant through it can remove a significant amount of heat allowing the windings to be much cooler than traditional end-turns [232]. This was achieved with windings that had slightly longer circular end-turns in order to allow the pipe to be assembled into them. Typically end-turns are as tight as possible to minimise the resistance of the phase by minimising the length of wire in the end-turns. However, with AM, the end turns can be fully customised in order to allow for better cooling so that heat does not build up and lead to lower efficiency and potential insulation failure.

This type of modification was designed and printed using copper as seen in Figure 4-20. In this redesign of a winding, similar but shorter to the AlSi10Mg windings earlier in this chapter, the cross-sectional area was maintained in the end-turns, however, the dimensions for the end-turns were changed so that when the coil is compressed into the slot and the turns in the slot are touching, there would be a slight air-gap between the end-turns so that they can be cooled through forced convection. This allows the resistance of the coil to remain nearly the same while increasing the surface area for enhanced convective cooling.

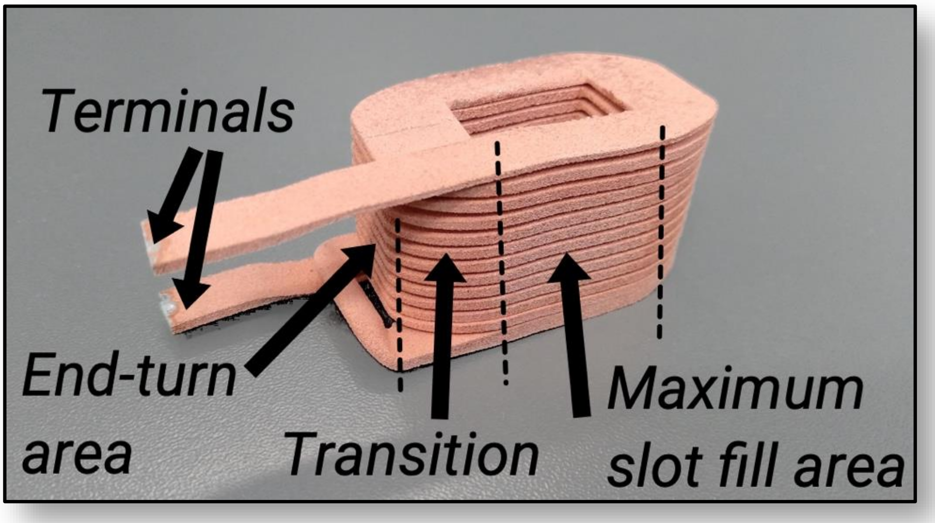

Figure 4-20: Example of a 3D printed copper coil with variable cross-section dimensions from the slot fill area to the end-turns in order to increase the end-turn surface area for improved cooling.

4.4.4 Decreased losses

In conventional machines, the top part of the slot near the air gap is a known area that contains high levels of flux leakage or flux that does not travel within the soft magnetic material. Due to this and the fact that it is difficult to wind and retain coils into this area, traditional machines typically do not fill this area with copper. However, AM could potentially change the resistance or geometry of the windings in those areas and reclaim unused space in the slot. Recent studies into power loss of windings at 400 Hz have been demonstrated by simulating different geometries, and then using AM to verify the results [111]. They found that by using AM, the power loss in the slot by the windings can be reduced by 75% for the layer of windings next to the air gap. They also calculated that using semi-square inside corners, like those seen in Figure 4-20, as opposed to traditional circular (Figure 4-19), can also reduce the power loss in the windings. While the AM winding they created only had 51% IACS (similar to the value found by this work and reported in Chapter 5.4), they calculated that with increased conductivity, the losses can be reduced by another 30%. By using AM to create windings, power densities can be increased by allowing more conductor material to be placed in the slot. In addition, AM can produce higher efficiencies due to lower losses in the windings, as demonstrated by that research, some of which is seen in Figure 4-21.

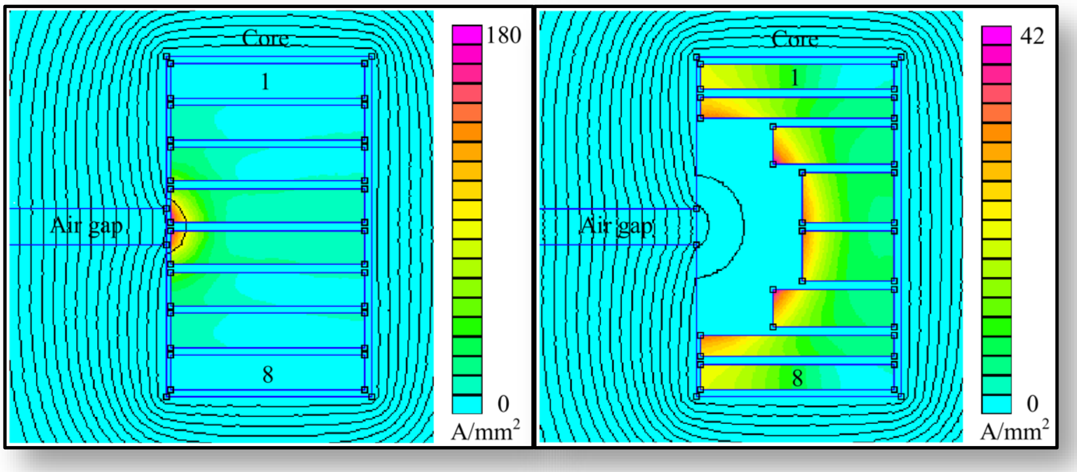

Figure 4-21: Examples of two geometries studied for high frequency applications with the corresponding current density distribution, a fixed width and height (left) and a variable width and height (right) [111].

4.4.5 Potential Insulation

While in this work, insulation was briefly investigated only with the aluminium windings in the form of anodisation (see Insulation techniques in the Appendix), there is little difficulty in insulating AM windings. For example, in previous research [111], they used Synthite AC-43 which is an air-drying polyester varnish to insulate the windings along with a rotary drip application method and post oven curing with rotation. The preparation of the coil prior to insulation as well as the finished part was seen previously in Figure 2-18. The method they used was the same process that is commonly used with coils that have been manufactured using traditional methods. These additional coatings are needed when materials other than pre-coated magnet wire are used such as bar stock or CNC machined windings. It can thus be seen that there are already a wide range of existing insulating materials and methods which can be used with AM windings.

Through improvements such as increased efficiency in high frequency applications, higher fill factor, and enhanced cooling through the end-turns, AM has the potential to be a part of current trends in the development of electric motors as discussed in Chapter 2.5. These include being an enabling technology in the manufacture and design of IE5 Ultra-Premium Efficiency electric motors [83]. Through increased reliability of the windings, they can be incorporated into applications that require added safety and robustness such as in electric vehicles. By increasing efficiency and power density, they can be included in weight sensitive applications, such as the more-electric and all-electric aircraft. AM can play a role in all these areas, as long as designers have the material properties with which they can design, and the design tools needed to exploit the freedom of design that AM provides for these applications. While further research is required to increase the conductivity of AM materials, to improve the surface finish of AM parts, and to lower the cost of parts made by AM, it has potential as a future manufacturing process for electric motor coils.

4.5 Summary

In this chapter, the design of electric motor coils using additive manufacturing was evaluated, modelled and created using the first principles of electric motors. These first principles indicated that AM could improve an electric motors efficiency by increasing the specific electrical loading by increasing the fill factor. Multiple coils were designed in order to explore variations of stacking loops within a winding and to evaluate the effect on resistance and overhanging area. The optimal coil was designed so that the loops of the winding were on top of each other, similar to a single-coil spring. The winding was designed to be built on its side in order to minimise the amount of support material needed, while also minimising the resistance of the winding. The ability to design the winding using custom shapes of variable size allowed the winding to maximise the use of the available area for the slot and hence increase its specific electrical loading.

The next step was to evaluate the type of motor into which a winding could be designed. Of all the different types of electric motors available, the motor which had the most potential for using AM windings, as well as to be entirely 3D printed in the future, was the switched reluctance motor. It typically has an open-slot geometry which allows easy assembly of a concentrated winding. A suitably sized switched reluctance motor was obtained and modelled in CAD. It was found that custom slot retainers could be designed in order to increase the total amount of slot area. Despite not being able to make use of the entire slot area due to assembly constraints, it was found that the fill factor could be maintained compared to the original area with similar clearances. This maximum fill factor was 93.5% compared to the original area and 91.3% for the newer larger slot area.

Two different windings were designed in order to maximise the fill-factor and to allow for assembly. One winding was in the shape of a ‘wedge’ and the other was in the shape of a ‘block’. These two windings were first printed in plastic to confirm the clearances and fit into the switched reluctance motor. The new redesigned slot retainer was also printed and fit into the existing grooves. The plastic windings were modified and reprinted to ensure a perfect fit before printing in AlSi10Mg. AlSi10Mg was chosen due to its ability to be printed to a high density and because the AM125 which was used for copper printing did not have a large enough build volume to manufacture the redesigned windings.

Despite the need to hand file the surfaces of the windings to remove the large attached particles, the windings were able to fit into the motor with very little effort. The windings were printed at the maximum fill-factor volume and no insulation was applied. However, these proof-of-concept windings were used to better evaluate the resistivity of AlSi10Mg. As a result, they show the potential that AM has to improve electric motor performance and efficiency. Previous researchers have demonstrated a fill factor that reached 78%, however this is as high as conventional methods can reach due to a breakdown of the existing insulation as it is compressed into the slot shape. AM does not suffer from this limitation and thus can push fill factors up to 90%. AM can also be used to redesign the end-turns so that they become better heat dissipating devices, reducing the losses in coils due to heat build-up.

This study explored how AM can redesign electric motor coils in order to maximise the fill-factor and incorporate additional features such as heat-dissipating end-turns. As such, it opens a new area of research into the use of AM as a new manufacturing technique for electric motor coils. It allows motor coil designs to make use of the freedom AM allows over traditional manufacturing methods and can pave the way for ultra-premium efficiency electric motors as well as light-weight motors that could be used in aerospace or the automotive industries. The next steps for this work are to validate these advantages through additional experimentation; unfortunately, these steps were not able to be undertaken due to this part of the work being completed at the end of the course of study. In the next chapter, pure copper will be explored as a material to be processed by LPBF and then tested for electrical resistivity. The challenges of printing pure copper will be discussed along with methods such as ML that can be used to aid in the parameter optimisation process.

Chapter 5 Processing of Pure Copper with LPBF

5.1 Introduction

While aluminium has an advantage in applications which are weight and cost sensitive, pure copper is more advantageous when the application is volume or heat sensitive. Due to its lower resistivity, pure copper will have lower losses for a given volume, meaning it will generate less waste heat compared to another material with the same volume. However, pure copper is difficult to process with LPBF, due to in part its high reflectivity and high thermal conductivity as discussed in Chapter 2.9. Because of these difficulties and the resulting lack of information on the resistivity of copper parts processed by LPBF, electric motor designers may be hindered from thinking of using AM for electric motors. This research helps fill this void of information of using copper in AM for electrical applications.

Despite the potential for high porosity, processing pure copper with AM can in turn enable printing of coils for electrical machines if the conductivity and strength are sufficiently high for such applications. Coils for electrical machines are traditionally hand-made and even today for small production runs of less than a few dozen motors, remain a limiting factor on the operation and rating of an electrical machine [60]. The ability to print coils would enable a step change in the design and manufacture of these components, where customised and/or modulated turns could be achieved. Another advantage would be the achievement of higher slot fill factors which would increase efficiency and power density. This could reduce the size and weight of electric motors, making them more suitable for aerospace and automotive applications [102].

Unlike AlSi10Mg, copper has not been as widely researched for LPBF, and thus, does not have a previously published optimised parameter set for any Renishaw LPBF equipment. This chapter explores the suitability of using an average powered (200 W) LPBF system with a small spot size to process copper to the maximum density achievable (which will be less than fully dense). Electrical testing using direct four-wire Kelvin measurements was undertaken with respect to initial build orientation. Post heat treatments were carried out to measure the effect on electrical resistivity. Finally, the use of ML was investigated to aid in the parameter optimisation and evaluation of test sets with copper and LPBF. These results are then discussed and summarised at the end of this chapter.

5.2 Parameter optimisation

5.2.1 Single scan tracks

For parameter optimisation, single scan tracks were investigated first. In determining the optimal laser scan speed, the range was set to the speeds previously reported in the literature as discussed in Chapter 2.9. Laser-scan speed with the Renishaw LPBF machines was defined as an exposure time and a point distance, and initially four point distances were investigated as seen in Figure 5-1.

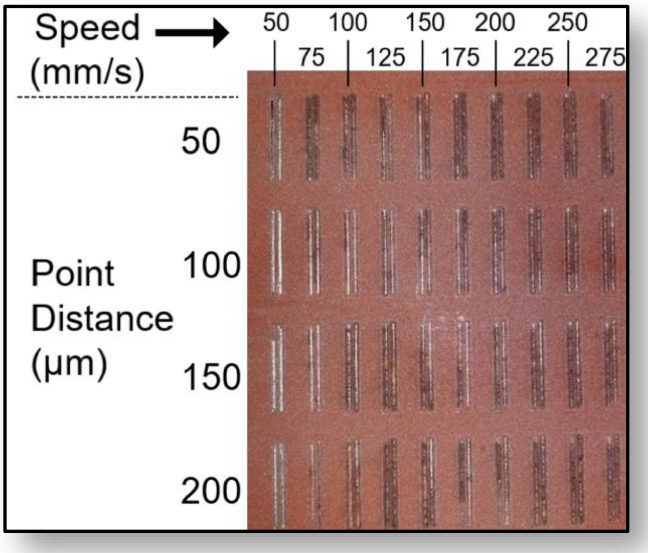

Figure 5-1: Single scan tracks on a thin plate showing the initial range of laser speeds.

Two 18 mm tracks were created per parameter set to average out variations in processing. Single scan tracks were created on a temporarily bonded (with ethyl 2-cyanoacrylate) thin steel plate that could be removed (by acetone and thin blades) and sectioned easily.

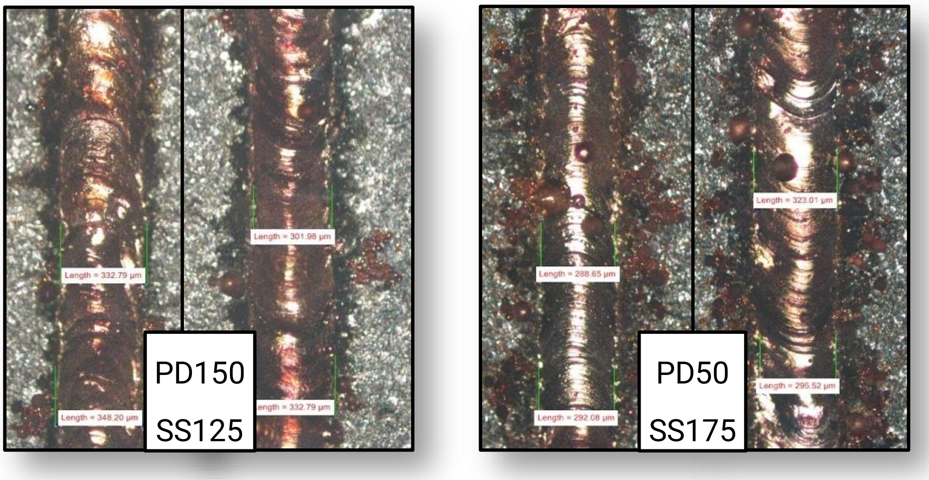

Figure 5-2: Example of single-track weld quality for different Point Distances (PD) and Scan Speeds (SS).

While initial observations showed good quality melt tracks (Figure 5-2), upon sectioning and EDX elemental analysis, it was seen that a considerable amount of iron had transported into the melt pool, as shown in Figure 5-3 (b). While this aided in bonding to the substrate which was also seen in [152], it altered the melt characteristics and did not provide accurate information on the parameters needed for processing pure copper parts. No cracks or pores were observed in the SEM micrographs of the cross-sectioned melt pools as shown in Figure 5-3 (a), proving that the laser power density was sufficient to melt copper. However, the highly elliptical shape of the melt pool indicated that even though the processing parameters were optimised, the laser melting process remained in the conduction melting regime. Higher laser power and slower scan speeds would cause an increase in energy density, thus, creating a deeper more stable melt pool through a transition towards keyhole melting [233].

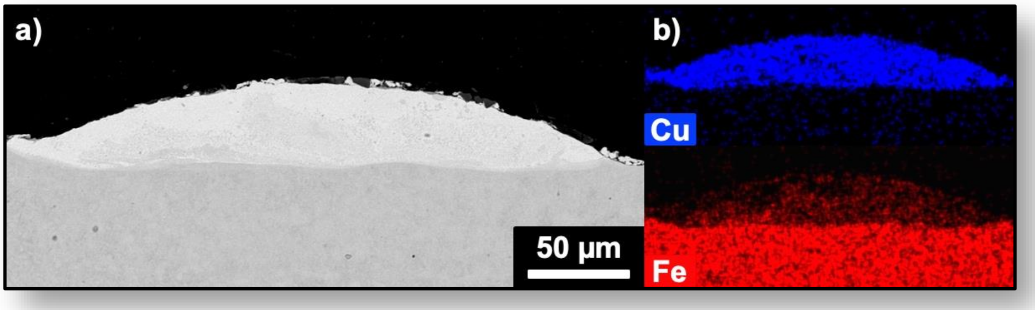

Figure 5-3: Cross-section of single scan track (a) along with EDX analysis for copper and iron content (b).

5.2.2 Thin Walls

After single tracks, thin walls were investigated as the next step of parameter optimisation. The same range of laser scan speeds and point distances were used to create thin walls which were 18 mm long, and 4 mm tall. Two walls were created per parameter set in order to compare the same processing parameters with the laser scanning in opposite directions. This test set was repeated for three different layer thicknesses, 30, 45, and 60 µm. As with the single tracks, there was a large amount of iron diffusion into the weld tracks at slower scan speeds. An extreme example can be seen in Figure 5-4. In this example of a thin wall processed at 50 mm/s, a large amount of iron had diffused into the melt pool for the first 1.5 mm. Once the copper concentration below the powder layer becomes high enough, the previously deposited layers with iron fail to re-melt and only pure copper was deposited. This transition from copper-iron to pure copper was characterised by a significant decrease in the wall thickness.

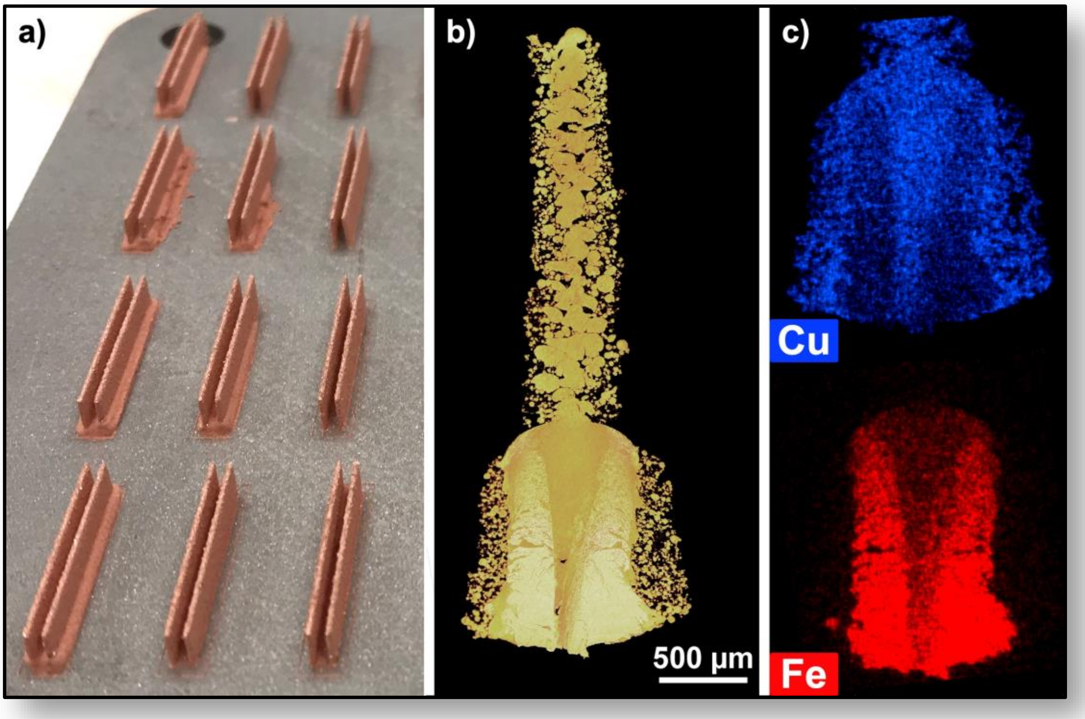

Figure 5-4: Thin walls in the first column on the left (a) were created at a high power and slow scan speeds, a sectioned view (b) and EDX analysis (c) reveal copper and iron content.

In order to optimise the processing parameters for thin walls, five tests were constructed as seen in Table 5-1. The best result for each test is also shown.

Thin Wall Parameter to Test	*Range*	*Best result*
1. *Layer thickness*	30, 45, 65 µm	45 µm
2. *Laser Beam Focus Position*	-10 mm to +10 mm	0 mm
3. *Multiple Scans*	Pre and post scans at 100, 150 and 200 W	None
4. *Laser Scanning Point Distance*	20 to 175 µm at speeds of 150, 175, 200 and 225 mm/s	50 µm
5. *Laser Scanning Speed*	200 to 1250 mm/s	300 mm/s

Table 5-1: Parameter optimisation results of thin wall tests.

In the first test, 30 µm layered thin walls resulted in some powder spreading issues, which caused the first row of thin walls to have a raised section nearest to the powder re-coater, with random portions of the thin wall missing. The 60 µm layered thin walls had much less consistent weld tracks with greater amounts of sintering rather than melting. The 45 µm layered walls showed no signs of powder spreading issues and had much better melting behaviour than the thicker layer. For all remaining tests, a 45 µm layer thickness was used.

The best parameter set from the previous test was chosen to study the effect of the laser beam focus position. Laser beam focus positions below -5 mm showed significant balling, and above 4 mm showed increased sintering without any improvements to track quality. Between -3 and 3 mm, the tracks showed similar quality with both continuity and width of sintered particles, so the focus position was kept at 0 for all remaining tests.

The third test investigated the use of multiple scans in order to improve the density by melting any particles that failed to form part of a continuous weld track, or to pre-sinter the material which was shown as a valid method to improve density in [183]. However, combinations of different laser powers and different orders of those laser powers failed to improve the continuity of the thin walls. Instead, multiple high-power passes only resulted in increased balling in the thin wall.

The fourth test was needed to determine the best laser scanning point distance. By comparing this test along with the previous tests, it was found that at many different speeds, a 50 µm point distance provided the most consistent thin wall and thus was used for the remaining tests.

The final test was expected to show that the highest laser scan speeds would not sufficiently melt the powder to form a thin wall, however, all parameters successfully resulted in thin walls. But the highest scan speeds did result in very thin walls with minimal bonding and low strength. After comparing the continuity of weld-tracks and thickness of the sintered particles, the best resulted from a laser scan speed of 300 mm/s.

5.2.3 Cubes

Cubes with an edge length of 5 mm were created using a power of 200 W and the parameters listed in Table 5-1, using the test conditions shown in Table 5-2. Hatch distances between 50 and 175 µm were investigated along with both single and multiple scan strategies which were seen previously in Figure 3-8. Cubes were created first with a stripes scan pattern testing the hatch distance range with respect to cross-sectioned optical density measurements. An example of a striped scan strategy with no rotation is shown in Figure 5-5, and an etched cross-section showing the grain boundaries of a test cube is shown in Figure 5-6. The average grain size as shown by the etched specimen in Figure 5-6 varies between 5 and 50 µm, with a mean of around 14 µm.

Cube Parameter to Test	*Range*	*Best result*
1. *Hatch Distance*	50 and 175 µm	100 µm
2. *Scan Strategies*	Shown in Figure 3-8	Rotation
3. *Rotation of scans*	0, 67, 90°	90°

Table 5-2: Parameter optimisation results of cube fabrication tests.

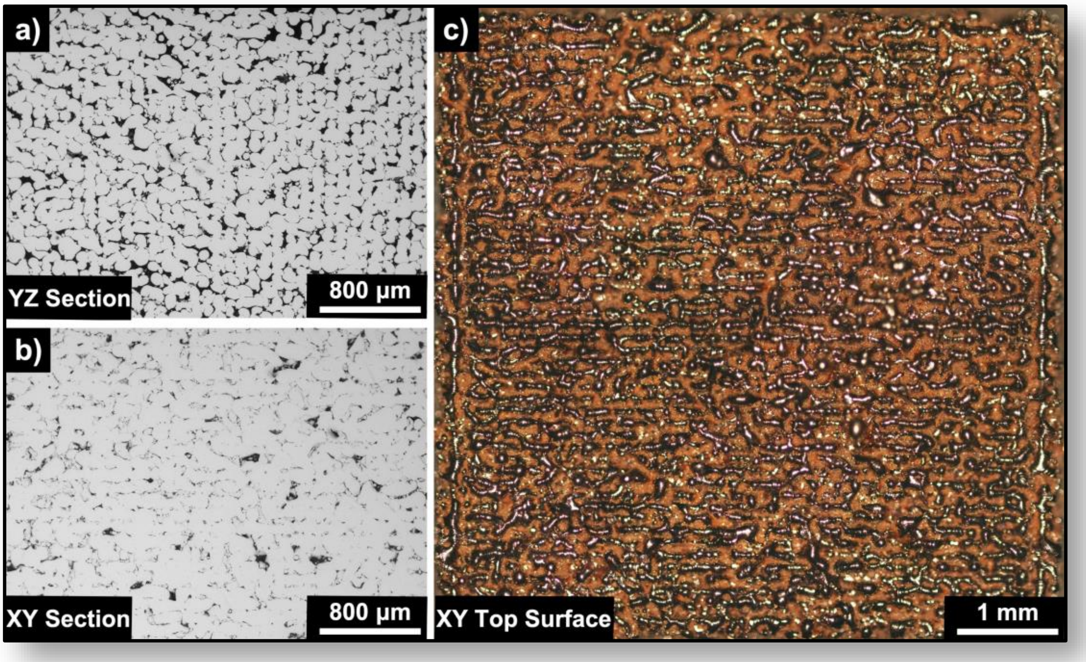

Figure 5-5: Cross-section of a cube processed with a stripes scan pattern with hatch distance of 100 µm, showing side plane (a), top plane (b) and an optical image of the top as-built surface (c).

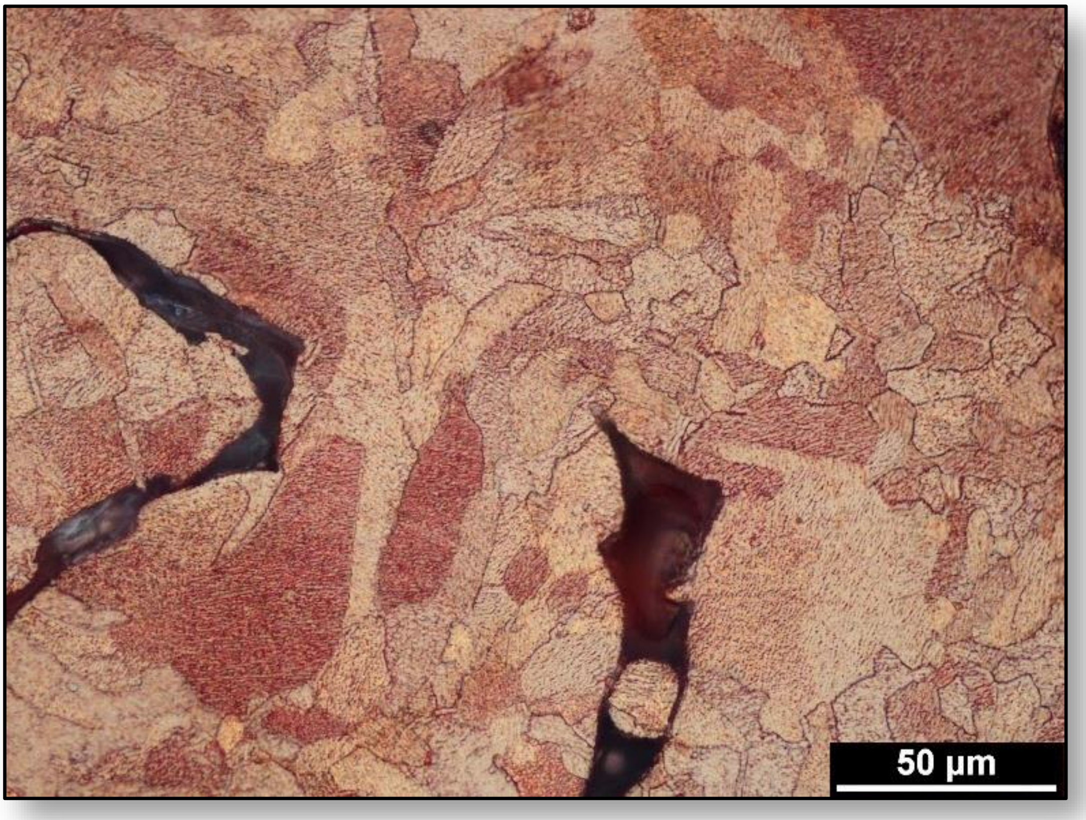

Figure 5-6: Etched cross-section of XY plane highlighting grain structure of LPBF processed pure copper.

After analysing cubes manufactured by the single scan strategies (stripes, islands, rotation, and nested), it was found that there were areas of loosely sintered powder within and between scan tracks. In an attempt to melt and fuse these areas, multiple scans were applied within a single layer (pre-sinter with lower laser powers, re-melt by repeating the scan, multiple scans, and an offset scan between tracks). Despite the wide range of tested scan strategies, little change was seen in the corresponding densities. It was found that the multiple scan strategies, whether the second was either directly on top of the previous scan, or offset by half the hatch distance, resulted in 5-15% lower densities than the highest from the single scan strategies. This could be due to a differential in absorptivity between powder and consolidated powder. The highest densities were found with a hatch distance of 100 μm with several of the scan strategies. Rotation of the scan pattern by either 67° or 90° resulted in higher densities compared with non-rotated tests. All single scan patterns resulted in densities that were within 5% of each other. After comparing all scan strategies, the final selected set of parameters used a 100 μm hatch distance with a 90° rotation each layer.

5.3 Density

Relative densities were initially measured by a single cross-section optical density measurement using thresholding limits. The region of interest for the optical measurements was a square inset from the outside edge by 0.1 mm (approximately half of the track width). The highest density using the best scan parameters as measured by optical measurements was 85.8% (± 0.91%). The range of densities for all the different single scan patterns were between 80.3-85.3%, with an average density for all single scan patterns being 83.0%. While an optical single cross-section does not necessarily represent the entire sample, it does provide a good measurement for the corresponding slice from the whole. In order to measure the bulk relative density, a helium pycnometer was also used.

Density measurements using the helium pycnometer were obtained using larger cubes printed in both 90-degree alternating layer scan directions, as well as 67-degrees, as these two patterns were nearly identical in optical densities. Due to the open pores of the test cubes, the resulting densities were approximately 98-99% the density of pure copper. The measured pycnometer volume was then compared to a caliper-measured external volume for a relative density measurement. The average for the 67-degree rotated cubes was 83.5% (± 0.96%) and for the 90-degree cubes was 84.2% (± 1.53%).

5.4 Resistivity

The test bars used for resistivity testing were additively manufactured using the cube parameters which resulted in the highest density. This parameter set was a scan strategy of stripes, rotated 90-degrees each layer, and included 3 mm high supports in order to avoid iron contamination. They were printed using the test cases laid out in Chapter 3.5.1. The resistivity was measured using a DC four-wire Kelvin resistance measurement meter, which directly measured the specimen's resistance. By individually measuring the dimensions of the specimen after heat treatment and a light file of the surface, the material resistivity was determined. The average standard deviation for the length of each specimen was 0.02 mm or 0.06% of the length and was 0.01 mm for width and height resulting in an average variance in cross-sectional area of 1.1%. The results of the resistivity measurements can be seen in Figure 5-7 along with the corresponding calculated standard deviations.

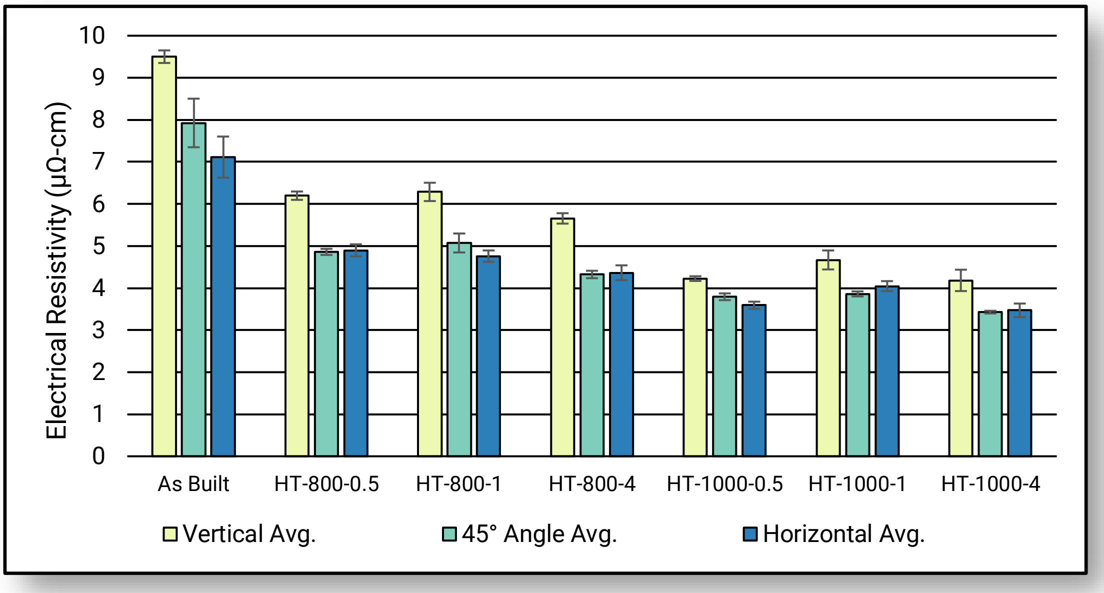

Figure 5-7: Averaged electrical resistivity under tested conditions of as-built, heat treatments at either 800 or 1000 °C with dwell times of 0.5 hours, 1 hour, and 4 hours with calculated standard deviations.

While the average resistivity of the as-built condition specimens was 8.18 µΩ-cm, with heat treatment, the resistivity dropped to the lowest average of 3.69 µΩ-cm for the 1000 °C heat treatment for four hours. The lowest average resistivity for a single build orientation for the 45-degree orientation heat-treated at 1000 °C for 4 hours was 3.43 µΩ-cm which equates to 50.3% IACS. Out of each group of heat treatments, the vertical orientation had on average 24% higher resistivity than the average of the other two orientations.

5.5 Using Machine Learning to assess quality

After running segmented images through the CAE as described in Chapter 3.8 and applying the clustering algorithm, clusters had populations of between 59 and 5168 images, with sixteen clusters having a population under 1000, and nine having more than 2500 images. Each cluster contained an average of 87 unique parameter sets within the cluster. As the images still retained the original parameter set which created it, the scores for the clusters were then applied to the entire scan track, giving a total score for the set of parameters which went into the creation of the tracks. Based on the scores, results were compared with observations from the traditional parameter optimisation process discussed earlier.

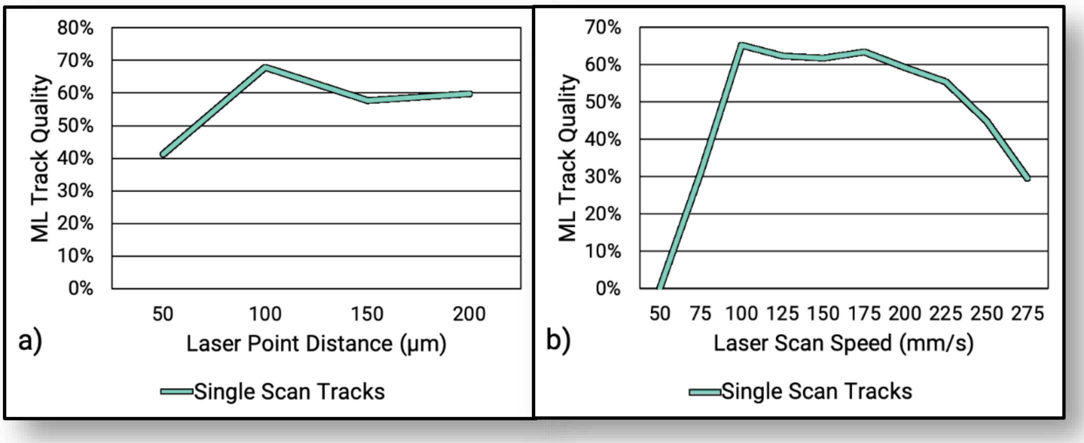

Figure 5-8: Single scan track ML quality verses laser point distance (a), and laser scan speed (b).

The first insight from analysis of the results of the ML exercise is in the quality of single scan tracks compared to thin walls. The average score for single tracks was 68%, compared to 3% for thin walls. This agrees with the results found from the microscopic study discussed previously, which demonstrated that for the single tracks, iron transported into the melt pool and created perfect looking weld tracks. These iron-infused weld tracks were well defined and showed very little signs of balling. In comparing the laser point distance for single tracks in Figure 5-8 (a), there was not much score variation, with 50 µm being the lowest despite it being chosen as the best point distance. In comparing laser scan speeds in Figure 5-8 (b), however, speeds below 100 mm/s scored poorly as those tracks had excess laser power and lacked any copper tracks due to keyhole welding of the iron causing the copper powder to be blown away from the scan track.

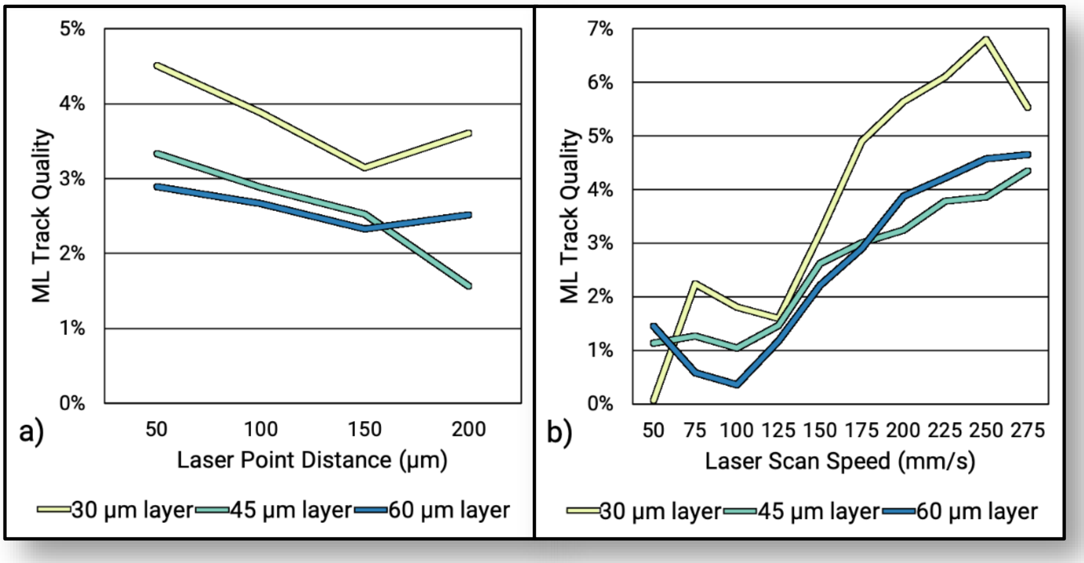

Figure 5-9: Thin wall ML track quality verses laser point distance (a), and scan speed (b) at different layer thicknesses.

The machine learned scores for different layer thicknesses with regards to the laser scan speed and point distance showed similar trends to the traditional parameter optimisation process. In Figure 5-9 (a), the scores show that for all layer thicknesses, a 50 µm point distance and laser scan speeds of 250 mm/s and above created the best tracks. In Figure 5-9 (b), it confirmed that if there were no powder spreading issues associated with the 30 µm layer, it would have produced better looking and higher quality tracks verses the 45 µm layer.

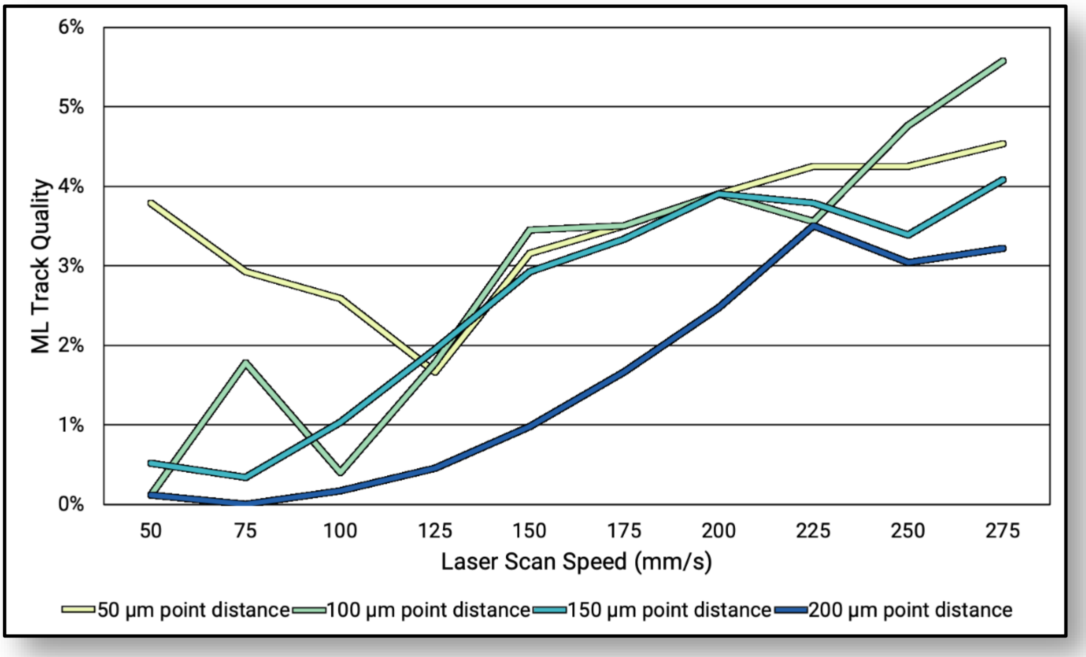

Figure 5-10: ML track quality for different laser scan speeds and at different laser point distances.

In the traditional parameter optimisation process, once the 45 µm layer thickness was chosen, additional thin walls were created in order to determine the best laser scan speed and laser point distance, as it was not as clear from the visual examination of the tracks that 50 µm was the best point distance. Again, as seen in Figure 5-10, the ML score results showed that 50 µm was still the best laser point distance with speeds of 275 mm/s (or greater) which resulted in the best quality tracks. However, in examining the ML results which explored point distances from 20 to 175 µm at speeds of 150 to 225 mm/s, there was no discernable difference in ML track quality scores, as all quality scores fell between 3-6% with no visible trend for either point distance or laser scan speed. This differed from visual examination which indicated that 50 µm was the best laser point distance.

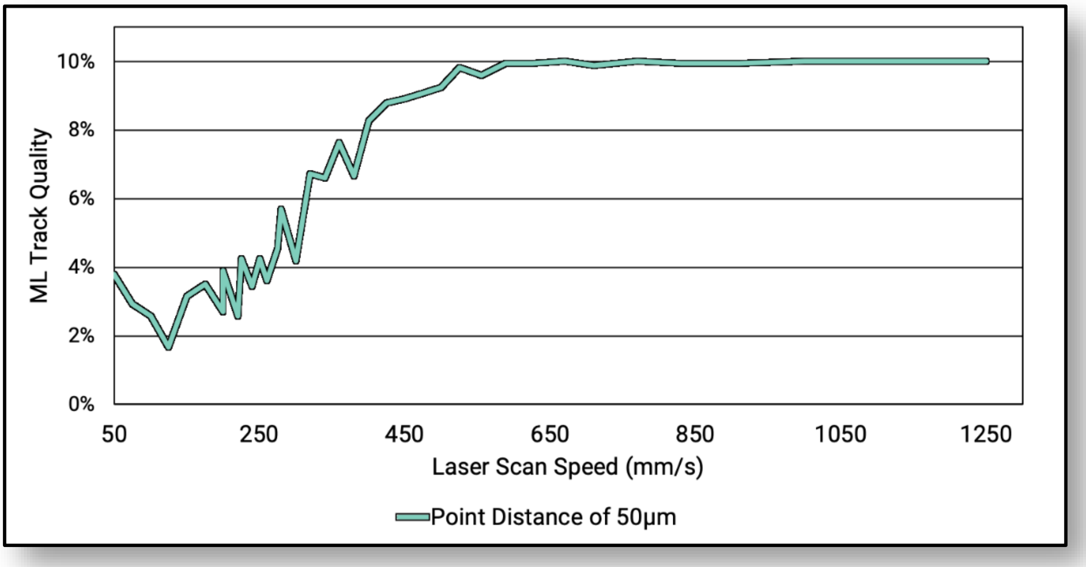

Figure 5-11: ML track quality for different laser scan speeds with the same 50 µm point distance.

In order to determine the best speed, the next test for parameter optimization was to increase the range of laser scan speeds up to 1250 mm/s, with ML scores seen in Figure 5-11. These high speeds were intended to go beyond the point that a track would no longer form, however, all speeds resulted in the creation of a track, although with the highest speeds creating very thin and weak walls. In terms of laser scan speed, the results from ML differed from the traditional parameter optimisation, the latter indicating that speeds of 300 mm/s resulted in the best quality, whereas ML indicated that speeds above 500 mm/s resulted in tracks of the highest quality. This was wrongly implied due to the scoring assignment used. There were many clusters which were given scores of 10 due to having some fine thin weld tracks, which were desirable, along with examples of discontinuous tracks within the cluster. As high speeds tended to result in consistent looking thin walls, they happened to also correspond to one of the resulting clusters which was scored as a 10. That was why speeds above 500 mm/s plateaued at 10%. This is however a reflection of the subjective scoring which was applied to the clusters. Much more data which includes high quality weld tracks needs to be included in order to remove this apparent subjectivity and to allow more validated results.

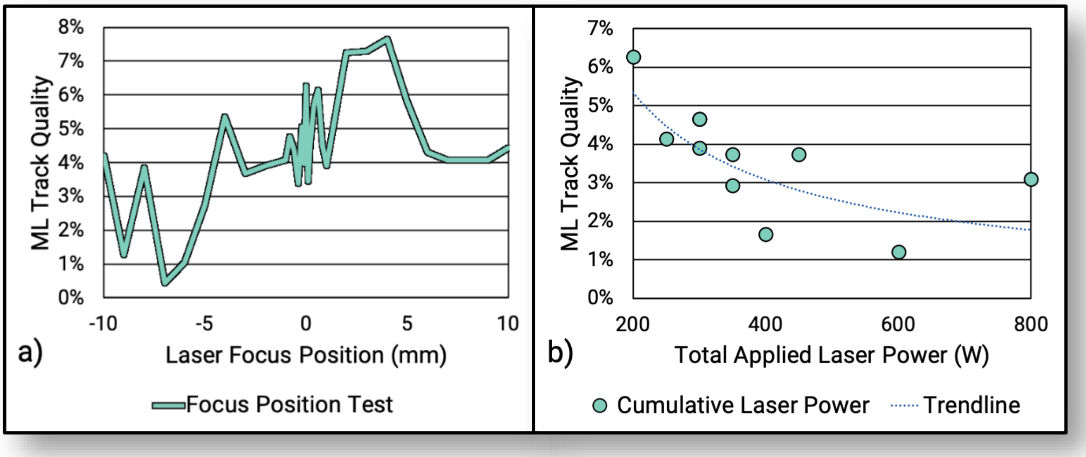

Figure 5-12: Track quality for laser focus tests (a) and total wattage applied for multiple laser passes (b).

In Figure 5-12 (a), the laser focus position test scores showed that the zero-position was just over 6%, with only the positions of two to four being higher at just over 7%. This closely matched the actual results which found that the positions between -3 to 3 were similar in quality. But this result could indicate that perhaps more tests should be performed to confirm if those higher scores are reliable. In Figure 5-12 (b), the scores were graphed against the total wattage applied by multiple passes of the laser. For example, the point above 200 was a single pass at 200 W, whereas 600 was generated by three passes at 200 W. These scores match the optimisation results as all multiple passes were found to be lower quality with high amounts of balling.

5.6 Discussion

The electrical resistance of a solid pure metal is derived from the number of disruptions found in the periodic atomic lattice structure [19]. In alloys, this disruption comes from elements that are not the main element of the alloy. However, in pure elements, this disruption comes from imperfections in the crystal lattice. These imperfections are either grain boundaries (seen in Figure 5-6), vacancies or voids in the lattice, and dislocations in the lattice structure. Larger grains result in lower resistivity due to the lower number of grain boundaries compared to small grain structures. But in the case where the material is not solid but porous, this porosity has the greatest influence on the resistance of the material.

Comparing the results in this study to EBM, it can be seen that the LPBF of copper does not create the same columnar grain structures due to a lack of fusion as seen in Figure 5-6. However, for fully dense high purity copper processed by EBM, the grain boundaries would dominate the resistivity. But due to the use of non-direct eddy-current measurement devices, no anisotropicity was reported in the results in any of the EBM copper studies as eddy-current measurement devices assume isotropic resistivity [19]. This is likely not the true case with EBM due to the columnar grain structure seen in [132], [136], [142] which is similar to the elongated grain structure and segmented texture of LPBF AlSi10Mg seen in [1] which did exhibit anisotropic resistivity. Thus, for copper LPBF in this study, porosity dominated the resistivity and not grain structure.

In additively manufactured materials, this porosity with respect to resistivity has been studied for a custom aluminium-magnesium alloy and shown to be linear [234]. This linear relationship has also been shown with porous metals manufactured with powder metallurgy methods [117], where the resistivity for copper with a porosity of 15% is approximately 2.5 µΩ-cm or 68.9% IACS. This is better than the best values for samples found in this study, as seen in Figure 5-7, which is perhaps due to the lack of having a powder compaction pressure in LPBF which is typically used in powder metallurgy methods. Despite having a similar density, this difference could be due to a lack of connection between particles and weld tracks as an investigation into the interior of the LPBF parts verses powder metallurgy parts could reveal this. This difference could also be due to the oxygen content of the powder which was used in this study. This oxygen contamination can be removed through high temperature heat treatments in a hydrogen atmosphere. This was done in conjunction with increasing density through a hot isostatic pressing (HIP) process. The HIP process has been used with additively manufactured copper created using binder jetting [121] where HIP was used after an initial de-binder heat treatment at 450 °C followed by a three-hour dwell at 1075 °C in a hydrogen atmosphere to promote sintering while also removing oxygen contamination. This HIP and heat treatment process achieved a density of 97.32% (which was aided by a bi-modal powder size distribution), but unfortunately, no resistivity measurements were reported. Heat treatment without HIP have resulted in densities of between 85.5 and 92%, but densities above 92% are needed for HIP because HIP cannot close any surface-connected porosity.

The resistivity of highly porous copper can be decreased with further heat treatments at increased temperatures, or through a hot isostatic pressing (HIP) process. The HIP process has been used with additively manufactured copper created using binder jetting [121] where HIP was used after an initial de-binder heat treatment at 450 °C followed by a three-hour dwell at 1075 °C in a hydrogen atmosphere. This HIP and heat treatment process achieved a density of 97.32% (which was aided by a bi-modal powder size distribution), but unfortunately, no resistivity measurements were reported. Heat treatment without HIP have resulted in densities of between 85.5 and 92%, but densities above 92% are needed for HIP because HIP cannot close any surface-connected porosity.

In all tested conditions, the specimens built in a horizontal orientation had the lowest value of electrical resistivity in comparison to the other two orientations, resulting in an anisotropic resistivity. This is reasoned by the cross-section of the top plane (XY) in Figure 5-5 (b) which shows more continuous tracks and fewer discontinuities than in the side plane (YZ) seen in Figure 5-5 (a). The weld tracks in-plane can be thought of as poorly connected wires travelling horizontally. The highest resistivities were found in the vertically built specimens regardless of the applied heat treatments. This is due to an accumulation of partially melted tracks in the build direction (z-axis), in addition to the interlayer and intralayer defects such as incomplete fusion holes and pores due to the unstable melt pool [235]. These accumulations can be thought of as layers of poorly connected thin sheets, which have a higher resistance than the in-plane poorly connected wires. These defects and lack of interlayer fusion reduced the amount of connected material in the direction of current flow in electrical testing which resulted in a higher electrical resistivity for the vertically built specimens.

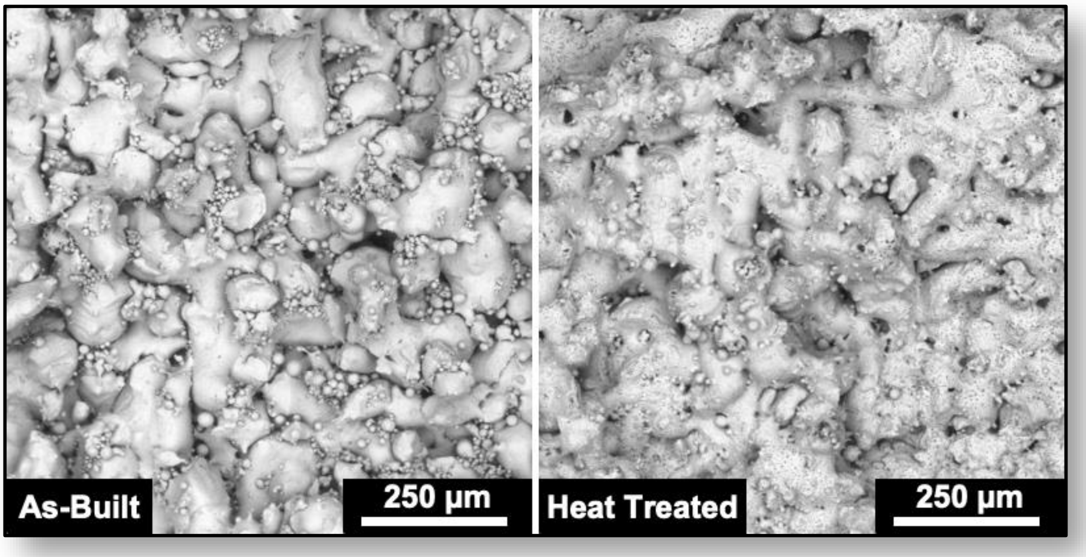

Figure 5-13: Comparison of a fractured section of as-built Cu vertical test bar (left) and heat treated at 1000 ℃ for 4 hours vertical test bar (right).

In comparing the as-built condition to the most intense heat treatment, the vertical specimen was fractured and analysed using SEM as seen in Figure 5-13, with the as-built samples on the left and the sample heat treated at 1000 °C for 4 hours on the right. As seen, in the as-built condition there are many un-melted powder particles in between the laser weld tracks. There are also noticeable defined edges between tracks. Comparing this to the heat-treated case, while there are still some attached powder particles, they appear to not be loose between the tracks but rather fused to them. The number of smaller un-melted powder particles was also reduced after the heat treatment, to indicate sintering or partial melting. The weld tracks also appear to be fused together and do not show the same defined edges between them.

This heat treatment effectively sintered the as-built components and caused necking to occur for both the un-melted powders and for tracks that were adjacent to each other. This necking can be seen below in Figure 5-14 where several fracture surfaces are identified. This necking and partial sintering decreased the number of discontinuities and gaps in the copper, minimizing the effective path length electricity must travel, and thus reducing the resistivity of the specimen. Signs of oxidation (as indicated by EDX) were seen as small spots in some areas of specimens but were not measured as the goal of this study was to find the trends of electrical properties with respect to orientation and heat treatment with this class of machine. Further studies with machines better suited to process copper to a higher density should have an oxygen threshold lower than the 500 ppm used in this study (which was a set standard operating condition) in order to maximise conductivity.

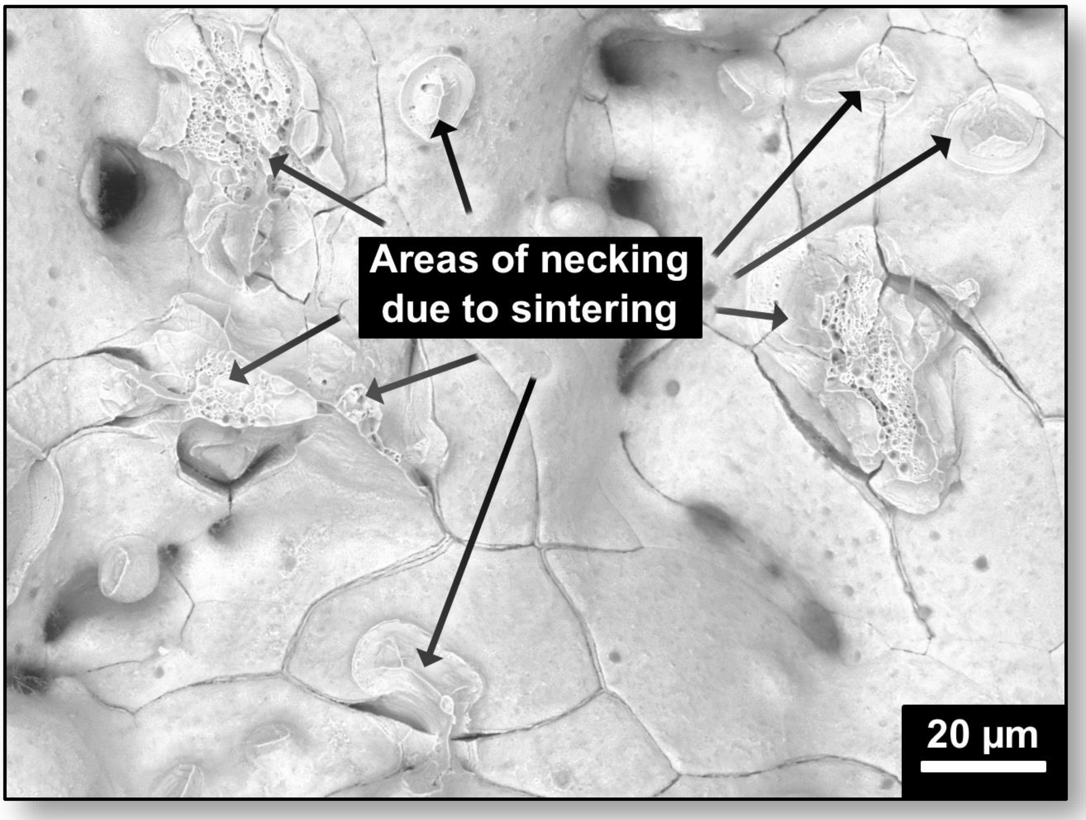

Figure 5-14: Areas on the fracture surface where localised necking of particles and weld tracks occurred but were broken off.

In order to minimise contact resistance in comparison to the actual material resistance, the ends of the test bars were soldered to the electrical tabs used for testing. However, this soldering could cause some of the variations seen in the measured resistivity values, as due to having a liquid phase metal on a porous surface, some wicking of solder into the ends of the test bars did occur. While this can help reduce porosity, the resistivity of solder is much higher than copper at 15 µΩ-cm, being composed of 50% tin and 50% lead. Additionally, some variations in resistivity can be attributed to small differences in porosity (2-4%) between specimens due to the unstable build process. This was confirmed by using EDX on a sectioned specimen as seen in Figure 5-15. Multiple specimens were sectioned to investigate this effect and it was observed that the solder wicked an average of 0.6 mm into the test surface. If the solder filled all the voids in this section, it would have a resistance of 3.8 µΩ which corresponds to between 0.9-1.95% of the resistance of the specimens.

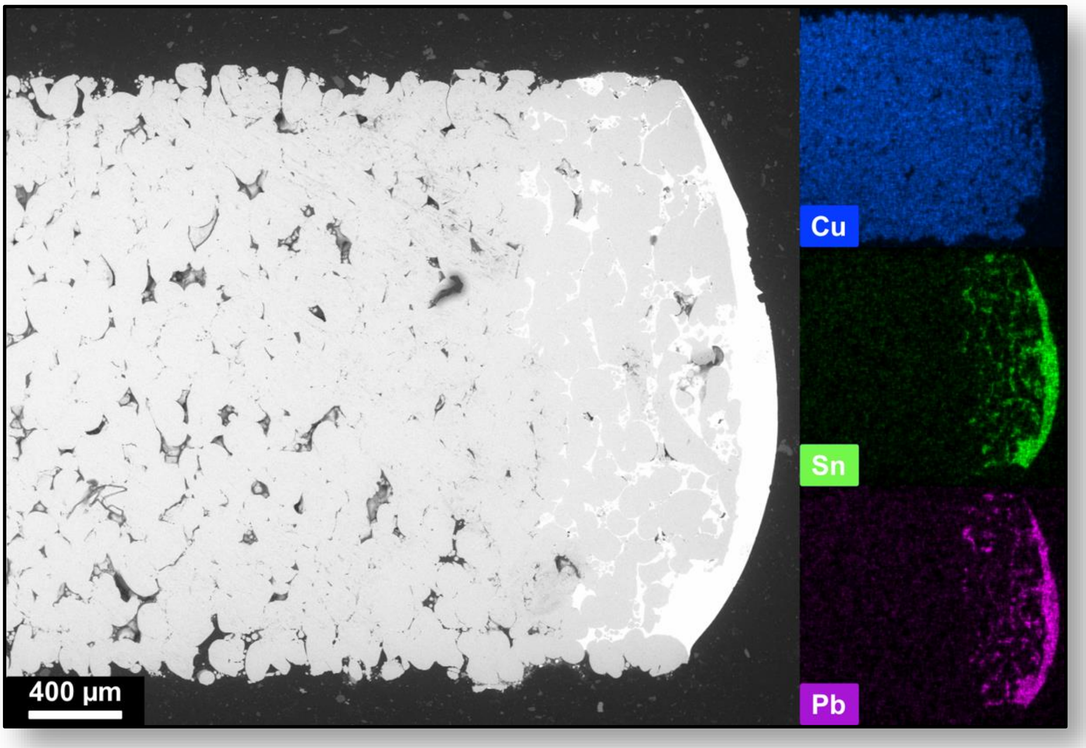

Figure 5-15: Sectioned SEM image of the soldered end of a copper test bar (top), along with EDX elemental analysis (bottom) showing copper, tin and lead.

Based on the results from this study, the resistivity of pure copper can be compared to the resistivity of other materials processed by LPBF. Despite having relatively high porosity, pure copper proves to be the best material choice in comparison to other metals and alloys processed with a 200W LPBF machine, in terms of conductivity. The best value from the bar specimens achieved was 50.3% IACS. This was better than AlSi10Mg at 30.4% IACS [1] and copper-tin alloys at 43.2% [166]. Only the copper alloy GRCOP-84 was potentially higher as the value for extruded bar stock was 70.7%, however, this does not necessarily represent the resistivity when processed by LPBF as those values have not been published to date.

The results represented in this chapter continue to confirm that using a medium powered near-infrared LPBF machine, even with a small laser spot size, cannot provide the energy needed to fully re-melt previous layers of copper. While it can melt the top layer of powder, it cannot completely fuse this newly melted powder to the solid layer below. This could be due to the fact that the copper powder absorbs more of the incoming thermal energy from the laser compared to the solid layer [133], [236]. The powder also retains more heat as it's unable to conduct this heat efficiently away to other powder particles, whereas the solid layers can conduct the heat away into the surrounding solid parts. By reducing the thermal gradient between the melt pool and the previously deposited layers, medium powered LPBF machines could potentially process copper more efficiently as has been seen with aluminium alloys [30]. This reduction in the temperature gradient requires a higher baseplate temperature, but most researchers already use the highest temperature allowed on the equipment. However, new LPBF machines are being developed which increase the baseplate temperature (up to 500 °C in [155]) above what has been available in the past.

In relation to ML and parameter optimisation, overall, the results of the clustering and subsequent scoring reflected many of the observations which were found in the traditional parameter optimisation process, and did match the trends for deciding the optimal laser point distance, powder layer thickness, and laser scanning speed. While disparities exist between ML and traditional optimization process, such as the convergence of scores at higher speeds, generally the trends followed the same results. As the only data used for this was gathered from a single parameter optimisation study for a single material, which couldn't be processed to a high density, there is a lot of room for improvement to create a more robust algorithm. However, it shows much potential and is only currently limited by a lack of data. As this is an emerging field, there is a lack of comparable sources to contrast this work with. It also includes some subjective analysis in terms of quality which needs further validation. Thus, by incorporating additional parameter optimisation studies with additional materials, the process could be made more accurate without the same subjectivity. There is also a potential to then apply labels to the clusters of data, so that the process could become more automated as the algorithm would be able to assess the quality of an image on-the-fly. This latter ability could then potentially be further developed to enable in-process parameter control and optimisation.

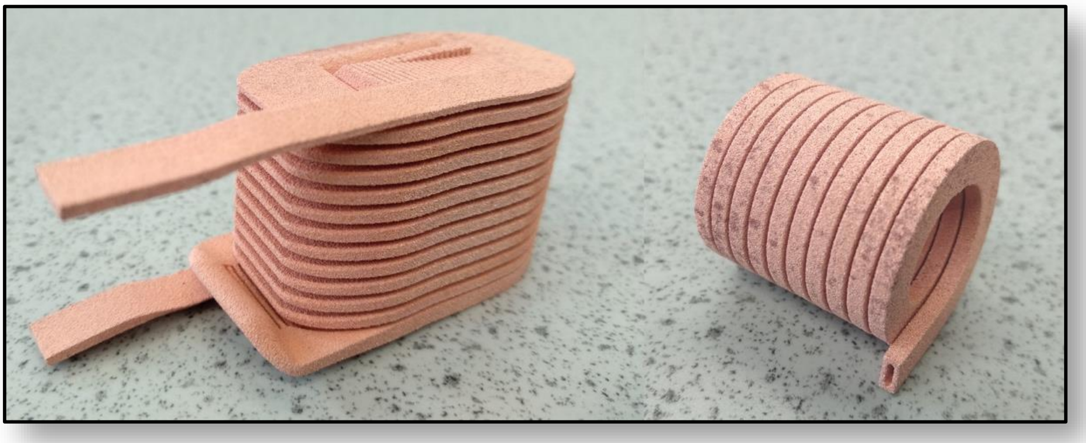

Figure 5-16: Examples of AM copper coils created by LPBF with a variable cross-section (left) and a hollow core (right).

Despite the lack of thermal energy and high porosity, in order to further refine the electrical resistivity of pure copper processed by LPBF and to investigate some design elements, some demonstration electrical coils were created as seen in Figure 5-16. They were manufactured in the same build as the previous samples using the same processing parameters as the resistivity test bars and were subjected to a heat treatment at 1000 °C for half an hour. The lack of insulation material in the samples was made up for by the controlled air-gaps between turns, which was another perceived advantage of printing coils and was one of the design elements investigated in Chapter 4. Resistance measurements were taken and were correlated using the CAD wire lengths of 1267 mm and 650 mm respectively and as-built cross-sectional geometries. Due to the variation between CAD values and the actual external sintered dimensions of the coils, the exact cross-sectional geometry for calculating resistivity was more difficult to estimate. Based on an average of these values for these two coils, the resistivity was determined as 54% IACS which represents the highest conductivity for this study. As has been widely reported elsewhere, the design freedom of AM allows for structures that cannot be created using traditional methods. In the case of Cu coils, these include varying the cross-sectional shape of a coil while maintaining the cross-sectional area in order to improve the cooling ability of end turn windings or to control local resistances within a coil, as seen in the left of Figure 5-16. Hollow shapes can also be made for applications which require additional cooling by running either air or a cooling liquid through the centre of the cross-section, as long as the resulting parts are non-porous, as seen in the right of Figure 5-16. These design elements and this design freedom, along with the ability to print low resistivity materials, can greatly aid in the development of new electromechanical applications.

5.7 Summary

In this chapter, pure copper was additively manufactured by Laser Powder Bed Fusion in a printer using a medium powered 200W laser powder bed fusion machine with a small laser spot diameter of 35 µm. The parameter optimisation process used single scan tracks and thin walls to narrow down the variables which would result in a high-density part. The process continued through the building of cubes and used density as a measure to compare results. Multiple scan patterns and strategies were used to increase the relative density. However, due to the high thermal conductivity and high reflectivity of copper, a maximum density of 85% was obtained. Despite the amount of high porosity, specimens could still be manufactured and thus several specimens were created in order to test the electrical resistivity.

The resistivity of test specimens that were built from the pure copper using AM were then measured. These test specimens were built in either a vertical, horizontal, or 45° orientation. They were then either left in an as-built condition or were subjected to a heat treatment at either 800 or 1000 °C for either 30 minutes, 1 hour or 4 hours. It was found that both orientation and heat treatment did, in fact, affect resistivity.

As-built specimens showed evidence of having relatively good bonding and connection of melted material within a layer, however, interlayer bonding was poor. This was due partly to solid copper having a higher thermal conductivity when compared to copper powder, and that copper powder having a higher absorption of the infrared laser energy than solid copper. This resulted in the copper powder being melted easier than solid, thus preventing the newly melted copper to be bonded to the previous layers. Electricity was able to pass easier within a layer than through layers leading to higher resistivity for vertical built specimens compared to horizontal specimens. Heat treatments at higher temperatures and for longer durations caused these previously poorly connected areas to be sintered together, increasing electrical conductivity and reducing resistivity.

ML was used in an attempt to see if it could aid in the parameter optimisation process. Parameter optimisation is currently a manual process which relies on human judgement to determine whether one set of parameters is better than another. But by using ML, an alternative method to determine this optimal set can be derived. Data in the form of optical images was collected over the course of the traditional parameter optimisation. These large images were segmented and fed into a convolutional autoencoder and then clustered in order to find the clusters which best represented a high-quality result. The clusters were manually scored according to quality and the results were applied to the original sets of parameters. It was found that this machine learned clustering and subsequent scoring reflected many of the observations which were found in the traditional parameter optimisation process, and did match the trends for deciding the optimal laser point distance, powder layer thickness, and laser scanning speed. While it is not a perfect predictor, with more data this approach could be made more robust and automated.

This was the first study to directly measure the electrical resistivity of pure copper processed on a higher than average laser power density LPBF machine and correlate the effect of AM build orientation to post heat treatments. It has proven that despite relatively high porosity, the resulting resistivity is lower than other currently available metals and alloys produced by LPBF such as AlSi10Mg which will be shown in the next chapter. ML opens up an opportunity to automate some steps of parameter optimisation to find new alloys which can be processed to a higher density and high conductivity. In the next chapter, AlSi10Mg will be tested for electrical resistivity, and the results will be discussed along with observations between resistivity and microstructure. While it does not have the same potential for low resistivity as a pure element, it will be able to be processed to a higher relative density and will not have the same processing issues seen with pure copper. The suitability for AlSi10Mg to be used for electrical applications will be discussed along with the challenges of dimensional accuracy and surface finish.

Chapter 6 Processing of LPBF AlSi10Mg

6.1 Introduction

Before electric motor designs can fully benefit from the design freedom that AM provides, the material properties of AM parts must be determined. To date, those who have attempted to investigate the electrical properties of AlSi10Mg have assumed that the material properties are isotropic like those of cast material [179], [180]. However, researching other materials indicate this is unlikely to be the case [237]. This chapter directly answers this question for the electrical properties of AlSi10Mg. In addition, the effects of build direction and post-build heat treatments are investigated.

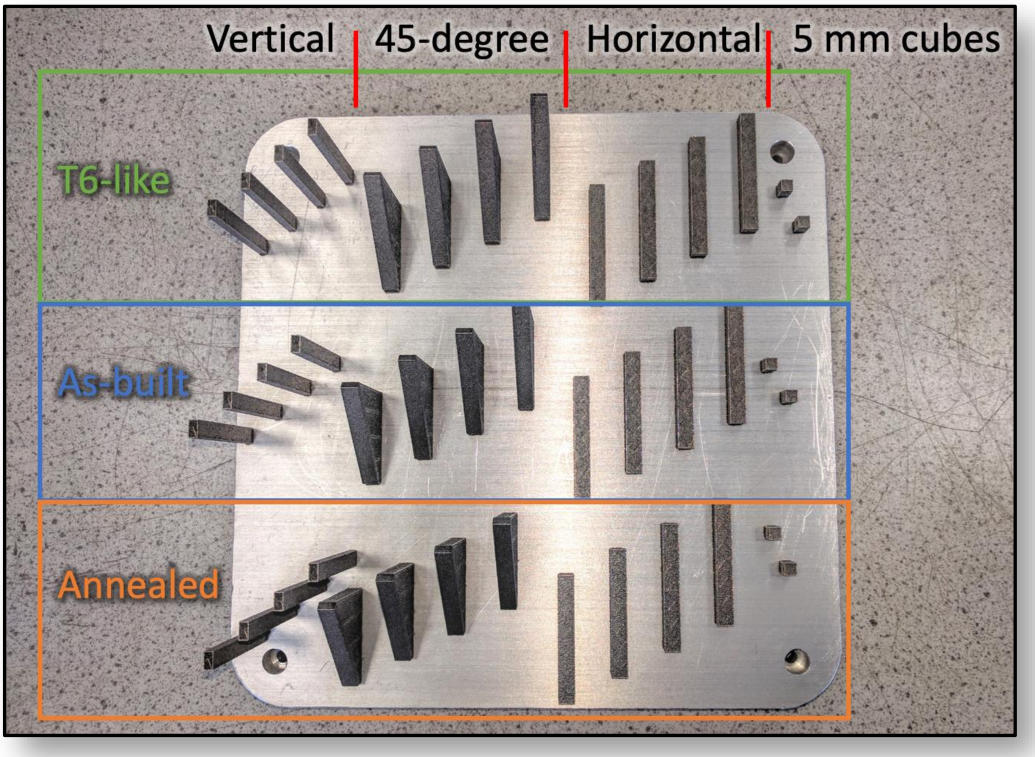

Figure 6-1: Electrical test specimens and cubes manufactured by LPBF out of AlSi10Mg.

In order to determine the resistivity of AlSi10Mg, test specimens were created which were 50 mm long, with a 6.5 mm x 3.5 mm cross section according to Chapter 3.5.2 and seen in Figure 6-1. These specimens were designed so that the resistance of each would be approximately 100 μΩ based on the best literature values for AlSi10Mg cast alloys. Four specimens of each test condition were created to average out any manufacturing differences and measurement errors. These conditions include as-built orientations of vertical, 45°, and horizontal, as well as a typical annealing heat treatment used as a stress relief [214], as well as a T6-like heat treatment [186] commonly used to increase mechanical properties. This resulted in thirty-six specimens being produced and tested. In addition, 5 mm test cubes were created to analyse microstructure, density and hardness.

This chapter reports several properties such as the microstructure, density, and elemental composition of the test cubes. It also reports the hardness measurements which were taken to compare the effects of the various heat treatments to the published literature. Following this, the results from the electrical measurements are analysed, with resistivity values being reported for each of the test cases. A study on the geometrical accuracy of the LPBF process with this alloy is also reported as it was conducted along with preliminary experiments for creating an insulating layer. These results are then discussed and summarised at the end of the chapter.

6.2 Microstructure and density

Density measurements were taken for all heat treatment states to establish a baseline between specimens and to examine if a low or highly variable porosity could contribute to possible variations in resistivity. To establish relative density measurements, the polished 5 mm test cubes were compared using images taken with the microscope and analysed in computer software, see Materials and Methods Chapter 3.5.2. It was found that the densities had an average of 99.72%, with only a small variation between all specimens, as seen in Table 6-1. This suggested that the differences in resistivity of the specimens should be due to the microstructure of the alloy and not due to voids from an increased amount of porosity or other variations in porosity. While there could be additional factors such as spatter or condensate formations within individual specimens, by using four samples per test condition, these factors are averaged out in the measurements.

	As-built	***Annealed***	***T6-like Heat Treatment***
XY plane (Top)	99.73% (± 0.12)	99.76% (± 0.12)	99.87% (± 0.08)
YZ plane (Side)	99.82% (± 0.12)	99.30% (± 0.57)	99.87% (± 0.12)

Table 6-1: Relative average densities of 5 mm test cubes.

In order to establish the grain and microstructure of the same 5 mm test cubes, optical micrographs were compared. All images in Figure 6-2 were taken under the same light and camera settings. Melt pool boundaries can be clearly seen in the as-built specimens as elongated ellipses in the XY (top) plane and as trough-like features in the YZ (side) plane. Annealed sections still showed some of the boundaries of the original melt pools but they were fainter and more difficult to see. The T6-like heat treated specimens did not show any discernible boundaries and were homogeneous in appearance. This suggested that there was a difference between the specimens, and that any variance between measured resistivity could be attributed to these observed differences.

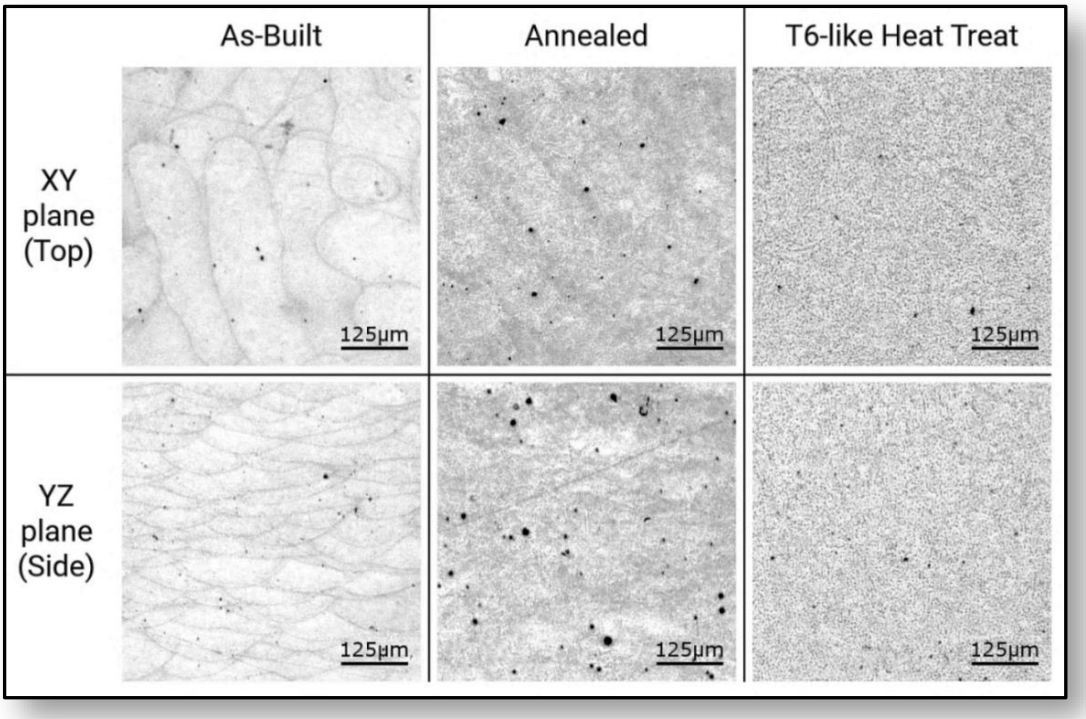

Figure 6-2: Optical micrographs of the polished 5 mm test cubes.

To further expose the grain structure, the polished cross-sections were etched with Keller's reagent for 10 seconds and then imaged using optical (Figure 6-3) and SEM (Figure 6-4) techniques. The as-built specimens showed very clear grain boundaries with regions of fine grain structures in the centre of melt pool boundaries, larger grain structures nearing the edge of the melt pool boundary, and varied disrupted structures at the edges of the melt pool boundaries, representing a heat affected zone (HAZ) [27]. The annealed specimen's microstructure was similar to the as-built, however, the grain structures did not appear to be as clearly defined. The T6-like heat treated specimens showed a very different structure, with no clear grain or melt pool boundaries, but showed regions of different sized spheroid structures.

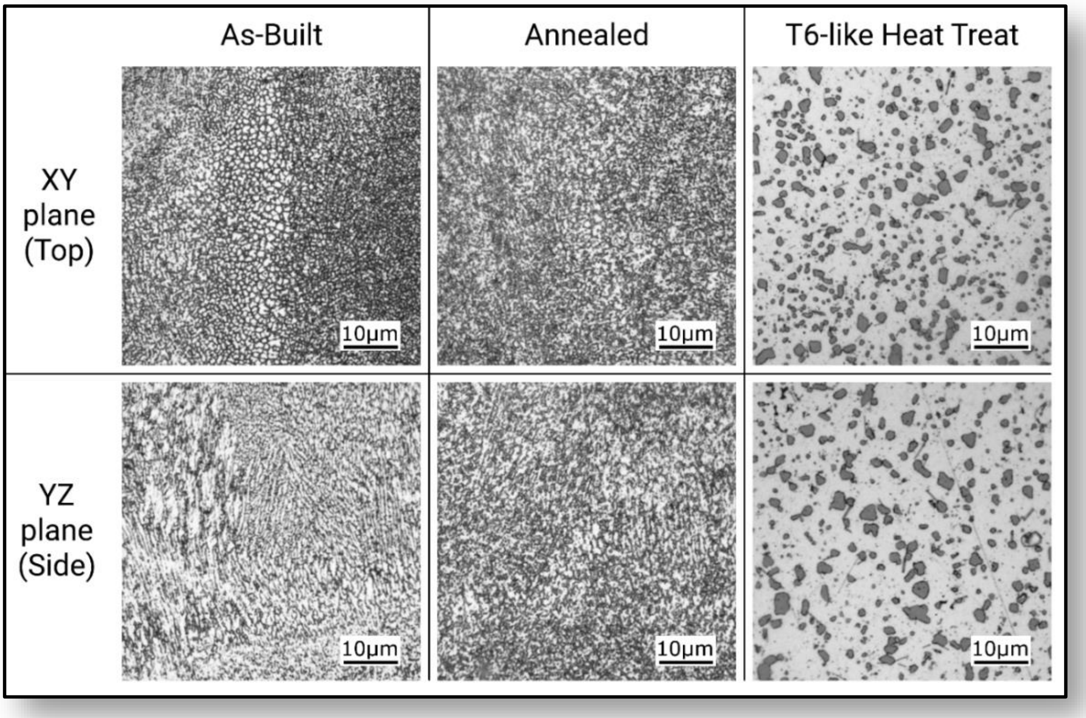

Figure 6-3: Optical micrographs of test cubes after being etched by Keller's reagent showing grain structure with silicon-rich areas that appear darker than the lighter aluminium areas.

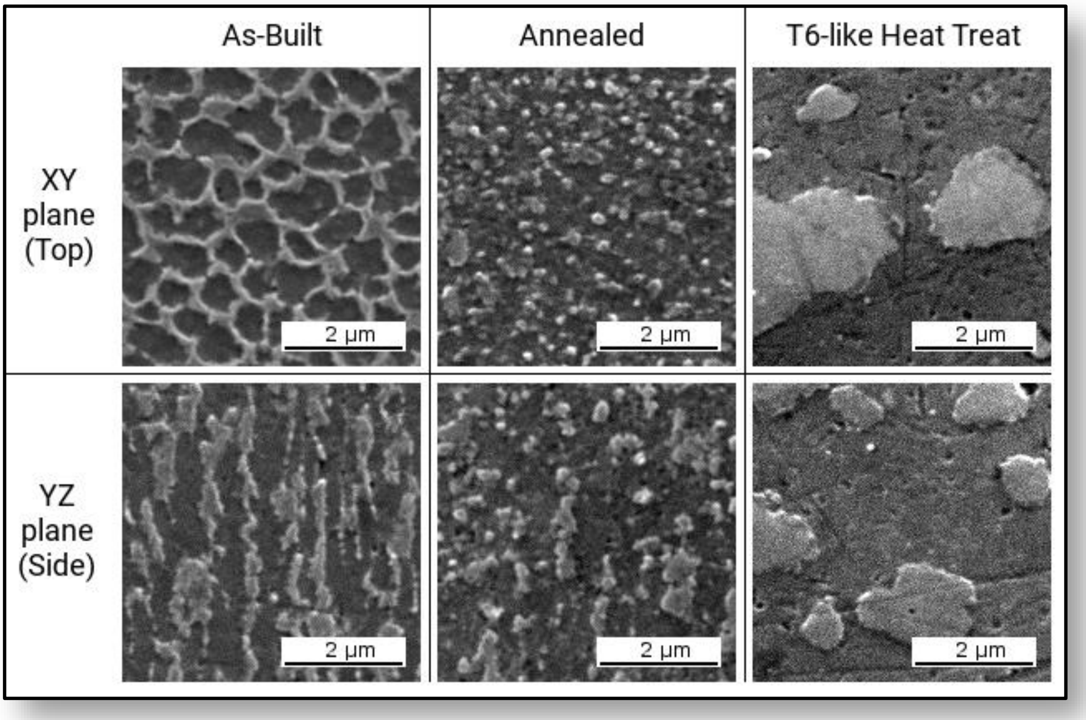

Figure 6-4: SEM images of the etched 5 mm test cubes showing close-up grain structure. Silicon-rich areas are light features, with aluminium areas shown as darker regions.

EDX was used to reveal silicon-rich areas, as seen in Figure 6-5, and to determine the elemental composition of the areas imaged. Silicon-rich features were seen in SEM imaging as lighter compared to the darker aluminium. As-built specimens showed clear regions of highly concentrated silicon at the boundaries of the grains. The annealing process broke these silicon-rich areas up into smaller spheroids. The T6-like heat treatment resulted in an agglomeration of these spheroids into larger silicon-rich regions. Despite the microstructure changes, the elemental composition of the specimens remained consistent, so any changes in resistivity were not due to changes in the composition of the alloy.

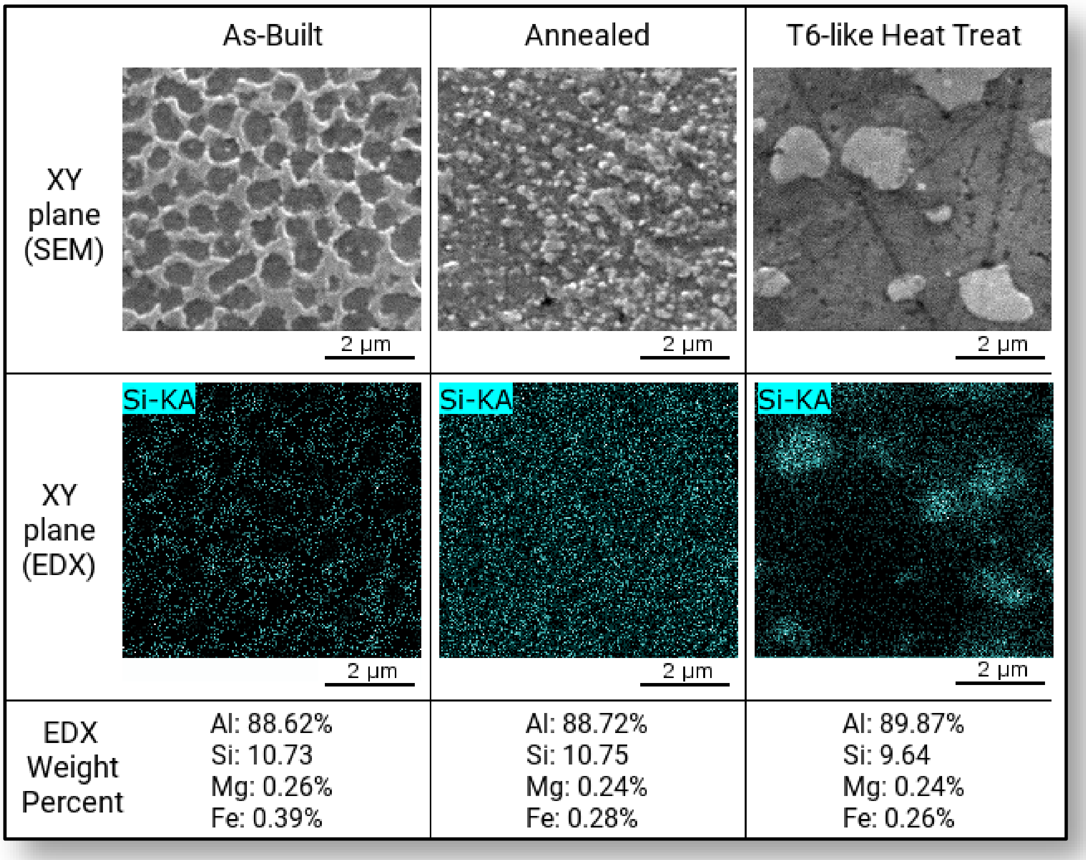

Figure 6-5: SEM images of the etched 5 mm test cubes with corresponding silicon elemental mapping and overall elemental composition expressed as a weight percentage.

6.3 Mechanical properties

To determine the hardness of the test specimens, fifteen nanoindentation measurements were made per specimen, spaced 30µm apart as seen in Figure 6-6. These measurements were undertaken in order to correlate the hardness to known literature values for this alloy and these heat treatments in [209]. By correlating the hardness, the other reported mechanical properties in [209] can also be correlated to this work.

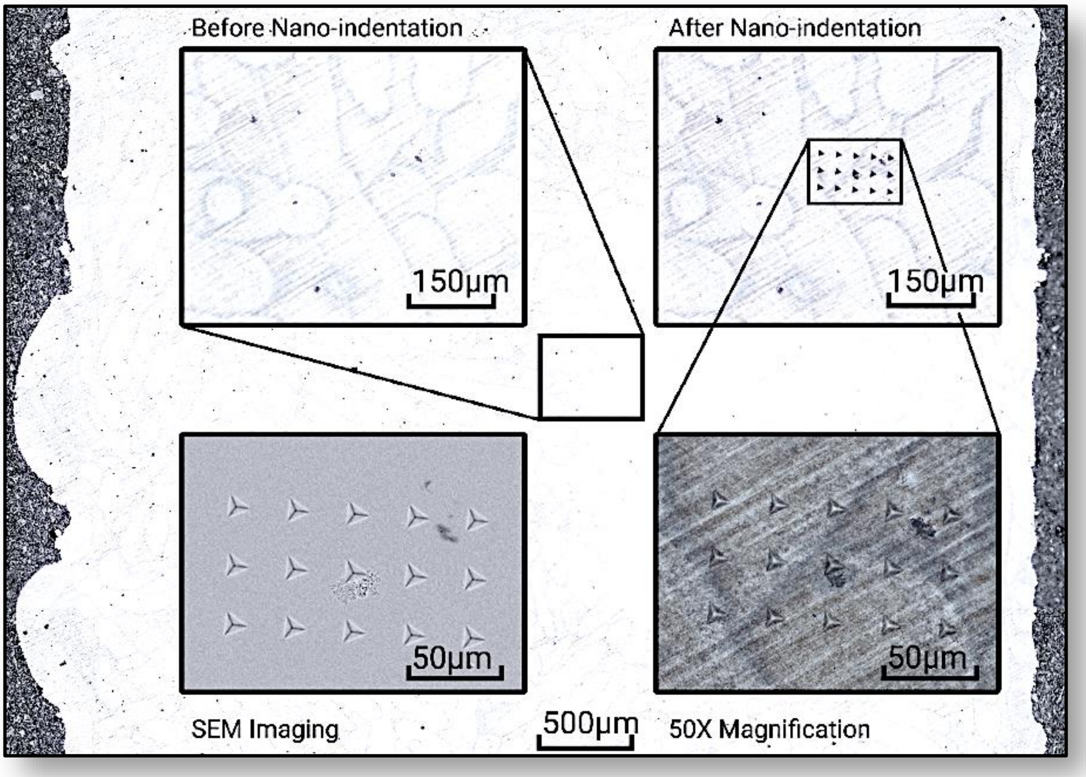

Figure 6-6: Location of nanoindentation within a cross-section of a 5 mm test cube.

The results from nanoindentation tests were compared, as seen in Figure 6-7. The average hardness of the as-built specimens was 1.54 GPa, annealed was 1.16 GPa and T6-like heat treatment was 1.39 GPa. These values match the trend reported by Aboulkhair in [209] and suggest that these post heat treatments are predictable processes that can be applied to AlSi10Mg AM parts. Further mechanical tests were not performed as part of this study as these results have been widely researched and published as in [184], [209], [238].

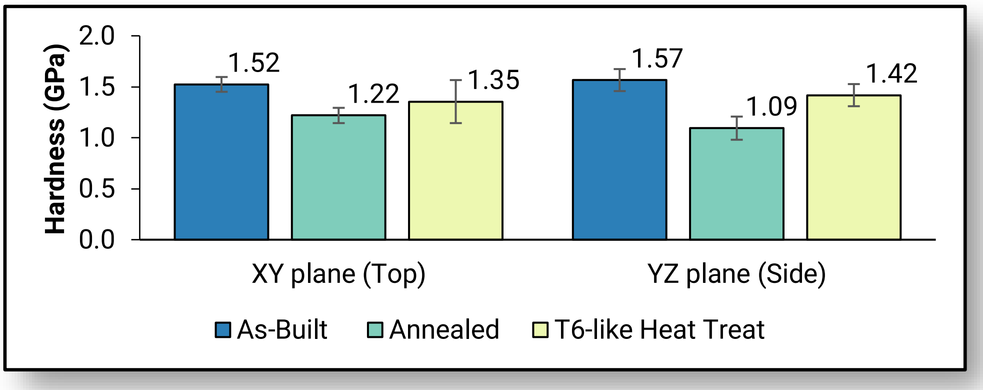

Figure 6-7: Nanoindentation hardness of 5 mm test cubes with corresponding standard deviation.

6.4 Electrical properties

To determine the electrical resistivity of the test specimens, each specimen was measured five times at room temperature using a micro-ohmmeter with results averaged and a standard deviation calculated. In the as-built specimens, the range of values for each specimen varied much greater than that of the annealed or T6-like heat treated specimens, as noted in the standard deviation seen in Figure 6-8. Both the annealed specimens and T6-like heat treated specimens showed no correlation between orientation and resistivity and were relatively similar to each other in terms of resistivity, with the average annealed resistivity being 5.943 μΩ-cm and the average T6-like heat treated specimens being 5.940 μΩ-cm. This is slightly higher than the literature resistivity values of 4.91 μΩ-cm and 4.26-5.56 μΩ-cm seen previously in Table 2-1. However, the as-built specimens showed a strong trend correlating resistivity and orientation. Among as-built specimens, ones built vertically showed a lower resistivity with an average of 7.78 μΩ-cm, with horizontal specimens being the highest in the group at an average of 9.87 μΩ-cm, with 45° in between the two at 9.01 μΩ-cm. The average of the as-built specimens was 8.88 μΩ-cm. This indicates that the microstructure found in the as-built specimens created anisotropic electrical resistivity.

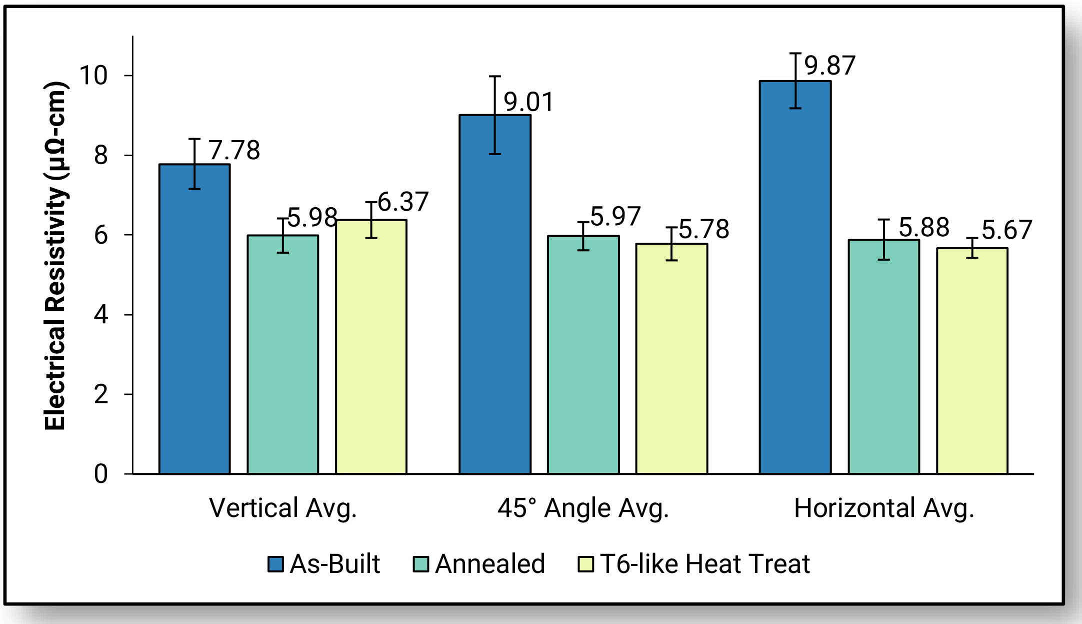

Figure 6-8: Averaged electrical resistivity of specimens under tested conditions with standard deviations.

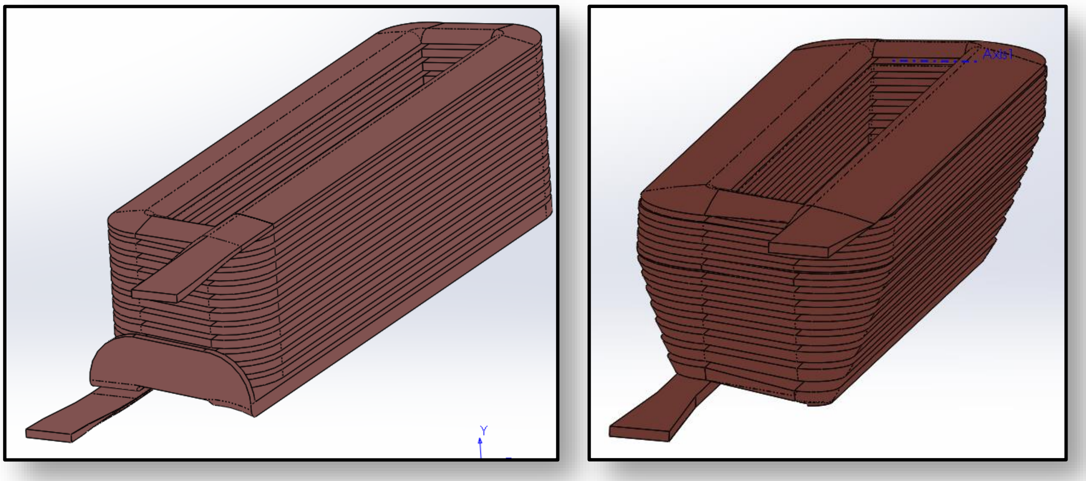

Figure 6-9: CAD design of electrical coils to be 3D printed, a 'block' shaped coil (left) and a 'wedge' shaped coil (right).

Two coils were designed as seen in Figure 6-9 to better represent geometry that would be seen in an electric motor. This design was discussed further in Chapter 4 Using AM in Electric Motor Coil Design. These were then printed in AlSi10Mg using LPBF with the parameters detailed in Chapter 3.4.2. These larger and longer specimens increased the electrical resistance in relation to the contact resistance and improved the accuracy of resistivity measurements. A temporary insulation was used to prevent short circuits during tests, which allowed the specimens to be available for other uses and tests. This insulation consisted of carefully positioned pieces of paper, seen in Figure 6-10. Specimens were heat treated with the annealing process discussed previously in order to minimise resistivity.

Figure 6-10: Paper insulation used for electrical testing of 3D printed electrical coil.

Resistivity measurements were taken over two days, where each day the insulation was reinstalled to ensure that no short-circuits occurred between windings. Four readings were taken for each coil on the first day, and an additional eight on the following. The average resistivity for the ‘block’ coil was 4.87 μΩ-cm, and the ‘wedge’ coil was 5.18 μΩ-cm. The average of these two coils was 5.03 μΩ-cm. Compared to the average resistivity of the original heat-treated test specimens (5.94 μΩ-cm), this represented a reduction of 15%. This confirmed that the resistivity of AM parts once heat treated was similar to the other literature values previously seen for this alloy in Table 2-1. This was due to the increased electrical resistance of the specimens compared to the measurement contact resistance which remained relatively the same.

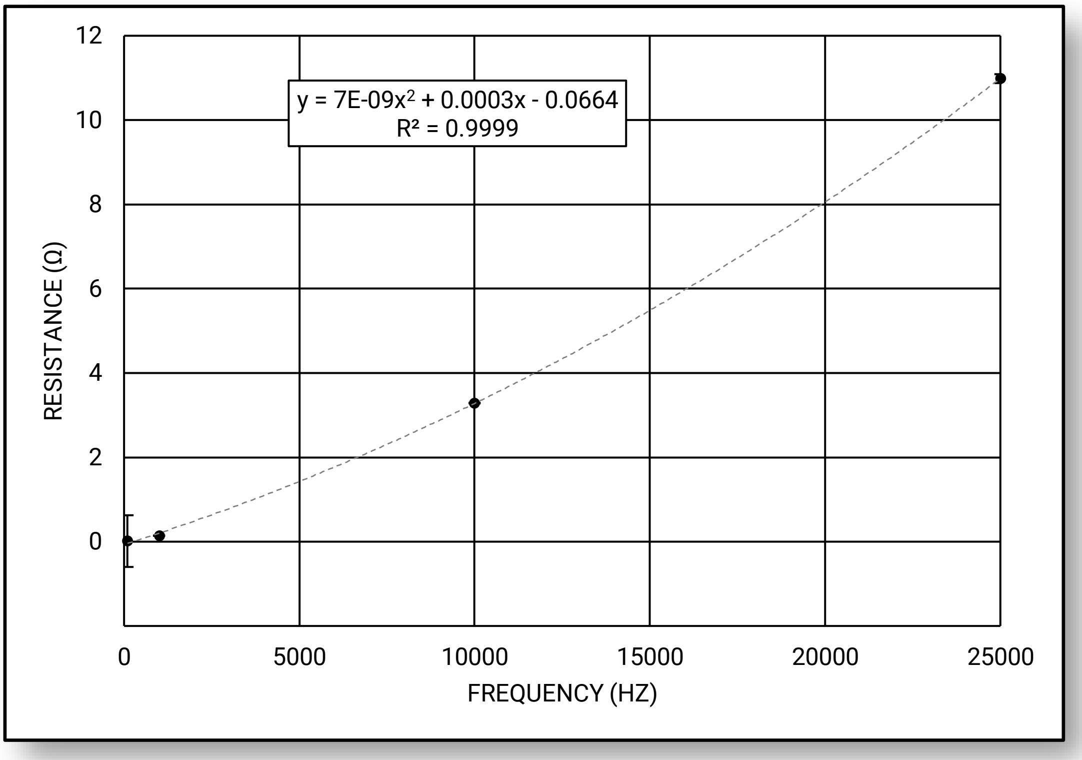

Figure 6-11: Averaged AC resistance of 3D printed coils vs. frequency with standard deviations.

To better understand how this alloy responds to AC currents as would be seen in actual electric motor applications, AC resistance measurements were taken at frequencies of 100 Hz, 1 kHz, 10 kHz, and 25 kHz. The same insulation method was used, and four measurements were taken at each frequency for each specimen. The averaged results can be seen in Figure 6-11. It was found that the 'wedge' configuration resistance values were higher than those of the 'block' configuration. This was the same trend as was seen in the DC measurements, which resulted in a slightly higher calculated resistivity.

The AC resistance values in Figure 6-11 do not actually show a change in the resistivity of the material with changing frequency. Instead, it is an apparent change due to the skin effect which is seen in AC applications [72], [73] and was discussed in Chapter 2.3.3. This was a proportional effect as seen in the nearly linear trend line of Figure 6-11, which despite having a squared term, the coefficient of that squared term is very small, and a linear trend line has a best fit R^2 value of 0.99.

6.5 Geometric analysis

To determine the geometrical accuracy of the LPBF process with the optimised processing parameters for AlSi10Mg in the Renishaw AM250, a variable thickness coil was created as a test geometry, as seen previously in Figure 3-14. This geometry was representative of an electrical coil, with the exception that the coil had a continuously variable thickness. A goal when creating electric coils is to increase an electric motors fill factor to as high as possible. This is limited in both AM and traditional manufacturing by coil and motor geometry, as well as manufacturing tolerances. Ideally, a fill factor of 100% would utilise all the available volume, however a layer of insulation would always be needed which reduces the maximum fill to a value below 100%. However, with AM, there is a much greater control over geometry, which can help increase a motor's fill factor. But in order to achieve as high a fill factor as possible, the tolerance of as-built parts needs to be understood, as well as potential methods to improve the as-built finish. As seen previously in Figure 3-14 (left), there were some larger particles that were attached to the surface. These particles reduce the ability of a coil to compress fully into smaller volumes and could also puncture insulating layers. Thus, improving the area between windings is of interest.

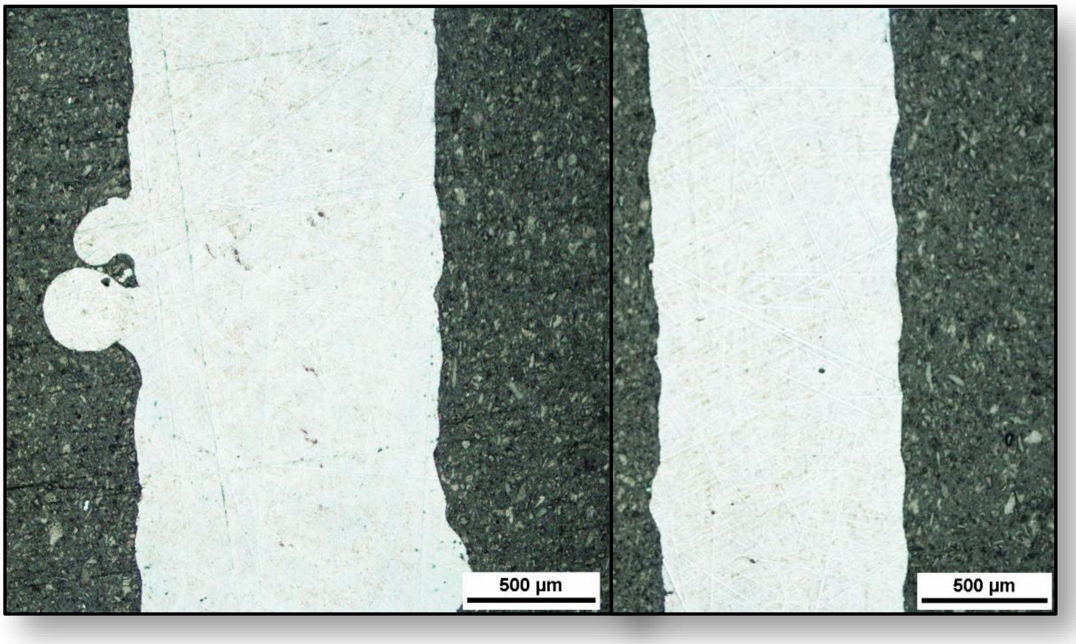

Figure 6-12: Example of sectioned coil widths. Left image shows attached particles which greatly influence maximum thickness, whereas the right shows a relatively constant thickness.

A section of the coil was modified in CAD to analyse the area between windings and was seen in Figure 3-14 (right). Four variations of this specimen were created to test as-built conditions, after being sand blasted, and after being tumble finished for either 1 or 2 weeks with 1 mm ceramic spheres. This long duration is due to the lack of vibration in the tumbler which would increase abrasive action. Specimens were then mounted, ground and polished, and then imaged with a microscope as seen in Figure 6-12 and measured using image software.

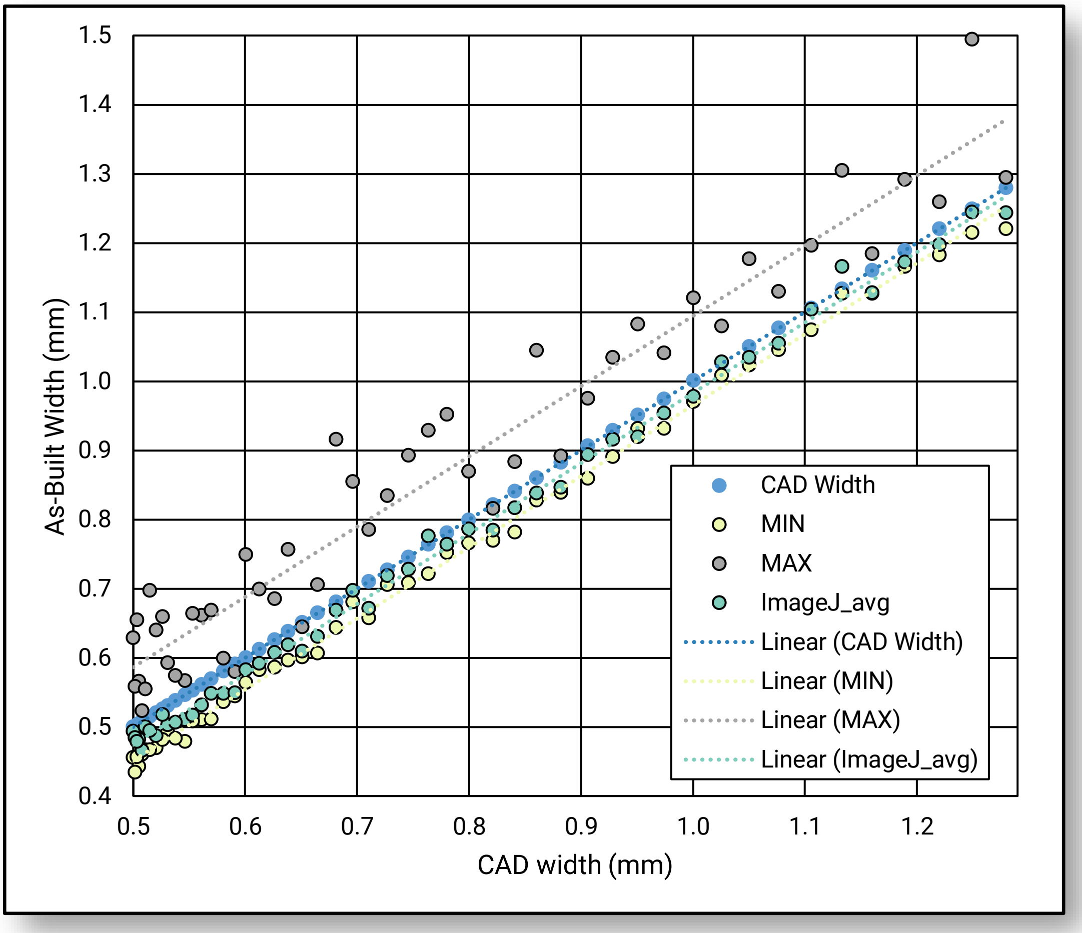

Figure 6-13: Analysis of As-Built line widths compared to CAD width.

The results for the as-built specimens are shown in Figure 6-13. For most measurements, the average reading from the ImageJ software showed that it was generally narrower than the CAD width when the large particles were removed. However, the maximum values which represent these particles were much higher than CAD values. If a sufficient post-finishing process could eliminate these maximum deviations, the printed accuracy could be seen as quite high. On average, the minimum width was about 41 µm less than CAD, the overall average being 20 µm smaller than CAD once large particles were removed, and the maximum being 91 µm larger than CAD.

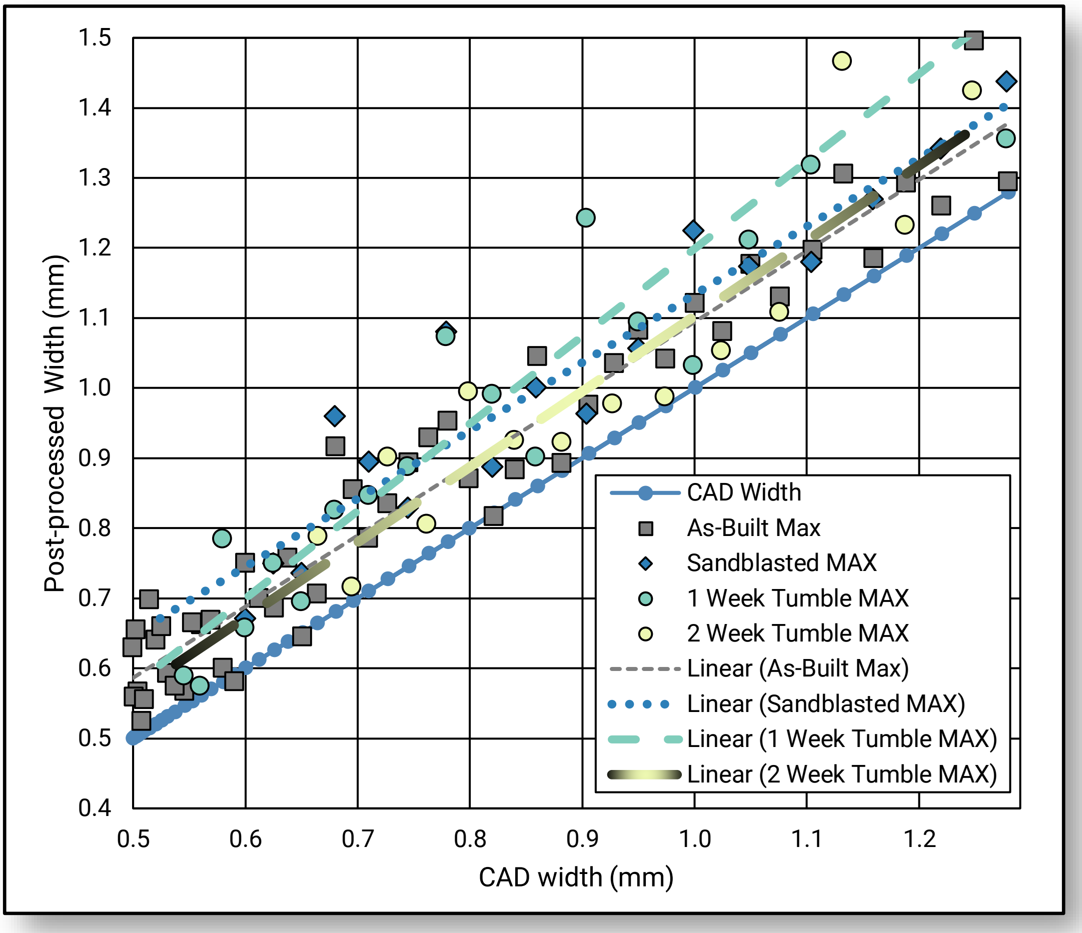

Figure 6-14: Results of post-processing on maximum line width measurements compared to designed CAD width.

Post-processing results for the maximum values are shown in Figure 6-14. Only the maximum values are shown as post-processing was designed to reduce the maximum values. The minimum and average values for the post-processed results were in line with Figure 6-13. It was found that the overall trends for the post-processed specimens matched that of the as-built specimens. On average over the distance between 0.5 - 1.3 mm, the minimum width was about 39 μm smaller than CAD, with the average being 27 μm smaller than CAD, and max being 132 μm larger. There was no significant difference between the sandblasted and tumbled parts. Despite altering the surface finish to appear visibly smoother, none of these processes were able to remove the large attached particles that were located between coils.

6.6 Discussion

Electrical resistance in solid conductors is due to a disruption to the periodic lattice structure found in the material at the atomic scale [19]. This disruption could be due to imperfections in the crystal lattice (grain boundaries, vacancies, dislocations), or from foreign elements occupying spaces in the lattice (impurities). In the case of alloyed metals with a secondary element comprising more than 5% of the total concentration, the impurity resistivity is the dominant form of electrical resistivity [19]. However, when the impurities are no longer randomly distributed but form their own ordered state, the resistivity can no longer be easily estimated or calculated through derived equations. In such cases, further analysis is needed to fully understand the materials electrical properties. A potential result of this ordered state is that the material no longer acts in an isotropic manner. Ohms law is typically written as $I = V/R$ where I is the applied current to the specimen, V is the voltage drop across the specimen and R is the resistance of the specimen. However, this law can also be written as $J = \sigma E$ where J is the current density, σ is the materials electrical conductivity and E is the static electromagnetic field in the specimen. This refined model is tensor-based and allows for σ to be expressed as either a 2 x 2 or 3 x 3 matrix for anisotropic materials [239]. To fully determine this matrix, a characterisation of the structure of each phase as well as the interphase boundaries would be needed [240]. This anisotropicity was the situation that existed in the as-built LPBF specimens due to the rapid cooling of the LPBF process which was in the order of 10^6 K/s [241]. Other materials processed by pulsed laser deposition have also seen anisotropic electrical resistivity [237].

The rapid cooling rate in LPBF results in a unique grain growth and microstructure compared to the cast version of the AlSi10Mg alloy, as previously reported [182], [242], [243]. Initially, α-Al solidifies into needle-like grains oriented towards the heat source (primarily in the Z built direction). As it solidifies, it rejects Si into the remaining liquid, which cools and leaves a saturated Si-rich structure surrounding these Al-rich cores which defines the cellular boundaries seen in Figure 6-4. Three slightly different grain structures can be seen in the as-built specimens; a finely grained melt pool core, a coarser boundary of the melt pool, and a disordered heat affected zone (HAZ) around the melt pool boundary [27]. Both the coarse and fine structures are elongated in the build direction and are surrounded by Si structures. HAZ areas show more fragmented Si structures due to the reheating that occurs from overlapping laser scan patterns. The annealing process breaks up these Si structures into small spherical particles [180]. The T6-like heat treatment further diffuses Si into the main α-Al areas [186] and precipitates Si into larger particles. Thus, both the annealing process and T6-like treatments result in the breaking down of the original as-built ordered Si structures.

The difference between resistivity in the as-built specimens to annealed and T6-like heat treated specimens indicates that microstructure was the cause of the differences in electrical properties. All specimens were built at the same time, using the same processes, using the same test equipment, with similar elemental composition and densities, allowing only post heat treatment and corresponding microstructure to account for the difference, all other variables having been eliminated. The relatively high and consistent density of the specimens seen in Table 6-1 means that porosity cannot account for the differences in resistivity. A correlation between porosity of LPBF parts with electrical conductivity has recently been shown as a linear relationship [234] with high porosity contributing to higher resistivity. Tang [180] also reported a correlation between Si microstructures and electrical conductivity of as-built and annealed specimens despite using a measurement setup which assumed isotropic properties.

The Si structures seen in the as-built samples created the orientation differences in resistivity. As seen in Figure 6-4, the Si was patterned in a network of cellular structures in the XY plane compared to the elongated dendritic structures in the YZ plane. The result is α-Al concentrated in elongated needle-like shapes which align generally with the Z build direction. As tested, the vertical built specimens had electricity pass into the XY plane in the build direction. Since the electricity passing into the XY plane was able to travel mostly in these concentrated elongated α-Al areas, the number of times it crosses the Si structures was minimised. As Si is a much inferior electrical conductor than Al (and acts as an insulator at room temperature) [19], electricity that passes through fewer Si structures will have a lower resistivity. Here this was seen in the lower resistivity of the vertical specimens compared to the horizontal ones.

The breaking up of these segregated Si structures was the key to the lower resistivity found in the annealed and T6 specimens. Even though this annealing process is sometimes referred to as a “stress relief” [180], [214], [244], a true stress relief should not alter grain structure which was not the case by this process and should be reclassified as annealing, noting that this will also perform a stress relief. As the heat treatments break down the Si-rich structures, electrons can find better pathways to flow through the Al material avoiding having to pass through these solid Si structures. Thus, the annealed resistivity was equivalent to the T6-like heat treatment due to the breakdown of the original Si-rich structures even though the final grain structures are different from one another.

The resistivity in this work was slightly higher than the literature values for this alloy. This difference could be the result of the tested heat treatments and corresponding grain structure as compared to cast versions. Generally, applying a T6 type heat treatment increases resistivity compared to the annealed version of a cast alloy. But since traditional manufacturing processes have a very different starting grain structure than AM, a more refined annealing process may be needed beyond the typical anneal to minimise resistivity. Therefore, the values reported in these tests may not represent the lowest possible resistivity that can be achieved with this alloy. As this is the first comprehensive work in characterising the electrical properties of this alloy processed by LPBF, there is no other literature on optimising heat treatments for conductivity.

The surface finishing techniques employed did not significantly reduce surface roughness or improve geometric accuracy. While the outside surfaces were visibly improved, the area of interest between coils remained unaffected. Additional processes such as vibrational finishing or chemical surface treatments could prove a better process for this type of geometry. Both vibrational finishing and chemical treatment of steel parts produced by LPBF has been reported recently [245] where the surface roughness reported was as low as 1 μm, and the treatment time was reduced significantly. Compared to the vibrational only treatment which after sixty-four hours achieved a surface roughness of just under 10 μm, the combined chemical and vibratory process was able to reach 7 μm after sixteen hours, and around 1 μm after thirty-two hours. This combined type of finishing could be of great benefit for AlSi10Mg and should be an area of future research.

While AlSi10Mg has not been used in electrical design applications traditionally, the number of additively manufactured aluminium alloys are limited. By providing the resistivity of this alloy, the potential for it to be used either directly in electrical applications or as a starting point for new lower resistivity AM alloys can begin. The AM design freedom can allow electrical designers to use the material properties of this alloy in new and creative ways that can overcome the limitations of the material resistivity.

6.7 Summary

In this chapter, the resistivity of test specimens that were built from the aluminium alloy AlSi10Mg using AM was measured. These test specimens were built in either a vertical, horizontal, or 45° orientation. They were then either left in an as-built condition or were annealed or treated with a T6-like heat treatment. The specimens were on average 99.72% dense. This high density allowed all specimens to have any resistivity differences to be accounted for by different grain structure and not density differences. It was found that the resulting grain structures did, in fact, create different resistivity.

As-built specimens have concentrated elongated α-Al structures that are elongated along the Z build direction. At the boundary of these structures was a silicon-rich area segregating each of these structures from each other. Electricity was able to pass easier through aluminium than silicon, thus the more times it needed to pass through silicon, the higher the resistivity. As-built specimens showed solidly defined Si-rich structures, whereas annealing broke up these structures and the T6-like heat treatment provided a coarsening of the Si-rich regions.

The resistivity of as-built specimens showed a trend of lower resistivity for vertically built specimens, and higher resistivity for horizontal specimens. This agreed with the premise where the current in vertical specimens passed through more connected aluminium structures and the current in horizontal specimens passed through more Si-rich areas. Both annealed and T6-like heat treated specimens showed no correlation between build direction and resistivity. Both also showed approximately equal values for resistivity at an average of 5.94 μΩ-cm which was slightly higher, but comparable, to known resistivity values for this alloy. By manufacturing larger specimens in the form of electrical coils, this resistivity was reduced by 15% to 5.03 μΩ-cm and better represents the actual resistivity by reducing the influence of contact resistance to the specimen's electrical resistance. Therefore, the use of AM to create electrical based designs leads to little penalty in higher resistivity once an appropriate heat treatment was applied.

In order to use AlSi10Mg in electrical based designs, the accuracy of the LPBF process needs to be known. In geometry studies with a variable thickness coil, it was found that the general accuracy of the LPBF process is high, being on average 40 μm less than CAD dimensions, however, the LPBF process generates a number of large attached particles which created localised maximums which are on average 100 μm larger than CAD dimensions. Techniques such as sandblasting or tumbling with small ceramic beads failed to sufficiently remove these particles which are located between coils.

This was the first study to directly measure the electrical resistivity of AlSi10Mg and correlate the effect of AM initial build orientation to post heat treatments. As such, it opens a new area of research for electrical design by making use of AM as a new manufacturing technique. It allows new electrical component designs to make use of the freedom AM allows over traditional manufacturing methods. This could be especially useful in designing coils for electric motors or other electromagnetic devices. The following chapter will discuss each of these results chapters, how they tie together and achieve the objectives that were set out in the first chapter, and how they have added to the existing body of knowledge.

Chapter 7 Discussion

7.1 Introduction

This discussion covers the findings and main points from the chapters. At the same time, it explains how these results add to the existing literature and fit into the larger discussion of using AM for electric motor design. It will also show how the results achieved the aims and objectives laid out at the beginning of this thesis.

7.2 General discussion and major findings

According to the electric motor trends laid out in Chapter 2.5, there is a need for new technologies which can accomplish them. According to de Almeida [83], one promising area of motor research which can achieve the IE5 Ultra-Premium efficiency class of motors are those which move away from the traditional 2D motor design such as an axial/oblique-flux motor. This type of motor has a more complicated 3D geometry which could be adapted and modified by AM to improve performance. This design freedom that AM can provide is why researchers like Lorenz and Rudolph [113] are investigating the use of AM for windings and motors such as the SRM for automotive applications. While the windings in their work achieved 87% dense (post sinter) with 71% IACS (post sinter), they failed to take into consideration using DfAM. Recently in [246], the challenges of controlling an AM SRM were investigated, but results were limited due to a lack of access to AM equipment and materials, although small demonstrator parts were fabricated with a control system designed. For AM to have the greatest impact in redesign, DfAM needs to be considered. To the best knowledge of the author, there has not been an electric motor fully designed for DfAM. While the motor casing built in [103] did use some DfAM principles, all active components were traditional materials with no active AM parts used. There have also been other individual parts printed for a motor as demonstrated in a recent review of AM electrical machines [247], however, there is a clear lack of active components like windings, and a lack of understanding how DfAM can be used in design. While there are those like Simpson and

Mellor [111], [248], who understand the advantages of using AM for windings including using algorithms to minimise AC losses while increasing fill factors, there still is no consideration for DfAM. Here, this is where this work fits in with providing design guidelines for creating windings in AM. It also showed how AM can fully make use of the slot geometry to enable fill factors of 90%. It also demonstrated coils that can modify end-turn geometry as to maintain cross-sectional area while increasing surface area to aid in heat dissipation. By increasing fill factors and reducing the temperature of a coil, more powerful and efficient electric motors can be designed and manufactured to achieve those future trends in Chapter 2.5.

Pure copper is a very difficult material to process to near 100% dense using LPBF as has been shown by all those who have tried and come short of that goal [137], [138], [249], [139], [149]–[152], [158], [169], [171]. The best from this group used a 1 kW laser and achieved 97.8% [138] while most others were between 80-90%. While the work presented here achieved a similar density to those shown here (85%), the goal of this work was not to achieve 100% density, but rather to present resistivity measurements for pure copper processed by LPBF. Despite the many attempts to process copper, not one of them presented any electrical properties for pure copper, only copper which was contaminated with phosphorus. The only AM process which has successfully processed pure copper to near 100% dense is EBM as discussed previously [132], [136], [142], [143] with the majority of them reporting electrical conductivities near 100% IACS. However, all EBM work presented with electrical measurements [132], [136], [142] used an indirect eddy-current measurement technique which assumes isotropic material properties [19]. But as discussed previously, the electrical resistance in solid conductors is due to a disruptions in the lattice structure at the atomic scale [19] which includes imperfections in the crystal lattice such as grain boundaries. It has been shown with pure copper processed by EBM for example, in [143] with a relative density of 99.95% and a conductivity of 96.24% IACS, that there is elongated grain growth, beyond layer thicknesses, in the build direction. As they neglected to take into consideration initial build orientation and did not use a direct resistivity measurement technique, they failed to find the potential anisotropic resistivity. From the work undertaken here, it is theorised that if a direct four-wire Kelvin resistivity measurement is taken for copper EBM parts, the resistivity will vary with initial build orientation due to the elongated grain structures which are orientated in the build direction (i.e. vertical specimens will have lower resistances than horizontal). These types of measurements and material information is important to understand if parts are going to be used in electrical applications. Here, it demonstrated that direct measurements can be used to determine the anisotropic resistivity in printed specimens.

While pure copper is attractive for its potentially high conductivity, it is not as easily processed by LPBF compared to alloys. To contrast a highly pure/low resistivity material, here, the aluminium alloy AlSi10Mg was directly measured for resistivity with respect to initial build orientation and common post heat treatments in order to determine anisotropic properties [1]. AlSi10Mg is an alloy which is based on the casting alloy A360 and was adopted early on for processing by LPBF [185] due to its ability to easily melt while resisting hot tearing and cracking while cooling and solidifying [30]. While this alloy has been widely studied [181], [182], there has not been a thorough investigation into its electrical properties. While there have been some attempts to measure the electrical resistivity of AlSi10Mg parts [178]–[180] , they have either neglected initial build orientation, have assumed isotropic properties by using indirect measurement techniques, or have neglected the effects of post heat treatment. One potential reason for using indirect methods for measuring the resistivity of aluminium and its alloys could be because of its inability to easily solder and join. Aluminium when exposed to oxygen in the air creates an oxide layer which is a ceramic (alumina) and is very difficult to break down and combine with common solder elements such as zinc and lead, thus preventing any wetting of the solder. This has traditionally caused issues with thermal management at locations of slicing or joining aluminium connections when used in residential applications. This is perhaps why most reported electrical measurements have been performed indirectly, as it is an easier way to obtain these measurements compared to direct methods which typically involve soldering. Despite this, direct measurements are required for materials that create anisotropic microstructures such as AlSi10Mg and can be achieved as seen by this work [1].

7.3 Revisiting aim and objectives

This research set out to show how AM can use materials and design to improve electric motors using DfAM. It has accomplished this, through theoretical analysis of designing an electric motor coil from first principles and using this analysis to design and build coils for a switched reluctance motor with a fill factor of over 90%. This research also set out to address the lack of directly measured electrical properties for metals processed by LPBF. It has accomplished this by providing the resistivities with respect to orientation and heat treatment for both 85% dense pure copper and fully dense AlSi10Mg processed by 200 W LPBF machines.

This research has:

- Designed and manufactured electric motor coils for an existing electric motor
- Determined the electrical resistivity of LPBF pure copper based on the maximum density achieved through parameter optimisation in a 200 W LPBF machine
- Used ML to show its potential to aid in the evaluation of process parameterisation
- Determined the electrical resistivity of an LPBF AlSi10Mg alloy and shown how to minimise resistivity through heat treatment post-processing

7.4 Summary

This work has shown the potential that AM has to enable new electrical designs through an exploration of how it can be used to redesign electric motor coils that maximise the fill-factor and incorporate additional features such as heat-dissipating end-turns. These advancements allow designers to make use of the freedom that AM has over traditional manufacturing methods. It opens up the possibility to use AM for ultra-premium efficiency electric motors and light-weight motors that could be used in aerospace and automotive applications. This was the first study to directly measure the electrical resistivity of pure copper processed on a LPBF machine and correlate the effects of AM build orientation and post heat treatments. This was also the first study to directly measure the electrical resistivity of AlSi10Mg and correlate the effects of AM build orientation and post heat treatments to properties and microstructure. By doing so, it has opened a new area of research for electrical design by making use of AM. It has also demonstrated that ML could aid in parameter optimisation. The following final chapter will briefly state some conclusions and introduce areas for future work.

Chapter 8 Conclusions and Future Work

8.1 Introduction

Over the course of this research, there has been a large amount of new information generated. Here, a concise summary of these results will be presented with the corresponding conclusions. In addition to this research, there are still further areas of research which can build upon this knowledge. A summary of these areas of future work will also be presented.

8.2 Conclusions

8.2.1 Design of electric coils for AM

- Electric motor design has not yet taken advantage of the design freedom which AM provides and requires further knowledge beyond the electrical properties.
- Geometrical accuracy is required, however processing AlSi10Mg by LPBF results in large attached particles which interfere with this accuracy and are unable to be fully removed through post-processing techniques such as sandblasting or tumbling, only by hand with a small file.
- Through the design of coils that specifically fit into existing slot geometries, AM has the potential to create higher fill factors than traditional manufacturing methods.
- The design freedom of AM allows custom end-turn geometry which can increase surface area while maintaining cross-sectional area in order to dissipate more heat.

8.2.2 Electrical materials for LPBF

- Due to the lack of available published data on the electrical properties for AM materials processed by LPBF, pure Cu and AlSi10Mg were investigated.

- For pure Cu, previously published data indicated that it is difficult to process by LPBF without the use of high-power lasers but did not report any electrical properties at lower densities. The findings here showed
    - Without higher laser power densities, copper cannot be processed to fully dense.
    - As-built specimens manifested anisotropic resistivity, however it was due to lack of fusion between layers, and inconsistent melting within layers.
    - Horizontal specimens had a lower resistivity than vertical ones.
    - Post-heat treatments aided in sintering together material and lowering resistivities but failed to create isotropic properties with vertical specimen's resistivity remaining higher than the other orientations.
    - ML mirrors many of the findings from a traditional parameter optimisation and can potentially aid in finding the processing parameters quicker than traditional methods.
- For AlSi10Mg, previously published electrical data ignored how the initial build orientation and post-heat treatments influenced the resistivity. The findings showed
    - It is easily processed by LPBF to a high density.
    - As-built specimens manifested anisotropic resistivity due to the unique LPBF grain structure.
    - Vertical as-built specimens had a lower resistivity than horizontal ones.
    - Post-heat treatments broke-up the LPBF grain structure and resulted in isotropic resistivity.

8.3 Future Work

There is a lot of potential to explore the topics discussed in this work of the manufacture and design of machine specific windings and of highly conductive metals processed by LPBF. Through the course of this research, there have been a number of areas identified which are suitable for future work, these include investigating methods to increase the density of Cu, processing high purity Al, investigating heat treatments that decrease electrical resistivity, improving the insulation of AM windings, improvements in surface finishing, furthering the potential of ML in AM, creating new alloys that have lower resistivities, and designing entire motors which can be created through AM.

8.3.1 Increase density of Cu

The laser power density and wavelength demonstrated in this research showed that it was inadequate to fully process pure Cu. In order to increase the density, alternative laser options should be explored such as green or blue wavelength lasers. Higher power lasers with wavelengths between 1060-1080 nm should be avoided due to the high reflectivity of copper to these wavelengths, as it has been recently shown that significant damage can occur to the laser scanning mirror after repeated exposure to it [236]. An alternative to exploring different laser wavelengths would be to increase the temperature of the powder bed in order to lower the energy requirement of the laser to melt the powder. While this would require changing an LPBF machine, it could be less expensive than replacing the existing infrared laser with blue or green wavelength lasers.

8.3.2 Process high purity Al

Pure aluminium has advantages over copper in terms of cost and density. While pure Al has been processed by LPBF [173], the electrical properties have not been measured. Processing pure AL via LPBF will have many of the same challenges of processing pure copper such as high thermal conductivity, high reflectivity, and oxidation. However, the resulting electrical resistivity will be lower than AlSi10Mg, and potentially lower than the resistivity values for pure copper in this research, as seen in Table 2-1. It also has the advantage that it can be anodised in order to electrically insulate the surface of printed parts.

8.3.3 Heat treatment optimisation for electrical resistivity

The heat treatments investigated for both AlSi10Mg and pure copper helped demonstrate the trend that they can decrease electrical resistivity. But they were not intended to find the absolute lowest resistivity from these alloys. A T6-like heat treatment typically increases a materials resistivity; however, it was the same as the annealing process. This potentially indicates there is a heat treatment which could lower the resistivity further than the lowest value found in this research. In addition to traditional heat treatment methods, a hot isostatic press process (HIP) has been demonstrated with binder jetted copper to increase density and could decrease the resistivity of highly porous copper if the porosity is closed, although geometrical accuracy would potentially be compromised.

8.3.4 Further exploration into surface finishing

Because of the potential improvements to surface roughness which were reported in [245], further investigation into chemical finishing techniques that are suitable for AlSi10Mg should be explored. This in combination with vibratory finishing could improve the accuracy of printed parts by removing attached particles and help in the manufacture of highly complex parts that require tighter tolerances than that of as-built.

8.3.5 Gather more data for machine learning

The potential for ML is limited by the availability of data. As the only data used for this was gathered from a single parameter optimisation study for a single material which couldn’t be processed to a high density, there is a lot of room for improvement to create a more robust algorithm. By incorporating additional parameter optimisation studies with additional materials, the process could be made more accurate. There is also a potential to then apply labels to the clusters of data, so that the process could become more automated as the algorithm would know what a good result looks like verses unlabelled clusters which were used here. This could provide the basis for a fully automated process parameter optimisation, or potentially on the fly laser corrections.

8.3.6 New material research

There are a limited number of available materials used by LPBF that are suitable for electrical windings. Currently, this is an active area of research which has resulted in additional materials with low resistivity based on copper. However, it has not been seen to develop an aluminium based low resistivity alloy to date. This area should be further explored due to aluminium’s low density, low cost, and ability to be anodised. However, it will be challenging to find an alloying composition which does not have a large negatively impact on conductivity as elemental disruptions tend to greatly increase resistivity. Elements which have been added to Al to improve strength while retaining low resistivity have been demonstrated with insoluble elements such as Fe and immiscible elements such as La and Ce [250].

8.3.7 New electric motor designs

While this research focused entirely on electrical properties and windings, there is a potential to create an entire electric motor based on first principles and manufactured through AM. It has already been demonstrated that soft magnetic materials can be manufactured through AM for stators and rotors. There have also been designs for additional components such as the outer casing of the motor [251]. The next stage is to design a motor which incorporates all the advantages that AM has to offer, while manufacturing it entirely by AM as a proof-of-concept to highlight the potential AM has for design.

References

[1] Silbernagel C., Ashcroft I., Dickens P., and Galea M., “Electrical resistivity of additively manufactured AlSi10Mg for use in electric motors,” *Additive Manufacturing*, vol. 21, pp. 395–403, May 2018 doi: 10.1016/j.addma.2018.03.027

[2] Hughes A. and Drury B., *Electric Motors and Drives*, 4th ed. Oxford, United Kingdom: Elsevier, 2013 doi: 10.1016/c2011-0-07555-5

[3] de Almeida A. T., Fonseca P., and Bertoldi P., “Energy-efficient motor systems in the industrial and in the services sectors in the European Union: characterisation, potentials, barriers and policies,” *Energy*, vol. 28, no. 7, pp. 673–690, Jun. 2003 doi: 10.1016/S0360-5442(02)00160-3

[4] McCaig M., *Permanent Magnets in Theory and Practice*, 2nd ed. London, United Kingdom: Pentech Press, 1987 ISBN: 9780727316158

[5] Buschow K. H. J., *Permanent-Magnet Materials and Their Applications*, vol. 5. Zürich, Switzerland: TransTech Publication, 1998 ISBN: 9780878497966

[6] Silwal B. and Sergeant P., “Thermally induced mechanical stress in the stator windings of electrical machines,” *Energies*, vol. 11, no. 8, p. 2113, Aug. 2018 doi: 10.3390/en11082113

[7] Jones R. I., “The more electric aircraft: The past and the future?,” in *IEE Colloquium Electrical Machines and Systems for the More Electric Aircraft*, 1999, pp. 1–4 doi: 10.1049/ic:19990830

[8] Wenping Cao, Mecrow B. C., Atkinson G. J., Bennett J. W., and Atkinson D. J., “Overview of electric motor technologies used for more electric aircraft (MEA),” *IEEE Transactions on Industrial Electronics*, vol. 59, no. 9, pp. 3523–3531, Sep. 2012 doi: 10.1109/tie.2011.2165453

[9] Kastinger G., “Design of a novel transverse flux machine,” in *Proceedings 15th International Conference on Electrical Machines (ICEM 2002)*, Bruges, Belgium, 2002. Available: http://web.mit.edu/kirtley/kirtley/binlustuff/literature/electric machine/Design_of_Tranverse_Flux_Machine.pdf

[10] Madhavan R. and Fernandes B. G., “Performance improvement in the axial flux-segmented rotor-switched reluctance motor,” *IEEE Transactions on Energy Conversion*, vol. 29, no. 3, pp. 641–651, Sep. 2014 doi: 10.1109/tec.2014.2314657

[11] Diko M., Rafajdus P., Makys P., Vavrus V., Makarovic J., and Saitz J., “Design and parameter analysis of short-flux path switched reluctance motor in electrical vehicles,” in *2017 IEEE International Conference on Environment and Electrical Engineering and 2017 IEEE Industrial and Commercial Power Systems Europe (EEEIC / I&CPS Europe)*, Milan, Italy, 2017, pp. 1–6 doi: 10.1109/eeeic.2017.7977486

[12] Garibaldi M., Ashcroft I., Hillier N., Harmon S. A. C., and Hague R., “Relationship between laser energy input, microstructures and magnetic properties of selective laser melted Fe-6.9%wt Si soft magnets,” *Materials Characterization*, vol. 143, pp. 144–151, Sep. 2018 doi: 10.1016/j.matchar.2018.01.016

[13] Garibaldi M., Ashcroft I., Lemke J. N., Simonelli M., and Hague R., “Effect of annealing on the microstructure and magnetic properties of soft magnetic Fe-Si produced via laser additive manufacturing,” *Scripta Materialia*, vol. 142, pp. 121–125, Jan. 2018 doi: 10.1016/j.scriptamat.2017.08.042

[14] Zhang B., Fenineche N.-E., Liao H., and Coddet C., “Magnetic properties of in-situ synthesized FeNi3 by selective laser melting Fe-80%Ni powders,” *Journal of Magnetism and Magnetic Materials*, vol. 336, pp. 49–54, Jun. 2013 doi: 10.1016/j.jmmm.2013.02.014

[15] Zhang B., Fenineche N.-E., Liao H., and Coddet C., “Microstructure and magnetic properties of Fe–Ni alloy fabricated by selective laser melting Fe/Ni mixed powders,” *Journal of Materials Science & Technology*, vol. 29, no. 8, pp. 757–760, Aug. 2013 doi: 10.1016/j.jmst.2013.05.001

[16] Zhang B., Fenineche N.-E., Zhu L., Liao H., and Coddet C., “Studies of magnetic properties of permalloy (Fe–30%Ni) prepared by SLM technology,” *Journal of Magnetism and Magnetic Materials*, vol. 324, no. 4, pp. 495–500, Feb. 2012 doi: 10.1016/j.jmmm.2011.08.030

[17] Mikler C. V., Chaudhary V., Borkar T., Soni V., Jaeger D., Chen X., Contieri R., Ramanujan R. V., and Banerjee R., “Laser additive manufacturing of magnetic materials,” *JOM*, vol. 69, no. 3, pp. 532–543, Mar. 2017 doi: 10.1007/s11837-017-2257-2

[18] Urban N., Meyer A., Kreitlein S., Leicht F., and Franke J., “Efficient near net-shape production of high energy rare earth magnets by laser beam melting,” *Applied Mechanics and Materials*, vol. 871, pp. 137–144, Oct. 2017 doi: 10.4028/www.scientific.net/amm.871.137

[19] Dyos G. T., *The Handbook of Electrical Resistivity: New Materials and Pressure Effects*. London: The Institution of Engineering and Technology, 2012 doi: 10.1049/pbed013e

[20] Hopkinson N., Hague R., and Dickens P. M., *Rapid Manufacturing*. Chichester, UK: John Wiley & Sons, Ltd, 2005 doi: 10.1002/0470033991

[21] Levy G. N. and Schindel R., “Overview of layer manufacturing technologies, opportunities, options and applications for rapid tooling,” *Proceedings of the Institution of Mechanical Engineers, Part B: Journal of Engineering Manufacture*, vol. 216, no. 12, pp. 1621–1634, Jan. 2002 doi: 10.1243/095440502321016350

[22] Kruth J.-P., Leu M. C., and Nakagawa T., “Progress in additive manufacturing and rapid prototyping,” *CIRP Annals - Manufacturing Technology*, vol. 47, no. 2, pp. 525–540, 1998 doi: 10.1016/s0007-8506(07)63240-5

[23] Gibson I., Rosen D. W., and Stucker B., *Additive Manufacturing Technologies*. Boston, MA: Springer US, 2010 doi: 10.1007/978-1-4419-1120-9

[24] Beaman J. J., Barlow J. W., Bourell D. L., Crawford R. H., Marcus H. L., and McAlea K. P., *Solid Freeform Fabrication: A New Direction in Manufacturing*. Boston, Massachusetts, USA: Springer US, 1997 doi: 10.1007/978-1-4615-6327-3

[25] *ASTM ISO/ASTM52900-15 Standard Terminology for Additive Manufacturing – General Principles – Terminology*. West Conshohocken, Pennsylvania, USA: ASTM International, 2015 doi: 10.1520/isoastm52900-15

[26] Gu D. D., Meiners W., Wissenbach K., and Poprawe R., “Laser additive manufacturing of metallic components: materials, processes and mechanisms,” *International Materials Reviews*, vol. 57, no. 3, pp. 133–164, May 2012 doi: 10.1179/1743280411y.0000000014

[27] Thijs L., Kempen K., Kruth J.-P., and Van Humbeeck J., “Fine-structured aluminium products with controllable texture by selective laser melting of pre-alloyed AlSi10Mg powder,” *Acta Materialia*, vol. 61, no. 5, pp. 1809–1819, Mar. 2013 doi: 10.1016/j.actamat.2012.11.052

[28] Fischer J., Kniepkamp M., and Abele E., “Micro laser melting: Analyses of current potentials and restrictions for the additive manufacturing of micro structures,” in *Proceedings of the 25th Solid Freeform Fabrication Symposium (SFF)*, Austin, Texas, USA, 2014, pp. 22–35. Available: http://sffsymposium.engr.utexas.edu/sites/default/files/2014-004-Fischer.pdf

[29] Buchanan N., “An example of Laser Powder Bed Fusion (LPBF).” 2018. Available: https://redheaddirection.com/

[30] Buchbinder D., Meiners W., Pirch N., Wissenbach K., and Schrage J., “Investigation on reducing distortion by preheating during manufacture of aluminum components using selective laser melting,” *Journal of Laser Applications*, vol. 26, no. 1, p. 012004, Feb. 2014 doi: 10.2351/1.4828755

[31] Conner B. P., Manogharan G. P., Martof A. N., Rodomsky L. M., Rodomsky C. M., Jordan D. C., and Limperos J. W., “Making sense of 3-D printing: Creating a map of additive manufacturing products and services,” *Additive Manufacturing*, vol. 1–4, pp. 64–76, Oct. 2014 doi: 10.1016/j.addma.2014.08.005

[32] Sing S. L., An J., Yeong W. Y., and Wiria F. E., “Laser and electron-beam powder-bed additive manufacturing of metallic implants: A review on processes, materials and designs,” *Journal of Orthopaedic Research*, vol. 34, no. 3, pp. 369–385, Mar. 2016 doi: 10.1002/jor.23075

[33] Igelström A., “Fully assembled 3D printable wrench,” *Pinshape*. [Online]. Available: https://pinshape.com/3d-printed-object/1068-fully-assembled-3d-printable-wrench. [Accessed: 22-May-2018]

[34] Business Wire, “EOS and Airbus group innovations team on aerospace sustainability study for industrial 3D printing.” [Online]. Available: https://www.businesswire.com/news/home/20140204005189/en/eos-airbus-group-innovations-team-aerospace-sustainability. [Accessed: 22-May-2018]

[35] Panesar A., Brackett D., Ashcroft I., Wildman R., and Hague R., “Design framework for multifunctional additive manufacturing: Placement and routing of three-dimensional printed circuit volumes,” *Journal of Mechanical Design*, vol. 137, no. 11, pp. 111414-1-11414–10, Oct. 2015 doi: 10.1115/1.4030996

[36] Aremu A., Ashcroft I., Wildman R., Hague R., Tuck C., and Brackett D., “The effects of bidirectional evolutionary structural optimization parameters on an industrial designed component for additive manufacture,” *Proceedings of the Institution of Mechanical Engineers, Part B: Journal of Engineering Manufacture*, vol. 227, no. 6, pp. 794–807, Jun. 2013 doi: 10.1177/0954405412463857

[37] Abdi M., Wildman R., and Ashcroft I., “Evolutionary topology optimization using the extended finite element method and isolines,” *Engineering Optimization*, vol. 46, no. 5, pp. 628–647, May 2014 doi: 10.1080/0305215x.2013.791815

[38] Gibson I., Rosen D. W., and Stucker B., “Design for additive manufacturing,” in *Additive Manufacturing Technologies: Rapid Prototyping to Direct Digital Manufacturing*, Boston, MA: Springer US, 2010, pp. 299–332 doi: 10.1007/978-1-4419-1120-9_11

[39] Leary M., Merli L., Torti F., Mazur M., and Brandt M., “Optimal topology for additive manufacture: A method for enabling additive manufacture of support-free optimal structures,” *Materials and Design*, vol. 63, pp. 678–690, 2014 doi: 10.1016/j.matdes.2014.06.015

[40] Ponche R., Hascoet J. Y., Kerbrat O., and Mognol P., “A new global approach to design for additive manufacturing,” *Virtual and Physical Prototyping*, vol. 7, no. 2, pp. 93–105, Jun. 2012 doi: 10.1080/17452759.2012.679499

[41] “The CFM LEAP fuel nozzle.” [Online]. Available: https://www.youtube.com/watch?v=rMzVSbNebCg&t=2m44s. [Accessed: 22-May-2018]

[42] Rao R., “How GE is using 3D printing to unleash the biggest revolution in large-scale manufacturing in over a century.” [Online]. Available: https://www.techrepublic.com/article/how-ge-is-using-3d-printing-to-unleash-the-biggest-revolution-in-large-scale-manufacturing/. [Accessed: 22-May-2018]

[43] Slusher S., “Areospace panel discussion,” *Canada Makes Additive Manufacturing Forum*. Waterloo, Ontario, Canada, 24-Oct-2018

[44] Mraz S., “3D printing takes parts count from 100 to 1 for antenna.” [Online]. Available: http://www.machinedesign.com/3d-printing/3d-printing-takes-parts-count-100-1-antenna. [Accessed: 22-May-2018]

[45] Ranjan R. and Tangudu J., “Thermal design of high power-density additively-manufactured induction motors,” in *2014 IEEE Energy Conversion Congress and Exposition (ECCE)*, 2014, no. Im, pp. 1325–1331 doi: 10.1109/ecce.2014.6953554

[46] Waterman J., Clucas A., Costa T. B., Zhang Y., and Zhang J., “Numerical modeling of 3D printed electric machines,” in *Proceedings of the 2015 IEEE International Electric Machines & Drives Conference (IEMDC)*, Coeur d’Alene, Idaho, USA, 2015, pp. 1286–1291 doi: 10.1109/iemdc.2015.7409227

[47] Hong H.-S., Liu H.-C., Jeong G.-C., and Lee J., “Design of high-end SynRM based on 3D printing technology,” in *2016 IEEE Conference on Electromagnetic Field Computation (CEFC)*, Miami, Florida, USA, 2016, pp. 1–1 doi: 10.1109/CEFC.2016.7816043

[48] Matula R. A., “Electrical resistivity of copper, gold, palladium, and silver,” *Journal of Physical and Chemical Reference Data*, vol. 8, no. 4, pp. 1147–1298, Oct. 1979 doi: 10.1063/1.555614

[49] Davis J. R., *Copper and Copper Alloys*. Materials Park, Ohio, USA: ASM International, 2001 ISBN: 0871707268

[50] Non-Ferrous Founders' Society and Copper Development Association, *Copper Casting Alloys*. New York, New York, USA: Copper Development Association Inc., 1994. Available: https://www.copper.org/publications/pub_list/pdf/7014.pdf

[51] Wire T. L., Conductors E., and Tem- I., "ASTM B193-02(2014), Standard test method for resistivity of electrical conductor materials," ASTM International, West Conshohocken, Pennsylvania, USA, 2014 doi: 10.1520/b0193

[52] Davey W. P., "Precision measurements of the lattice constants of twelve common metals," *Physical Review*, vol. 25, no. 6, pp. 753–761, Jun. 1925 doi: 10.1103/physrev.25.753

[53] Ellis D. L. and Keller D. J., "Thermophysical properties of GRCop-84," Cleveland, Ohio, USA, 2000. Available: https://ntrs.nasa.gov/search.jsp?R=20000064095

[54] Davis J. R., *ASM Specialty Handbook: Aluminum and Aluminum Alloys*. ASM International, 1993 ISBN: 9780871704962

[55] Aluminum Association, *Aluminum Electrical Conductor Handbook*, 3rd ed. Washington, D.C., USA: Aluminum Association, 1989. Available: https://lccn.loc.gov/89080540

[56] Brandt R. and Neuer G., "Electrical resistivity and thermal conductivity of pure aluminum and aluminum alloys up to and above the melting temperature," *International Journal of Thermophysics*, vol. 28, no. 5, pp. 1429–1446, Nov. 2007 doi: 10.1007/s10765-006-0144-0

[57] Uliasz P., Knych T., Piwowarska M., and Wiecheć J., "The influence of heat treatment parameters on the electrical conductivity of AlSi7Mg and AlSi10Mg aluminum cast alloys," in *Proceedings of the 13th International Conference on Aluminum Alloys (ICAA13)*, Hoboken, New Jersey, USA: John Wiley & Sons, Inc., 2012, pp. 129–135 doi: 10.1002/9781118495292.ch20

[58] Haynes W. M., *CRC Handbook of Chemistry and Physics, 97th Edition*. Boca Raton, Florida, USA: CRC Press/Taylor and Francis, 2017 ISBN: 9781498754286

[59] Tong W., *Mechanical Design of Electric Motors*. Boca Raton, Florida, USA: CRC Press/Taylor and Francis, 2014 ISBN: 9781138072213

[60] Galea M., Gerada C., Raminosoa T., and Wheeler P., "A thermal improvement technique for the phase windings of electrical machines," *IEEE Transactions on Industry Applications*, vol. 48, no. 1, pp. 79–87, Jan. 2012 doi: 10.1109/tia.2011.2175470

[61] Garibaldi M., Ashcroft I., Simonelli M., and Hague R., "Metallurgy of high-silicon steel parts produced using selective laser melting," *Acta Materialia*, vol. 110, no. May, pp. 207–216, May 2016 doi: 10.1016/j.actamat.2016.03.037

[62] Żrodowski Ł., Wysocki B., Wróblewski R., Kurzydłowski K. J., and Święszkowski W., "The novel scanning strategy for fabrication metallic glasses by selective laser melting," in *Proceedings of the 3rd Fraunhofer Direct Digital Manufacturing Conference (DDMC 2016)*, Berlin, Germany, 2016, pp. 443–448 ISBN: 9783839610015

[63] Mahbooba Z., Thorsson L., Unosson M., Skoglund P., West H., Horn T., Rock C., Vogli E., and Harrysson O., “Additive manufacturing of an iron-based bulk metallic glass larger than the critical casting thickness,” *Applied Materials Today*, vol. 11, pp. 264–269, Jun. 2018 doi: 10.1016/j.apmt.2018.02.011

[64] EL-Refaie A. M., “Fractional-slot concentrated-windings synchronous permanent magnet machines: Opportunities and challenges,” *IEEE Transactions on Industrial Electronics*, vol. 57, no. 1, pp. 107–121, Jan. 2010 doi: 10.1109/tie.2009.2030211

[65] Ma Q., Ge B., Bi D., Ferreira F. J. T. E., and de Almeida A. T., “A new switched reluctance motor with distributed winding,” *COMPEL - The International Journal for Computation and Mathematics in Electrical and Electronic Engineering*, vol. 33, no. 6, pp. 2158–2179, Oct. 2014 doi: 10.1108/compel-08-2013-0275

[66] Libert F. and Soulard J., “Manufacturing methods of stator cores with concentrated windings,” in *The 3rd IET International Conference on Power Electronics, Machines and Drives (PEMD 2006)*, Dublin, Ireland, 2006, pp. 676–680. Available: https://ieeexplore.ieee.org/abstract/document/4123608

[67] Mecrow B. C., “Simplifying the manufacturing process for electrical machines,” in *Second IEE International Conference on Power Electronics, Machines and Drives*, Edinburgh, United Kingdom, 2004, vol. 1, pp. 169–174 doi: 10.1049/cp:20040279

[68] Schunk H. and Vollmer R., “Stator for a synchronous machine,” U.S. Patent 6,812,612 B2, 02-Nov-2004. Available: https://patents.google.com/patent/US6812612B2

[69] Kliman G. B., Premerlani W. J., Koegl R. A., and Hoeweler D., “A new approach to on-line turn fault detection in AC motors,” in *IAS ’96. Conference Record of the 1996 IEEE Industry Applications Conference Thirty-First IAS Annual Meeting*, San Diego, California, USA, 1996, vol. 1, pp. 687–693 doi: 10.1109/IAS.1996.557113

[70] Nandi S., Toliyat H. A., and Li X., “Condition monitoring and fault diagnosis of electrical motors—A review,” *IEEE Transactions on Energy Conversion*, vol. 20, no. 4, pp. 719–729, Dec. 2005 doi: 10.1109/tec.2005.847955

[71] Tavner P., Ran L., Penman J., and Sedding H., *Condition Monitoring of Rotating Electrical Machines*, vol. 56. The Institution of Engineering and Technology, Michael Faraday House, Six Hills Way, Stevenage SG1 2AY, UK: IET, 2008 doi: 10.1049/PBPO056E

[72] Gatous O. M. . and Pissolato J., “Frequency-dependent skin-effect formulation for resistance and internal inductance of a solid cylindrical conductor,” *IEE Proceedings - Microwaves, Antennas and Propagation*, vol. 151, no. 3, pp. 212–216, Jun. 2004 doi: 10.1049/ip-map:20040469

[73] Wheeler H. A., “Formulas for the skin effect,” *Proceedings of the IRE*, vol. 30, no. 9, pp. 412–424, Sep. 1942 doi: 10.1109/jrproc.1942.232015

[74] Stone G. C., Sasic M., Dunn D., and Culbert I., “Recent problems experienced with motor and generator windings,” in *2009 Record of Conference Papers - Industry Applications Society 56th Annual Petruleum and Chemical Industry Conference*, 2009, pp. 1–9 doi: 10.1109/PCICON.2009.5297173

[75] Pyrhönen J., Jokinen T., and Hrabovcová V., *Design of Rotating Electrical Machines*, 2nd ed. Chichester, UK: John Wiley & Sons Ltd, 2013 doi: 10.1002/9781118701591

[76] Fink D. G. and Beaty H. W., *Standard Handbook for Electrical Engineers*, 12th ed. New York, New York, USA: McGraw-Hill, 1987 ISBN: 9780071762328

[77] Bouiabady M. M., Aliabad A. D., and Amiri E., "Switched Reluctance Motor Topologies: A Comprehensive Review," in *Switched Reluctance Motor - Concept, Control and Applications*, InTech, 2017 doi: 10.5772/intechopen.69149

[78] Krishnan R., *Switched Reluctance Motor Drives: Modeling, Simulation, Analysis, Design, and Applications*. Boca Raton, Florida, USA: CRC Press, 2001 ISBN: 9780849308383

[79] Radun A. V., "Design considerations for the switched reluctance motor," *IEEE Transactions on Industry Applications*, vol. 31, no. 5, pp. 1079–1087, 1995 doi: 10.1109/28.464522

[80] Miller T. J. E., "Optimal design of switched reluctance motors," *IEEE Transactions on Industrial Electronics*, vol. 49, no. 1, pp. 15–27, 2002 doi: 10.1109/41.982244

[81] Gieras J. F., *Advancements in Electric Machines*. Dordrecht, Netherlands: Springer Netherlands, 2008 doi: 10.1007/978-1-4020-9007-3

[82] de Almeida A. T., Ferreira F. J. T. E., and Both D., "Technical and economical considerations in the application of variable-speed drives with electric motor systems," *IEEE Transactions on Industry Applications*, vol. 41, no. 1, pp. 188–199, 2005 doi: 10.1109/tia.2004.841022

[83] de Almeida A. T., Ferreira F. J. T. E., and Baoming G., "Beyond induction motors—Technology trends to move up efficiency," *IEEE Transactions on Industry Applications*, vol. 50, no. 3, pp. 2103–2114, May 2014 doi: 10.1109/tia.2013.2288425

[84] International Electrotechnical Commission, *IEC 60034-30-1:2014 Rotating Electrical Machines : Efficiency Classes of Line Operated AC Motors*, 1.0. Geneva, Switzerland: International Electrotechnical Commission (IEC), 2014 ISBN: 978-2-8322-1415-2

[85] Ferreira F. J. T. E., Silva A. M., Aguiar V. P. B., Pontes R. S. T., Quispe E. C., and de Almeida A. T., "Overview of retrofitting options in induction motors to improve their efficiency and reliability," in *2018 IEEE International Conference on Environment and Electrical Engineering and 2018 IEEE Industrial and Commercial Power Systems Europe (EEEIC / I&CPS Europe)*, Palermo, Italy, 2018, pp. 1–12 doi: 10.1109/eeeic.2018.8493887

[86] Yong J. Y., Ramachandaramurthy V. K., Tan K. M., and Mithulananthan N., "A review on the state-of-the-art technologies of electric vehicle, its impacts and prospects," *Renewable and Sustainable Energy Reviews*, vol. 49, pp. 365–385, Sep. 2015 doi: 10.1016/j.rser.2015.04.130

[87] International Energy Agency, *Global EV Outlook 2017: Two Million and Counting*. Paris, France: OECD, 2017 doi: 10.1787/9789264278882-en

[88] Sarlioglu B., Morris C. T., Han D., and Li S., "Driving toward accessibility: A review of technological improvements for electric machines, power electronics, and batteries for electric and hybrid vehicles," *IEEE Industry Applications Magazine*, vol. 23, no. 1, pp. 14–25, Jan. 2017 doi: 10.1109/mias.2016.2600739

[89] Zeraoulia M., Benbouzid M. E. H., and Diallo D., "Electric motor drive selection issues for hev propulsion systems: A comparative study," *IEEE Transactions on Vehicular Technology*, vol. 55, no. 6, pp. 1756–1764, Nov. 2006 doi: 10.1109/tvt.2006.878719

[90] Dent P. C., "High performance magnet materials: Risky supply chain," *Advanced Materials & Processes*, vol. 167, no. 8, pp. 27–30, 2009. Available: https://www.asminternational.org/news/magazines/am-p/-/journal_content/56/10192/AMP16708P27/PERIODICAL-ARTICLE

[91] Riba J.-R., López-Torres C., Romeral L., and Garcia A., "Rare-earth-free propulsion motors for electric vehicles: A technology review," *Renewable and Sustainable Energy Reviews*, vol. 57, pp. 367–379, May 2016 doi: 10.1016/j.rser.2015.12.121

[92] Wheeler P. and Bozhko S., "The more electric aircraft: Technology and challenges," *IEEE Electrification Magazine*, vol. 2, no. 4, pp. 6–12, Dec-2014 doi: 10.1109/mele.2014.2360720

[93] Moir I., Seabridge A., and Jukes M., "Electrical systems," in *Civil Avionics Systems*, Chichester, UK: John Wiley & Sons, Ltd, 2013, pp. 235–290 doi: 10.1002/9781118536704.ch7

[94] Boglietti A., Cavagnino A., Tenconi A., Vaschetto S., and di Torino P., "The safety critical electric machines and drives in the more electric aircraft: A survey," in *2009 35th Annual Conference of IEEE Industrial Electronics*, Porto, Portugal, 2009, pp. 2587–2594 doi: 10.1109/iecon.2009.5415238

[95] Wheeler P., "Technology for the more and all electric aircraft of the future," in *2016 IEEE International Conference on Automatica (ICA-ACCA)*, Curico, Chile, 2016, pp. 1–5 doi: 10.1109/ica-acca.2016.7778519

[96] Hoffman A. C., Hansen I. G., Beach R. F., Plencner R. M., Dengler R. P., Jefferies K. S., and Frye R. J., "Advanced secondary power system for transport aircraft," Cleveland, Ohio, USA, 1985. Available: https://ntrs.nasa.gov/search.jsp?R=19850020632

[97] Sarlioglu B. and Morris C. T., "More electric aircraft: Review, challenges, and opportunities for commercial transport aircraft," *IEEE Transactions on Transportation Electrification*, vol. 1, no. 1, pp. 54–64, Jun. 2015 doi: 10.1109/tte.2015.2426499

[98] Raminosoa T., Hamiti T., Galea M., and Gerada C., "Feasibility and electromagnetic design of direct drive wheel actuator for green taxiing," in *2011 IEEE Energy Conversion Congress and Exposition*, 2011, no. August 2016, pp. 2798–2804 doi: 10.1109/ecce.2011.6064145

[99] Galea M., Roggia S., Papini L., Xu Z., Tighe C., Hamiti M., Gerada C., and Pickering S., "Design aspects of a high torque density machine for an aerospace traction application," in *Proceedings of the 17th International Conference on Electrical Machines and Systems (ICEMS)*, Hangzhou, China, 2014, pp. 2773–2778 doi: 10.1109/icems.2014.7013970

[100] Rossignol P., "Paris air show pictures 2015." Reuters, Paris, France, 2015. Available: https://www.reuters.com/news/picture/paris-air-show-idJPRTX1HBWY/1057663402

[101] Juvé L., Fosse J., Joubert E., and Fouquet N., "Airbus group electrical aircraft program, The E-fan project," in *52nd AIAA/SAE/ASEE Joint Propulsion Conference*, Salt Lake City, Utah, USA, 2016, p. 4613 doi: 10.2514/6.2016-4613

[102] Madonna V., Giangrande P., and Galea M., "Electrical power generation in aircraft: Review, challenges, and opportunities," *IEEE Transactions on Transportation Electrification*, vol. 4, no. 3, pp. 646–659, Sep. 2018 doi: 10.1109/tte.2018.2834142

[103] Aguilera E., Ramos J., Espalin D., Cedillos F., Muse D. W., Wicker R. B., and MacDonald E., "3D printing of electro mechanical systems," in *Proceedings of the 24th Solid Freeform Fabrication Symposium (SFF)*, Austin, Texas, USA, 2013, pp. 950–961. Available: http://sffsymposium.engr.utexas.edu/Manuscripts/2013/2013-76-Aguilera.pdf

[104] Ellery A., "Universal construction based on 3D printing electric motors: Steps towards self-replicating robots to transform space exploration," in *2017 IEEE International Symposium on Robotics and Intelligent Sensors (IRIS)*, 2017, vol. 2018-Janua, pp. 81–85 doi: 10.1109/iris.2017.8250102

[105] Lammers S., Adam G., Schmid J. H., Mrozek R., Oberacker R., Hoffmann M. J. J., Quattrone F., Ponick B., Schmid H. J., Mrozek R., Oberacker R., Hoffmann M. J. J., Quattrone F., and Ponick B., "Additive manufacturing of a lightweight rotor for a permanent magnet synchronous machine," in *2016 6th International Electric Drives Production Conference (EDPC)*, Nuremberg, Germany, 2016, vol. 13, pp. 41–45 doi: 10.1109/edpc.2016.7851312

[106] Pippuri J., Metsä-Kortelainen S., Lindroos T., Savolainen M., Jokinen A., Revuelta A., Pasanen A., and Ruusuvuori K., "3D printing of soft magnetic cores for electrical machines," in *Proceedings of the 1st Annual SMACC Research Seminar 2016*, Tampere, Finland, 2016, pp. 48–51 ISBN: 978-952-15-3832-2

[107] Tseng G., Jyun K. J., Huang P., and Lee W., "Application of additive manufacturing for low torque ripple of 6 / 4 switched reluctance motor," in *Proceedings of the 19th International Conference on Electrical Machines and Systems (ICEMS)*, Chiba, Japan, 2016, pp. 3–6. Available: http://ieeexplore.ieee.org/document/7837094/

[108] An B. W., Kim K., Lee H., Kim S.-Y., Shim Y., Lee D.-Y., Song J. Y., and Park J.-U., "High-resolution printing of 3D structures using an electrohydrodynamic inkjet with multiple functional inks," *Advanced Materials*, vol. 27, no. 29, pp. 4322–4328, Aug. 2015 doi: 10.1002/adma.201502092

[109] Gröninger M., Horch F., Kock A., Pleteit H., Ponick B., Schmidt D., and Wostmann F.-J., "Casting production of coils for electrical machines," in *Proceedings of the 2011 1st International Electric Drives Production Conference (EDPC 2011)*, Nuremberg, Germany, 2011, pp. 159–161 doi: 10.1109/edpc.2011.6085534

[110] Gröninger M., Kock A., Jakob M., Gmbh L. D., Kg C., Groninger M., Horch F., Kock A., Jakob M., and Ponick B., "Cast coils for electrical machines and their application in automotive and industrial drive systems," in *2014 4th International Electric Drives Production Conference (EDPC 2014)*, Nuremberg, Germany, 2014, pp. 1–7 doi: 10.1109/edpc.2014.6984384

[111] Simpson N. and Mellor P. H., "Additive manufacturing of shaped profile windings for minimal AC loss in gapped inductors," in *2017 IEEE International Electric Machines and Drives Conference (IEMDC)*, Miami, Florida, USA, 2017, no. 1, pp. 1–7 doi: 10.1109/iemdc.2017.8002337

[112] Urdaneta M. G., Probst R., Stepanov P. Y., Weinberg I. N., and Fricke S. T., “Goodbye wires and formers: 3-D additive manufacturing and fractal cooling applied to construction of MRI gradient coils,” in *Proceedings of the 2011 IEEE Nuclear Science Symposium and Medical Imaging Conference (NSS/MIC 2011)*, Valencia, Spain, 2011, pp. 2479–2482 doi: 10.1109/nssmic.2011.6152672

[113] Lorenz F., Rudolph J., and Wemer R., “Design of 3D printed high performance windings for switched reluctance machines,” in *Proceedings of the 13th International Conference on Electrical Machines (ICEM)*, Alexandroupoli, Greece, 2018, pp. 2451–2457 doi: 10.1109/icelmach.2018.8506845

[114] Veronesi W. A., El-Wardany T. I., Dardona S., and Schmidt W. R., “Additive manufacturing of a component having a laminated stack of layers,” U.S. Patent 9,419,502 B2, 16-Aug-2016. Available: https://patents.google.com/patent/US9419502B2

[115] Bott E., Bähr H., and Vollmer R., “Electrical machine with a cooling channel and method for manufacturing the same,” U.S. Patent 8,922,072, 30-Dec-2014. Available: https://www.google.com/patents/US8922072

[116] O’Donnell J., Kim M., and Yoon H.-S., “A review on electromechanical devices fabricated by additive manufacturing,” *Journal of Manufacturing Science and Engineering*, vol. 139, no. 1, p. 010801, Aug. 2016 doi: 10.1115/1.4033758

[117] Grootenhuis P., Powell R. W., and Tye R. P., “Thermal and electrical conductivity of porous metals made by powder metallurgy methods,” *Proceedings of the Physical Society. Section B*, vol. 65, no. 7, pp. 502–511, Jul. 1952 doi: 10.1088/0370-1301/65/7/305

[118] Rasa M. V. and Slot M., “Method for applying an image of an electrically conductive material onto a recording medium and device for ejecting droplets of an electrically conductive fluid,” U.S. Patent 9,922,870 B2, 20-Mar-2018. Available: https://patents.google.com/patent/US9922870B2

[119] Vader S., Vader Z., Karampelas I. H., and Furlani E. P., “Magnetohydrodynamic liquid metal jet printing,” *TechConnect Conference*, no. 716, pp. 2–4, 2015 ISBN: 9781498747301

[120] Bai Y. and Williams C. B., “An exploration of binder jetting of copper,” *Rapid Prototyping Journal*, vol. 21, no. 2, pp. 177–185, Mar. 2015 doi: 10.1108/rpj-12-2014-0180

[121] Yegyan Kumar A., Bai Y., Eklund A., and Williams C. B., “The effects of hot isostatic pressing on parts fabricated by binder jetting additive manufacturing,” *Additive Manufacturing*, vol. 24, pp. 115–124, Sep. 2018 doi: 10.1016/j.addma.2018.09.021

[122] Kumar A., Bai Y., Eklund A., and Williams C. B., “Effects of hot isostatic pressing on copper parts fabricated via binder jetting,” *Procedia Manufacturing*, vol. 10, pp. 935–944, 2017 doi: 10.1016/j.promfg.2017.07.084

[123] Bai Y., Wagner G., and Williams C. B., “Effect of Bimodal Powder Mixture on Powder Packing Density and Sintered Density in Binder Jetting of Metals,” *2015 Annual International Solid Freeform Fabrication Symposium*, p. 62, 2015 doi: 10.1017/CBO9781107415324.004

[124] Syed W. U. H., Pinkerton A. J., Liu Z., and Li L., “Single-step laser deposition of functionally graded coating by dual ‘wire–powder’ or ‘powder–powder’ feeding—A comparative study,” *Applied Surface Science*, vol. 253, no. 19, pp. 7926–7931, Jul. 2007 doi: 10.1016/j.apsusc.2007.02.174

[125] Unocic R. R. and DuPont J. N., “Composition control in the direct laser-deposition process,” *Metallurgical and Materials Transactions B*, vol. 34, no. 4, pp. 439–445, Aug. 2003 doi: 10.1007/s11663-003-0070-5

[126] Sciammarella F. M., Gonser M. J., and Styrcula M., “Laser additive manufacturing of pure copper,” in *Rapid 2013 Conference*, Pittsburgh, Pennsylvania, USA, 2013. Available: https://www.researchgate.net/publication/282266869_Laser_Additive_Manufacturing_of_Pure_Copper

[127] Hildreth O. J., Nassar A. R., Chasse K. R., and Simpson T. W., “Dissolvable metal supports for 3D direct metal printing,” *3D Printing and Additive Manufacturing*, vol. 3, no. 2, pp. 90–97, Jun. 2016 doi: 10.1089/3dp.2016.0013

[128] Tan J. C. and Low H. Y., “Embedded electrical tracks in 3D printed objects by fused filament fabrication of highly conductive composites,” *Additive Manufacturing*, vol. 23, pp. 294–302, Oct. 2018 doi: 10.1016/j.addma.2018.06.009

[129] Vaithilingam J., Simonelli M., Saleh E., Senin N., Wildman R. D., Hague R. J. M. M., Leach R. K., and Tuck C. J., “Combined inkjet printing and infrared sintering of silver nanoparticles using a swathe-by-swathe and layer-by-layer approach for 3-dimensional structures,” *ACS Applied Materials and Interfaces*, vol. 9, no. 7, pp. 6560–6570, Feb. 2017 doi: 10.1021/acsami.6b14787

[130] Park B. K., Kim D., Jeong S., Moon J., and Kim J. S., “Direct writing of copper conductive patterns by ink-jet printing,” *Thin Solid Films*, vol. 515, no. 19, pp. 7706–7711, Jul. 2007 doi: 10.1016/j.tsf.2006.11.142

[131] Visser C. W., Pohl R., Sun C., Römer G.-W., Huis in ’t Veld B., Lohse D., Huis in ‘t Veld B., and Lohse D., “Toward 3D printing of pure metals by laser-induced forward transfer,” *Advanced Materials*, vol. 27, no. 27, pp. 4087–4092, Jul. 2015 doi: 10.1002/adma.201501058

[132] Guschlbauer R., Momeni S., Osmanlic F., and Körner C., “Process development of 99.95% pure copper processed via selective electron beam melting and its mechanical and physical properties,” *Materials Characterization*, vol. 143, pp. 163–170, Sep. 2018 doi: 10.1016/j.matchar.2018.04.009

[133] Khan M. and Dickens P. M., “Selective laser melting (SLM) of pure gold,” *Gold Bulletin*, vol. 43, no. 2, pp. 114–121, Jun. 2010 doi: 10.1007/bf03214976

[134] Sriraman M. R., Babu S. S., and Short M., “Bonding characteristics during very high power ultrasonic additive manufacturing of copper,” *Scripta Materialia*, vol. 62, no. 8, pp. 560–563, Apr. 2010 doi: 10.1016/j.scriptamat.2009.12.040

[135] Lee J. W., Lee I. H., and Cho D.-W., “Development of micro-stereolithography technology using metal powder,” *Microelectronic Engineering*, vol. 83, no. 4–9, pp. 1253–1256, Apr. 2006 doi: 10.1016/j.mee.2006.01.192

[136] Frigola P., Harrysson O. A., Horn T. J., West H. A., Aman R. L., Rigsbee J. M., Ramirez D. A., Medina F., Wicker R. B., Rodriguez E., Murr L. E., Medina F., Wicker R. B., and Rodriguez E., “Fabricating copper components with electron beam melting,” *Advanced Materials & Processes*, vol. 172, no. 7, ASM International, Materials Park, Ohio, USA, pp. 20–24, Jul-2014. Available: https://www.asminternational.org/c/portal/pdf/download?articleId=19739462&groupId=10192

[137] Zhang D., Liu Z., and Chua C., “Investigation on forming process of copper alloys via selective laser melting,” in *High Value Manufacturing: Advanced Research in Virtual and Rapid Prototyping*, CRC Press, 2013, pp. 285–289 ISBN: 9781138001374

[138] Colopi M., Caprio L., Demir A. G., and Previtali B., “Selective laser melting of pure Cu with a 1 kW single mode fiber laser,” in *Proceedings of the 10th CIRP Conference on Photonic Technologies [LANE 2018]*, Fürth, Germany, 2018, vol. 74, pp. 59–63 doi: 10.1016/j.procir.2018.08.030

[139] Dyer B. R., “Additive manufacturing of copper electrodes and bus work for resistance welding,” Youngstown State University, 2017. Available: http://rave.ohiolink.edu/etdc/view?acc_num=ysu1495803338676301

[140] Niendorf T., Leuders S., Riemer A., Richard H. A., Tröster T., and Schwarze D., “Highly anisotropic steel processed by selective laser melting,” *Metallurgical and Materials Transactions B: Process Metallurgy and Materials Processing Science*, vol. 44, no. 4, pp. 794–796, 2013 doi: 10.1007/s11663-013-9875-z

[141] Sames W. J., List F. A., Pannala S., Dehoff R. R., and Babu S. S., “The metallurgy and processing science of metal additive manufacturing,” *International Materials Reviews*, vol. 61, no. 5, pp. 315–360, Jul. 2016 doi: 10.1080/09506608.2015.1116649

[142] Raab S. J., Guschlbauer R., Lodes M. A., and Körner C., “Thermal and electrical conductivity of 99.9% pure copper processed via selective electron beam melting,” *Advanced Engineering Materials*, vol. 18, no. 9, pp. 1661–1666, Sep. 2016 doi: 10.1002/adem.201600078

[143] Lodes M. A., Guschlbauer R., and Körner C., “Process development for the manufacturing of 99.94% pure copper via selective electron beam melting,” *Materials Letters*, vol. 143, pp. 298–301, Mar. 2015 doi: 10.1016/j.matlet.2014.12.105

[144] Zhu H. H., Lu L., and Fuh J. Y. H., “Development and characterisation of direct laser sintering Cu-based metal powder,” *Journal of Materials Processing Technology*, vol. 140, no. 1–3, pp. 314–317, Sep. 2003 doi: 10.1016/s0924-0136(03)00755-6

[145] Maiti S., “Study of the basic process mechanism of laser sintering of copper powder,” Jadavpur University, Kolkata, India, 2013. Available: http://dspace.jdvu.ac.in/handle/123456789/28171

[146] Gu D. and Shen Y.-F., “Balling phenomena during direct laser sintering of multi-component Cu-based metal powder,” *Journal of Alloys and Compounds*, vol. 432, no. 1–2, pp. 163–166, Apr. 2007 doi: 10.1016/j.jallcom.2006.06.011

[147] Tang Y., Loh H. T., Wong Y. S., Fuh J. Y. H., Lu L., and Wang X., “Direct laser sintering of a copper-based alloy for creating three-dimensional metal parts,” *Journal of Materials Processing Technology*, vol. 140, no. 1–3, pp. 368–372, Sep. 2003 doi: 10.1016/s0924-0136(03)00766-0

[148] Gebhardt A., Fateri M., Hötter J.-S. J.-S., Knothe M., Schmidt F. M., Rieper H., Gebhardt A., Hötter J.-S. J.-S., Knothe M., Schmidt F. M., and Rieper H., “Numerical and experimental investigation of selective laser melting of silver,” in *Fraunhofer Direct Digital Manufacturing Conference (DDMC 2012)*, Berlin, Germany, 2012. Available: https://www.researchgate.net/publication/264548342

[149] Lykov P. A., Safonov E. V., and Akhmedianov A. M., “Selective laser melting of copper,” *Materials Science Forum*, vol. 843, no. March, pp. 284–288, Feb. 2016 doi: 10.4028/www.scientific.net/msf.843.284

[150] Becker D., Meiners W., and Wissenbach K., “Additive manufacturing of copper alloys by selective laser melting,” in *Proceedings of the 5th International WLT-Conference on Lasers in Manufacturing (LiM2009)*, Munich, Germany, 2009, pp. 195–200 ISBN: 9783000279942

[151] Jones J. B., Wimpenny D. I., Chudasama R., and Gibbons G. J., “Printed circuit boards by selective deposition and processing,” in *Proceedings of the 22nd Solid Freeform Fabrication Symposium (SFF)*, Austin, Texas, USA, 2011, pp. 639–656. Available: http://sffsymposium.engr.utexas.edu/Manuscripts/2011/2011-50-Jones.pdf

[152] Pogson S. R. R., Fox P., Sutcliffe C. J. J., and O’Neill W., “The production of copper parts using DMLR,” *Rapid Prototyping Journal*, vol. 9, no. 5, pp. 334–343, Dec. 2003 doi: 10.1108/13552540310502239

[153] Aerojet Rocketdyne, “Additive manufacturing - Aerojet Rocketdyne,” 2017. [Online]. Available: http://www.rocket.com/article/aerojet-rocketdyne-achieves-3-d-printing-milestone-successful-testing-full-scale-rl10-copper-thrust. [Accessed: 29-Mar-2019]

[154] “Fraunhofer launches ‘SLM in green’ project for 3D printed copper,” 2017. [Online]. Available: https://www.ilt.fraunhofer.de/en/press/press-releases/press-release-2017/press-release-2017-08-30.html. [Accessed: 31-Aug-2017]

[155] Hönl R., “World premiere at Formnext: green laser from TRUMPF prints copper and gold,” *TRUMPF Global Press release*, Frankfurt, Germany, 13-Nov-2018. Available: https://www.trumpf.com/en_INT/company/press/global-press-releases/press-release-detail-page/release/world-premiere-at-formnext-green-laser-from-trumpf-prints-copper-and-gold/

[156] Khan M., “Selective laser melting (SLM) of gold (Au),” Loughborough University, Loughborough, United Kingdom, 2010. Available: https://dspace.lboro.ac.uk/2134/6163

[157] Kruth J. P., Wang X., Laoui T., and Froyen L., “Lasers and materials in selective laser sintering,” *Assembly Automation*, vol. 23, no. 4, pp. 357–371, Dec. 2003 doi: 10.1108/01445150310698652

[158] Kaden L., Seyfarth B., Ullsperger T., Matthäus G., and Nolte S., “Selective laser melting of copper using ultrashort laser pulses at different wavelengths,” in *Proceedings of SPIE - Laser 3D Manufacturing V*, 2018, vol. 10523, p. 41 doi: 10.1117/12.2289959

[159] Kaiser E., Dold E., Killi A., and Zaske S., “Application benefits of welding copper with a 1 kW , 515 nm continuous wave laser,” in *Industrial Contributions to the 10th CIRP Conference on Photonic Technologies (LANE 2018)*, Fürth, Germany, 2018. Available: https://www.lane-conference.org/app/download/12333125349/11162_LANE2018_Kaiser.pdf

[160] Haubold M., Ganser A., Eder T., and Zäh M. F., “Laser welding of copper using a high power disc laser at green wavelength,” *Procedia CIRP*, vol. 74, pp. 446–449, 2018 doi: 10.1016/j.procir.2018.08.161

[161] Pelaprat J.-M., Finuf M., Fritz R., and Zediker M., “Seeing things in a new light: High power blue lasers for metal processing,” *Laser Technik Journal*, vol. 15, no. 4, pp. 39–41, Oct. 2018 doi: 10.1002/latj.201800028

[162] Balck A., Baumann M., Malchus J., Marfels S., Witte U., Dinakaran D., Ocylok S., Weinbach M., Bachert C., Kösters A., Krause V., Lell A., König H., Stojetz B., Strauss U., Löffler A., and Chacko R. V, “700 W blue fiber-coupled diode-laser emitting at 450 nm,” in *Proceedings of SPIE - High-Power Diode Laser Technology XVI*, San Francisco, California, USA, 2018, vol. 10514, p. 2 doi: 10.1117/12.2286631

[163] Minneci R., Rawn C., Bunn J., Floyd J., and Jones Z., “Preliminary residual stress mapping of GRCop-84 fabricated by SLM,” Oak Ridge, Tennessee, USA, 2017. Available: https://ntrs.nasa.gov/search.jsp?R=20170009044

[164] Gradl P. R., Protz C., Greene S. E., Ellis D., Lerch B., Locci I., Msfc N. M., Lerch B., and Grc N. G., “Development and hot-fire testing of additively manufactured copper combustion chambers for liquid rocket engine applications,” in *53rd AIAA/SAE/ASEE Joint Propulsion Conference*, Reston, Virginia, USA, 2017 doi: 10.2514/6.2017-4670

[165] Cooper K. G., Lydon J. L., LeCorre M. D., Jones Z. C., Scannapieco D. S., Ellis D. L., and Lerch B. A., “Three-dimensional printing GRCop-42,” Huntsville, Alabama, USA, 2018. Available: https://ntrs.nasa.gov/search.jsp?R=20190001243

[166] Ventura A. P., Marvel C. J., Pawlikowski G., Bayes M., Watanabe M., Vinci R. P., and Misiolek W. Z., “The Effect of Aging on the Microstructure of Selective Laser Melted Cu-Ni-Si,” *Metallurgical and Materials Transactions A*, vol. 48, no. 12, pp. 6070–6082, Dec. 2017 doi: 10.1007/s11661-017-4363-8

[167] Ventura A. P., “Microstructural evolution and mechanical property development of selective laser melted copper alloys,” Lehigh University, Bethlehem, Pennsylvania, USA, 2017. Available: http://preserve.lehigh.edu/etd/2857

[168] Ventura A. P., Wade C. A., Pawlikowski G., Bayes M., Watanabe M., and Misiolek W. Z., “Mechanical properties and microstructural characterization of Cu-4.3 pct Sn fabricated by selective laser melting,” *Metallurgical and Materials Transactions A*, vol. 48, no. 1, pp. 178–187, Jan. 2017 doi: 10.1007/s11661-016-3779-x

[169] El-Wardany T., She Y., Jagdale V., Garofano J. K., Liou J., and Schmidt W., “Challenges in 3D printing of high conductivity copper,” in *ASME 2017 International Technical Conference and Exhibition on Packaging and Integration of Electronic and Photonic Microsystems*, San Francisco, California, USA, 2017 doi: 10.1115/ipack2017-74306

[170] Neikov O. D., Murashova I. B., Yefimov N. A., and Naboychenko S., *Handbook of Non-Ferrous Metal Powders: Technologies and Applications*. Elsevier, 2009 ISBN: 9780081005477

[171] Lykov P., Baytimerov R., Vaulin S., Safonov E., and Zherebtsov D., “Selective laser melting of copper by 200 W CO2 laser,” in *SAE technical paper series*, 2016, vol. 20, pp. 215–227 doi: 10.4271/2016-01-0333

[172] Louvis E., Fox P., and Sutcliffe C. J., “Selective laser melting of aluminium components,” *Journal of Materials Processing Technology*, vol. 211, no. 2, pp. 275–284, Feb. 2011 doi: 10.1016/j.jmatprotec.2010.09.019

[173] Kimura T., Nakamoto T., Mizuno M., and Araki H., “Effect of silicon content on densification, mechanical and thermal properties of Al-xSi binary alloys fabricated using selective laser melting,” *Materials Science and Engineering: A*, vol. 682, no. September 2016, pp. 593–602, Nov. 2016 doi: 10.1016/j.msea.2016.11.059

[174] Widmer J. D., Spargo C. M., Atkinson G. J., and Mecrow B. C., “Solar plane propulsion motors with precompressed aluminum stator windings,” *IEEE Transactions on Energy Conversion*, vol. 29, no. 3, pp. 681–688, Sep. 2014 doi: 10.1109/tec.2014.2313642

[175] Widmer J. D., Martin R., and Mecrow B. C., “Precompressed and stranded aluminum motor windings for traction motors,” *IEEE Transactions on Industry Applications*, vol. 52, no. 3, pp. 2215–2223, May 2016 doi: 10.1109/tia.2016.2528226

[176] Sullivan C. R., “Aluminum windings and other strategies for high-frequency magnetics design in an era of high copper and energy costs,” *IEEE Transactions on Power Electronics*, vol. 23, no. 4, pp. 2044–2051, Jul. 2008 doi: 10.1109/tpel.2008.925434

[177] Flemings M. C., “Solidification Processing,” in *Materials Science and Technology*, R. W. Cahn, P. Haasen, and E. J. Kramer, Eds. Weinheim, Germany: Wiley-VCH Verlag GmbH & Co. KGaA, 2006 doi: 10.1002/9783527603978.mst0173

[178] Zhao X., Song B., Fan W., Zhang Y., and Shi Y., “Selective laser melting of carbon/AlSi10Mg composites: Microstructure, mechanical and electronical properties,” *Journal of Alloys and Compounds*, vol. 665, pp. 271–281, Apr. 2016 doi: 10.1016/j.jallcom.2015.12.126

[179] Mauduit A., Pillot S., and Frascati F., “Application study of AlSi10Mg alloy by selective laser melting: Physical and mechanical properties, microstructure, heat treatments and manufacturing of aluminium metallic matrix composite (MMC),” *Metallurgical Research & Technology*, vol. 112, no. 6, p. 605, Nov. 2015 doi: 10.1051/metal/2015039

[180] Tang M., “Inclusions, porosity, and fatigues of AlSi10Mg parts produced by selective laser melting,” Carnegie Mellon University, 2017. Available: http://repository.cmu.edu/dissertations/903

[181] Olakanmi E. O., Cochrane R. F., and Dalgarno K. W., “A review on selective laser sintering/melting (SLS/SLM) of aluminium alloy powders: Processing, microstructure, and properties,” *Progress in Materials Science*, vol. 74, no. 1, pp. 401–477, Oct. 2015 doi: 10.1016/j.pmatsci.2015.03.002

[182] Aboulkhair N. T., Everitt N. M., Maskery I., Ashcroft I., and Tuck C., “Selective laser melting of aluminum alloys,” *MRS Bulletin*, vol. 42, no. 04, pp. 311–319, Apr. 2017 doi: 10.1557/mrs.2017.63

[183] Aboulkhair N. T., Everitt N. M., Ashcroft I., and Tuck C., “Reducing porosity in AlSi10Mg parts processed by selective laser melting,” *Additive Manufacturing*, vol. 1–4, pp. 77–86, Oct. 2014 doi: 10.1016/j.addma.2014.08.001

[184] Aboulkhair N. T., Maskery I., Tuck C., Ashcroft I., and Everitt N. M., “On the formation of AlSi10Mg single tracks and layers in selective laser melting: Microstructure and nano-mechanical properties,” *Journal of Materials Processing Technology*, vol. 230, pp. 88–98, Apr. 2016 doi: 10.1016/j.jmatprotec.2015.11.016

[185] Brandl E., Heckenberger U., Holzinger V., and Buchbinder D., “Additive manufactured AlSi10Mg samples using selective laser melting (SLM): Microstructure, high cycle fatigue, and fracture behavior,” *Materials & Design*, vol. 34, pp. 159–169, Feb. 2012 doi: 10.1016/j.matdes.2011.07.067

[186] Aboulkhair N. T., Tuck C., Ashcroft I., Maskery I., and Everitt N. M., “On the precipitation hardening of selective laser melted AlSi10Mg,” *Metallurgical and Materials Transactions A*, vol. 46, no. 8, pp. 3337–3341, Aug. 2015 doi: 10.1007/s11661-015-2980-7

[187] Karg M., Ahuja B., and Schmidt M., “Processability of high strength aluminium-copper alloys AW-2022 and 2024 by laser beam melting in powder bed,” in *Proceedings of the 25th Solid Freeform Fabrication Symposium (SFF)*, Austin, Texas, USA, 2014, pp. 420–436. Available: http://sffsymposium.engr.utexas.edu/sites/default/files/2014-036-Karg.pdf

[188] Fulcher B. A., Leigh D. K., and Watt T. J., “Comparison of AlSi10Mg and Al 6061 processed through DMLS,” in *Proceedings of the 25th Solid Freeform Fabrication Symposium (SFF)*, Austin, Texas, USA, 2014, pp. 404–419. Available: http://sffsymposium.engr.utexas.edu/sites/default/files/2014-035-Fulcher.pdf

[189] Montero Sistiaga M. L., Mertens R., Vrancken B., Wang X., Van Hooreweder B., Kruth J.-P. P., and Van Humbeeck J., “Changing the alloy composition of Al7075 for better processability by selective laser melting,” *Journal of Materials Processing Technology*, vol. 238, pp. 437–445, Dec. 2016 doi: 10.1016/j.jmatprotec.2016.08.003

[190] Wigley P. B., Everitt P. J., van den Hengel A., Bastian J. W., Sooriyabandara M. A., McDonald G. D., Hardman K. S., Quinlivan C. D., Manju P., Kuhn C. C. N., Petersen I. R., Luiten A. N., Hope J. J., Robins N. P., and Hush M. R., “Fast machine-learning online optimization of ultra-cold-atom experiments,” *Scientific Reports*, vol. 6, no. 1, p. 25890, Sep. 2016 doi: 10.1038/srep25890

[191] Silver D., Hubert T., Schrittwieser J., Antonoglou I., Lai M., Guez A., Lanctot M., Sifre L., Kumaran D., Graepel T., Lillicrap T., Simonyan K., and Hassabis D., “Mastering chess and shogi by self-play with a general reinforcement learning algorithm,” Dec. 2017. Available: http://arxiv.org/abs/1712.01815

[192] Silver D., Schrittwieser J., Simonyan K., Antonoglou I., Huang A., Guez A., Hubert T., Baker L., Lai M., Bolton A., Chen Y., Lillicrap T., Hui F., Sifre L., van den Driessche G., Graepel T., and Hassabis D., “Mastering the game of Go without human knowledge,” *Nature*, vol. 550, no. 7676, pp. 354–359, Oct. 2017 doi: 10.1038/nature24270

[193] De Fauw J., Ledsam J. R., Romera-Paredes B., Nikolov S., Tomasev N., Blackwell S., Askham H., Glorot X., O'Donoghue B., Visentin D., van den Driessche G., Lakshminarayanan B., Meyer C., Mackinder F., Bouton S., Ayoub K., Chopra R., King D., Karthikesalingam A., Hughes C. O., Raine R., Hughes J., Sim D. A., Egan C., Tufail A., Montgomery H., Hassabis D., Rees G., Back T., Khaw P. T., Suleyman M., Cornebise J., Keane P. A., and Ronneberger O., "Clinically applicable deep learning for diagnosis and referral in retinal disease," *Nature Medicine*, vol. 24, no. 9, pp. 1342–1350, Sep. 2018 doi: 10.1038/s41591-018-0107-6

[194] Lecun Y., Bottou L., Bengio Y., and Haffner P., "Gradient-based learning applied to document recognition," *Proceedings of the IEEE*, vol. 86, no. 11, pp. 2278–2324, 1998 doi: 10.1109/5.726791

[195] Krizhevsky A., Sutskever I., and Hinton G. E., "ImageNet classification with deep convolutional neural networks," *Proceedings of the 26th Annual Conference on Neural Information Processing Systems (NIPS2012)*, Lake Tahoe, Nevada, USA, pp. 1106–1114, Dec-2012. Available: https://papers.nips.cc/paper/4824-imagenet-classification-with-deep-convolutional-neural-networks

[196] Hinton G. E. and Salakhutdinov R. R., "Reducing the dimensionality of data with neural networks," *Science*, vol. 313, no. 5786, pp. 504–507, Jul. 2006 doi: 10.1126/science.1127647

[197] Chaitanya C. R. A., Kaplanyan A. S., Schied C., Salvi M., Lefohn A., Nowrouzezahrai D., and Aila T., "Interactive reconstruction of Monte Carlo image sequences using a recurrent denoising autoencoder," *ACM Transactions on Graphics*, vol. 36, no. 4, pp. 98:1-98–12, Jul. 2017 doi: 10.1145/3072959.3073601

[198] van der Maaten L. and Hinton G., "Visualizing data using t-SNE," *Journal of Machine Learning Research*, vol. 9, no. Nov, pp. 2579–2605, 2008. Available: http://www.jmlr.org/papers/v9/vandermaaten08a.html

[199] Scime L. and Beuth J., "Anomaly detection and classification in a laser powder bed additive manufacturing process using a trained computer vision algorithm," *Additive Manufacturing*, vol. 19, pp. 114–126, Jan. 2018 doi: 10.1016/j.addma.2017.11.009

[200] Gobert C., Reutzel E. W., Petrich J., Nassar A. R., and Phoha S., "Application of supervised machine learning for defect detection during metallic powder bed fusion additive manufacturing using high resolution imaging.," *Additive Manufacturing*, vol. 21, no. 2010, pp. 517–528, May 2018 doi: 10.1016/j.addma.2018.04.005

[201] Kappes B., Moorthy S., Drake D., Geerlings H., and Stebner A., "Machine learning to optimize additive manufacturing parameters for laser powder bed fusion of Inconel 718," in *Proceedings of the 9th International Symposium on Superalloy 718 & Derivatives: Energy, Aerospace, and Industrial Applications*, Pittsburgh, Pennsylvania, USA, 2018, pp. 595–610 doi: 10.1007/978-3-319-89480-5_39

[202] Wang T., Kwok T.-H., Zhou C., and Vader S., "In-situ droplet inspection and closed-loop control system using machine learning for liquid metal jet printing," *Journal of Manufacturing Systems*, vol. 47, no. May 2017, pp. 83–92, Apr. 2018 doi: 10.1016/j.jmsy.2018.04.003

[203] Zhu Z., Anwer N., Huang Q., and Mathieu L., "Machine learning in tolerancing for additive manufacturing," *CIRP Annals*, vol. 67, no. 1, pp. 157–160, May 2018 doi: 10.1016/j.cirp.2018.04.119

[204] Guo X., Liu X., Zhu E., and Yin J., "Deep clustering with convolutional autoencoders," in *Lecture Notes in Computer Science (including subseries Lecture Notes in Artificial Intelligence and Lecture Notes in Bioinformatics)*, vol. 10635 LNCS, 2017, pp. 373–382 doi: 10.1007/978-3-319-70096-0_39

[205] Guo X., "XifengGuo/DCEC," 2017. [Online]. Available: https://github.com/xifengguo/dcec. [Accessed: 22-Jun-2018]

[206] "keras/mnist_cnn.py at master · keras-team/keras," 2015. [Online]. Available: https://github.com/keras-team/keras/blob/master/examples/mnist_cnn.py. [Accessed: 20-Jul-2018]

[207] David Robinson, "Exploring handwritten digit classification: A tidy analysis of the MNIST dataset," 2018. [Online]. Available: http://varianceexplained.org/r/digit-eda/. [Accessed: 15-Aug-2018]

[208] Tzoreff E., Kogan O., and Choukroun Y., "Deep discriminative latent space for clustering," *arXiv preprint: 1805.10795*, May 2018. Available: https://arxiv.org/abs/1805.10795v1

[209] Aboulkhair N. T., Maskery I., Tuck C., Ashcroft I., and Everitt N. M., "The microstructure and mechanical properties of selectively laser melted AlSi10Mg: The effect of a conventional T6-like heat treatment," *Materials Science and Engineering: A*, vol. 667, pp. 139–146, Jun. 2016 doi: 10.1016/j.msea.2016.04.092

[210] Cable R. I. and Gupta T. K., "Intermediate stage sintering," in *Proceedings of the International Conference on Sintering and Related Phenomena 1965 held at the University of Notre Dame*, New York, New York, USA, 1967, vol. 423, p. 894. Available: https://www.copper.org/resources/properties/129_6/consolidation.html#a2

[211] Hitzler L., Hirsch J., Heine B., Merkel M., Hall W., and Öchsner A., "On the anisotropic mechanical properties of selective laser-melted stainless steel," *Materials*, vol. 10, no. 10, p. 1136, Sep. 2017 doi: 10.3390/ma10101136

[212] Awd M., Stern F., Kampmann A., Kotzem D., Tenkamp J., and Walther F., "Microstructural characterization of the anisotropy and cyclic deformation behavior of selective laser melted AlSi10Mg structures," *Metals*, vol. 8, no. 10, p. 825, Oct. 2018 doi: 10.3390/met8100825

[213] Mfusi B. J., Tshabalala L. C., Popoola A. P. I., and Mathe N. R., "The effect of selective laser melting build orientation on the mechanical properties of AlSi10Mg parts," *IOP Conference Series: Materials Science and Engineering*, vol. 430, no. 1, p. 012028, Oct. 2018 doi: 10.1088/1757-899X/430/1/012028

[214] Renishaw plc., "Data sheet: AlSi10Mg-0403 (200 W) powder for additive manufacturing," 2015. [Online]. Available: https://resources.renishaw.com/en/details/data-sheet-alsi10mg-0403-200-w-powder-for-additive-manufacturing--73121. [Accessed: 16-Jun-2017]

[215] Bakhtiyarov S. I., Overfelt R. A., and Teodorescu S. G., "Electrical and thermal conductivity of A319 and A356 aluminum alloys," *Journal of Materials Science*, vol. 36, no. 19, pp. 4643–4648, 2001 doi: 10.1023/a:1017946130966

[216] Schindelin J., Arganda-Carreras I., Frise E., Kaynig V., Longair M., Pietzsch T., Preibisch S., Rueden C., Saalfeld S., Schmid B., Tinevez J.-Y., White D. J., Hartenstein V., Eliceiri K., Tomancak P., and Cardona A., “Fiji: An open-source platform for biological-image analysis,” *Nature Methods*, vol. 9, no. 7, pp. 676–682, Jul. 2012 doi: 10.1038/nmeth.2019

[217] Van Rossum G. and Drake Jr F. L., “Python reference manual,” Centrum voor Wiskunde en Informatica Amsterdam, Amsterdam, The Netherlands, The Netherlands, 1995. Available: https://docs.python.org/3/

[218] Pedregosa F., Varoquaux G., Gramfort A., Michel V., Thirion B., Grisel O., Blondel M., Prettenhofer P., Weiss R., and Dubourg V., “Scikit-learn: Machine learning in Python,” *Journal of Machine Learning Research*, vol. 12, no. Oct, pp. 2825–2830, 2011. Available: https://dl.acm.org/citation.cfm?id=2078195

[219] Abadi M., Agarwal A., Barham P., Brevdo E., Chen Z., Citro C., Corrado G. S., Davis A., Dean J., Devin M., Ghemawat S., Goodfellow I., Harp A., Irving G., Isard M., Jozefowicz R., Jia Y., Kaiser L., Kudlur M., Levenberg J., Mané D., Schuster M., Monga R., Moore S., Murray D., Olah C., Shlens J., Steiner B., Sutskever I., Talwar K., Tucker P., Vanhoucke V., Vasudevan V., Viégas F., Vinyals O., Warden P., Wattenberg M., Wicke M., Yu Y., and Zheng X., “TensorFlow: Large-scale machine learning on heterogeneous systems.” 2015. Available: https://www.tensorflow.org/

[220] Chollet F., “Keras.” 2015. Available: https://keras.io

[221] Tibshirani R., Walther G., and Hastie T., “Estimating the number of clusters in a data set via the gap statistic,” *Journal of the Royal Statistical Society: Series B (Statistical Methodology)*, vol. 63, no. 2, pp. 411–423, May 2001 doi: 10.1111/1467-9868.00293

[222] Sculley D., “Web-scale k-means clustering,” in *Proceedings of the 19th International World Wide Web Conference (WWW ’10)*, Raleigh, North Carolina, USA, 2010, pp. 1177–1178 doi: 10.1145/1772690.1772862

[223] Scherillo F., “Chemical surface finishing of AlSi10Mg components made by additive manufacturing,” *Manufacturing Letters*, vol. 19, pp. 5–9, Jan. 2019 doi: 10.1016/j.mfglet.2018.12.002

[224] Fathi P., Mohammadi M., Duan X., and Nasiri A. M., “A comparative study on corrosion and microstructure of direct metal laser sintered AlSi10Mg_200C and die cast A360.1 aluminum,” *Journal of Materials Processing Tech.*, vol. 259, no. October 2017, pp. 1–14, Sep. 2018 doi: 10.1016/j.jmatprotec.2018.04.013

[225] Atzeni E., Barletta M., Calignano F., Iuliano L., Rubino G., and Tagliaferri V., “Abrasive fluidized bed (AFB) finishing of AlSi10Mg substrates manufactured by direct metal laser sintering (DMLS),” *Additive Manufacturing*, vol. 10, pp. 15–23, 2016 doi: 10.1016/j.addma.2016.01.005

[226] Ma C., Dong Y., and Ye C., “Improving surface finish of 3D-printed metals by ultrasonic nanocrystal surface modification,” *Procedia CIRP*, vol. 45, pp. 319–322, 2016 doi: 10.1016/j.procir.2016.02.339

[227] Pradel P., Zhu Z., Bibb R., and Moultrie J., “A framework for mapping design for additive manufacturing knowledge for industrial and product design,” *Journal of Engineering Design*, vol. 29, no. 6, pp. 291–326, Jun. 2018 doi: 10.1080/09544828.2018.1483011

[228] Say M. G., *Alternating Current Machines*, 4th ed. London, United Kingdom: Pitman Publishing Ltd, 1976 ISBN: 027336197X

[229] Jack A. G., Mecrow B. C., Dickinson P. G., Stephenson D., Burdess J. S., Fawcett N., and Evans J. T., “Permanent-magnet machines with powdered iron cores and prepressed windings,” *IEEE Transactions on Industry Applications*, vol. 36, no. 4, pp. 1077–1084, 2000 doi: 10.1109/28.855963

[230] Baker N. J., Widmer J. D., Kulan M. C., and Lambert S. M., “Modelling the mechanical and thermal properties of compressed stator windings,” *8th IET International Conference on Power Electronics, Machines and Drives (PEMD 2016)*, Institution of Engineering and Technology, Glasgow, United Kingdom, Apr-2016 doi: 10.1049/cp.2016.0132

[231] Wawrzyniak B. I. and Tangudu J., “Design analysis of high power density additively manufactured induction motor,” in *SAE Technical Paper 2016-01-2063*, 2016 doi: 10.4271/2016-01-2063

[232] Madonna V., Walker A., Giangrande P., Serra G., Gerada C., and Galea M., “Improved Thermal Management and Analysis for Stator End-Windings of Electrical Machines,” *IEEE Transactions on Industrial Electronics*, vol. 66, no. 7, pp. 5057–5069, Jul. 2019 doi: 10.1109/TIE.2018.2868288

[233] King W. E., Barth H. D., Castillo V. M., Gallegos G. F., Gibbs J. W., Hahn D. E., Kamath C., and Rubenchik A. M., “Observation of keyhole-mode laser melting in laser powder-bed fusion additive manufacturing,” *Journal of Materials Processing Technology*, vol. 214, no. 12, pp. 2915–2925, Dec. 2014 doi: 10.1016/j.jmatprotec.2014.06.005

[234] Shi Y., Rometsch P., Yang K., Palm F., and Wu X., “Characterisation of a novel Sc and Zr modified Al–Mg alloy fabricated by selective laser melting,” *Materials Letters*, vol. 196, pp. 347–350, Jun. 2017 doi: 10.1016/j.matlet.2017.03.089

[235] Zhang B., Li Y., and Bai Q., “Defect formation mechanisms in selective laser melting: A review,” *Chinese Journal of Mechanical Engineering*, vol. 30, no. 3, pp. 515–527, May 2017 doi: 10.1007/s10033-017-0121-5

[236] Jadhav S. D., Dadbakhsh S., Goossens L., Kruth J.-P., Van Humbeeck J., and Vanmeensel K., “Influence of selective laser melting process parameters on texture evolution in pure copper,” *Journal of Materials Processing Technology*, vol. 270, no. February, pp. 47–58, Aug. 2019 doi: 10.1016/j.jmatprotec.2019.02.022

[237] Espinal A. E., Yan Y., Zhang L., Espinal L., Morey A., Wells B. O., Aindow M., and Suib S. L., “Substrate control of anisotropic resistivity in heteroepitaxial nanostructured arrays of cryptomelane manganese oxide on strontium titanate,” *Small*, vol. 10, no. 1, pp. 66–72, Jan. 2014 doi: 10.1002/smll.201300713

[238] Kempen K., Thijs L., Van Humbeeck J., and Kruth J.-P., “Mechanical properties of AlSi10Mg produced by selective laser melting,” *Physics Procedia*, vol. 39, pp. 439–446, 2012 doi: 10.1016/j.phpro.2012.10.059

[239] Ko M.-S. and Kim Y.-J., “Resistivity tensor imaging via network discretization of Faraday’s law,” *SIAM Journal on Imaging Sciences*, vol. 10, no. 1, pp. 1–25, Jan. 2017 doi: 10.1137/16m1074643

[240] Rossiter P. L., *The Electrical Resistivity of Metals and Alloys*. Cambridge University Press, 1991 ISBN: 9780521408721

[241] Rosenthal I., Stern A., and Frage N., “Microstructure and mechanical properties of AlSi10Mg parts produced by the laser beam additive manufacturing (AM) technology,” *Metallography, Microstructure, and Analysis*, vol. 3, no. 6, pp. 448–453, Dec. 2014 doi: 10.1007/s13632-014-0168-y

[242] Trevisan F., Calignano F., Lorusso M., Pakkanen J., Aversa A., Ambrosio E. P., Lombardi M., Fino P., and Manfredi D., “On the selective laser melting (SLM) of the AlSi10Mg alloy: Process, microstructure, and mechanical properties,” *Materials*, vol. 10, no. 1, p. 76, Jan. 2017 doi: 10.3390/ma10010076

[243] Lam L. P., Zhang D. Q., Liu Z. H., and Chua C. K., “Phase analysis and microstructure characterisation of AlSi10Mg parts produced by Selective Laser Melting,” *Virtual and Physical Prototyping*, vol. 10, no. 4, pp. 207–215, Oct. 2015 doi: 10.1080/17452759.2015.1110868

[244] EOS GmbH, “Material data sheet EOS aluminium AlSi10Mg for EOSINT M 270,” *[Online]*, May-2011. [Online]. Available: http://www.eos.info/8837de942d78d3b3

[245] Hamidi Nasab M., Falzetti A., Redaelli A., Lecis N., Giussani A., Sala L., and Vedani M., “Finishing of internal and external surfaces produced by powder bed fusion,” in *SIG Additive Manufacturing*, Leuven, Belgium, 2017, no. October 2017. Available: https://www.euspen.eu/knowledge-base/AM17104.pdf

[246] Rassolkin A., Kallaste A., Vaimann T., and Tiismus H., “Control challenges of 3D printed switched reluctance motor,” in *2019 26th International Workshop on Electric Drives: Improvement in Efficiency of Electric Drives (IWED)*, 2019, vol. 1, pp. 1–5 doi: 10.1109/IWED.2019.8664282

[247] Kallaste A., Vaimann T., and Rassalkin A., “Additive design possibilities of electrical machines,” in *2018 IEEE 59th International Scientific Conference on Power and Electrical Engineering of Riga Technical University (RTUCON)*, 2018, pp. 1–5 doi: 10.1109/RTUCON.2018.8659828

[248] Simpson N. and Mellor P. H., “Additive manufacturing of shaped profile windings for minimal AC loss in electrical machines,” in *2018 IEEE Energy Conversion Congress and Exposition (ECCE)*, 2018, pp. 5765–5772 doi: 10.1109/ECCE.2018.8557999

[249] Trevisan F., “Study and characterisation of different metal alloys processed through laser powder bed fusion,” Politecnico di Torino, 2018. Available: http://hdl.handle.net/11583/2709711

[250] Murashkin M. Y., Sabirov I., Sauvage X., and Valiev R. Z., “Nanostructured Al and Cu alloys with superior strength and electrical conductivity,” *Journal of Materials Science*, vol. 51, no. 1, pp. 33–49, Jan. 2016 doi: 10.1007/s10853-015-9354-9

[251] “Design challenge 2016 - Additive world,” 2016. [Online]. Available: https://additiveworld.com/design-challenge/design-challenge-2016. [Accessed: 23-Mar-2016]

[252] Verkens D., “Study of the anodizing behaviour of additive manufactured AlSi10Mg aluminium alloy,” Vrije Universiteit Brussel, 2016. Available: https://www.scriptiebank.be/sites/default/files/thesis/2017-10/Donovan_Verkens.pdf

[253] Critchlow G., Ashcroft I., Cartwright T., and Bahrani D., “Anodising aluminum alloy,” Google Patents, USA, 12-Apr-2011. Available: https://patents.google.com/patent/US7922889B2

[254] *43-2013 - IEEE Recommended Practice for Testing Insulation Resistance of Electric Machinery*. Institute of Electrical and Electronics Engineers (IEEE), 2014 doi: 10.1109/ieeestd.2014.6754111

[255] “Military Specification: Anodic coatings for aluminum and aluminum alloys,” in *MIL-A-8625F*, Philadelphia, Pennsylvania, USA: Department of Defense Single Stock Point, 1993

[256] Walker H., “High temperature (Al2O3) insulation and light weight conductors,” in *Proceedings of the Conference on High-temperature Electronics*, Tucson, Arizona, USA, 1981, pp. 123–219. Available: https://ntrs.nasa.gov/search.jsp?R=19820007464

[257] Rajashekara K., “Present status and future trends in electric vehicle propulsion technologies,” *IEEE Journal of Emerging and Selected Topics in Power Electronics*, vol. 1, no. 1, pp. 3–10, Mar. 2013 doi: 10.1109/jestpe.2013.2259614

[258] Revilla R. I., Verkens D., Couturiaux G., Malet L., Thijs L., Godet S., and De Graeve I., “Galvanostatic anodizing of additive manufactured Al-Si10-Mg alloy,” *Journal of The Electrochemical Society*, vol. 164, no. 14, pp. C1027–C1034, Dec. 2017 doi: 10.1149/2.1121714jes

[259] Zhu B., Seifeddine S., Persson P. O. Å., Jarfors A. E. W., Leisner P., and Zanella C., “A study of formation and growth of the anodised surface layer on cast Al-Si alloys based on different analytical techniques,” *Materials & Design*, vol. 101, pp. 254–262, Jul. 2016 doi: 10.1016/j.matdes.2016.04.013

[260] Fratila-Apachitei L. E., Tichelaar F. D., Thompson G. E., Terryn H., Skeldon P., Duszczyk J., and Katgerman L., “A transmission electron microscopy study of hard anodic oxide layers on AlSi(Cu) alloys,” *Electrochimica Acta*, vol. 49, no. 19, pp. 3169–3177, Aug. 2004 doi: 10.1016/j.electacta.2004.02.030

[261] Walsh F. C., Low C. T. J., Wood R. J. K., Stevens K. T., Archer J., Poeton A. R., and Ryder A., “Plasma electrolytic oxidation (PEO) for production of anodised coatings on lightweight metal (Al, Mg, Ti) alloys,” *Transactions of the IMF*, vol. 87, no. 3, pp. 122–135, 2009 doi: 10.1179/174591908x372482

[262] Wang L. and Nie X., “Silicon effects on formation of EPO oxide coatings on aluminum alloys,” *Thin Solid Films*, vol. 494, no. 1–2, pp. 211–218, 2006 doi: 10.1016/j.tsf.2005.07.184

[263] Shrestha S. and Dunn B. D. D., “Advanced plasma electrolytic oxidation treatment for protection of light weight materials and structures in a space environment,” *Surface World*, pp. 40–44, Nov-2007. Available: http://esmat.esa.int/Publications/Published_papers/Keronite2007paper.pdf

Appendix

Insulation techniques

NOTE: For a more complete look at anodising AlSi10Mg which has been processed by AM, refer to this Master's thesis [252].

For an electric coil to properly function and generate the desired magnetic field, every loop in the coil needs to be insulated from each other to prevent a short circuit. While this can be done with any material that is non-conductive (i.e. has a very high electrical resistance), there are other properties that need to be considered. These include having a high breakdown voltage, a low dissipation factor (low AC losses), and a high thermal class rating (temperature at which it is still sufficiently insulative). An ideal insulation material that can exhibit all these properties is ceramic. An advantage of using aluminium as a base material in electrical applications is that the surface of a specimen can be converted to the ceramic Aluminium Oxide (also known as alumina or Al_2O_3) through the process of anodisation.

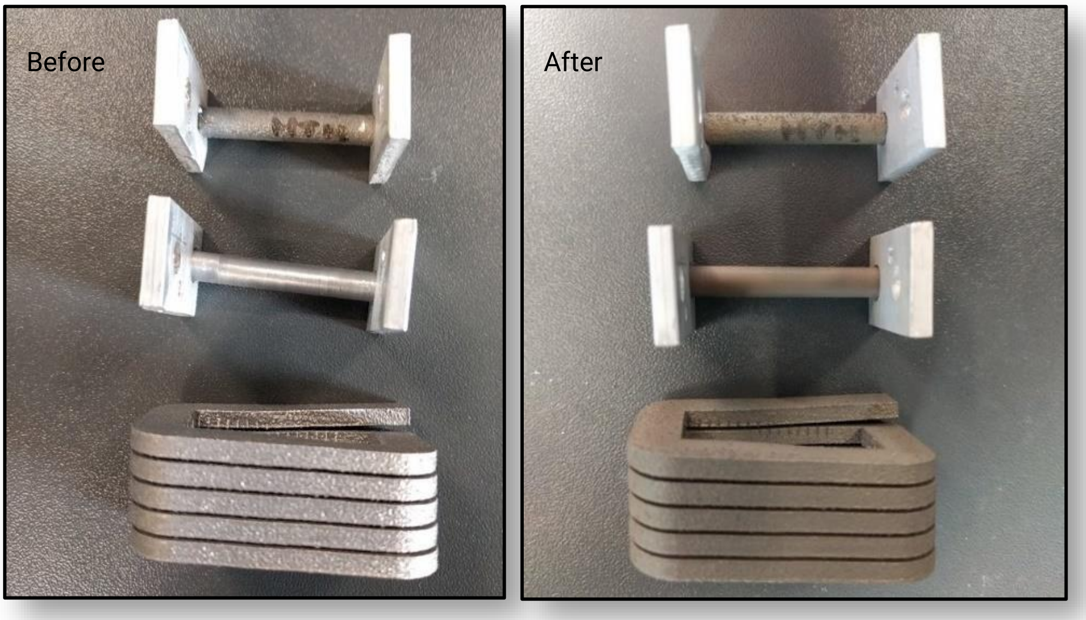

Figure 0-1: Before (left) and after (right) of an anodisation test on AlSi10Mg parts.

An anodic oxide AC anodisation process using sulphuric acid was used on some specimens as seen in Figure 0-1. The top two specimens in Figure 0-1 have non-3D printed end tabs which were welded to the AlSi10Mg cylinders as part of an early investigative test for reducing contact resistances. Additional details of this process were not shared as it was performed by a third-party. However, AC anodisation processes can utilise chemicals such as sulphuric acid, hexavalent chromium, or boric acid [253], some of which are a hazard to health and the environment, which was why a third-party process was sought. This process reacted differently for the two alloys as evident by the large colour difference between the 3D printed and non-3D printed alloys.

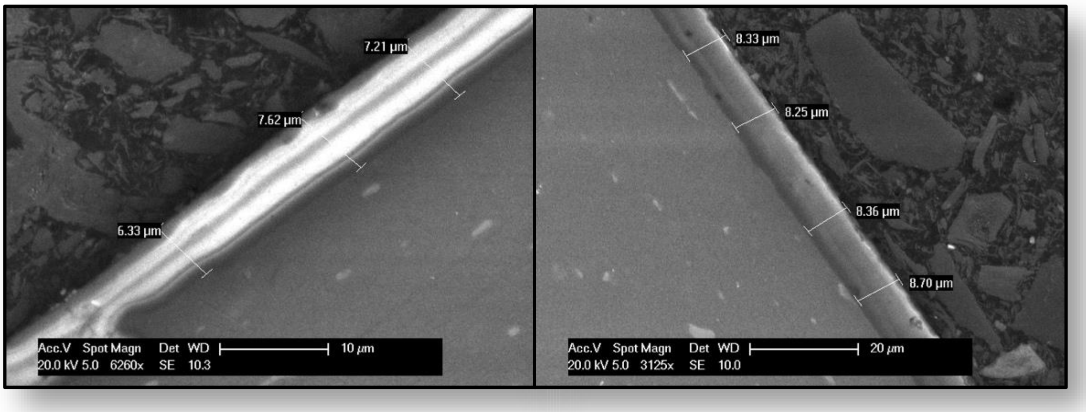

Figure 0-2: Anodisation thickness for a traditional aluminium alloy between 6 and 9 µm.

Figure 0-3: Anodisation thickness for the AlSi10Mg alloy between 2 and 3 µm.

Using SEM and EDX, it was revealed that the end tabs had approximately 1% manganese-Mn (AlSi10Mg has 0.06%) and had less than 0.5% silicon (AlSi10Mg has 10%). These end tabs were likely a 6061 aluminium alloy which typically has 1.2% Mn but less than 0.8% Si and is also a common alloy for use in bar stock. The anodisation layer for the end tabs had an almost clear appearance and resulted in a thickness of between 6 to 9 µm, as seen in Figure 0-2. However, for the AlSi10Mg, the anodisation layer was a dark grey-brown colour and was a third of the thickness of the end tabs at between 2 and 3 µm, as seen in Figure 0-3.

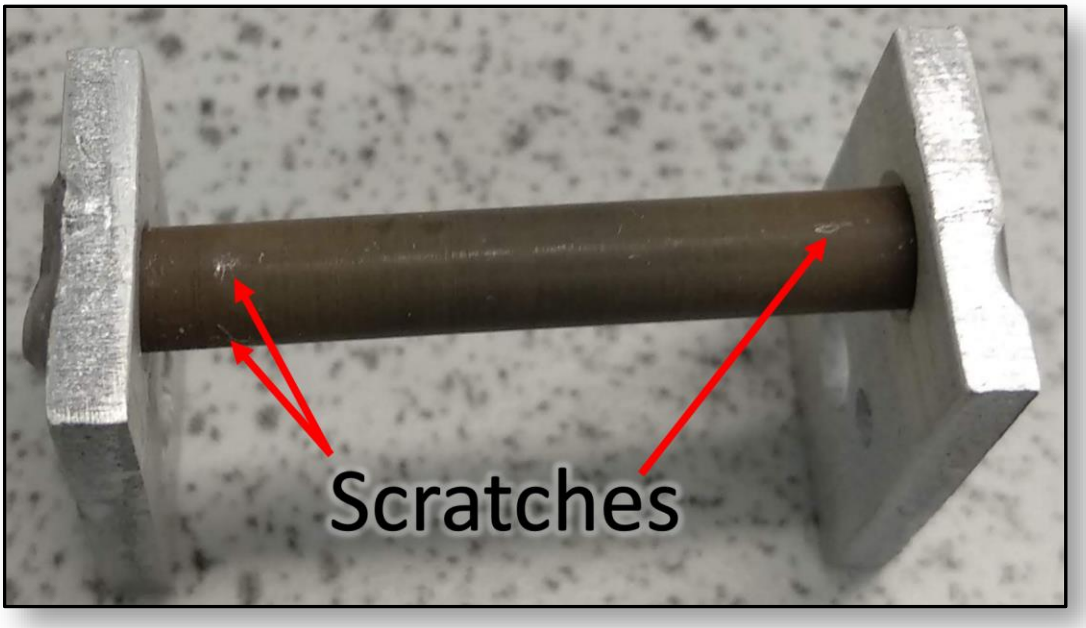

Figure 0-4: After testing the insulative ability of the anodised AlSi10Mg, scratches appeared on the surface.

Tests were performed on the durability and insulative ability of the anodised layer on both the AlSi10Mg and the non-printed end tabs using an LCR meter. The end tabs when tested with a light pressure registered an infinite resistance, and with hard pressure measured between an infinite resistance and 99 MΩ. A standard calculation from the Institute of Electrical and Electronics Engineers (IEEE) for electrical insulation is that one megaohm (MΩ) is required for every kV of operating voltage, plus one extra megaohm [254] (i.e., a 1 kV application requires 2 MΩ, and a 10 kV application requires 11 MΩ). For AlSi10Mg, when tested with a light pressure, an infinite resistance was also encountered. However, when a hard pressure was applied, the resistance greatly changed and became around 45 µΩ which was a short circuit. Afterward, it could be seen where the probes were touching the specimen, as scratches exposed the bare aluminium below as seen in Figure 0-4. When re-testing at those same locations, even a light pressure resulted in the short circuit values. This indicated that the anodised surface had been removed and no longer provided any insulation ability.

For a reference on insulation, the military specification MIL-A-8625 (Type II) which uses sulphuric acid, typically creates an anodisation thickness of between 1.7 and 25 μm [255]. In addition, Al_2O_3 has a breakdown voltage of between 35 to 40 volts per μm [256]. In the case of AlSi10Mg, the maximum voltage the 2 to 3 μm thick anodisation could withstand before breakdown is between 70 and 120 volts. But in order to take advantage of the weight advantage which aluminium has over copper for electric motor applications in transport, the voltage rating needs to be between 240 and 1000 volts [257] as most inverters used in propulsion operate within this range. This would require an insulation layer of between 8 and 30 μm thick. Despite the end tabs having an average thickness of 8 μm, the AlSi10Mg was significantly less. Recent attempts at anodising AlSi10Mg processed by LPBF and by casting [258] has shown that the LPBF specimens have a reduced thickness compared to cast due to the unique microstructure, however, only as-built samples were used in that study. The LPBF microstructure causes the silicon in the alloy to be more evenly distributed within the material than the cast version which has much larger silicon particles randomly throughout the material. Silicon in general disrupts the oxide growth in the anodisation process, as it causes the front of the growth to move around the particle [259], [260] which slows growth overall and can cause additional voids and pores to form in the oxide layer. It was found in [259] that both high silicon content as well as alloys which were solidified at high cooling rates caused the oxide layer to be thinner than those with lower silicon and slower cooling rates.

In order to achieve thicker insulative layers, the anodisation process could be applied to non-as-built specimens such as the T6-like heat treatment [186] which causes the silicon to precipitate into larger particles that are not as evenly dispersed. Alternate anodisation techniques could be explored such as hard anodisation which works at colder temperatures (-10 to 0 °C) compared to normal anodisation (above room temperature) and which uses lower currents and voltages. Hard anodisation typically can produce a thickness of 50 µm with traditional Al alloys and has been shown to create a thickness of up to 90 µm with an aluminium alloy with 10 per cent by weight silicon [260]. Another alternative for creating thicker oxide layers is plasma electrolytic oxidation (PEO) [261]. In this process, an oxide layer is created by an electrochemical reaction along with dissolution and dielectric breakdown of the material. It operates at higher voltages (120-300 V) and can create layers up to 200 µm thick. It has been used with high silicon content aluminium alloys with results of thickness of over 50 µm [262] with a conclusion that for thicker layers, the silicon content in the base material is less significant for creating thicker layers as the layer build-up after this point relies more on the electrolyte and less on the underlying substrate. However, PEO does produce a much rougher surface than anodisation and contains a higher amount of internal porosity within the coating.

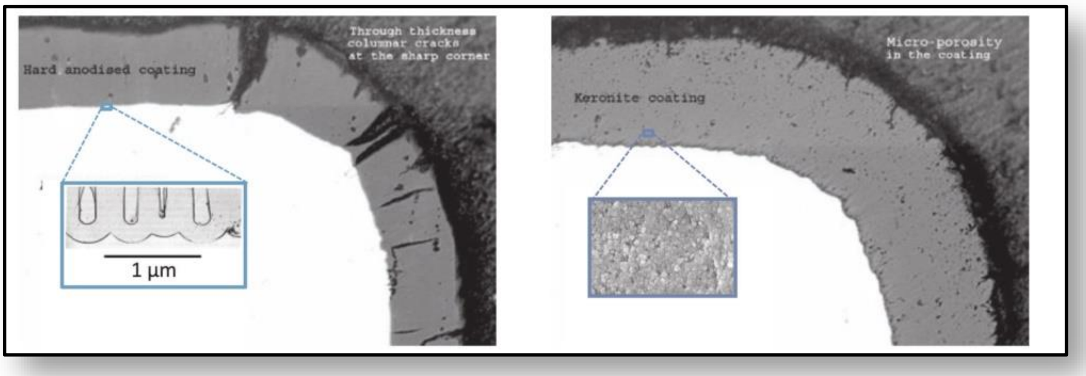

Figure 0-5: Comparison of a hard-anodising layer and a PEO layer [263].

Insulation is required between coils, and while it is possible to anodise AlSi10Mg, the high Si content disrupts the oxide formation and results in a very thin and brittle layer.

One last area for this alloy to be used in electrical applications which needed to be explored was the ability to electrically insulate the surface. Anodisation of aluminium creates an oxide ceramic layer which is electrically insulative. Samples that were created by AM were anodised along with tabs which were composed of an aluminium alloy with a lower silicon content than AlSi10Mg. Despite showing signs of being insulated, the resulting layer on the AM portion was thin and fragile compared to the traditional tabs. The increased silicon content along with the more uniform distribution of that silicon due to the LPBF process inhibited the growth of the oxide layer. However, there are several other techniques which could be favourable for insulating LPBF AlSi10Mg such as hard anodisation and plasma electrolytic oxidation that could be explored in the future.

Insulation through an anodisation process can greatly improve the surface electrical resistance, however, with this alloy, the high amount of silicon and the unique microstructure caused the thickness of the anodisation layer to be reduced to below what is desirable for electrical applications. Several other insulations techniques exist which can create thicker insulating layers which could be explored in the future.

Insulation techniques and qualification

While the anodisation results showed potential, there is much room for improvement. Processes such as hard anodisation or plasma electrolytic oxidation should be explored to create a uniform and predictable and robust electrically insulative layer. Traditional insulation methods such as dipping should be investigated to prove their effectiveness on geometry created by AM as they provide a cost-effective alternative to oxidation techniques for Al alloys, and may be the only solution for pure Cu. However, oxidation techniques may create a more uniform insulation layer when the geometry is complex as dipping may lead to uneven distribution of the coating. The thickness of the insulation and its associated thermal conductivity need to be investigated in order to achieve high fill-factors and end-turn thermal dissipation features that AM manufactured coils can provide.